
Experiments on Multiphoton Entanglement

Nikolai Kiesel

Dissertation
an der Fakultät für Physik
der Ludwig-Maximilians-Universität
in München

vorgelegt von
Nikolai Kiesel
aus Nürnberg

München, den 03.08.07

Erstgutachter: Prof. Dr. Harald Weinfurter
Zweitgutachter: Prof. Dr. Axel Schenzle
Tag der mündlichen Prüfung: 05.11.07

Zusammenfassung

Als zentrales Element der Quantenmechanik fordert Verschränkung nicht nur immer wieder die Intuition von Physikern heraus, sondern bildet dabei auch die elementare Ressource für verschiedene Schemata der Quantenkommunikation und des Quantenrechnens. Wichtiger Bestandteil vieler dieser Anwendungen ist die Vielteilchenverschränkung. Daher wurde deren Beschreibung, Erzeugung und Manipulation ein sehr aktives Gebiet der theoretischen und experimentellen Quanteninformationswissenschaften. Die Herausforderung liegt hierbei im Verständnis und der Charakterisierung der verschiedenen Typen von Vielteilchenverschränkung, dem Finden neuer Anwendungen sowie der experimentellen Kontrolle und Analyse von Quantenzuständen.

Die vorliegende Dissertation beschäftigt sich mit der experimentellen Beobachtung und Analyse von zwei verschiedenen Typen polarisationsverschränkter Vier-Photonen-Zustände: Denen des Cluster-Zustands und des symmetrischen Dicke-Zustands mit zwei Anregungen. Die zu diesem Zweck entwickelten Versuchsaufbauten basieren auf einer Kombination aus spontaner parametrischer Fluoreszenz und linearer Optik sowie bedingter Detektion. Der Cluster-Zustand kann damit mit einer Fidelity von 74.1% und der symmetrische Dicke-Zustand mit einer Fidelity von 84.4% nachgewiesen werden. Im Rahmen des Clusterzustandsexperiments wurde ferner ein Instrument entwickelt, das von allgemeinem Interesse für Anwendungen ist, die auf linear-optischer Quantenlogik beruhen: Ein probabilistisches kontrolliertes Phasengatter das durch die Verbesserung einer bereits früher realisierten Version sehr stabil und daher besonders gut für die Verwendung in Mehrphotonenexperimenten geeignet ist. Um die Qualität des Gatters zu untersuchen, wurde dessen Fähigkeit Verschränkung zu erzeugen eingehend untersucht sowie eine Prozesstomographie durchgeführt. Die erzielten Resultate stellen eine erfolgreiche Anwendung des Gatters in verschiedenen Quanteninformationsprotokollen in Aussicht.

Zur genaueren Untersuchung der beobachteten Zustände, werden effiziente Analysemethoden vorgestellt. Diese ermöglichen den Nachweis verschiedener grundlegender Eigenschaften der idealen Zustände im Experiment; unter anderem echte Vierteilchenverschränkung. Ein besonderer Schwerpunkt liegt auf der Untersuchung des Verhaltens der Zustände bei projektiven Messungen und dem Verlust einzelner Photonen. Dabei werden neue Einsichten in die Verschränkungsstruktur der Zustände gewonnen und experimentell bestätigt. Des Weiteren werden Eigenschaften, die für die Verschränkungsklasse der Zustände charakteristisch sind, aufgezeigt. Die gewonnen Erkenntnisse können benutzt werden um die Verwendbarkeit der Zustände für bestimmte Quantenkommunikationsanwendungen abzuleiten.

Die gezeigten Experimente sind generisch für den Entwurf experimenteller Aufbauten zur Beobachtung von Cluster- und symmetrischen Dicke-Zuständen mit höherer Photonenzahl. Selbiges gilt auch für die verwendeten effizienten nicht-tomographischen Methoden zur Zustandsanalyse, wobei die damit verbundene Reduzierung des experimentellen Aufwands besonders bei hohen Photonenzahlen eine entscheidende Rolle spielt.

Summary

Entanglement lies at the heart of quantum mechanics and challenged the intuition of physicists ever since it was discovered. At the same time, it is a powerful tool that serves as a key resource for quantum communication and quantum computation schemes. Many of these applications rely on multiparticle entanglement, whose description, generation and manipulation became therefore a very active field in theoretical and experimental quantum information science. The goals are here to classify and understand the different types of entanglement, to find new applications and to control and analyze the quantum states experimentally.

In this thesis, the experimental observation and analysis of two different types of four-photon polarization entangled states is presented: The cluster state and the symmetric Dicke state with two excitations. For this purpose, experimental setups based on spontaneous parametric down conversion and linear optics with conditional detection were designed. They allowed to observe the cluster state with a fidelity of 74.1% and the symmetric Dicke state with a fidelity of 84.4%. The cluster state experiment included the development of a new instrument that is of interest for linear optics quantum logic in general: A probabilistic controlled phase gate that is, due to the simplification of a previous approach, highly stable and can actually be used in multiphoton experiments. The quality of the gate is evaluated by analyzing its entangling capability and by performing full process tomography. The achieved results demonstrate that this device is well suited for implementation in various multiphoton quantum information protocols.

In order to study the observed quantum states, efficient analysis tools are introduced. It was possible to verify that essential properties of the ideal states are indeed reproduced in the experiment, among others, the presence of genuine four-partite entanglement. A particular focus is put on the behavior of the states under projective measurements and photon loss. Several new insights in their entanglement structure are revealed and verified experimentally. We further demonstrate properties that are characteristic for the entanglement classes of the states. These can be used to infer the applicability of the observed states for certain distributed quantum communication applications.

The presented experiments are generic for the design of setups to observe cluster- and symmetric Dicke states with a higher number of photons. Furthermore, also the efficient non-tomographic methods for state analysis we employ can directly be generalized to experiments with higher qubit numbers, where the reduction of the experimental effort for state analysis is even more crucial.

Contents

1	Introduction	1
2	Entanglement of Qubits	5
2.1	Description of qubit states	5
2.1.1	The quantum bit	5
2.1.2	Multiqubit states	7
2.1.3	Mixed states	8
2.2	Bipartite entanglement	10
2.2.1	Bell states	10
2.2.2	Mixed entangled states	11
2.2.3	Two-qubit operations	12
2.2.4	Quantum teleportation	14
2.3	Separability criteria and entanglement measures	16
2.3.1	Definition of entanglement measures	16
2.3.2	Entropy, entanglement of formation and concurrence	17
2.3.3	The Peres-Horodecki criterion and negativity	18
2.3.4	Entanglement witnesses and the geometric measure	19
2.4	Summary	22
3	Classifications of Multipartite Entanglement	23
3.1	Classification via SLOCC	24
3.1.1	Three-qubit classification	24
3.1.2	Four-qubit classification	27
3.2	Phenomenology of quantum states	28
3.2.1	Graph states	28
3.2.2	Dicke states	30
3.2.3	Overview of important four-qubit entangled states	33
3.3	Properties of entangled states	35
3.3.1	Permutation symmetry	36
3.3.2	Entanglement persistency	38
3.3.3	Connectedness	40
3.4	Summary	41
4	Entanglement Engineering with Polarized Photons	43
4.1	Generation of photons	43
4.1.1	Spontaneous parametric down conversion	43
4.1.2	Experimental implementation	46
4.2	Processing photons	47
4.2.1	Wave plates	48

4.2.2	Beam splitters	49
4.3	From clicks to density matrices	51
4.3.1	Correlation measurements	51
4.3.2	Quantum state tomography	52
4.3.3	Evaluation of relevant values	55
4.3.4	Quantum process tomography	57
4.4	Summary	60
5	The Phase Gate	61
5.1	Basic idea and model	62
5.1.1	Scheme for ideal phase gate	62
5.1.2	Modeling distinguishable photons	64
5.1.3	Modeling general components	65
5.2	Experimental setup	67
5.3	Experimental analysis of the gate	70
5.3.1	Description of the experimental process	71
5.3.2	Entangling capability of the gate	75
5.4	Summary	77
6	The Cluster State	79
6.1	Experimental setup	79
6.2	Experimental analysis	81
6.2.1	Global properties	82
6.2.2	Connectedness	87
6.2.3	Persistency against photon loss	91
6.3	Summary	93
7	The symmetric Dicke state with two excitations	95
7.1	Experimental setup	95
7.2	Experimental analysis	97
7.2.1	Global properties	98
7.2.2	Connectedness	102
7.2.3	Persistency against photon loss	107
7.3	Summary	110
8	Conclusions and Outlook	113
A	Geometric measures of entanglement	117
B	Relation between different states	118
B.1	Local transformations between G_3 and GHZ_3	118
B.2	Direct proof of state classification	118
C	Linear multiqubit tomography	121
D	Publication list	122

List of Figures

2.1	Bloch sphere	6
2.2	Scheme for quantum teleportation	15
2.3	Schematic drawing of mixed states with nested convex set of separable states and entanglement witnesses	20
3.1	Classification of three-qubit states	25
3.2	Inequivalent connected three- and four-vertices graphs	29
3.3	Four-qubit Dicke states	31
3.4	Visualization of relevant symmetry groups	36
3.5	Schemes for open destination teleportation and quantum telecloning	39
4.1	Collinear and non-collinear SPDC, type II	45
4.2	Beam splitters: notation and polarization analysis	49
4.3	Superoperator of an ideal phase gate	60
5.1	Setup of linear optics controlled phase gate	63
5.2	Picture of experimental linear optics controlled phase gate setup	68
5.3	Two-photon Hong-Ou-Mandel interference	69
5.4	Overview of process tomography evaluation	70
5.5	Process matrices of experimental controlled phase gate	72
5.6	Process matrices with indistinguishable photons	73
5.7	Entanglement capability of the controlled phase gate	76
6.1	Cluster state setup	80
6.2	Four-photon Hong-Ou-Mandel interference	81
6.3	Cluster state: counting statistics	82
6.4	Cluster state: local entropy	84
6.5	Cluster state: density matrices after two projective measurements	91
6.6	Cluster state: density matrices after loss of two photons	93
7.1	Dicke state setup	96
7.2	Dicke state: counting statistics	98
7.3	Dicke state: local entropy	99
7.4	Dicke state: experimental density matrix	100
7.5	Dicke State: three-qubit density matrices after projective measurements or loss of one photon	103
7.6	Dicke state: witness measurements after after projective measurements or loss of one photon	104
7.7	Dicke state: density matrices after two projective measurements	106

List of Figures

7.8	Dicke state: entanglement and fidelity after two projective measurements	107
7.9	Dicke state: density matrices after loss of two photons	108
7.10	Dicke state: quantifying entanglement after loss of two photons	109
8.1	Comparison of four-qubit entangled symmetric Dicke and graph states . .	114

List of Tables

2.1	Operations of two-qubit gates on the computational basis	13
3.1	Geometric measure of multipartite quantum states	35
4.1	SPDC, experimental parameters	47
5.1	Fidelity of controlled phase gate output states	71
6.1	Cluster state: stabilizer correlations	85
6.2	Cluster state: GHZ witness after one projective measurement	88
6.3	Stabilizer correlations of $ \mathcal{C}^\pm\rangle_{abc}$	89
6.4	Cluster state: entanglement and fidelity after projective measurements on two qubits	90
6.5	Cluster state: witness measurements after loss of one photon	92

1 Introduction

With the beginning of the last century, a new era in physics started. Planck's derivation of the radiation law based on the quantum hypothesis constitutes the birth of quantum theory. Without any doubt, the following years have been one of the most exciting periods in the history of science. Scientists were impelled to invent new concepts that eluded man's intuition. Naturally, there was no consensus about the interpretation of the new theory. This also led to the historical debate between the distinguished physicists Albert Einstein and Niels Bohr [1].

One of the late objections Einstein raised together with Boris Podolski and Nathan Rosen is presented in the famous EPR-paper, published in 1935 [2]. They pointed at another puzzling element that is intrinsic to quantum theory and that was baptized "Verschränkung" (entanglement) by Erwin Schrödinger [3]. EPR argued that the counterintuitive features of entangled systems cause effects that demonstrate the incompleteness of quantum mechanics. In the following years, even though most physicists believed in the new theory, the doubts EPR had raised were not refuted in a satisfying way. Many years later, in 1964, John Bell resurrected the discussion about entanglement by showing that the intuitive assumptions made by EPR indeed lead to experimentally testable predictions that are not consistent with the predictions of quantum mechanics [4]. Since then, several tests of these so-called Bell inequalities have been performed: Already in the early ones, Bell inequalities were violated [5–7] in favor of quantum mechanics. However, certain loopholes that could "save" the classical description of the world were still open and have partly been closed later on [8, 9]. Yet, a really conclusive experiment is still missing.

In addition to these fundamental considerations, a new insight inspired the study of entanglement: Quantum mechanics enables new applications that are not, or less efficiently, achievable with classical mechanics and in most of the cases entanglement is an indispensable ingredient. Examples are quantum communication tasks like dense coding [10], (entanglement based) quantum cryptography [11] and quantum teleportation [12]. Further, it was shown that at least certain computational tasks can be solved more efficiently by quantum computers [13–16]. All these developments that raise the hope for secure communication networks and a new generation of supercomputers are part of the fastly growing field of quantum information. Entanglement lies at the heart of this young discipline.

Today, a considerable effort is put into the research on entanglement with no restriction to, but a strong emphasis on, two-level systems, i.e. qubits. Bipartite entanglement is well understood and has been prepared in many different physical systems. Naturally, the ambitious goals mentioned before also require entanglement between many parties. It was, however, understood that multipartite entangled systems have qualitatively different properties in comparison to bipartite ones: There exist different types of entanglement. Thus, it is necessary to classify entangled states, to understand their properties and to learn which states are interesting for which applications. The development of the ex-

perimental instruments to implement the different types of entanglement is required in addition to the complication to create and control entanglement between many particles at all. Finally, the analysis of such states requires methods for the detection and distinction of different quantum states. It is desirable that such methods are efficient, i.e. rely only on a relevant instead of a complete set of measurement data, because the experimental effort to determine the latter grows exponentially with the number of particles.

The first experiments on multipartite entanglement, conducted in the end of the 1990's, used entanglement in the polarization degree of freedom of photons. Important steps were the observation of a three-photon GHZ state [17], its violation of a new and more restrictive version of Bells inequality [18] and the first quantum teleportation [19]. Since then, entanglement of up to six photons was observed [20]. Entangled states were prepared in a variety of other physical systems, e.g. most notably, up to eight ions were entangled [21, 22]. Further, another type of multipartite states, i.e. W states, moved into the center of interest and were prepared experimentally. GHZ- and W states are the only two types of entanglement between three qubits [23]. The situation changes, however, drastically when we look at entanglement of even more particles: New types of entanglement appear [24–26].

This thesis describes the experimental implementation and characterization of two different types of four-photon entangled states, i.e. the cluster state and the symmetric Dicke state with two excitations. They belong, together with the GHZ- and the W states, to the families of graph and symmetric Dicke states, respectively:

Graph states are generated by next-neighbor interactions and occur naturally in solid state systems. They can be easily obtained in experiments on atomic lattices [27]. They are basic elements of various quantum error correcting codes [28] and multiparty quantum communication protocols [29–32]. A particular subfamily is formed by the cluster states, which moved into the center of interest in the context of the so-called one-way quantum computer scheme suggested by Briegel and Raussendorf [33, 34]. There, the cluster states serve as the initial resource of a universal computation scheme based on single-qubit operations only. Proof of principle experiments of such applications have very recently been demonstrated [35–38]. For four qubits, the GHZ and the cluster state form the only two inequivalent types of graph states.

Entangled symmetric Dicke states exhibit a very different type of entanglement that is closely related to their symmetry under permutation of particles. They are eigenstates of the spin operator in z direction with maximal total spin. R.H. Dicke identified them as the eigenstates of "super-radiant" gases where enhanced radiation caused by coherence occurs [39]. From the quantum information point of view, they are important because they exhibit a strong persistency against particle loss, showing that "significantly entangled states need not be fragile" [40]. For four qubits there are two entangled inequivalent representatives of symmetric Dicke states: The W state and the symmetric Dicke state with two excitations.

To experimentally implement the states, we rely on the techniques of spontaneous parametric down conversion for photon generation and linear optics setups and conditional detection for further processing. Linear optics solutions for the observation of the symmetric Dicke state with two excitations and the cluster state are developed, where the latter relies on a new component of high significance for photonic quantum logic in general: As the core of the cluster state setup, we designed, based on a simplification of a recent

approach [41–44], a linear optics controlled phase gate that is stable enough to allow the first application of a universal quantum gate in a multiphoton application. The gate is characterized by performing full process tomography, further by matching an accurate model of the gate to the obtained process matrix and by the analysis of its entangling capability.

The investigation of the observed quantum states has a two-fold goal: We want, on the one hand, to demonstrate the observation of the desired entanglement, on the other hand, to characterize the states, i.e. to investigate their properties. It is common to calculate the fidelity between the observed and the ideal quantum state to quantify their distance and thus to gain information about the experimentally achieved quality. In general, however, the fidelity does not tell whether the observed state exhibits the same, or a completely different type of entanglement. To date, there is no general strict method to discriminate different kinds of four-partite entangled *mixed* states from each other. We approach this task by a systematic study of the desired states’ properties and by testing whether and to which degree the observed states exhibit these properties. The characteristics we study can be related to the entanglement class and families of the desired states. We put a focus on the investigation of entanglement persistency and connectedness, i.e. the entanglement in the states after projective measurements or loss of qubits. Particularly here, we gain further insights in the entanglement structure of the states. In addition, we find methods to discriminate different types of entanglement and ways to deduce the applicability of the states for certain quantum communication protocols.

The analysis of the experimentally observed states with respect to these properties usually requires only a very restricted, relevant, part of information about a state. Thus, it is in general not necessary to determine its complete density matrix. Instead, we rely largely on efficient, non-tomographic tools, i.e. tools that allow to derive the states’ properties without the use of a complete set of data. To this end, we make extensive use of entanglement witnesses, which allows a partial classification of the observed states. We develop a strategy to study the permutation symmetry with a restricted set of measurements. The application of state tomography on subsets of particles allows, amongst others, to use the broad spectrum of tools that exist for the description of bipartite entangled states. For the cluster state, the efficient analysis is particularly simple due to its special entanglement structure. In case of the Dicke state we achieved a sufficiently high count rate and stability that we could indeed perform a full tomography of the state and apply our analysis tools to the complete set of data.

The thesis is structured as follows: Chapters two and three introduce theoretical concepts of two- and multiqubit entanglement. Then, in chapter four, we present the experimental methods and the evaluation strategies used in the experiments that are presented in chapters five, six and seven.

2 Entanglement of Qubits

The main goal in this thesis is the experimental implementation of polarization entangled four-photon states and their analysis with respect to strength, type and applicability of entanglement. Polarized photons are merely one possibility for the physical implementation of qubits, along with the spin- $\frac{1}{2}$ particles or two-level systems. Therefore, the following chapter concerns the description of single- and multiqubit states. Entanglement arises naturally from the superposition principle when states of more than one qubit are considered. Implications of entanglement are discussed on the example of some bipartite states, multiqubit entanglement is mainly considered in chapter 3. Several quantum operations that can be used to change the entanglement of states are introduced. Further, a prominent example for the application of entanglement in quantum communication is shown. Finally, theoretical tools for the detection and quantification of entanglement are presented.

2.1 Description of qubit states

In this section, the necessary notations and tools for the description of single- and multiqubit states are introduced. It is just a short overview and more detailed discussions on this subject can be found in standard literature like [45, 46]. First, the Hilbert space of a single qubit along with related measurements and quantum operations is introduced. Then, these concepts are generalized to multipartite quantum states and to statistical mixtures of quantum states.

2.1.1 The quantum bit

The notion of "qubit" (quantum bit) was introduced in a publication by Schumacher [47] in 1995. It expresses the fact that a qubit is the quantum mechanical counterpart of the classical bit. The physical implementation is in either case based on a system with two distinct states. In contrast to the classical case, however, quantum states are basis vectors in a Hilbert space. Any normalized linear combination of two states is, according to the superposition principle, another valid quantum state.

In this thesis, qubits are implemented as polarization states of photons. They can be expressed in terms of the two states $|H\rangle$ and $|V\rangle$ representing horizontal and vertical polarization, respectively. These states form the so-called Z -basis and are the common choice for the representation of vectors and matrices, i.e. the *computational basis*. The most general single qubit state is then given by (in different notations):

$$|\psi_{\theta,\phi}\rangle = \cos(\theta/2)|H\rangle + \sin(\theta/2)e^{i\phi}|V\rangle \hat{=} \begin{pmatrix} \cos(\theta/2) \\ \sin(\theta/2)e^{i\phi} \end{pmatrix}, \quad (2.1)$$

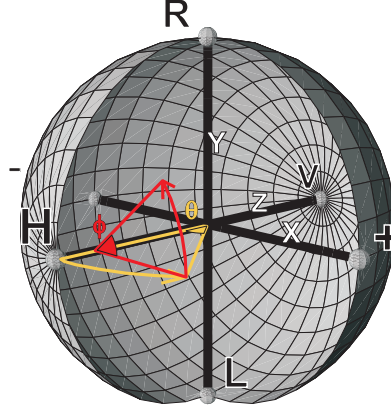


Figure 2.1: The surface of the Bloch sphere represents the Hilbert space of one qubit. The grid lines on the surface correspond to constant ϕ and θ of $|\psi_{\theta,\phi}\rangle$ in equation 2.1, respectively. The state is thus found via θ -rotation around the Y-axis and a ϕ -rotation around the Z-axis as indicated by the arrows. The eigenstates of the Pauli matrices ($\hat{\sigma}_x$, $\hat{\sigma}_y$, $\hat{\sigma}_z$) lie on the corresponding three orthogonal axis (X, Y, Z).

where $\theta \in [0, \pi]$ and $\phi \in [0, 2\pi[$. The Hilbert space of one qubit can conveniently be represented graphically by the Bloch sphere, figure 2.1. The state $|\psi_{\theta,\phi}\rangle$ is a vector corresponding to a point on the surface of the Bloch sphere figure 2.1. It is found by a rotation of the vector $|H\rangle$ with angle θ around the Y axis followed by a ϕ -rotation around the Z axis.

Measurements on quantum states are represented by observables, i.e. hermitian operators \hat{O} . Thereby, a quantum state $|\psi\rangle$ is projected onto one of the eigenstates of the operator and the measurement outcome is the corresponding eigenvalue. The expectation value obtained for a measurement on a certain state $|\psi\rangle$ is calculated as $\langle \psi | \hat{O} | \psi \rangle$.

Measurements on qubits have two possible measurement outcomes, +1 and -1, resulting in a projection of $|\psi\rangle$ onto a basis of two orthogonal states $|\psi_{\theta,\phi}\rangle$ and $|\psi_{\theta+\pi,-\phi}\rangle$, respectively. The corresponding observable is:

$$\hat{\sigma}_{\theta,\phi} = \cos(\theta)\hat{\sigma}_z + \cos(\phi)\sin(\theta)\hat{\sigma}_x + \sin(\phi)\sin(\theta)\hat{\sigma}_y. \quad (2.2)$$

where $\hat{\sigma}_z$, $\hat{\sigma}_x$ and $\hat{\sigma}_y$ are the Pauli spin matrices:

$$\hat{\sigma}_z = \begin{pmatrix} 1 & 0 \\ 0 & -1 \end{pmatrix} \quad \hat{\sigma}_x = \begin{pmatrix} 0 & 1 \\ 1 & 0 \end{pmatrix} \quad \hat{\sigma}_y = \begin{pmatrix} 0 & -i \\ i & 0 \end{pmatrix}. \quad (2.3)$$

The eigenstates of the Pauli matrices lie on the Z-, X- and Y- axes in the Bloch sphere figure 2.1. They are defined as:

$$\hat{\sigma}_z |H/V\rangle = \pm |H/V\rangle, \quad (2.4)$$

$$\hat{\sigma}_x |+/\rangle = \hat{\sigma}_x \frac{1}{\sqrt{2}}(|H\rangle \pm |V\rangle) = \pm |+/\rangle, \quad (2.5)$$

$$\hat{\sigma}_y |R/L\rangle = \hat{\sigma}_y \frac{1}{\sqrt{2}}(|H\rangle \pm i|V\rangle) = \pm |R/L\rangle, \quad (2.6)$$

where $|+/-\rangle$ correspond to $\pm 45^\circ$ linear and $|R/L\rangle$ to right and left circular polarizations.

When a measurement of the observable $\sigma_{\theta,\phi}$ is performed on a state $|\psi\rangle$, we can calculate the probability of occurrence for each measurement result with the expectation value of the corresponding projector $P_{\theta,\phi}^\pm$: $\langle\psi|P_{\theta,\phi}^\pm|\psi\rangle$. Here, the superscript $+$ or $-$ denotes the measurement outcomes $+1$ or -1 , respectively. The projector is given by:

$$P_{\theta,\phi}^\pm = |\psi_{\theta,\phi}^\pm\rangle\langle\psi_{\theta,\phi}^\pm| = \frac{1}{2}(\mathbb{1} \pm \sigma_{\theta,\phi}). \quad (2.7)$$

Unitary transformations in the Hilbert space of one qubit correspond to rotations of all states on the Bloch sphere around some angle ω . Each axis corresponds to a Pauli matrix $\hat{\sigma}_{\theta,\phi}$. This can be easily seen by the fact that the eigenstates of $\hat{\sigma}_{\theta,\phi}$ are left unchanged by a rotation around the corresponding axis. A general unitary transformation is then:

$$U_{\theta,\phi}^\omega = i\cos(\omega/2)\mathbb{1} + \sin(\omega/2)\hat{\sigma}_{\theta,\phi}. \quad (2.8)$$

In the language of quantum information, these transformations are single qubit quantum gates. A very important example is the Hadamard gate \mathcal{H} :

$$\mathcal{H} = \hat{\sigma}_{\pi/4,0} = U_{\pi/4,0}^\pi = \frac{1}{\sqrt{2}} \begin{pmatrix} 1 & 1 \\ 1 & -1 \end{pmatrix}. \quad (2.9)$$

2.1.2 Multiqubit states

Let us now consider quantum states of N qubits. We assume that they can be numbered, in other words, another degree of freedom in the physical implementation of the qubits allows to distinguish them¹. The Hilbert space of the multiqubit system is then described by the tensor product of the single qubit systems. This means that a basis for the new Hilbert space can be obtained by tensorial multiplication of the single qubit basis vectors:

$$\begin{aligned} |HH\dots H\rangle &= |H\rangle_1 \otimes |H\rangle_2 \otimes \dots \otimes |H\rangle_N \\ |HV\dots H\rangle &= |H\rangle_1 \otimes |V\rangle_2 \otimes \dots \otimes |H\rangle_N \\ &\dots \\ |VV\dots V\rangle &= |V\rangle_1 \otimes |V\rangle_2 \otimes \dots \otimes |V\rangle_N. \end{aligned} \quad (2.10)$$

Accordingly, the new state space has 2^N dimensions. States that can be expressed as tensor product of single qubit states are called separable. Naturally, any superposition thereof is another valid state of the quantum system and is called non-separable if it cannot be expressed in terms of a tensor product of single qubit states.

In analogy, the tensorial products of Pauli spin matrices form a basis for the observables of a multipartite quantum system. Thus, each observable can be expressed as a linear combination of the form:

$$\hat{O} = \sum_{\forall k, i_k=0} \Gamma_{i_1, i_2, \dots, i_N} \hat{\sigma}_{i_1} \otimes \hat{\sigma}_{i_2} \otimes \dots \otimes \hat{\sigma}_{i_N}, \quad (2.11)$$

¹In this work the indices usually denote the spatial mode of the observed photons.

where $\hat{\sigma}_0 = \mathbb{1}$, $\hat{\sigma}_1 = \hat{\sigma}_z$, $\hat{\sigma}_2 = \hat{\sigma}_x$, $\hat{\sigma}_3 = \hat{\sigma}_y$ and $\Gamma_{i_1, i_2, \dots, i_N}$ are complex coefficients. Observables that can be expressed in terms of a tensor product of single qubit observables are called local. Note that local observables do not necessarily need to be products of the Pauli matrices. In the experiments that are presented here, each photon is analyzed independently, i.e., the measurement outcomes are expectation values of local observables and are called *correlations* in the following. The reason is that their expectation values express dependencies in the measurement outcomes of each qubit, as can be seen in the following example. Consider the expectation value of $\hat{\sigma}_z \otimes \hat{\sigma}_z$ with the state $\frac{1}{\sqrt{2}}(|HH\rangle + |VV\rangle)$:

$$\begin{aligned}
 K_{ZZ} &= \frac{1}{2}(\langle HH| + \langle VV|)\hat{\sigma}_z \otimes \hat{\sigma}_z(|HH\rangle + |VV\rangle) \\
 &= \frac{1}{2}(\langle HH|\hat{\sigma}_z \otimes \hat{\sigma}_z|HH\rangle + \langle HH|\hat{\sigma}_z \otimes \hat{\sigma}_z|VV\rangle + \\
 &\quad \langle VV|\hat{\sigma}_z \otimes \hat{\sigma}_z|HH\rangle + \langle VV|\hat{\sigma}_z \otimes \hat{\sigma}_z|VV\rangle) \\
 &= \frac{1}{2}(\langle HH|HH\rangle + (-1) \cdot (-1)\langle VV|VV\rangle) = 1
 \end{aligned} \tag{2.12}$$

The expectation value 1 expresses the fact that the measurement results of both qubits in this basis are always equal, i.e. correlated in the ZZ-basis. Accordingly, uncorrelated states result in $K = 0$, anticorrelated ones in $K = -1$.

Any unitary transformation can, analogous to what was discussed for observables, be expressed by a linear combination of tensor products of unitary operations acting on single qubit systems. Transformations that can be expressed as $U_{\theta, \phi}^\omega \otimes U_{\theta, \phi}^\omega \otimes \dots U_{\theta, \phi}^\omega$ are called *local* unitary transformation (LU).

2.1.3 Mixed states

The quantum states that have been used so far were pure states, described by their state vector. Often, however, we can only make statistical statements about the state vector of a quantum system. For example, when an experimental source of quantum states is subject to uncontrollable changes, or when we study a subsystem of a larger quantum state. The resulting states are described by statistical mixtures of pure quantum states $|\psi_i\rangle$, each one occurring with a certain probability p_i , respectively. A convenient way to treat these mixed states mathematically is the density operator formalism.

The density operator of a pure quantum state $|\psi_i\rangle$ is simply given by its projector:

$$\rho_i = |\psi_i\rangle\langle\psi_i| \tag{2.13}$$

Then the statistical mixture of several states, each occurring with the probability p_i is the convex linear combination:

$$\rho = \sum_i p_i |\phi_i\rangle\langle\phi_i|, \text{ with } \sum_i p_i = 1 \tag{2.14}$$

It is important to note that this decomposition into pure states is not unique. The density operator ρ , however, exclusively describes one mixed state and contains our complete knowledge. From equation 2.14 one can directly deduce some properties of density matrices [45]:

- ρ is normalized: $Tr(\rho) = 1$.
- ρ is positive semi definite (has real positive eigenvalues).
- $Tr(\rho^2) \leq 1$, where the equality is fulfilled only for pure states $\rho = |\phi\rangle\langle\phi|$.

By fixing a certain orthonormal basis for the representation the density operator ρ can be expressed as a matrix:

$$\rho_{mn} = \langle m | \rho | n \rangle, \quad (2.15)$$

where $m, n \in \{1, 2, \dots, N\}$ with $|n\rangle$ and $|m\rangle$ as basis vectors. Usually one uses the computational basis (equation 2.10) with $|1\rangle = |HH\dots HH\rangle$, $|2\rangle = |HH\dots HV\rangle, \dots$, $|N\rangle = |VV\dots V\rangle$.

As the determination of density matrices for experimentally observed states constitutes a major tool in this work, their interpretation will shortly be explained by comparing two single qubit examples. The equally weighted mixture of all basis vectors is the white noise state. For one qubit it is: $\rho_{wn} = 1/2(|H\rangle\langle H| + |V\rangle\langle V|)$. The other example is the superposition of the two basis vectors $\rho_+ = |+\rangle\langle +|$. The corresponding matrices are:

$$\rho_{wn} = \frac{1}{2} \begin{pmatrix} 1 & 0 \\ 0 & 1 \end{pmatrix}, \quad \rho_+ = \frac{1}{2} \begin{pmatrix} 1 & 1 \\ 1 & 1 \end{pmatrix}. \quad (2.16)$$

The diagonal elements are called populations because they express the probabilities to observe the different basis states. Thus, they are always positive real values. In contrast, the off-diagonal elements are complex numbers. They are called coherences as they express the interference effects between the populated states that can appear when they are superimposed, i.e. they indicate coherence between the corresponding terms.

The expectation value of an operator \hat{O} with a certain mixed state ρ is, in the density matrix formalism, given by the trace of their product:

$$\langle \hat{O} \rangle_\rho = Tr [\hat{O} \rho] \quad (2.17)$$

The probability to detect a mixed state ρ in a certain pure state $|\psi\rangle$ is calculated the same way using $\hat{O} = |\psi\rangle\langle\psi|$.

An important tool for the characterization of quantum states is the fidelity. Uhlmann [48] presented this measure of the distance between two mixed states ρ and σ in 1976. It is given by:

$$F_\rho^\sigma = \left(Tr \left[\sqrt{\sqrt{\sigma} \rho \sqrt{\sigma}} \right] \right)^2 \quad (2.18)$$

The name fidelity reflects the common application of this measure to quantify how well a certain imperfect version ρ of a quantum state resembles the perfect one σ .

In case one of the two states is pure, e.g. $\sigma = |\psi\rangle\langle\psi|$, equation 2.18 can be simplified to:

$$F_\rho^\psi = Tr [\rho |\psi\rangle\langle\psi|] = \langle \psi | \rho | \psi \rangle, \quad (2.19)$$

where the property of pure states $|\psi\rangle\langle\psi|^2 = |\psi\rangle\langle\psi|$ was used. In other words, the fidelity is then simply the probability to project the state ρ onto the state $|\psi\rangle$.

2.2 Bipartite entanglement

Non-separable pure states, i.e. states that cannot be expressed in terms of a tensor product of single qubit states, are called entangled. In this section, properties of maximally entangled bipartite states will be introduced. The notion of separability and entanglement is generalized to mixed states. Further, quantum gates that allow the manipulation of entanglement will be presented followed by a prominent application of entanglement as resource for quantum communication.

2.2.1 Bell states

The Hilbert space of two qubits is spanned by four orthonormal basis vectors. One possible basis is the computational basis as presented in equation 2.10. Alternatively, one can define a basis of non-separable states, the Bell-basis:

$$\begin{aligned}
 |\psi^-\rangle &= \frac{1}{\sqrt{2}}(|HV\rangle - |VH\rangle), \\
 |\psi^+\rangle &= \frac{1}{\sqrt{2}}(|HV\rangle + |VH\rangle), \\
 |\phi^-\rangle &= \frac{1}{\sqrt{2}}(|HH\rangle - |VV\rangle), \\
 |\phi^+\rangle &= \frac{1}{\sqrt{2}}(|HH\rangle + |VV\rangle).
 \end{aligned} \tag{2.20}$$

These states are maximally entangled. The exact meaning of this will be subject of section 2.3. Here, some properties of these states will be discussed. As mentioned, none of these Bell states can be expressed as a tensor product of single qubit states. Several interesting properties follow from this seemingly harmless fact.

Firstly, each Bell state can be transformed into every other Bell state via a unitary transformation on one of the two qubits. It is easy to see that:

$$|\psi^-\rangle = (\mathbb{1} \otimes \hat{\sigma}_z)|\psi^+\rangle = (\mathbb{1} \otimes \hat{\sigma}_x)|\phi^-\rangle = (\mathbb{1} \otimes \hat{\sigma}_y)|\phi^+\rangle, \tag{2.21}$$

where global phase factors were neglected. This observation expresses the fact that the operation on a single qubit of entangled states influences the complete bipartite state. This is not the case for separable states.

Secondly, measurements on a single qubit of a Bell state yield random results. In order to determine the state of a single qubit subsystem we need to calculate the partial trace over the other. This is exemplarily performed for the state $|\psi^-\rangle$:

$$Tr_A[|\psi^-\rangle_{AB}\langle\psi^-|] = \sum_{i=\{H,V\}} A\langle i|\psi^-\rangle_{AB}\langle\psi^-|i\rangle_A = \frac{1}{2}(|H\rangle_B\langle H| + |V\rangle_B\langle V|) = \frac{1}{2}\mathbb{1}_B, \tag{2.22}$$

here the indices A and B were used in order to indicate the numbering of qubits implied by usage of the tensor product. The calculation shows that the state of qubit B is equal to the white noise state when information about qubit A is not available. The same is, of course, true when the other qubit is traced out.

Thirdly, the Bell states are perfectly (anti-) correlated in more than one measurement basis. Let us compare the separable state $|HV\rangle$ and the Bell state $|\psi^-\rangle$ expressed in the Z- and the X-basis:

$$\frac{1}{\sqrt{2}}(|HV\rangle - |VH\rangle) = \frac{1}{\sqrt{2}}(|+-\rangle - | -+\rangle), \quad (2.23)$$

$$|HV\rangle = \frac{1}{2}(|++\rangle + |+-\rangle + | -+\rangle - |--\rangle). \quad (2.24)$$

For the entangled state, anticorrelation is observed in the Z- and X-basis. In contrast, the separable state is correlated only in one basis. As we have seen in the previous section this can also be determined from the expectation value of the operators $\hat{\sigma}_z \otimes \hat{\sigma}_z$ and $\hat{\sigma}_x \otimes \hat{\sigma}_x$:

$$\langle HV | \hat{\sigma}_z \otimes \hat{\sigma}_z | HV \rangle = -1, \quad \langle \psi^- | \hat{\sigma}_z \otimes \hat{\sigma}_z | \psi^- \rangle = -1, \quad (2.25)$$

$$\langle HV | \hat{\sigma}_x \otimes \hat{\sigma}_x | HV \rangle = 0, \quad \langle \psi^- | \hat{\sigma}_x \otimes \hat{\sigma}_x | \psi^- \rangle = -1 \quad (2.26)$$

In general, each single qubit of a pure separable state is itself in a pure state, thus perfect correlations are only observed in one pair of measurement bases as the measurement outcomes in other bases are for each qubit random and independent. In contrast, as we have seen before, the single qubits of entangled states are statistically mixed, but the measurement outcomes are correlated in many measurement bases. Thus, knowing the measurement outcome for one qubit allows prediction of the state of the other one.

All of these properties clearly demonstrate that the two qubits in a bipartite entangled state are strongly linked and cannot be described separately. This property of entangled states lies at the heart of quantum mechanics. It led to the formulation of the EPR-Paradox [2] and the related Bell Inequalities ([4, 49]), which are not further considered here. This thesis, however, focuses on the experimental investigation of the multitude of entanglement properties of multipartite states as discussed in chapter 3.

2.2.2 Mixed entangled states

When mixed states are considered, it is not as clear as in the pure state case how to distinguish between separable and entangled states. The decomposition of a mixed state into pure states is not unique. Thus, the occurrence of a pure entangled state in a decomposition is no guarantee for the presence of entanglement. Therefore, Werner presented in 1989 the following definition of separable mixed states [10]:

A state is called separable if and only if it can be approximated by density matrices of the form:

$$\rho = \sum_i p_i (\rho_1 \otimes \rho_2), \quad \forall i : p_i \geq 0, \quad \sum_i p_i = 1 \quad (2.27)$$

otherwise the state is called entangled. This seemingly simple definition is hard to test for an arbitrary state. There is no analytical solution to decide this so-called separability problem in general². Partial solutions that even allow application in experiments will be presented in section 2.3. First, however, some more details on the manipulation and application of entanglement will be discussed.

²That means, for many particles and/or higher dimensional systems.

2.2.3 Two-qubit operations

So far, only the existence of entangled states was discussed, not how they can be obtained. From the quantum information point of view, one is studying quantum logic operations (gates) that are capable to create and destroy entanglement regardless of the physical implementation. A major interest concerns universal sets of quantum gates, which means that every quantum operation can be implemented by concatenation of these elementary gates in a quantum logic network³. A universal set cannot consist of local operations (LO) only:

$$(LO_1 \otimes LO_2 \dots)(|\psi_1\rangle \otimes |\psi_2\rangle \dots) = [(LO_1|\psi_1\rangle) \otimes (LO_2|\psi_2\rangle) \dots]. \quad (2.28)$$

It was shown [50], however, that local and certain two-qubit operations are indeed sufficient to build universal networks and to implement arbitrary operations. In the following we will present three two-qubit operations. One of them, the swap operation, will then be generalized to the multiqubit case.

The controlled-phase gate C_P is (together with single qubit operations) universal. It is further a key-element in the initialization procedure of the one-way quantum computer scheme [33]. The transformation is explicitly written for the computational basis in table 2.1 a) - the corresponding two-qubit matrix is:

$$C_P = \begin{pmatrix} 1 & 0 & 0 & 0 \\ 0 & 1 & 0 & 0 \\ 0 & 0 & 1 & 0 \\ 0 & 0 & 0 & -1 \end{pmatrix} \quad (2.29)$$

The negative sign in the last contribution corresponds to a π -phase shift on the $|VV\rangle$ term. Whether it applies depends on both qubits, therefore the gate cannot be realized by single qubit operations only. This becomes also visible when rewriting this operation as:

$$C_P = \frac{1}{2}(\mathbb{1} \otimes \mathbb{1} + \mathbb{1} \otimes \hat{\sigma}_z + \hat{\sigma}_z \otimes \mathbb{1} - \hat{\sigma}_z \otimes \hat{\sigma}_z). \quad (2.30)$$

In chapter 5 an experimental realization of such a gate with linear optics is demonstrated.

The controlled-NOT gate C_{NOT} introduces the transformation shown in table 2.1 b). The two qubit input consists of a control and a target qubit. The term $|V\rangle$ in the control qubit triggers a spin flip of the target qubit, otherwise the state is not changed. It is represented by the matrix:

$$C_{NOT} = \begin{pmatrix} 1 & 0 & 0 & 0 \\ 0 & 1 & 0 & 0 \\ 0 & 0 & 0 & 1 \\ 0 & 0 & 1 & 0 \end{pmatrix} = \frac{1}{2}(\mathbb{1} \otimes \mathbb{1} + \mathbb{1} \otimes \hat{\sigma}_x + \hat{\sigma}_z \otimes \mathbb{1} - \hat{\sigma}_z \otimes \hat{\sigma}_x). \quad (2.31)$$

A comparison with equation 2.30 shows that a simple Hadamard transformation (equation 2.9) turns one qubit entering a C_P gate into a target qubit of the C_{NOT} gate: $C_P = (\mathbb{1} \otimes \mathcal{H}) C_{NOT} (\mathbb{1} \otimes \mathcal{H})$.

³There are also other approaches, like the one-way quantum computer. Theoretically, however, the corresponding formalism is still useful for the analysis of these schemes [33].

	IN	OUT		IN	OUT		IN	OUT
a)	$ HH\rangle$	$ HH\rangle$	b)	$ HH\rangle$	$ HH\rangle$	c)	$ HH\rangle$	$ HH\rangle$
	$ HV\rangle$	$ HV\rangle$		$ HV\rangle$	$ HV\rangle$		$ HV\rangle$	$ VH\rangle$
	$ VH\rangle$	$ VH\rangle$		$ VH\rangle$	$ VV\rangle$		$ VH\rangle$	$ HV\rangle$
	$ VV\rangle$	$- VV\rangle$		$ VV\rangle$	$ VH\rangle$		$ VV\rangle$	$ VV\rangle$

Table 2.1: Operations of the a) controlled-phase gate C_P , b) the controlled-NOT gate C_{NOT} and c) the permutation operator S acting on the computational basis.

The swap operator S (e.g. [46, 51]) simply exchanges two qubits with each other. Remember (equation 2.10) that the tensor product used here implies a labeling of the qubits. By swapping the qubits, their indices are exchanged: $S_{21}(|\alpha\rangle_1 \otimes |\beta\rangle_2) = (|\beta\rangle_1 \otimes |\alpha\rangle_2)$, where the index of the swap operator expresses the ordering after the operation. As one would expect, a simple relabeling cannot change the entanglement in the state. It is, however, relevant as a tool to efficiently analyze the symmetry of an experimentally observed state as will be demonstrated in section 3.3. The action of the gate in the computational basis is summarized in table 2.1 c) and the corresponding matrix is:

$$S_{21} = \begin{pmatrix} 1 & 0 & 0 & 0 \\ 0 & 0 & 1 & 0 \\ 0 & 1 & 0 & 0 \\ 0 & 0 & 0 & 1 \end{pmatrix} = \frac{1}{2}(\mathbb{1} \otimes \mathbb{1} + \hat{\sigma}_x \otimes \hat{\sigma}_x + \hat{\sigma}_y \otimes \hat{\sigma}_y + \hat{\sigma}_z \otimes \hat{\sigma}_z). \quad (2.32)$$

The swap gate, unlike the previously presented gates, can neither create nor destroy entanglement. One can, however, easily modify it such that the new operation symmetrizes quantum states:

$$Z = \frac{\mathbb{1}^{\otimes 2} + S}{2} = \begin{pmatrix} 1 & 0 & 0 & 0 \\ 0 & \frac{1}{2} & \frac{1}{2} & 0 \\ 0 & \frac{1}{2} & \frac{1}{2} & 0 \\ 0 & 0 & 0 & 1 \end{pmatrix}. \quad (2.33)$$

This has the form of a projector (compare with equation 2.7) and is indeed the projection into the symmetric subspace [45]. As we will see in the following, this is in most cases a projection onto an entangled state with state dependent success probability. Exemplarily, this shall be demonstrated for the antisymmetric and a non-symmetric separable state:

$$Z|\psi^-\rangle = \frac{1}{2}(|\psi^-\rangle - |\psi^-\rangle) = 0, \quad (2.34)$$

$$Z|HV\rangle = \frac{1}{2}|HV\rangle + |VH\rangle = \frac{1}{\sqrt{2}}|\psi^+\rangle. \quad (2.35)$$

As expected, the antisymmetric state is projected with zero probability onto the symmetric subspace. The separable state is projected with a probability of 1/2 onto the maximally entangled state $|\psi^+\rangle$. Thus, entanglement is obtained probabilistically, but for almost all separable states (the only exceptions are tensor products of identical single qubit states $|\psi_{\theta,\phi}\rangle \otimes |\psi_{\theta,\phi}\rangle$). In contrast, the unitary operations like the C_P or C_{NOT} only introduce entanglement for few states, but with certainty.

As a last step, let us generalize the swap operator to many qubits. Actually it is generalized to many operations which correspond to different permutations of the indices. It is known from group theory [46] that any permutation operation can be expressed by concatenated application of several swap operations (which defines the product in the permutation group). One can, for example, show that all of the 24 permutations of four qubits can simply be built from three swap operations between qubits (1,2), (2,3) and (3,4): S_{2134} , S_{1324} and S_{1243} . For example, the cyclic permutation of qubits 1,2 and 3 clockwise S_{3124} is given by:

$$S_{3124} = S_{1324} S_{3214} = (\mathbb{1} \otimes S_{32} \otimes \mathbb{1})(S_{21} \otimes \mathbb{1} \otimes \mathbb{1}). \quad (2.36)$$

The projection operator of these permutation operations is defined exactly as for the simple swap operator in equation 2.33. Without going into further detail, let me note that one can also obtain entanglement between more than two qubits with this kind of projectors by projection into higher dimensional symmetric subspaces [45].

2.2.4 Quantum teleportation

Entangled states exhibit different correlations in comparison to separable states because a bipartite quantum state cannot be perceived as two single particles. This alone can, however, not be used to transmit information, which would imply the possibility of superluminal communication [46]. Furthermore, the measurement result on a qubit is still just a classical bit value. Thus, one can ask the question whether there exist advantages of quantum over classical correlations at all. It was recognized over the last decades that the answer is positive and entanglement is now considered a powerful resource. The list of possible applications is long and includes, as prominent examples, quantum cryptography⁴ [11], which has already reached a mature state of development [53–55] and quantum computers, which are still a vague dream. Doubtlessly, the invention and experimental realization of quantum teleportation [12, 19] were key steps in terms of the applications of entanglement. For this reason and also because it is the starting point for some applications of the states investigated in chapter 6 and chapter 7, we continue with a short description of this quantum communication protocol.

The task is to transfer a quantum state to a remote location without physically sending it. Imagine scientists on Earth that want to transmit an arbitrary, unknown quantum state to their colleagues on Mars. The strategy to simply measure the qubit (destroying the actual input state) and transfer the measurement basis and result via a classical channel to Mars where the state is then prepared accordingly, is not very satisfying. The achieved, so-called classical, fidelity of the (statistically mixed) state prepared on Mars would be, averaged over all possible input states, $F_{class} = 2/3$.

The idea of quantum teleportation is that one can use a shared entangled state as quantum resource that allows the transfer of quantum information from the input state to the remote particle of the shared state on Mars. The scheme is depicted in figure 2.2. Mars and Earth share each one particle of a Bell state, e.g. $|\psi^-\rangle$. Together with the

⁴Note that most schemes do not need entanglement, e.g. [52].

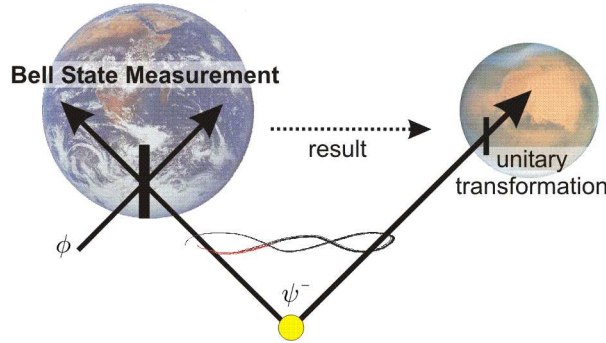


Figure 2.2: Quantum teleportation between Earth and Mars. The transfer of an input qubit $|\phi\rangle$ between the two remote locations is achieved using a Bell state $|\psi^-\rangle$ as quantum resource and two classical bits. The latter is the result of a Bell state measurement on Earth and enables Mars to transform his state to the original state $|\phi\rangle$.

initial state $|\phi\rangle = (\alpha|H\rangle_{\mathfrak{E}} + \beta|V\rangle_{\mathfrak{E}})$ on earth the total three qubit state is:

$$\begin{aligned}
 |\phi\rangle_{\mathfrak{E}}|\psi^-\rangle_{\mathfrak{E}\mathfrak{M}} &= (\alpha|H\rangle_{\mathfrak{E}} + \beta|V\rangle_{\mathfrak{E}})|\psi^-\rangle_{\mathfrak{E}\mathfrak{M}} \\
 &= |\phi^+\rangle_{\mathfrak{E}\mathfrak{E}}(\beta|H\rangle_{\mathfrak{M}} - \alpha|V\rangle_{\mathfrak{M}})_{\mathfrak{M}} \\
 &\quad + |\psi^+\rangle_{\mathfrak{E}\mathfrak{E}}(\alpha|H\rangle_{\mathfrak{M}} - \beta|V\rangle_{\mathfrak{M}})_{\mathfrak{M}} \\
 &\quad + |\phi^-\rangle_{\mathfrak{E}\mathfrak{E}}(\beta|H\rangle_{\mathfrak{M}} + \alpha|V\rangle_{\mathfrak{M}})_{\mathfrak{M}} \\
 &\quad - |\psi^-\rangle_{\mathfrak{E}\mathfrak{E}}(\alpha|H\rangle_{\mathfrak{M}} + \beta|V\rangle_{\mathfrak{M}})_{\mathfrak{M}} \\
 &= i|\phi^+\rangle_{\mathfrak{E}\mathfrak{E}}\hat{\sigma}_y|\phi\rangle_{\mathfrak{M}} \\
 &\quad + |\psi^+\rangle_{\mathfrak{E}\mathfrak{E}}\hat{\sigma}_z|\phi\rangle_{\mathfrak{M}} \\
 &\quad + |\phi^-\rangle_{\mathfrak{E}\mathfrak{E}}\hat{\sigma}_x|\phi\rangle_{\mathfrak{M}} \\
 &\quad - |\psi^-\rangle_{\mathfrak{E}\mathfrak{E}}\mathbb{1}|\phi\rangle_{\mathfrak{M}},
 \end{aligned}$$

where the indices \mathfrak{E} and \mathfrak{M} represent Earth and Mars, respectively. As one can see, the state can be rewritten as a superposition of four terms that consist each of one Bell state on Earth and the initial state on Mars, up to a transformation that is correlated with the Bell state. Thus, a projective measurement onto the Bell basis⁵ allows to prepare the input state on Mars up to a local transformation that depends on the measurement result of a Bell state measurement on earth. This is not a superluminal information transfer, because we need to tell Mars the transformation that has to be applied via a classical channel, otherwise there is just white noise at Mars. Important is, however, that the initial state is teleported with a fidelity of 100%. Thus it is possible to transfer the two real parameters that define the input state (θ and ϕ in equation 2.1) to the output state using the entangled resource and communication of only two classical bits. Thereby we can gain no knowledge about the teleported state itself. If we exactly knew the state to be transferred, this task would need an infinite number of classical bits without the use of a quantum resource.

What, if there is for some reason no perfect Bell state shared between Earth and Mars, e.g. the source of entangled photons is not perfect and emits some mixed state. The question is then, what is the best possible fidelity between the teleported and the initial

⁵Which can be realized, among others, with the phase gate described in chapter 5.

state that can be achieved. Horodecki [56] found that the decisive quantity is the shared state's distance to the closest maximally entangled pure state. This state can always be transformed to a singlet state via LU. The resulting distance is then called maximal singlet fraction:

$$F_{MSF}(\rho) = \max_{LU} (\langle \psi^- | LU \rho LU^t | \psi^- \rangle), \quad (2.37)$$

where the maximum is taken over all LU-operations. The fidelity of teleportation F_{tel} achieved with the state ρ , averaged over all possible input states, is then given by the equation

$$F_{tel} = (2F_{MSF} + 1)/3. \quad (2.38)$$

One might intuitively think that this quantifies the entanglement of the quantum state. The maximal singlet fraction does not fulfill, however, several criteria that are expected from entanglement measures, which will be described in the following.

2.3 Separability criteria and entanglement measures

The intuitive definition of separability (equation 2.27) is in strong contrast to the hard task of testing, whether a quantum state is separable (separability problem). Criteria that allow to test for the separability of a quantum state are fundamental tools for experiments where we seek to prove that entanglement can indeed be observed. For multipartite systems such criteria should also be able to test whether parts of the system are separable from the rest. Here, some criteria will be introduced for later application to the quantum states observed in our experiments. Closely related and also of importance for experiments with entangled states is the quantification of entanglement. Thus, also some results on entanglement measures will be introduced here. For a more extensive overview on this subject, the interested reader is referred to [57–60].

2.3.1 Definition of entanglement measures

There are several reasonable ways to quantify entanglement. For example, by the violation of a Bell inequalities, or how well it is suited for a certain task (e.g. teleporation by calculation of the maximal singlet fraction). Not all of these values are, however, proper entanglement measures. Whether a quantity is a good measure, can be decided using a certain set of conditions that should be fulfilled [61, 62]. Three conditions are broadly accepted as criteria for an entanglement measure and define entanglement monotones [63].

The function E of a quantum state is an entanglement monotone if:

- It vanishes for all separable states,
 $E(\rho_{sep}) = 0$.
- It does not increase using only local operations and classical communication (which means, without the use of quantum channels).
 $E(\Lambda_{LOCC} \rho \Lambda_{LOCC}^t) \leq E(\rho) \Rightarrow E(U \rho U^*) = E(\rho)$.
- It is convex (because mixing of states can only decrease the overall entanglement).
 $E(\lambda \rho_1 + (1 - \lambda) \rho_2) \leq \lambda E(\rho_1) + (1 - \lambda) E(\rho_2)$.

In the following, several entanglement measures will be introduced. First, however, let us remember the maximal singlet fraction, section 2.2.4. This quantity gives information about how well a quantum state can be used for teleportation, a fundamental protocol relying on the entanglement between two parties. Intuitively one might expect that this also should provide a good entanglement measure. But as it turns out, the maximal singlet fraction is not an entanglement monotone as it can be increased under local operations and classical communication (LOCC). This example shows that it is not easy to guess whether some function of quantum states serves as a good entanglement measure.

2.3.2 Entropy, entanglement of formation and concurrence

For the simplest case, bipartite pure quantum states, we have already mentioned a property that is related to the question, whether the state is entangled: In section 2.2.1 it was discussed that one photon of a Bell state appears locally as white noise. In contrast, the particles of a pure separable state are pure at both locations. For example:

$$\text{Tr}_A(|\psi^-\rangle_{AB}\langle\psi^-|) = \mathbf{1}/2_B \quad (2.39)$$

$$\text{Tr}_A(|(H \otimes L)\rangle_{AB}\langle(H \otimes L)|) = |H\rangle_B\langle H| \quad (2.40)$$

Thus, a pure quantum state is separable if tracing out one qubit results in a pure residual qubit. As it turns out, this insight can be used as one approach to quantify pure state entanglement. To do so, the von Neumann Entropy S of the residual state is calculated (see e.g. [46]).

$$E_S(\rho_{AB}) = S(\text{Tr}_A(\rho_{AB})) = S(\text{Tr}_B(\rho_{AB})), \quad (2.41)$$

where $\rho_{AB} = |\psi\rangle\langle\psi|$, and S is the von Neumann Entropy

$$S(\rho) = -\text{Tr}(\rho \log_2(\rho)). \quad (2.42)$$

This was shown to be a good entanglement measure according to the previously mentioned conditions [64]. This works obviously only for pure bipartite quantum states. If the state we look at is mixed, then it is not clear whether the mixedness in the single qubits results from entanglement or from the mixedness of the two-qubit state.

There is a rather formal method how to generalize entanglement measures from pure to mixed states. As we have seen, an infinity of decompositions of a mixed state into pure states $\rho = \sum_i p_i |\psi_i\rangle\langle\psi_i|$ exists. From the entropies of the pure states $|\psi_i\rangle$ one can easily calculate their weighted average entropies. As the value of the average entropy depends on the decomposition, it is not an entanglement monotone. The infimum of all averaged entropies, however, defines an entanglement monotone called *entanglement of formation* E_F :

$$E_F(\rho) \equiv \inf_{\rho = \sum_i P_i |\psi_i\rangle\langle\psi_i|} \sum_i P_i E_S(|\psi_i\rangle) \quad (2.43)$$

The entanglement of formation can roughly be interpreted as the amount of quantum resources needed to form a certain state [65, 66]. This way of generalizing pure state entanglement measures to mixed states is called convex roof construction. The task of minimizing over all possible decompositions is, however, hard.

Fortunately, Wootters and coworkers [66] succeeded to find an explicit form for the entanglement of formation. They showed that there is a relation between the entanglement

of formation and the spinflip symmetry of two-qubit states. Hereby, they introduced a completely new entanglement measure, the concurrence C . The concurrence is defined as the fidelity of a quantum state to its spinflipped counterpart. A look at the Bell states (equation 2.20) suggests that this is sensible as a spinflip operation on both qubits leads always to the same quantum state. For separable states this is obviously not the case. To formally obtain the universal⁶ spin flip of a general single qubit state $|\phi\rangle$ we act with the $\hat{\sigma}_y$ Pauli matrix on the complex conjugate state: $\hat{\sigma}_y |\phi^*\rangle$. Thus, for pure states, we have [66]:

$$C = \langle \psi | \hat{\sigma}_y \otimes \hat{\sigma}_y | \psi^* \rangle \quad (2.44)$$

To obtain the concurrence for mixed states we need to calculate the eigenvalues λ_i of the product of the state ρ and its spin flipped counterpart $\tilde{\rho}$. The concurrence is given by:

$$C = \max(0, \sqrt{\lambda_1} - \sqrt{\lambda_2} - \sqrt{\lambda_3} - \sqrt{\lambda_4}) \quad (2.45)$$

where λ_1 is the maximal eigenvalue. From this easily calculable quantity, the entanglement of formation can now be derived by [67]:

$$E_F(\rho) = h\left(\frac{1 + \sqrt{1 - C^2(\rho)}}{2}\right) \quad (2.46)$$

where $h(x)$ is the binary entropy function:

$$h(x) = -x \log_2 x - (1 - x) \log_2(1 - x). \quad (2.47)$$

Thus, the entanglement of formation and the concurrence are entanglement measures for mixed states that are closely related despite of their very different origin. In the investigation of two-qubit states the concurrence is the value that is more used. Also in the analysis in the experimental part of this thesis, we will rely on the concurrence. In addition we will further make use of another entanglement measure that is not equivalent to the concurrence and will be introduced in the following.

2.3.3 The Peres-Horodecki criterion and negativity

A different separability criterion was introduced by Horodecki et al. [68, 69]. It is, in its nature, applicable to mixed quantum states. Imagine a transformation M that maps all physical quantum states onto physical quantum states. Note that this does not mean that the transformation is itself physical⁷. Such a transformation is called positive map, because physical states have positive density operators (property 2 on page 9). Now we consider two subsets of a quantum system that are separable, i.e. that can be written as a tensor product of the states of the subsets. When a positive map acts on one subset, then the result is again a tensor product of two physical states, i.e. another physical state having only positive eigenvalues. In contrast, after the maps action on an entangled state, the complete resulting state is not necessarily physical.

The Peres-Horodecki criterion uses the transposition as positive map. This map is closely related to a time-reversal of the corresponding system [70]. A transposition of

⁶The $\hat{\sigma}_y$ rotation only, does not flip $R \leftrightarrow L$.

⁷A counterexample is the universal spin-flip discussed in the last section.

a subset of particles is called a partial transposition. Here, a simple two-qubit example where the second qubit is transposed:

$$\begin{aligned} |\phi^+\rangle\langle\phi^+| &= \frac{1}{2} (|HH\rangle\langle HH| + |HH\rangle\langle VV| + |VV\rangle\langle HH| + |VV\rangle\langle VV|) \\ &\xrightarrow{PT} \frac{1}{2} (|HH\rangle\langle HH| + |HV\rangle\langle VH| + |VH\rangle\langle HV| + |VV\rangle\langle VV|) \end{aligned} \quad (2.48)$$

This is not a physical state as the second and third term indicate coherence between unpopulated terms, i.e. $|HV\rangle\langle HV|$ and $|VH\rangle\langle VH|$. Accordingly, the partially transposed density matrix has a negative eigenvalue of $-1/2$. We can conclude that the two subsets of particles (in this case the two qubits) are entangled.

The Peres-Horodecki criterion says that two states (or multipartite sets of states) are entangled if the partially transposed density matrix has a negative eigenvalue. It is a necessary criterion, but only sufficient for the dimensions 2×2 (two qubits) and 2×3 (one qubit and one qutrit). In all other cases there exist non-separable states with a positive partial transposition (PPT) ⁸.

This criterion is a very good starting point for an entanglement measure that is computable for mixed states. One can indeed prove that the sum of the negative eigenvalues forms a own entanglement measure, the negativity E_N [70]. As the density matrix is normalized, the negativity is given by:

$$E_N = \frac{1}{2} \left(\sum_{i=1}^4 |\lambda_i^T| - 1 \right), \quad (2.49)$$

where λ_i^T denote the eigenvalues of the partially transposed density matrix. For the Bell state in the example (equation 2.48) the maximal value of $E_N = 1/2$ is reached. To obtain an additive⁹ and normalized entanglement measure one can, instead, calculate the logarithmic negativity: $E_{LN} = \log_2(2E_N + 1)$, reaching the value $E_{LN} = 1$ for the Bell states.

There are several issues necessary to discuss in this context. On the one hand, as we have seen before, the Peres-Horodecki criterion does not detect entanglement for two systems in any dimension, thus there are entangled states (called bound entangled states) that have zero negativity. Further the ordering of mixed states given by the negativity is different from the one induced by the entanglement of formation [57]: One state can be more entangled than another according to one measure and vice versa according to the other.

2.3.4 Entanglement witnesses and the geometric measure

If the density operator of a state is known, then the Peres-Horodecki criterion is a very easy-to-use tool to test entanglement between two subsets of particles. To experimentally obtain the density operator means to gather the complete information about a quantum state. This requires a lot of experimental effort in the sense that data for a lot of different

⁸These states are called bound entangled as it was shown, that one cannot distill an negative partial transpose state (NPT) from many copies of such a state.

⁹The logarithmic negativity of a tensor product of states equals the sum of the logarithmic negativities of each state.

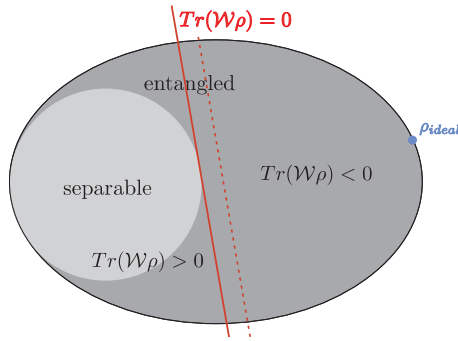


Figure 2.3: An entanglement witness is a hyperplane in the convex space of mixed states (dashed line), separating all separable states from a subset of entangled states. An optimal witness (non-dashed line) is tangent to the separable states and provides the optimal separation for the state that one seeks test (ρ_{ideal}).

measurement settings need to be collected, growing approximately exponentially with the number of qubits (a detailed discussion follows in section 4.3.2). Thus, tools for a more efficient detection of entanglement are required.

An elegant solution to this problem are *entanglement witnesses*. Using the convexity of the space of mixed states they allow to efficiently detect entanglement. In addition, the criteria and measures introduced so far were, apart from the tangle, tailored to study entanglement between two systems, including multipartite subsets of multiqubit states. Entanglement witnesses are not based on this kind of bisplitting and can be tailored such that genuine multipartite entanglement is studied directly. It makes entanglement witnesses a powerful tool for the analysis of multipartite states. Here, we will shortly present the idea of entanglement witnesses and their connection to the geometric measure of entanglement, a measure that applies to mixed multipartite entanglement.

The space of all density matrices (figure 2.3) is a convex space, as the decomposition into pure states is always a convex linear combination. In this space we can, using an operator \mathcal{W} , define a hyperplane of all states ρ that fulfill the equality:

$$\text{Tr}(\mathcal{W}\rho) = 0 \quad (2.50)$$

The main idea is that the space of all separable states ρ_{sep} is a convex subspace, too. This holds due to the fact that they are given by convex combinations of pure separable states. Therefore it is always possible to define the hyperplane such that the whole space is cut into a part that contains only entangled states and another one that includes all separable states ρ_{sep} :

$$\text{Tr}(\mathcal{W}\rho_{sep}) > 0 \quad (2.51)$$

The operator \mathcal{W} is called an entanglement witness, because it is constructed such that:

$$\text{Tr}(\mathcal{W}\rho) < 0 \implies \rho \text{ entangled.} \quad (2.52)$$

A negative expectation value of a state with this operator proves its entanglement. Furthermore, it was shown that a particular state ρ_0 is entangled if and only if such an entanglement witness exists, i.e. if one can find an operator \mathcal{W} that fulfills the mentioned

conditions with $Tr(\mathcal{W}\rho_0) < 0$. A disadvantage is that, while the Peres-Horodecki criterion detects all distillable entangled states with only one test, entanglement witnesses do not detect the entanglement of all states, i.e. the states in the dark region on the left hand side of the witness hyperplane in figure 2.3. In practice we need to use a witness that is tailored to the state we want to detect. This is, however, not a major disadvantage for the experimentalist, as we try to achieve a certain known entangled state ρ_{ideal} and expect the actually prepared state to be in its vicinity, detectable by the same entanglement witness.

Still, it is important to find entanglement witnesses such that as many entangled states as possible are detected. In the ideal case the corresponding hyperplane is a tangent to the set of separable states; then the witness is called optimal (figure 2.3). The generic way to define a witness \mathcal{W}_ψ detecting entanglement in the vicinity of a certain pure state $\rho_{ideal} = |\psi\rangle\langle\psi|$ is the following:

$$\mathcal{W}_\psi = \alpha\mathbb{1} - |\psi\rangle\langle\psi|, \quad (2.53)$$

where, for an optimal entanglement witness, $\alpha = \sup_{|\phi_{sep}\rangle} \|\langle\phi_{sep}|\psi\rangle\|$ with the supremum taken over all separable pure states $|\phi_{sep}\rangle$.

The generic form of the operator is merely one possibility of building an entanglement witness. In the experimental part of this thesis, several witnesses, that rely on properties of the quantum states we desire to analyze experimentally, are used. The goal is, in general, to obtain witnesses that give a strong separation from separable states with little experimental effort, i.e. few measurement settings. For example, the entanglement of both of the four-party entangled quantum states obtained in this thesis can be detected with 2 measurement settings. In comparison, 16 and 21 settings are needed for the generic witness, respectively and 81 for a complete state estimation.

Intuitively one might guess that there should be a relation between the witness expectation value and the strength of entanglement in a certain quantum state. It took, however, quite long until, only recently, these relations were revealed [71, 72]. Conclusion from the expectation values of entanglement witnesses can be drawn for several entanglement measures. Out of those, the geometric measure of entanglement (GME, [73, 74]) is particularly closely related to the generic form of entanglement witnesses [75] and will be introduced in the following. It is a multipartite entanglement measure and has a intuitive meaning: The GME is simply the distance of a given pure quantum state to the next separable state:

$$E_G(\psi) = \min_{|\phi\rangle_{sep}} (\|\psi\rangle - |\phi\rangle\|) \quad (2.54)$$

Goldbart and Wei [75] generalized this measure of entanglement to mixed states via a convex roof construction (similar to the method to obtain the entanglement of formation from the von Neumann entropy). In general it is not a simple task to calculate the GME for a given density matrix, as several optimizations have to be performed. Only recently Gühne and coworkers [72] presented a simple way to calculate lower bounds on the GME out of the results of witness measurements and applied it to some experiments. There is an particularly simple expression to obtain this bound on the GME based on generic entanglement witness:

$$E_G(\rho) \geq \max_r (r\langle\mathcal{W}_\psi\rho - \hat{E}_G(r\mathcal{W}_\psi)), \quad (2.55)$$

where $\hat{E}_G(r\mathcal{W}_\psi)$ is defined as:

$$\hat{E}_G(r\mathcal{W}_\psi) = \frac{1-r}{2} + \frac{1}{2}\sqrt{(1-r)^2 + 4rE_G(\psi)} + r\alpha - 1. \quad (2.56)$$

\mathcal{W}_ψ , α and $|\psi\rangle$ are defined as in equation 2.53 and the geometric measure of the theoretical state $E_G(\psi)$ has to be known. If the optimal generic entanglement witness is known this measure can be obtained from the simple relation $E_G(\psi) = 1 - \alpha_{opt}$, presented in [75].

2.4 Summary

In this chapter, several fundamental principles of quantum information theory have been presented for further use throughout this thesis. A focus was hereby put on the introduction to the concept of entanglement.

Entanglement is a natural consequence of the quantum mechanical superposition principle in multipartite systems resulting in states, where the individual particles cannot be completely described separately. To create entanglement we need, in the language of quantum information, non-local quantum gates like the C_{NOT} or C_P gates, where an experimental implementation of the latter is presented in chapter 5. Once prepared, entangled states can be used for various applications, for example for quantum teleportation, which plays a central role for many other applications. The entangled states presented in this thesis will be shown to be useful as resource for multiparty extensions of quantum teleportation.

Despite of the relatively simple definition of entanglement, it is hard to decide whether a certain state is separable or entangled, in particular for mixed states. Thus, methods to approach this *separability problem* are necessary in order to test whether the states observed in our experiments are entangled. For two-qubit mixed states there exist conclusive separability criteria and even the quantification of entanglement with different measures is possible. Out of those, we will use here two inequivalent entanglement measures that can be explicitly computed for mixed states: the concurrence and the logarithmic negativity. The presented methods can, however, not be directly generalized to multipartite states and the separability problem becomes hard to decide in general. Yet, there is a versatile tool to detect entanglement of multipartite states in the experiment, namely entanglement witnesses. Based on these, it is even possible to deduce lower bounds on the geometric measure of entanglement. When studying multipartite entangled states it is, however, not sufficient to restrict to a mere detection or quantification of entanglement, because there exist different types of entanglement, as will be discussed in the next chapter.

3 Classifications of Multipartite Entanglement

Multipartite entanglement has many facets and is therefore much more difficult to understand than entanglement in bipartite systems. This chapter is devoted to a discussion of the different types of multipartite entanglement. It is not obvious what "different types" exactly means and there are various ways to perceive this. Several aspects will be discussed, starting from the most abstract classification and finishing with a very concrete introduction of experimentally testable properties of quantum states, which are investigated in the presented experiments (chapter 6 and 7).

The abstract classification based on stochastic local operations and classical communication (SLOCC) allows to identify classes of pure states that are useful for the same kind of quantum communication tasks [76]. The classification for a certain fixed number of N qubits covers all pure N -qubit states and has recently been developed for arbitrary N [23–26].

While the classification via SLOCC constitutes a framework where relations between all multipartite entangled states become visible, it does not provide full understanding of their entanglement. There are other approaches to deepen this understanding, e.g. to focus on families of quantum states that share a common structure allowing a simplified description. In this context, one section is dedicated to two extraordinary families of quantum states that are especially relevant in this work: graph and symmetric Dicke states.

The graph states are strongly entangled and can be treated more simply due to their representation by mathematical graphs and the stabilizer formalism [77–79]. Dicke states are eigenstates of the spin-z operator (\hat{J}_z) and the total spin (\hat{J}^2) [39]. We consider states with maximal total spin, which are symmetric under permutation of qubits. That, again, simplifies their description and is the cause of extraordinary properties [80]. Representatives of both groups exist for any multipartite system; therefore, this approach includes also relations between states of a different number of qubits.

After these more general approaches to the classification of entangled states, several concrete examples of four-qubit entangled states that were important in the field of experimental analysis and application of states will be introduced.

A physical analysis of quantum states needs to include an investigation of their entanglement properties. Particularly in experiments, it is of importance to test how well the observed quantum state reproduces the properties of the desired state. Thus, the identification of relevant properties, especially with respect to potential applications, is an important step. Permutation symmetry will be discussed as one of those. Further, entanglement persistency (sometimes called robustness) and connectedness [81], which play an important role in our experimental analysis, will be introduced and shown to be useful tools to specify a state's applicability for certain quantum communication protocols [82, 83].

3.1 Classification via SLOCC

If different types of entanglement exist, then a single value, like an entanglement measure, alone is not a satisfying description of the entanglement in a multipartite state.

Entanglement measures were designed such, that they cannot increase under LOCC (section 2.3). This does, however, not mean that two states that have the same value can necessarily be converted into one another via LOCC. If it is not the case then we can interpret this such that these two states belong to different kinds, or equivalence classes, of entanglement with respect to LOCC.

Imagine the particles of a multiqubit state to be distributed between many parties. Their task is to transform this state into another one and back by using a certain set of operations. If this is possible, then we consider the two states as equivalent with respect to these operations. In the context of entanglement monotones, LOCC have already been used to identify states with the same amount of entanglement. They do, however, not seem to be preferable for a classification, because then even two states with a different amount of entanglement necessarily belong to separate entanglement classes, as they cannot be transformed into one another via LOCC. Thus, operations that are more general are necessary. There are several possibilities to loosen the restrictions of LOCC operations [76]. The parties might use LOCC operation acting not only to a single but a huge amount of copies of the same quantum state (asymptotic LOCC). Other possibilities are that a small amount of additional quantum resources are shared between the different parties or that they can locally use additional ancillary qubits (catalytic LOCC) that help converting between different states, similar like a catalyzer in a chemical reaction. Another approach turned out to be very successful, first in the three qubit case [23], later in the four qubit case [24] and recently it was even generalized recursively to N qubits [25]. This approach relies on stochastic equivalence (stochastic LOCC or SLOCC operations): Two states are defined as equivalent if there is a *non-vanishing probability* to convert the one into the other (and back) via LOCC. Here, the classification based on this approach is presented.

3.1.1 Three-qubit classification

In 2000, Dür and coworkers [23] pointed out that six equivalence classes exist for pure states of three qubits, with respect to SLOCC operations. They are shown in figure 3.1 a). As one can see, there is also a hierarchy between the states. It is caused by the possibility to irreversibly transform from the upper to the lower types of entanglement. As one would expect, the completely separable states (symbolized by A-B-C) are at the very bottom. In the middle, there are biseparable¹ states, where two qubits are entangled but separated from the third one (A-BC, C-AB and B-AC). These are three distinct classes, as one cannot create entanglement between the separated qubit and any of the others via SLOCC. The surprise that came with this classification was that there exist two distinct kinds of, so-called, genuine tripartite entanglement: the GHZ- and W- class. They are

¹Biseparable states consist of at least two separable subsets of particles.

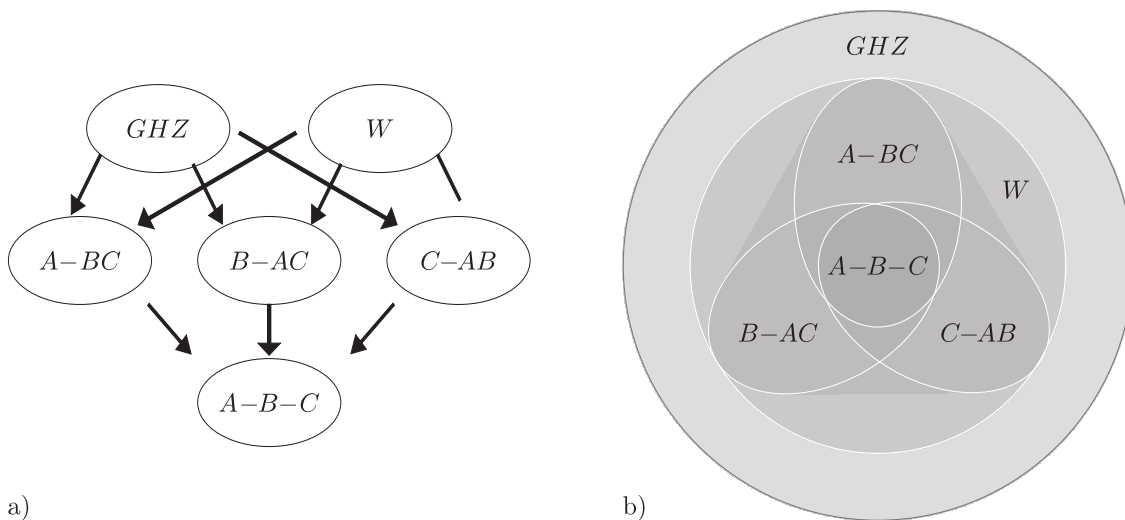


Figure 3.1: The classification of pure states (a) consists of three hierarchies: separable states (A-B-C), biseparable states (A-BC and permutations) and genuinely tripartite entangled states (GHZ and W). SLOCC operations allow one-way transformations from top to bottom. The mixed state classification (b) has an onion type structure. Starting from the smallest subset consisting of convex combinations of separable state, successively different other types of less separable states can be added by extending the convex hull. First, by adding biseparable, then W_3 and finally GHZ_3 states.

named after the respective representative states, the states $|GHZ_3\rangle$ and $|W_3\rangle$:

$$|GHZ_3\rangle = \frac{1}{\sqrt{2}}(|HHH\rangle + |VVV\rangle), \quad (3.1)$$

$$|W_3\rangle = \frac{1}{\sqrt{3}}(|HHV\rangle + |HVH\rangle + |VHH\rangle). \quad (3.2)$$

Apart from the fact that members of these two different classes cannot be converted into one another via SLOCC, it was shown that even some shared quantum resource of bi- or tripartite entangled states cannot catalyze the transformation [84]. It is worth mentioning that the space of three particle states is five dimensional (according to a parameterization by Acín et al. [85]). A general W_3 state is described by three parameters only and thus W_3 states have zero measure in contrast to the GHZ_3 states, which are characterized by five parameters.

In [23], a method to decide to which kind of equivalence class a certain pure state belongs to is presented. It relies on a pure state three-qubit entanglement measure called Wootters tangle τ [67], which is closely related to the concurrence (section 2.3.2). Imagine a tripartite state $|\psi\rangle$, where one qubit, e.g. A , shares some entanglement with qubit B (with the concurrence C_ψ^{A-B}) and also with qubit C (C_ψ^{A-C}) after tracing over the respective other qubit. The question is, whether the entanglement shared between A and the complete subsystem BC (C_ψ^{A-BC}) is simply the sum of the entanglement with each single qubit? The answer is no! There might still be entanglement between $A-BC$ on top of the pairwise entanglement.

The difference between the total and the pairwise concurrence squared is the definition of Wootters tangle τ :

$$\tau_\psi = \left(C_\psi^{A-BC}\right)^2 - \left(C_\psi^{A-B}\right)^2 - \left(C_\psi^{A-C}\right)^2 \quad (3.3)$$

$$= \left(C_\psi^{B-AC}\right)^2 - \left(C_\psi^{B-A}\right)^2 - \left(C_\psi^{B-C}\right)^2. \quad (3.4)$$

Hereby the value τ_ψ does not depend on the qubit chosen as starting point (as shown here for A and B). In order to decide which class of entanglement a pure state belongs to, it is sufficient to evaluate Wootters tangle and the concurrence between two-qubit subsets: For the class A-B-C, there is no entanglement between any of the pairs. For the three different biseparable classes there is a non-vanishing concurrence only between one pair of qubits. By definition, Wootters tangle is zero for all of these cases. Somewhat surprisingly, this is also true for the W_3 states. Thus, a vanishing tangle, together with a non-zero concurrence between all qubit pairs in the state indicates a W_3 state. All states with non-vanishing tangle belong to the GHZ_3 class. Its representative, the GHZ_3 state, is not entangled in any pair of qubits after tracing out the third qubit. However, its Wootters tangle equals one:

$$\tau_{W_3} = 0 \quad , \quad \tau_{GHZ_3} = 1 \quad (3.5)$$

$$C_{W_3}^{ij} = 2/3 \quad , \quad C_{GHZ_3}^{ij} = 0, \quad (3.6)$$

where C^{ij} denotes the concurrence between for the qubits pairs $i \neq j$.

States where all concurrences and the tangle take a value greater than zero are sometimes called mixed three qubit entangled (still, they are pure states) [86]. A very important member of these states is the so-called G_3 state [87]:

$$\begin{aligned} |G_3\rangle &= \frac{1}{\sqrt{2}} (|W_3\rangle + |\bar{W}_3\rangle) \\ &= \frac{1}{\sqrt{6}} (|HHV\rangle + |HVV\rangle + |VHH\rangle + |HVH\rangle + |VHV\rangle + |VVH\rangle). \end{aligned} \quad (3.7)$$

The concurrence between each pair is $C_{G_3}^{ij} = 1/3$ and Wootters tangle has also the value $\tau = 1/3$ proving that it is indeed a GHZ_3 class state. For higher numbers of qubits, G states are always defined as the superposition of a W and a spin flipped W (\bar{W}) state: $|G_N\rangle = \frac{1}{\sqrt{2}}(|W_N\rangle + |\bar{W}_N\rangle)$.

The generalization of the presented classification to mixed states is not straightforward. The mentioned criterion for the distinction of the different classes does not apply. To demonstrate the difficulty, consider for example an equally weighted mixture of three bipartite entangled states ($\rho_{fool} = 1/3(\rho_{A-BC} + \rho_{B-AC} + \rho_{C-AB})$, [88]). Here, all pairs are entangled (like in W_3), even though it is a biseparable and not a genuinely tripartite entangled state.

Despite of this, mixed three qubit states have been classified in [89] and the corresponding structure is depicted in figure 3.1 b). The set A-B-C consists of all convex combinations of pure completely separable states. The set of mixed biseparable states is the convex combination of all pure biseparable states of the three different classes of biseparable entanglement and the convex hull thereof. Any state that belongs to the set GHZ

but not W (GHZ/W) has a GHZ_3 state in every decomposition. Note that the mixed states of type W/B are of non-zero measure in the space of mixed states (in contrast to the W class for pure states).

With a classification of mixed quantum states available, how can one judge where a certain measured state belongs to? At this point, entanglement witnesses show their full strength. Again an entanglement witness corresponds to a hyperplane in the space depicted in figure 3.1 b). Thus, it allows distinguishing between, for example, GHZ_3 and W_3 states or genuine tripartite and biseparable states. Acín and coworkers also showed the generic witnesses for the representative states in [89]. The generic witness that detects states close to $|GHZ_3\rangle$ that belong to GHZ/W is:

$$\mathcal{W}_{GHZ_3} = \frac{3}{4}\mathbb{1} - |GHZ_3\rangle\langle GHZ_3| \quad (3.8)$$

and there are two kinds of generic W_3 witnesses, i.e., witnesses that detect genuine tripartite entanglement:

$$\mathcal{W}_{W_3}^1 = \frac{1}{2}\mathbb{1} - |GHZ_3\rangle\langle GHZ_3| \quad \text{and} \quad \mathcal{W}_{W_3}^2 = \frac{2}{3}\mathbb{1} - |W_3\rangle\langle W_3| \quad (3.9)$$

These W_3 witnesses were, for example, used to confirm the tripartite entanglement in the experimentally observed W_3 state [90, 91]. A fact that we could only prove strictly by using entanglement witnesses [92].

3.1.2 Four-qubit classification

The transfer of the results on three-qubit entanglement to multiqubit entanglement is not straightforward. Already for four qubits, there is an infinite number of classes with respect to SLOCC. Verstraete and coworkers [24] found a continuous set of representatives for all pure four-partite quantum states. These representative states are split into nine families of SLOCC-classes (SLOCC-families), where each is parameterized with up to four independent complex parameters. The first one is:

$$\begin{aligned} G_{abcd} = & \frac{a+d}{2}(|HHHH\rangle + |VVVV\rangle) + \frac{a-d}{2}(|HHVV\rangle + |VVHH\rangle) \\ & + \frac{b+c}{2}(|HVHV\rangle + |VHVV\rangle) + \frac{b-c}{2}(|HVVH\rangle + |VHHV\rangle). \end{aligned} \quad (3.10)$$

The parameters a, b, c, d are complex with non-negative real part. The corresponding state G_{abcd} is genuinely four-partite entangled, except when it takes the form $|Bell\rangle \otimes |Bell\rangle$ (e.g. $a = 1, b = 0, c = 0, d = 0$). Most of the states that have so far been identified as important (see also the next section) belong to this SLOCC-family. The most prominent exception is the four-qubit W_4 state. It is the natural extension of the W_3 state: ($|W_4\rangle = 1/2(|HHHV\rangle + |HVHH\rangle + |HHVH\rangle + |VHHH\rangle)$) and belongs to the SLOCC-family represented by:

$$\begin{aligned} L_{ab3} = & \frac{a-b}{2}(|HVVH\rangle + |VHHV\rangle) + \frac{a+b}{2}(|HVHV\rangle + |VHVV\rangle) + \quad (3.11) \\ & a(|HHHH\rangle + |VVVV\rangle) + \frac{i}{\sqrt{2}}(|HHHV\rangle + |HHVH\rangle + |HVVV\rangle + |VHVV\rangle). \end{aligned}$$

Both types of states, G_{abcd} and L_{ab_3} , contain genuine four-partite entanglement. However, the states G_{abcd} are the most remarkable. In [24], they are claimed to be the states with maximal four-partite entanglement as they are shown to maximize several entanglement monotones. A simple argument supporting this claim is the fact that for any of these representatives the residual state after tracing out all except for one qubit is maximally mixed. In section 2.3.2 (page 17) it was shown that such maximal local entropy is a sign for maximal entanglement in the two-qubit case. According to [93], this property is unique for states of the form G_{abcd} .

It is important to mention that the work on SLOCC classification of four-qubit entangled states is still in progress. Very recently, another scheme how to inductively construct SLOCC entanglement classes for any number of qubits was introduced [25, 26]. The classification reproduces the results presented for three qubits [23] but gives eight inequivalent types of four-qubit entanglement (apart from the degenerate classes), thus is not equivalent to the classification in [93], which was discussed here.

3.2 Phenomenology of quantum states

In recent years, several multipartite entangled states have been identified as interesting with respect to their applicability for certain tasks or due to particular properties like a high degree of entanglement concerning violation of Bell inequalities, high persistency against loss of photons and others.

In the following, the two families of multiqubit states of importance for this work will be introduced: The graph states and the symmetric Dicke states. Especially the study of Graph states with their unique properties turned out to be extremely fruitful in quantum information science. But also the symmetric Dicke states offer, as we will see, outstanding properties, like their high persistency against photon loss. In the last part, several examples of four-partite entangled states that have been studied and partly realized experimentally in the past will be introduced for a later comparison with the Cluster and Dicke state.

3.2.1 Graph states

Graph states are, as the name indicates, multipartite entangled quantum states that can be represented by mathematical graphs (see figure 3.2). The vertices of the graph correspond to qubits and the edges to a next neighbor Ising-type interaction between the connected vertices. In the language of quantum information this interaction can be seen as a two qubit phase gate, which was discussed in section 2.2.3. The cluster states are a particularly interesting subgroup of graph states, because they are the resource for one-way quantum computation [33, 81]. Cluster states are graph states that are represented by a periodical lattice.

The way graph states are constructed leads to a simple mathematical description via the stabilizer formalism [94]. The graph state $|g\rangle$ represented by a certain graph g fulfills a set of eigenvalue equations that are constructed in the following way. The vertices of g (and with them, the qubits) are numbered. For each vertex i we can define a stabilizing operator S_i as a tensor product of single qubit Pauli operators according to the following rules: The Pauli operator corresponding to vertex i is $\hat{\sigma}_z$, the ones corresponding to

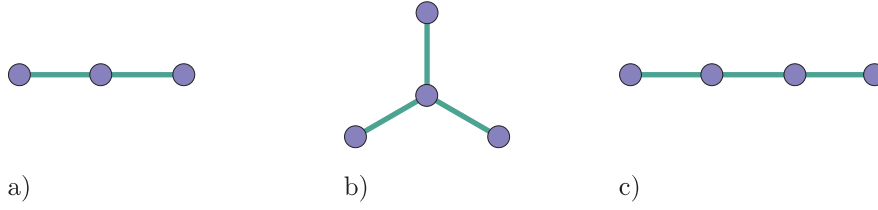


Figure 3.2: Overview of the graphs of three (a) and four qubits (b and c). For three qubits, the only graph corresponds to a GHZ_3 state. The star configuration of four qubits (b) represents the GHZ_4 state, the linear configuration the state $|\mathcal{C}_4\rangle$.

connected vertices are $\hat{\sigma}_x$ and the rest by $\hat{\sigma}_0 = \mathbb{1}$. For a state of N qubits we find therefore N stabilizing operators. The corresponding graph state is completely defined by the conditions:

$$S_i |g\rangle = \pm 1 |g\rangle \quad \forall \text{ vertices } i. \quad (3.12)$$

The signs in these eigenvalue equations can be chosen arbitrarily in the sense that the resulting states differ only up to local unitary transformations. It is obvious, by definition, that any products of the stabilizers S_i are again stabilizing operators. All of them form together the stabilizer group consisting of N^2 operators including the identity.

All inequivalent graphs of three and four qubits are shown in figure 3.2. For three particles there is only one type of graph, which corresponds to the state GHZ_3 . For four qubits, exist two inequivalent graphs, a star and a linear configuration. They correspond to the GHZ_4 (see equation 3.19) and the cluster state $|\mathcal{C}_4\rangle$, respectively. Before we discuss the properties of graph states, let us shortly demonstrate the way of construction on the example of the cluster state represented in figure 3.2 c). The corresponding eigenvalue equations are:

$$\begin{aligned} \hat{\sigma}_x \otimes \hat{\sigma}_z \otimes \hat{\sigma}_0 \otimes \hat{\sigma}_0 |\mathcal{C}_4\rangle &= |\mathcal{C}_4\rangle \\ \hat{\sigma}_z \otimes \hat{\sigma}_x \otimes \hat{\sigma}_z \otimes \hat{\sigma}_0 |\mathcal{C}_4\rangle &= |\mathcal{C}_4\rangle \\ \hat{\sigma}_0 \otimes \hat{\sigma}_z \otimes \hat{\sigma}_x \otimes \hat{\sigma}_z |\mathcal{C}_4\rangle &= |\mathcal{C}_4\rangle \\ \hat{\sigma}_0 \otimes \hat{\sigma}_0 \otimes \hat{\sigma}_z \otimes \hat{\sigma}_x |\mathcal{C}_4\rangle &= |\mathcal{C}_4\rangle. \end{aligned} \quad (3.13)$$

These equations are fulfilled by²:

$$|\mathcal{C}_4\rangle = \frac{1}{2}(|+H+H\rangle + |+H-V\rangle + |-V-H\rangle + |-V+V\rangle). \quad (3.14)$$

Multipartite graph states have been presented in many experiments. The first one was the observation of the state $|GHZ_3\rangle$ with photons [17]. Meanwhile, GHZ states of up to six qubits have been demonstrated in multiphoton experiments [18, 95, 96]. In a recent experiment also other six-photon graph states were observed [20]. Up to six trapped ions have been prepared in GHZ states [22]. Further GHZ entanglement could be demonstrated in NMR experiments [97] and also in continuous variable experiments similar correlations could be demonstrated [98, 99].

Concerning applications, graph states play a significant role in quantum error correction and multiparticle quantum communication [28, 79, 94]. As mentioned before, cluster

²The whole stabilizing group can be found in, up to Hadamard gates acting on qubits 1 and 4, in table 6.1.

states are the resource for one-way quantum computation [33]. In particular, GHZ states have a variety of possible applications, for example in multiparty quantum secret sharing [30–32], teleportation [100], quantum key distribution [101, 102], dense coding [103], quantum cloning [104] and open destination teleportation [96].

The eigenvalue equations for the stabilizers already imply that graph states have N^2 perfect correlations (the expectation values of the stabilizers). As in the standard basis the sum of *all* correlations squared add, for pure states, up to N^2 , we can directly conclude that for graph states all the non-stabilizer correlations must be zero. This allows a simple evaluation of the fidelity of a state ρ to the four-photon cluster state ($N^2 = 16$):

$$F_\rho^{\mathcal{C}_4} = \langle \mathcal{C}_4 | \rho | \mathcal{C}_4 \rangle = \frac{1}{16} \sum_{i=1}^{256} \text{Tr}(\rho \hat{K}_i) \langle \mathcal{C}_4 | \hat{K}_i | \mathcal{C}_4 \rangle = \frac{1}{16} \sum_{i=1}^{16} \text{Tr}(\rho \hat{K}_i^{stab}) \langle \mathcal{C}_4 | \hat{K}_i^{stab} | \mathcal{C}_4 \rangle \quad (3.15)$$

where \hat{K}_i are all tensor products of Pauli matrices and \hat{K}_i^{stab} the stabilizers of the Cluster state, with their signs chosen such that $\langle \mathcal{C}_4 | \hat{K}_i^{stab} | \mathcal{C}_4 \rangle = 1$. As one can see, the resulting fidelity is the average of all sixteen stabilizer correlations. Thus, already in the four-qubit case, instead of the 255 correlations constituting a density matrix, only 16 are necessary to determine the fidelity. For higher numbers of qubits the reduction in measurement settings increases strongly (2^N instead of 4^N).

The stabilizer formalism also allows to detect the entanglement of an experimentally observed state more easily. It was shown that special entanglement witnesses can be constructed from the stabilizers of a state [105]. For cluster and GHZ states it is even possible to detect genuine N -partite entanglement using only two measurement settings [106]. In addition, the expectation values of certain sets of stabilizers do not allow a description by local hidden variable theories. Thus, one can deduce Bell inequalities for entangled graph states [107–109].

Apart from this special structure of correlations, graph states also show an interesting behavior under projective measurements. In case one qubit is projected in the X- or Z- basis, the resulting states are also graph states³, where the exact form depends on the measurement result. For both bases the qubit is, obviously, not part of the state anymore. The difference is that Z-basis projections disconnect the neighboring qubits, while X-basis measurements leave them connected. By choosing the right measurement it is thus possible to reduce the state to two qubits such that the residual state is entangled independent of the outcome, i.e. with certainty! This property was studied in [33] and is called maximal connectedness (see also section 3.3.3).

We might also ask the question, how many measurements are necessary to disentangle a certain quantum state. For example, GHZ states become disentangled after projection of only one qubit in the Z-basis. In contrast $N/2$ measurements are necessary to completely disentangle a cluster state – the entanglement is more persistent [33].

3.2.2 Dicke states

Dicke states are the eigenstates of the total spin operator \hat{J}^2 and the spin operator in the z -direction \hat{J}_z in a coupled system of N spin- $\frac{1}{2}$ particles. The eigenvalues are $j(j+1)$ and m ,

³The resulting states are possibly biseparable.

	m=-2	m=-1	m= 0	m= 1	m= 2
j=2	$ HHHH\rangle$	$ W_4\rangle$	$ D_4^{(2)}\rangle$	$ W_4\rangle$	$ VVVV\rangle$
j=1		$ HH\rangle \otimes \psi^-\rangle$	$ GHZ_4^0\rangle$	$ VV\rangle \otimes \psi^-\rangle$	
j=0			$ \Psi^{(4)}\rangle$ $ \psi^-\rangle \otimes \psi^-\rangle$		

Figure 3.3: Scheme of all Dicke states of four qubits sorted by the eigenvalues of the \hat{J}^2 (lines) and \hat{J}_z (columns). The two states for $j = 0$ span a two dimensional subspace, while the three subspaces for $j = 1$ are three-dimensional spanned by the three states obtained by qubit permutation of depicted state. Our major interest concerns the states with maximal total spin, i.e. the symmetric Dicke states in the top row.

respectively. These Dicke states form a basis of the N-spin Hilbert space. Figure 3.3 shows all Dicke states of four qubits (up to permutations of qubits). Here, we are interested in the Dicke states that are completely symmetric under particle exchange. They are depicted in the upper row, as all of them have a maximal total spin. Thus, these states may either be described by the spin-z component m , or by the number of V 's, which corresponds in other physical systems, like e.g. atoms in a cavity, to the number of excitations. Here, the latter notation is used and an N -qubit symmetric Dicke state with E excitations is denoted by:

$$|D_N^{(E)}\rangle = \binom{N}{E}^{-1/2} \sum_k \mathcal{P}_k (|V_1, V_2, \dots, V_E, H_{E+1}, \dots, H_N\rangle), \quad (3.16)$$

where \mathcal{P}_k denote all possible permutations of qubits. Note, that a $\hat{\sigma}_x$ -transformation (spin-flip in the computational basis) on each qubit transforms $|D_N^{(E)}\rangle$ to $|D_N^{(N-E)}\rangle$, i.e. $|D_N^{(E)}\rangle \equiv_{LU} |D_N^{(N-E)}\rangle$. Therefore, they have exactly the same entanglement properties. W states can, in this notation, be written as $|W_N\rangle = |D_N^1\rangle$, their spin flipped counterpart as $|\bar{W}_N\rangle = |D_N^{(N-1)}\rangle$. Note that GHZ_4 states are not symmetric Dicke states, but can be expressed as superposition thereof and are equivalent under LU to the state with $j=1$ and $m=0$: $|GHZ_4^0\rangle = 1/\sqrt{2}(|HHVV\rangle - |VVHH\rangle)$.

In the following, a short overview of the ideas how to observe Dicke states in experimental setups will be presented. Concerning the creation of arbitrary superpositions of symmetric Dicke states in quantum dots, there was a scheme proposed in [110]. Xiao et al. [111] presented a scheme for the generation of Dicke state entanglement between the excitations of atoms in a cavity. A way how to dynamically create Dicke states with atoms in a cavity or trapped ions was presented in [112, 113]. Another way to obtain these states, via an adiabatic process, in trapped ions was proposed by Unanyan et al. [114]. Further, Stockton et al. [80] proposed the preparation of those states via collective spin measurements of an atomic ensemble. Experimentally, the focus was so far put on the observation

of W states. We observed the first three-photon W state via an interferometric linear optics setup [88, 90, 115] based on non-collinear parametric down conversion (section 4.1.1). A more efficient scheme based on collinear down conversion and a weak coherent beam was presented by Mikami et al. [116] recently. Photonic experiments, despite many proposals, did to our knowledge not demonstrate four-qubit W state entanglement up to now. With trapped ions, however, W states of up to eight particles have been prepared by Häffner et al. [21]. Concerning the applications of symmetric Dicke states, so far most of the research focused on W states. For those, quantum telecloning [117, 118], generation of the universal entangled state [119], quantum teleportation [120–125], quantum key distribution [126], and dense coding [124] have been proposed.

In chapter 7, the first experiment on the analysis of a symmetric Dicke state with more than one excitation [127], the state $D_4^{(2)}$ is presented. There have been a few theoretical investigations on this type of quantum states. Entanglement properties of symmetric Dicke states are studied extensively in [40], in particular the behavior for a growing number of qubits. I would like to note that some theoretical studies on symmetric entangled states in general are presented in [51], which include also all superpositions of symmetric Dicke states, in particular also GHZ states. Apart from this, there have been some general studies on entanglement detection for these states, which I will discuss shortly in the following. Thereby a focus is put on results that are useful for our investigation of $D_4^{(2)}$.

Just like for graph states one can find entanglement witnesses for the analysis of symmetric Dicke states in general [128]. One particularly peculiar example are the entanglement witnesses of the form:

$$\mathcal{W}_s = \langle \hat{J}_x^2 \rangle + \langle \hat{J}_y^2 \rangle \leq B, \quad (3.17)$$

where $\hat{J}_{x/y} = 1/2 \sum_k \sigma_{x/y}^k$ with e.g. $\sigma_x^3 = \mathbb{1} \otimes \mathbb{1} \otimes \sigma_x \otimes \mathbb{1}$. The bound B depends on the number of qubits and which type of separability should be excluded (complete separability, biseparability, ...). The witness can easily be rewritten to the standard form, where a negative expectation value proves entanglement: $\mathcal{W}'_s = B - \mathcal{W}_s$. We preferred the notation in equation 3.17, as it can be interpreted physically. To do so, we rewrite $\langle \hat{J}_x^2 \rangle + \langle \hat{J}_y^2 \rangle = \langle \hat{J}^2 \rangle - \langle \hat{J}_z^2 \rangle$ where $\hat{J} = (\hat{J}_x, \hat{J}_y, \hat{J}_z)$. As for symmetric states $\langle \hat{J}^2 \rangle = N/2(N/2 + 1)$ our criterion requires $\langle \hat{J}_z^2 \rangle \geq B$, i.e. the collective spin squared of biseparable symmetric states in any direction cannot be arbitrarily small [129–131]. For Dicke states, however, the expectation value $\langle \hat{J}_z^2 \rangle$ can even vanish when the number of excitations approaches $N/2$. Thus, it is the difference between maximal total spin and zero spin squared in one direction that cannot be achieved by separable, but only by entangled quantum states. One example where this contrast is maximal is the state $|D_4^{(2)}\rangle$, which is subject of this thesis. It should also be noted that the application of this criterion does not require the ability to access individual qubits, but is intrinsically collective. For other physical implementations of qubits, this might be a big advantage.

The behavior of entangled Dicke states under photon loss is completely different in comparison to Graph states. The residual photons' state after tracing out one qubit is a mixed state of the following kind:

$$\text{Tr}_A(|D_N^{(E)}\rangle\langle D_N^{(E)}|) = E/N |D_{N-1}^{(E-1)}\rangle\langle D_{N-1}^{(E-1)}| + (N-E)/N |D_{N-1}^{(E)}\rangle\langle D_{N-1}^{(E)}|. \quad (3.18)$$

At least one of the two terms is genuinely (N-1)-partite entangled, and so is the resulting

mixed state. Thus, the entanglement persistency in Dicke states is very high, i.e. the entanglement cannot be destroyed by qubit loss.

The behavior under projective measurements is also different from graph states. If both terms in the previous equation are entangled, then any projective measurement will result in a superposition of Dicke states. Otherwise, i.e. in case we start from a W state, there is the possibility to disentangle the state with a certain probability. This is in strong contrast to the behavior of graph states, where one can choose whether the entanglement should be kept by choice of the measurement basis. Here, this is additionally dependent on the measurement outcome.

In the following, we will restrict our investigation to four particles. This is the smallest number of qubits where in addition to the W_4 states also a Dicke state of the form $|D_N^{(N/2)}\rangle$ exists. In other words, there exists a symmetric state with a z-spin component $m = 0$. The two kinds of states show very different behavior when studied for a large number of particles [40]. On the one hand, when the entanglement between the pairs after tracing out all other qubits was studied, the W states showed the maximal entanglement compared to all other Dicke states (it was conjectured even in comparison to all quantum states [23]). On the other hand the maximal entanglement between bisplittings⁴ is maximized for the states $D_N^{(N/2)}$. This is, however, only true with respect to other Dicke states. There are other states [51] that show a higher degree of entanglement in this respect.

3.2.3 Overview of important four-qubit entangled states

After these more general considerations, several relevant examples of four-photon entangled states are presented in the following. This will allow later comparison with the states that were prepared experimentally.

- The GHZ_4 state

The four-qubit GHZ_4 state is the natural extension of its tripartite relative $|GHZ_3\rangle$ (equation 3.1):

$$|GHZ_4\rangle = \frac{1}{\sqrt{2}}(|HHHH\rangle + |VVVV\rangle). \quad (3.19)$$

It is interesting to note that solely in the case of four qubits it can be transformed into a G_4 state via LU, i.e., by application of $\hat{\sigma}_z^{1/4}$ and a Hadamard gate \mathcal{H} on each qubit⁵ [87]:

$$|G_4\rangle = (\overline{\mathcal{H}} \otimes \overline{\mathcal{H}} \otimes \overline{\mathcal{H}} \otimes \overline{\mathcal{H}}) |GHZ_4\rangle = \frac{1}{\sqrt{2}}(|W_4\rangle + |\overline{W}_4\rangle), \quad (3.20)$$

with $\overline{\mathcal{H}} = \mathcal{H} \cdot \hat{\sigma}_z^{1/4}$. GHZ states are often considered as maximally entangled, partly because they offer the highest possible violation of two setting Bell inequalities [132–134]. One should emphasize, however, that this perception depends strongly on the measures taken. The GHZ_4 state is neither maximally entangled with respect to

⁴Bisplitting: The state is virtually cut in two parts and the entanglement between these parts is calculated.

⁵Application of $\hat{\sigma}_z^{1/4}$ switches the sign between the two terms in GHZ_4 .

bisplittings [51], nor with respect to the geometric measure of entanglement (table 3.2.3). As we have seen, GHZ states are graph states. The graph of the state $|GHZ_4\rangle$ (up to LU) is shown in figure 3.2 b).

- The Cluster State

The four-photon cluster state is the only other graph state in four-qubit systems (figure 3.2 c)). Therefore, it also shares some properties with the state $|GHZ_4\rangle$. A detailed theoretical and experimental analysis will be discussed in chapter 6. We implemented the state experimentally in the form:

$$|C_4\rangle = \frac{1}{2}(|HHHH\rangle + |VVHH\rangle + |HHVV\rangle - |VVVV\rangle) \quad (3.21)$$

The major interest in cluster states stems from the applicability for one-way quantum computing. In an experiment that was performed simultaneously with our study of the cluster state (see chapter 6 and [135]), the implementation of a C_{NOT} -gate and the Grover search algorithm in a one-way quantum computation scheme was shown [35].

- The W_4 state

The four qubit W state is the natural extension of its three-qubit relative $|W_3\rangle$ (equation 3.2):

$$|W_4\rangle = \frac{1}{2}(|HHHV\rangle + |HHVH\rangle + |HVHH\rangle + |VHHH\rangle). \quad (3.22)$$

It belongs to the symmetric Dicke states (figure 3.3) and is the only example of a four-qubit entangled state discussed here that is not part of the G_{abcd} - but the L_{ab_3} SLOCC-family (equation 3.11). It is known to have the highest concurrence between the pairs of subsets. It has, however, not the highest singlet fraction and negativity, as we will see in chapter 7.

- The symmetric Dicke state with two excitations $|D_4^{(2)}\rangle$

This state had only few appearances in the literature (e.g. [75, 136]) before. This is very surprising as it is also another very natural extension of the three-qubit W state. It is defined by:

$$|D_4^{(2)}\rangle = \sqrt{\frac{1}{6}} (|HHVV\rangle + |HVHV\rangle + |HVVH\rangle + |VHHV\rangle + |VHVH\rangle + |VVHH\rangle) \quad (3.23)$$

and as an interesting curiosity it can be rewritten as:

$$(\mathcal{H} \otimes \mathcal{H} \otimes \mathcal{H} \otimes \mathcal{H})(|D_4^{(2)}\rangle) = \frac{1}{2}(\sqrt{3}|GHZ_4\rangle - |D_4^{(2)}\rangle). \quad (3.24)$$

Despite of the different properties of the states $|GHZ_4\rangle$ and $|D_4^{(2)}\rangle$, there is a strong similarity between them in this representation, which is also visible in the experiment (figure 7.2). The state $|D_4^{(2)}\rangle$ is, like the W_4 state, an entangled symmetric Dicke state (figure 3.3). Note that it does, however, not belong to the same SLOCC-family as the W_4 state. In chapter 7 (see also [127].), a detailed theoretical and experimental analysis is presented.

- The state $|\Psi^{(4)}\rangle$

Another Dicke state, which is however not symmetric under permutation of all particles is the state $|\Psi^{(4)}\rangle$. It has zero total spin and contains the same terms as the Dicke state but with a different weighting:

$$\begin{aligned} \Psi^{(4)} = & \frac{1}{\sqrt{3}} (|HHVV\rangle + |VVHH\rangle) \\ & - \frac{1}{\sqrt{12}} (|HVHV\rangle + |HVVH\rangle + |VHHV\rangle + |VHVH\rangle) \end{aligned} \quad (3.25)$$

it does not change under operations of the type:

$$(LU \otimes LU \otimes LU \otimes LU)\Psi^{(4)} = \Psi^{(4)} \quad (3.26)$$

Therefore this quantum state can be used for decoherence free quantum communication, which was demonstrated experimentally in [137]. It contains the same terms like the state $D_4^{(2)}$, but the symmetry S_{1324} is broken due to the different weightings and the minus sign. The state was prepared with polarized photons [115, 138]. We demonstrated an extensive experimental study of the states' entanglement persistency in [83]. It is ideal for universal $1 \rightarrow 2$ telecloning as shown by [118, 139]. In addition some modified kind of secret sharing was demonstrated experimentally using this state [140, 141].

As we have seen, all of these quantum states belong to the first SLOCC-family, G_{abcd} , according to the classification introduced in section 3.1.2, apart from the state $|W_4\rangle$. This can easily be seen from their maximal local entropy. The explicit transformations are summarized in appendix B.2. Apart from this, the cluster and GHZ_4 states constitute the representatives of the graph states, and the states $|W_4\rangle$ and $|D_4^{(2)}\rangle$ represent the entangled symmetric Dicke states. For further comparison, the geometric measures of entanglement of all the states that were presented here are summarized in table 3.2.3. In the following, we will take a closer look at some of the properties that are going to be studied here.

	4 qubit states					3 qubit states		
States	$ D_4^{(2)}\rangle$	$ W_4\rangle$	$ C_4\rangle$	$ GHZ_4\rangle$	$ \Psi^{(4)}\rangle$	$ GHZ_3\rangle$	$ W_3\rangle$	$ G_3\rangle$
E_G	0.625	0.578	0.750	0.500	0.667	0.500	0.556	0.250

Table 3.1: Geometric measure of entanglement of several genuinely three- and four- qubit entangled states. The sources for these values are summarized in appendix A.

3.3 Properties of entangled states

To identify the family and SLOCC-family a quantum state belongs to, and how strongly it is entangled with respect to a certain entanglement measure, are important steps in the characterization of the state. A description is, however, never complete without a look at the properties exhibited by the object being studied. Therefore, this section is devoted to some properties of entangled states which will be explored in the experimental part.

Here, we are mainly interested in properties that are easily accessible experimentally, i.e., that can be studied without complete knowledge of the quantum state. As experimentally prepared states are never perfect and in general mixed, a demonstration of how well certain properties are reproduced are better indicators of how well a quantum state was reproduced, than e.g. simply giving a value for the fidelity.

Several properties of quantum states are specific to only one or a few examples, like the symmetry under local unitary transformations in $|\Psi^{(4)}\rangle$. These special issues will be discussed in detail for the two states of interest, $|\mathcal{C}_4\rangle$ and $|D_4^{(2)}\rangle$, in the corresponding chapters. Apart from this, one can also identify some properties that are in general a good subject of investigation and that, at the same time, fulfill our demand of easy accessibility. Here, we study three properties of general interest: permutation symmetry, entanglement persistency and connectedness.

3.3.1 Permutation symmetry

Interestingly, all of the discussed four-photon quantum states exhibit some kind of permutation symmetry. They can be put into two groups using the description introduced in section 2.2.3 (page 12). The states $|D_4^{(2)}\rangle$, $|W_4\rangle$ and $|GHZ_4\rangle$ are symmetric under all permutations of qubits and therefore eigenstates of all operators in the symmetry group generated by the swap operators S_{2134} , S_{1324} and S_{1243} , which has 24 elements (figure 3.4 a). The states $|\mathcal{C}_4\rangle$, $|\Psi^4\rangle$ and $|\text{Bell}\rangle \otimes |\text{Bell}\rangle$ do not fulfill the symmetry S_{1324} . Instead they follow the permutation group generated by S_{2134} , S_{3412} and S_{1243} (eight elements, figure 3.4 b). Thus, permutation symmetry is a characteristic of many strongly entangled states, even though it is not an entanglement criterion by itself as separable symmetric states exist (e.g. $|HHHH\rangle$). This observation is supported by the arguments that were discussed in the context of the witnesses for symmetric Dicke states (section 3.2.2). There, we saw that the violation of the bounds on $\langle J^2 \rangle - \langle J_z^2 \rangle$ (equation 3.17) for biseparable states is related to a combination of high local entropy and complete permutation symmetry, leading to a separability criterion.

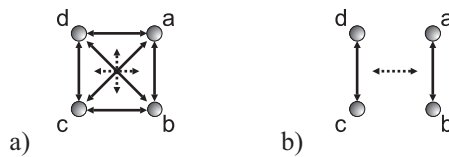


Figure 3.4: Representation of the two symmetry groups encountered in the presented examples of four-qubit entangled states. Straight lines means exchange of qubits, dashed lines exchange of qubit pairs. By concatenation either all possible permutations (a) or a permutation subgroup (b) is formed.

Permutation symmetry can therefore be considered as a property worth being studied in more detail. In the following, the expectation value of the permutation operator is used to study the symmetry of an experimentally observed state. This approach is efficient, as it does not require complete knowledge about the state, but only few measurements⁶. To

⁶This issue is addressed in more detail in section 4.3.

illustrate its interpretation, it is contrasted to another one that is, however, not advantageous experimentally.

We chose to analyze the symmetry of a pure quantum state $|\psi\rangle$ by studying its overlap with its permuted counterpart $S|\psi\rangle$:

$$\langle S \rangle_\psi = \langle \psi | S | \psi \rangle. \quad (3.27)$$

Thus, the result is simply the expectation value of the permutation operator S . This value can vary between $+1$ for symmetry (e.g. $\langle S_{21} \rangle_{\psi^+} = +1$) and -1 for antisymmetry (e.g. $\langle S_{21} \rangle_{\psi^-} = -1$), respectively.

One way to generalize this approach to mixed states is to calculate the expectation value of the swap operator for mixed states ρ which is simply given by:

$$\langle S \rangle_\rho = \text{Tr} [S\rho] = \sum_i p_i \langle \psi_i | S | \psi_i \rangle, \quad (3.28)$$

for any decomposition of ρ into pure states $|\psi_i\rangle$. Here, we can directly see that the resulting value is the weighted average over the symmetries (i.e., swap operator expectation values) of the pure states. The resulting value is closely related to the probability to project the state ρ onto the symmetric subspace. This can be seen by using the relation given in equation 2.33:

$$\begin{aligned} \text{Tr} [Z\rho Z] &= \text{Tr} [Z Z\rho] = \text{Tr} [Z\rho] = \\ \langle Z \rangle_\rho &= \text{Tr} \left[\frac{\mathbb{1} + S}{2} \rho \right] = \frac{1}{2} (1 + \langle S \rangle_\rho) \end{aligned} \quad (3.29)$$

It is important to note that $\langle S \rangle_\rho$ is not the overlap of the mixed state with its permuted counterpart! It is a stricter criterion on permutation symmetry, because not only the whole mixed state needs to be symmetric under permutations, but also all of the pure states it consists of, to reach the maximal value 1. The overlap for mixed states would constitute another route to quantify symmetry of mixed states by using the corresponding definition of fidelity, which was introduced in equation 2.18. Then, the overlap between a mixed state and its permuted counterpart is given by:

$$f_\psi^{\mathcal{P}} = \text{Tr} \left[\sqrt{\sqrt{\rho} S_{\mathcal{P}}^\dagger \rho S_{\mathcal{P}} \sqrt{\rho}} \right] \quad (3.30)$$

where \mathcal{P} is a certain permutation of the qubits. While, on the one hand, this value is the overlap of a mixed state with its permuted counterpart it does, on the other hand, not show any difference between symmetry and antisymmetry. To exemplify this, we calculate both quantities for white noise of two qubits:

$$f_{\rho_{wn}} = \text{Tr} \left[\sqrt{\sqrt{\frac{\mathbb{1} \otimes \mathbb{1}}{4}} S \frac{\mathbb{1} \otimes \mathbb{1}}{4} S \sqrt{\frac{\mathbb{1} \otimes \mathbb{1}}{4}}} \right] = \frac{\text{Tr} [\mathbb{1} \otimes \mathbb{1}]}{4} = 1 \quad (3.31)$$

$$\langle S \rangle_{\rho_{wn}} = \text{Tr} \left(S \frac{\mathbb{1} \otimes \mathbb{1}}{4} \right) = \frac{1}{2} (\langle S \rangle_{\psi^+} + \langle S \rangle_{\phi^+} + \langle S \rangle_{\phi^-} - \langle S \rangle_{\psi^-}) = \frac{1}{2} \quad (3.32)$$

Thus, even though white noise is still white noise after a permutation of qubits ($f_{\rho_{wn}} = 1$), it cannot be expressed as a mixture of symmetric pure states and therefore is not considered completely symmetrical according to the stricter criterion ($\langle S \rangle_{\rho_{wn}} = 1/2 < 1$). This

is due to the fact that white noise always has anticorrelated components. An example of a mixed separable state that is symmetric is the state:

$$\rho_{sym} = 1/2(|HH\rangle\langle HH| + |VV\rangle\langle VV|) \quad \text{with} \quad f_{\rho_{sym}} = \langle S \rangle_{\rho_{sym}} = 1 \quad (3.33)$$

Another example is the comparison of the state $|W_3\rangle$ with ρ_{fool} . The latter was shortly defined in section 3.1.1 and is explained in more detail in [88] as an example of a state that can experimentally easily be confused with $|W_3\rangle$ despite the fact that ρ_{fool} is only bipartite entangled. The W_3 state is indeed symmetric under all of the six permutations of three qubits generated by S_{213} and S_{132} . As it is also a pure state the two values for symmetry are equal $f_{W_3} = \langle S \rangle_{W_3} = 1$ for any permutation S in the mentioned group. The state ρ_{fool} is symmetric in sense of the second criterion $f_{\rho_{fool}}^{213} = f_{\rho_{fool}}^{132} = 1$. It is not, however, in the sense of the expectation value of the swap operator $\langle S_{213} \rangle_{\rho_{fool}} = \langle S_{132} \rangle_{\rho_{fool}} = \langle S_{321} \rangle_{\rho_{fool}} = \frac{1}{2}$, because the pure states in the decomposition are not symmetric. This example also shows that in certain cases studying the symmetry is even a useful tool for state discrimination.

In summary, two ways to study symmetry in a state were presented. One is based on the pure state decomposition of mixed quantum states, the other on the symmetry of the mixed states themselves. Which of the criteria is to be used, depends on the information that one wants to gather. The latter analysis reflects how much the state is changed when two qubits are exchanged. The first one is, however, stricter, as it requires symmetry of all pure states in the state's decomposition. Therefore, it is a lower bound on the value for mixed state symmetry. Further, it is better suited for experimental evaluation, because it does not require complete knowledge about the state.

3.3.2 Entanglement persistency

When studying entanglement persistency [81, 83], one is interested in how much and what kind of entanglement remains from a quantum state after one or several photons are lost. Several remarks on entanglement persistency have already been made in the presentation of different types of quantum states. For example, the entanglement in a GHZ state, known to exhibit strong correlations, is already destroyed after loss of only one particle. It is a well-known fact, that W states are much more robust in this respect (e.g. [23]). As it turns out, there exist also many other multipartite entangled states that still exhibit a significant amount of entanglement even after the loss of several particles [40].

As pointed out in [23, 82, 83], especially the analysis of the bipartite residual states is fruitful: On the one hand, bipartite entanglement is understood much better than multipartite and thus enables an alternative route for the characterization of multipartite entanglement. On the other hand, studying the bipartite subsystem of a state requires less effort than the description of the whole state. Quantum state tomography on a bipartite subsystem of the investigated quantum states opens, with a small number of measurements, the possibility to apply the entire theoretical framework introduced in chapter 1. In particular, the concurrence and negativity of the reduced quantum states can be used to quantify the entanglement in the residual state.

In addition, the study of entanglement persistency opens another point of view on multiparty quantum communication schemes. There, some parties might not want to

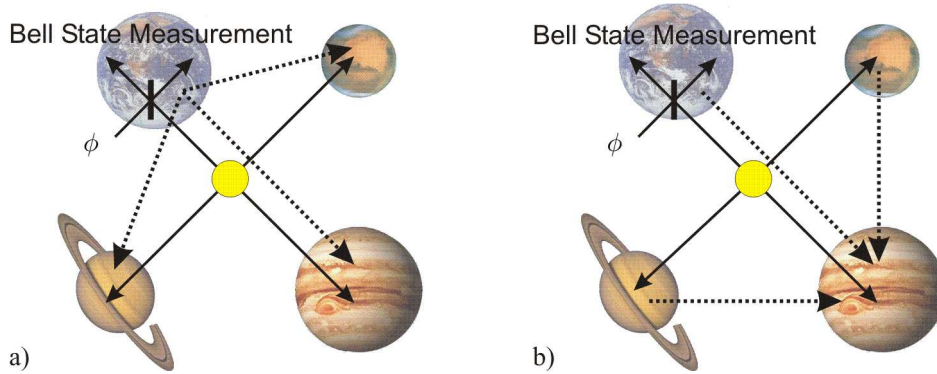


Figure 3.5: Two four-party quantum communication schemes that are related to persistency and connectedness, respectively. The solid arrows represent the quantum channels distributing the quantum state to four parties. Dashed lines correspond to classical communication channels. In quantum telecloning (a), three receiving parties obtain a clone of the input state. The sender needs to broadcast the result of the Bell state measurement allowing them to perform a corresponding unitary transformation on their qubit. In open destination teleportation (b) the parties cooperate to send a perfect copy of the state to one of the three receivers, here exemplarily Jupiter. The measurement results on Mars and Saturn and the Bell state measurement on Earth allow to (probabilistically) obtain the teleported state on Jupiter.

cooperate, or the information about particles is not accessible for other reasons. Both situations can be described by particle loss. Even more interesting is the fact that the applicability of a quantum state for quantum telecloning (QTC) [118] can be derived from this property. Somewhat surprisingly, none of the entanglement measures is needed to do so, but the maximal singlet fraction F_{MSF} (equation 2.37) of the bipartite residual state.

The reason is that one can calculate the teleportation fidelity when using a particular bipartite quantum state out of F_{MSF} , as we have seen in section 2.2.4. Now, consider a configuration similar to the one for teleportation, only with four parties (figure 3.5). Let us say Earth, Mars, Saturn and Jupiter share a certain quantum state as resource. Again, Earth has some input state $|\phi\rangle$ that is supposed to be sent to the other three parties. The bipartite resource that Earth shares with *one* other party is exactly the state after tracing out the other two qubits (Saturn and Jupiter). The corresponding teleportation fidelity achieved between Earth and Mars can then be calculated from F_{MSF} of their shared residual state. Because this is valid for all of the pairs that Earth shares with the other parties, one Bell state measurement is used for the transfer to all of the other planets at the same time. Classical transfer of the measurement outcome (dashed lines in figure 3.5 a) to Mars, Saturn and Jupiter allows them to reconstruct the states with a quality that corresponds to the entanglement in the pairs, i.e. to the entanglement persistency. Note, that this quality is never perfect, as the three clones are forbidden to be perfect copies of the input states by the No-Cloning theorem [142].

It turns out that the pure state with the highest F_{MSF} in *two* qubit pairs is the state $\Psi^{(4)}$ [83]. It allows telecloning from one sender to two receivers with the best achievable theoretical fidelity of $5/6$. Indeed, we also performed an experiment where a fifth photon was used as input qubit [140].

It was already mentioned that symmetric Dicke states are very persistent against loss of photons. Due to their permutation symmetry, they share the same entanglement between all pairs of qubits in the state. The W states exhibit the highest amount of entanglement in the pairs according to the concurrence. In contrast, concerning the maximal singlet fraction the state $|D_4^{(2)}\rangle$ reaches the maximally achievable value [143]. Thus, it is optimal for telecloning from one sender to *three* receivers, with an average⁷ telecloning fidelity of $7/9$. In case of the state $D_4^{(2)}$ the teleportation of input states of the form $\phi_{cov} = \frac{1}{\sqrt{2}}(|H\rangle + e^{i\phi}|V\rangle)$ has a higher fidelity of $5/6$. This is the limit for the so-called covariant telecloning fidelity from one sender to three receivers [144].

3.3.3 Connectedness

Entanglement persistency concerned the entanglement in a state after tracing out qubits, corresponding to the case when the other parties do not cooperate or when particles are lost. When all parties do cooperate, more entanglement in the subsets of states can be obtained (at least probabilistically), because we can choose a basis for the measurement on some of the particles and the residual state depends on the measurement outcome. We study the connectedness of the state by looking at the entanglement between the residual qubits conditioned on the outcomes of projective measurements on the other qubits.

Connectedness was originally discussed in relation with cluster states in [81]. There, it means the maximal number of projective measurements that can be performed such that the residual state is still entangled with certainty. In order to use it for all of the states mentioned here, we need to extend the meaning, i.e., we do not require certainty. Then two values are interesting: The maximal quality of the residual states after the projective measurements and their probability of occurrence. As we have seen that different types of multipartite entanglement exist, it is for multipartite reduced states also important to ask what kind of entanglement can be achieved. Thus, a relation between types of multipartite entanglement of a different number of qubits is revealed. An example for these relations was discussed in section 3.2.1: Graph states are transferred to other graph states with a reduced number of qubits after projective measurements.

Again, the investigation of the bipartite subsets gives an insight in possible applications. Consider the configuration for quantum telecloning. Instead of the distribution of three quantum clones to the receiving parties, the task is now to send a perfect copy of the input state to one receiver (Mars, Jupiter or Saturn) after the quantum resource has already been distributed. Thus, the protocol is in principle a teleportation, but the destination of the sent qubit can be chosen by the cooperating receivers. In other words, the shared quantum state needs to exhibit connectedness such that by cooperation of the parties, a perfect Bell state can be obtained between Earth and the receiving party, e.g. Jupiter, with a certain probability. To achieve this, again Earth needs to send the result of the Bell state measurement to Jupiter which allows the final transformation of the received qubit. Further, Mars and Saturn need to send their measurement result to Jupiter, as well, allowing the decision whether the protocol worked. This protocol is called open destination teleportation (ODT) and was introduced and demonstrated experimentally for the five-qubit GHZ state by Zhao and coworkers [96].

⁷The average is taken over all possible input states.

As it turns out, again the state $|D_4^{(2)}\rangle$ is suited for this task. A projective measurement of two qubits in the same basis leads to a Bell state in the other pair, if the measurement results are orthogonal. The protocol works with a probability of $2/3$. In addition, due to the permutation symmetry of the state, every party can take the role of the sender. Note further, that even the decision whether the quantum information should be distributed between the receivers or transferred to one receiver only (QTC or ODT) can be made after the Bell state analysis, i.e., after the state was "sent".

3.4 Summary

In conclusion, many different types of entanglement can be identified for multiqubit quantum systems. While several quantum states are known to have special properties or to be useful for applications, it is a natural goal to find systematic ways to classify and to describe the different kinds of entanglement.

A very abstract way to gain insight into the structure of multipartite entanglement is to use the equivalence of quantum states under SLOCC, i.e. probabilistic local operations that can be performed without quantum channels. This leads to classes of quantum states that are suitable for the same type of communication tasks [23, 24, 89]. This way, a structure can be identified in the variety of different states. For four qubits, these entanglement classes are split into nine superordinate families. The states investigated in this theses, $|C_4\rangle$ and $|D_4^{(2)}\rangle$, belong to the same SLOCC-family G_{abcd} [24].

A second approach is to focus on the investigation of families of quantum states with similar structure. In contrast to the SLOCC classification, one does then not cover all entangled states of a certain number of qubits. Instead, a family contains states of different qubit numbers, thereby showing relations between entangled states of different size. One family that is relevant in the following are the graph states, which have two four-qubit representatives: The well-known GHZ_4 state, and the cluster state, which has been observed only recently in the context of this work (chapter 6 and [135]) and by Walther et al. [35]. The second family are the symmetric Dicke states, which also contain two entangled four-qubit states: The state $|W_4\rangle$, which also has already received some attention, and the state $D_4^{(2)}$, whose first experimental observation and analysis is presented in chapter 7 and [127].

Further, quantum states are characterized by their specific properties. To study these properties is an inevitable part of understanding the various types of entanglement. The states $|C_4\rangle$ and $|D_4^{(2)}\rangle$ exhibit different permutation symmetries. With the method that we presented here it will be possible to efficiently study this property in the experimentally observed quantum states. The investigation of entanglement persistency and connectedness concern the entanglement in subsets of particles of a quantum state. It allows a deeper insight in the entanglement structure of the states and is particularly relevant for judging the applicability of quantum states in multiparty quantum communication. They describe the potential use of the state in situations were, for example, particles are lost. Furthermore, they can be used to concretely quantify the quality achieved in quantum telecloning and open destination teleportation protocols, when the state is used as quantum resource.

4 Entanglement Engineering with Polarized Photons

Experiments on multipartite entanglement started in the end of the 1990's in the group of Anton Zeilinger with polarization entangled photons. Meanwhile, many other physical systems were brought to a stage where entanglement can be studied, most notably trapped ions. Here, we use the "old" approach based on spontaneous parametric down conversion (SPDC) and linear optics to observe photonic quantum states. An advantage of this approach is that we can already use the non-classicality of the creation process of the photons as a starting point for their further processing. While the necessary interaction of the particles is basically a difficult task for photons, the use of linear optics together with conditional detection has proved as a flexible and successful method to obtain different types of entangled quantum states. Today, more different kinds of entanglement have been observed in multiphoton experiments compared to any other way of implementation.

In the following, the different stages of this type of experiment will be presented. We start with the creation of photons via SPDC. The process itself and the experimental implementation is described shortly. Further, tools for linear optics quantum processing based on birefringent crystals and beam splitters are explained followed by the detection process .

Finally, the further processing of the obtained data will be outlined. The evaluation of the observed states' correlations, reconstruction of density matrices and determination of characteristic values that will be used for the state analysis of the last three chapters are presented. Additionally, quantum process tomography will be introduced for later use as a tool to characterize our controlled phase gate.

4.1 Generation of photons

4.1.1 Spontaneous parametric down conversion

When an electromagnetic field interacts with a dielectric medium it induces electric dipole moments. The macroscopic sum thereof results in a polarization \vec{P} that is, for an anisotropic crystal, related to the electromagnetic field \vec{E} via [145]:

$$P_i = \epsilon_0 \left(\sum_j \chi_{ij}^{(1)} E_j + \sum_{j,k} \chi_{ijk}^{(2)} E_j E_k + \sum_{j,k,l} \chi_{ijkl}^{(3)} E_j E_k E_l + \dots \right) \quad (4.1)$$

where ϵ_0 is the permittivity for a vacuum, χ are the nonlinear susceptibilities and the indices $i, j, k, l \in \{1, 2, 3\}$.

For a strong pump field, the second order contribution cannot be neglected and two new electromagnetic fields are created. In second quantization this corresponds to the

spontaneous decay of a pump photon with energy $\hbar\omega_p$ and momentum $\hbar\vec{k}_p$ into two so-called signal and idler photons with energies $\hbar\omega_s, \hbar\omega_i$ and momentum $\hbar\vec{k}_s, \hbar\vec{k}_i$. Due to energy and momentum conservation we have:

$$\omega_p = \omega_i + \omega_s \quad (4.2)$$

$$\vec{k}_p = \vec{k}_i + \vec{k}_s \quad (4.3)$$

For a more detailed quantum mechanical description of the process, refer to e.g. [146].

When a birefringent crystal is pumped by an extraordinarily polarized beam, there are two different types of SPDC:

Type I: The signal and idler photons are ordinarily polarized.

Type II: Signal and idler photons are orthogonally polarized, i.e. one ordinarily, the other extraordinarily.

Due to energy and momentum conservation the created photons are strongly correlated in these two degrees of freedom. In our experiments, the photons are distinguished by spatial mode and polarization, therefore we seek to achieve indistinguishability in all other degrees of freedom. Thus, we select only the degenerate SPDC emission, where the created photons have half the frequency of the pump beam.

We want to take advantage of the orthogonality of the polarizations of the signal and idler photons and use therefore SPDC of type II. The momentum conservation ensures that the photons are always emitted symmetrically around the pump beam. As they have different polarizations, the signal and the idler photon are emitted onto two emission cones, as can be seen in figure 4.1. The angle between these cones is varied by tilting the optical axes of the crystal relative to the pump beam. For the experiments presented in this thesis two configurations have been used. In figure 4.1 a) the most common configuration for the creation of polarization entangled photons is shown [147]. The two cones intersect and it is not possible to know which photon is emitted into which crossing mode. In figure 4.1 b) a collinear configuration is shown. The cones only touch in a mode collinear with the pump beam and the created photon pair is collected in one spatial mode, only. These two configurations will be studied in a little more detail in the following.

Non Collinear Configuration

For the non-collinear configuration, entangled photon pairs can be emitted onto two spatial modes a and b , given by the directions where the two emission cones overlap (figure 4.1 a). If, like in our case (see section 4.1.2), intense and short pump pulses are applied, then multiple emission events during a single pulse lead to the following state [148, 149]:

$$\begin{aligned} Z e^{-ic(a_V^\dagger b_H^\dagger + a_H^\dagger b_V^\dagger)} |0\rangle = \\ Z \left(ic(a_V^\dagger b_H^\dagger + a_H^\dagger b_V^\dagger) - \frac{c^2}{2}(a_V^\dagger b_H^\dagger + a_H^\dagger b_V^\dagger)^2 + \dots \right) |0\rangle \end{aligned} \quad (4.4)$$

where Z is a normalization constant, c depends on parameters of the crystal and is proportional to the pump beam intensity¹ and $a_V^\dagger, b_H^\dagger, a_H^\dagger$ and b_V^\dagger represent the photon creation operators for the modes a and b .

¹Only valid for $c \ll 1$

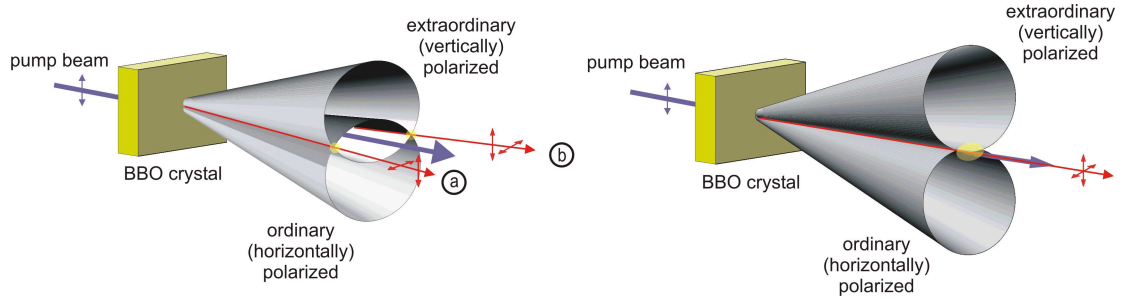


Figure 4.1: Two configurations to create photons with SPDC of type II. In the non-collinear configuration (a) the two characteristic emission cones intersect and entangled photon pairs are emitted onto the crossing modes. The collinear configuration (b) uses touching emission cones to obtain photon pairs of orthogonal polarization to be emitted into the same spatial mode.

The first order term is simply the emission of the entangled photon pairs into modes a and b. Thus with the probability $2Z^2c^2$ a Bell state is created:

$$|\psi^+\rangle = \frac{1}{\sqrt{2}}(|H_a V_b\rangle + |H_b V_a\rangle). \quad (4.5)$$

The second order term corresponds to the emission of four photons resulting in the following superposition of photon number states created with the probability $3Z^2c^4$:

$$\frac{1}{\sqrt{3}}(|2H_a, 2V_b\rangle + |2V_a, 2H_b\rangle + |1H_a, 1V_a, 1H_b, 1V_b\rangle). \quad (4.6)$$

Note that the terms where equal polarizations are in the same mode have a higher amplitude than one would expect from a simple two-pair emission. This second order emission was already used to observe the three photon W_3 state [88, 90, 91] and the four photon entangled state $\Psi^{(4)}$ [115, 138]. For the observation of the Cluster state in chapter 6 we use, however, twice the first order emission and the four photon emission enters only as an unwanted contribution to noise.

Collinear Configuration

The emission of the collinear configuration can be treated in a similar way. The only difference is that modes a and b collapse to one single spatial mode:

$$\begin{aligned} & Z e^{-i\sqrt{2}c(a_H^\dagger a_V^\dagger)} |0\rangle = \\ & Z \left(i\sqrt{2}c(a_H^\dagger a_V^\dagger) - \frac{(\sqrt{2}c)^2}{2}(a_H^\dagger a_V^\dagger)^2 - i\frac{(\sqrt{2}c)^3}{6}(a_H^\dagger a_V^\dagger)^3 + \dots \right) |0\rangle \end{aligned} \quad (4.7)$$

The three terms correspond to emission of the states $|1H, 1V\rangle_a$, $|2H, 2V\rangle_a$ and $|3H, 3V\rangle_a$ into one mode with the probabilities $2Z^2c^2$, $4Z^2c^4$ and $8Z^2c^6$, respectively². In this type

²The parameters were chosen such that for the same value of c the same probability of a pair emission in collinear and non collinear configuration is obtained.

of source, the probability for a multiple emission is even stronger compared to the non collinear case, which is an advantage for the count rates obtained in chapter 7. The disadvantage is, however, that there is also a stronger contribution of the third order emission, which adds some additional mixed state in the experiment.

4.1.2 Experimental implementation

As we have seen, we can use the down conversion process to probabilistically create several photons. To do so it is necessary to use an extremely intense pump beam, as the probability to create four photons is proportional to the square of the intensity of the pump beam. Furthermore the photons need to be indistinguishable, independent of whether they are created in two independent sources or in one process. This means that their time of creation or detection needs to be much shorter than their coherence time. Both, a high intensity and short creation time window can be achieved by using a femtosecond pulsed laser system, guaranteeing a high peak intensity and a very short time window for the photons to be created. Here I will shortly describe our realization of such a pump laser system.

To create femtosecond UV pulses at a wavelength of 390 nm we frequency-double the output of a mode-locked Ti:sapphire laser. This combination of a Millennia³ Nd:Yag laser pumping a Tsunami³ Ti:Sa with 10 W cw pump power provides 82 MHz pulsed light (pulse length ≈ 130 fs) with an average power of 2.1 W at a wavelength of 780 nm. A 3 mm long Lithium-Borate crystal (LBO) is used for second harmonic generation (SHG) creating between 600 and 800 mW UV-pulses at 390 nm. Mirrors of high reflectivity for UV and high transmittivity for IR serve to separate the created UV beam from the residual IR light. Cylindric lenses serve to focus the pump beam to a circular spot onto the down conversion crystal, a 2 mm β -Barium Borate crystal (BBO) which is cut for collinear second harmonic generation (SHG). For the non-collinear down conversion the focus has a diameter of 200 μm , for the collinear down conversion a spot size of 100 μm was experimentally verified to be preferable. In the latter case, the UV pump beam is filtered from the down conversion emission by two mirrors with high transmission at IR and high reflection at UV under 0° . Walk-off effects due to birefringence are compensated by a combination of a half wave plate, switching horizontal and vertical polarization, and a 1 mm BBO crystal. Coupling the photons into single mode fibers exactly defines the spatial mode desired to collect from the down conversion emission [150]. The spectral selection is achieved with a narrow bandwidth interference filters (usually $\Delta\lambda = 3$ nm if not mentioned otherwise) that are located at convenient positions dependent on the setup.

The disadvantage of the femtosecond pulsed pump beam is the, in comparison with a cw pump beam, broad spectrum ($\Delta\lambda_{p,UV} \approx 1.2$ nm). It leads to a broader spectrum of the down conversion emission, because the emitted light into the collected spatial modes also stems from a decay of photons that are not at the central wavelength. Further, the probability to detect both photons of an emitted pair is reduced, as we will see.

Usually, the coincidence to single ratio is used to quantify the probability for a created photon to be detected.

$$\eta_a = \frac{C_{ab}}{C_a}, \quad (4.8)$$

³Spectra Physics

where C_{ab} and C_a denote the probability of detecting photons in modes a and b simultaneously and a detection in mode a, respectively. As the photons are always created in pairs we know that each single photon detection indicates a lost partner qubit, which is why η corresponds to the total detection efficiency, i.e. the probability that a created photon is really detected. As argued before, emission stems also from pump photons that are slightly off the central wavelength, therefore it is important to remember that spectral filtering often filters one photon of a pair that is emitted from a photon slightly off the central wavelength, while the other is transmitted. This decreases the coincidence to single ratio strongly. An additional effect is that the bandwidth of the emissions is slightly different for the two polarizations, therefore also η is polarization dependent.

We can also estimate the value of c in equation 4.1.1 and equation 4.7 from the single and coincidence detection. The probability for a coincidence is the probability for creation of a photon pair $\approx 2c^2$ (for $Z \approx 1$) times the probability that both photons are detected η_a and η_b :

$$K_{ab} = 2c^2\eta_a\eta_b \Rightarrow 2c^2 = \frac{K_{ab}}{S_a S_b} \quad (4.9)$$

The probability for the pair creation and the efficiency of detecting the photons are basic parameters in the description of our photon sources and valuable for estimating, for example, the admixed noise due to higher order emissions. Thus, I conclude this section by summarizing typical values of these parameters and the corresponding coincidence count rate estimated from the detection rates with both configurations using 3 nm bandwidth filtering. Note that without further explanation of details the additional factors entering due to splitting of the photons from the collinear configuration have been taken into account.

	non collinear	collinear
Creation Probability $2c^2$	0.008	0.034
Total Efficiency η	0.09	0.1
Coincidences [1/s]	5500	28000

Table 4.1: Approximate values of the parameters describing the two configurations of SPDC used in our experiments.

4.2 Processing photons

In order to observe a certain quantum state, the photons need to be processed further, as the source of photons does in general not directly create the desired state. Due to the fact that interactions of photons rely on extremely inefficient nonlinear processes, other more efficient methods to control the states need to be found. Such methods rely on linear optics and interferometry.

In a celebrated work, Knill, Laflamme and Milburn showed that universal linear optics quantum computation is indeed possible [151], i.e. any quantum operation can be realized with linear optics networks. Thus, one can also create an arbitrary quantum state with

single photon sources and linear optics. At the current stage, even small networks require practically an unrealistic amount of resources. Even though combinations of their ideas with the one-way quantum computer approach require much less resources [34, 152, 153], some further research is necessary until it is possible to create and control the large amount of photons needed, even for small experiments.

Here, like in many other experiments⁴, we rely on the technique of conditional detection. A linear optics setup and interferometric methods are used to observe a quantum state under the condition of detecting one photon in each of four specified output modes. Basically, the nonlinearity is introduced by a projection of the complete photonic state onto the part of the state, where one photon is in each spatial mode – in the experiment this projection is realized by selecting the four-fold coincidences. The disadvantage is that the observed entangled state cannot be used for further processing, if the projection onto this subspace cannot be guaranteed. On the other hand, multiparty communication tasks rely on the distribution of the quantum state onto several parties, thus it is ensured that the photons do not need to interact anymore.

4.2.1 Wave plates

Unitary transformations of single qubits can easily (and without conditional detection) be implemented with birefringent crystals. The most important ones are half and quarter wave plates that introduce a phase shift of π and $\pi/2$ respectively, between the linear polarizations parallel to the fast and slow axis of the crystal. This introduces the transformations $U_{\theta,0}^{\pi} = \hat{\sigma}_{\theta,0}$ for the HWP and $U_{\theta,0}^{\pi/2} = (i \cdot \mathbb{1} + \hat{\sigma}_{\theta,0})/\sqrt{2}$ for the QWP⁵. Here, θ is the angle between the rotation axis and the horizontal axis. In our experiments we use zero order HWP and QWP⁶ in order to have little error on the introduced phase shift.

Another important tool are birefringent elements that shift the phase between the horizontal and vertical polarizations, represented by the operation $U_{0,\phi}^{\omega} = i \cos(\omega/2) \mathbb{1} + \sin(\omega/2) \hat{\sigma}_z$. Here, the fast and slow axes are aligned along horizontal and vertical polarizations, and the thickness of the plate, which determines the phase ω , is changed by rotation around the vertical axis. Thus, no zero order plates can be used. In our experiments we use for each compensation a pair of custom made Yttrium-Vanadate crystals (YVO_4) of 200 μm thickness⁷. They were chosen due to their strong birefringence at 780 nm (for more detail see [154]). The pair configuration allows to compensate dispersion effects that depolarize the photons strongly due to their comparably broad band width of about 3 nm. Here, we use the YVO_4 crystals to compensate phase shifts that are usually introduced by imperfect beam splitters.

⁴See e.g. the experiments cited in context of state analysis in the overview of four-qubit states (section 3.2.3) and implementations of quantum gates in the introduction to the C_P experiment (chapter 5)

⁵The upper index of $U_{\theta,0}^{\omega}$ corresponds the phase shift ω introduced by arbitrary waveplates. For definitions see section 2.1.1.

⁶Zero order, optically contacted, CeNing Optics/FOCtek

⁷FOKtek

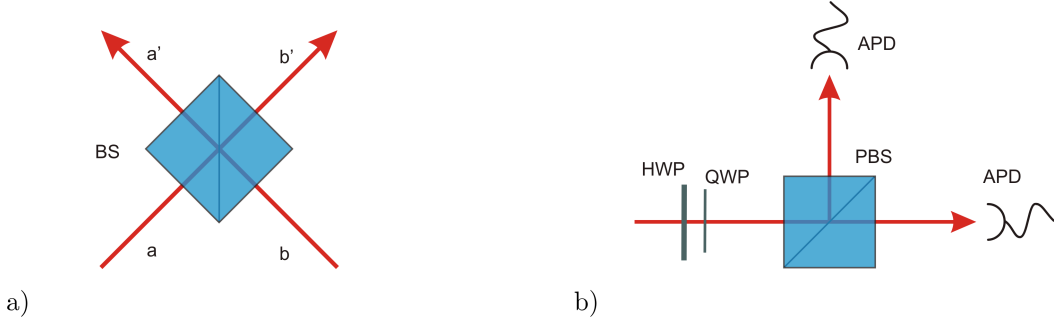


Figure 4.2: The notation of the in- and output modes of a general beam splitter are shown in a). In b) the polarization analysis as used in all of the presented experiments is depicted. A half and a quarter wave plate (HWP and QWP) serve to choose the basis of analysis. A polarizing beam splitter (PBS) separates photons with two corresponding eigenstates for detection in Silicon avalanche photo diodes (APD).

4.2.2 Beam splitters

The basic elements for making joint operations on photon pairs are beam splitters (they are, however, also useful for some single qubit operation). An ideal general beam splitter⁸ introduces the following transformations, where the creation operators are named according to the modes in figure 4.2 a):

$$a_H^\dagger \rightarrow \frac{1}{\sqrt{2}} (T_H \cdot a_H^\dagger + iR_H \cdot b_H^\dagger) \quad (4.10)$$

$$b_H^\dagger \rightarrow \frac{1}{\sqrt{2}} (T_H \cdot b_H^\dagger + iR_H \cdot a_H^\dagger) \quad (4.11)$$

$$a_V^\dagger \rightarrow \frac{1}{\sqrt{2}} (T_V \cdot a_V^\dagger + iR_V \cdot b_V^\dagger) \quad (4.12)$$

$$b_V^\dagger \rightarrow \frac{1}{\sqrt{2}} (T_V \cdot b_V^\dagger + iR_V \cdot a_V^\dagger), \quad (4.13)$$

where T_H (R_H) is the transmission (reflection) amplitude of the horizontal polarization and analogously for vertical polarizations. The phase i for the reflected modes is responsible for a negative phase between the cases where photons from both input modes are transmitted or reflected. Without this, the transformation is not unitary (see article [155]). One imperfection of real beam splitters is that they introduce an additional phase shift between horizontal and vertical polarization in each mode. We use the phase shifters introduced before to compensate this effect (see setup for Dicke state figure 7.1 on page 96).

Beam splitters can be designed with basically any splitting ratio, there are however some special cases. Symmetric or 50/50 beam splitters (SBS) exhibit equal values for the parameters $|T_H|^2 = |T_V|^2 = |R_H|^2 = |R_V|^2 = 1/2$.

Usually, the commercially available beam splitters are not perfect and exhibit some asymmetry between the polarizations or the spatial modes (or both). They can, however, usually be aligned to behave as polarization independent beam splitters (BS) that

⁸In the notation of the second quantization.

behave equally for both polarizations, but with different transmission and reflection amplitudes. After aligning the beam splitters⁹ for polarization independence they take values of $|T_H|^2 = |T_V|^2 \approx 0.6$, $|T_V|^2 = |R_V|^2 \approx 0.4$. In our experiment this influences, as we will see, only the efficiency, not the quality of the state.

Polarizing beam splitters (PBS) are specified by zero reflectivity of horizontal and zero transmittivity of vertical polarization $|T_H|^2 = |R_V|^2 = 1$, $|T_V|^2 = |R_H|^2 = 0$. Again the experimentally used beam splitters are not perfect. As we will see, we use PBSs for polarization analysis, where mainly $|T_V|^2 = |R_H|^2 = 0$ is important. Again by alignment, we reach with our PBSs¹⁰ a very good value of approximately $|T_V|^2 = |R_H|^2 \approx 0.002$.

The only other kind of beam splitter that is relevant here is used in the controlled phase gate (chapter 5) and will simply be called polarization dependent beam splitter (PDBS). Its splitting ratios are in the ideal case $|T_H|^2 = 1$, $|R_H|^2 = 0$, $|T_V|^2 = \frac{1}{3}$, $|R_V|^2 = \frac{2}{3}$. A detailed characterization of our custom made¹¹ beam splitters can be found in the Diploma thesis by Ulrich Weber [156].

If one relies on conditional detection, there are several tasks beams splitters can be used for:

- Attenuation of one polarization. Polarization dependent beam splitters can be used to attenuate one polarization under the condition that the transmitted photon is detected. This is a non-unitary transformation and corresponds, together with the conditional detection, to a POVM measurement [157].
- Splitting of photons from one into two modes. Two photons that are incident on a polarization independent BS split up probabilistically. As conditional detection discards the other cases, the BS effectively works as a lossy photon splitter, where the smallest losses are achieved for a symmetric BS.
- Via second order interference (HOM-type, see [158]) the overlap of photons from different input modes allows the implementation of quantum gates and Bell state analysis (see e.g. [159–161]). The implementation of a controlled phase gate with this technique is demonstrated in detail in chapter 5.
- Polarization dependent beam splitters can in combination with half- and quarter wave plates, be used for polarization analysis, as demonstrated in figure 4.2 b). The measurement basis to be analyzed is turned to the Z axes of the Bloch sphere¹² and 'clicks' in the output modes of the PBS indicate the detection of one or the other eigenstate.

In all of the experiments presented here the configuration shown in figure 4.2 b) is used for the analysis of each photon. In order to optimize the analysis of a state the wave plates for the choice of the basis are motorized and driven according to a computer program. This allows to frequently change the setting automatically (which is usually done in intervals of 10 minutes). Thus all measurement settings are a time average of

⁹LINOS

¹⁰Newport

¹¹EXPLA, former EKSMa

¹²From the waveplate transformations it is easy to see that this is possible for any axis.

the whole measurement period. Further, this allows to monitor the behavior of the setup during the measurement process.

Finally, the photon in each mode is detected in one of the two outputs of the polarization analysis in the respective spatial mode. Multimode fibers guide the photons to passively quenched silicon avalanche photodiodes that are used in Geiger mode for single photon detection (APD¹³). No resolution of the photon number is possible. The signals of up to eight detectors are fed to an ultrafast coincidence logic [162]. This eight bit signal leads to 255 possible detection events which are triggered each time at least one of the detectors 'clicks'. A histogram of these detection events is stored for later evaluation.

4.3 From clicks to density matrices

So far, the creation of photons and their processing with the goal to detect a certain state was discussed. The last section of this chapter is devoted to linking the output of the experimental setup, which are basically detector clicks, with the theoretical framework that has been developed in the first two chapters. The calculation of correlations and linear functions thereof will be shown. Further, the efficient derivation of a complete density matrix with our detection scheme and how non-linear dependences, i.e. entanglement measures, are found is discussed. Finally, for the purpose of analyzing the experimental quantum gate that is presented in the next chapter, the principles for a complete reconstruction of a non-trace preserving quantum process will be shown.

4.3.1 Correlation measurements

The raw data obtained in a measurement consists of the number of coincident or single clicks of detectors sampled over a certain time period. As the experiments rely on conditional detection, we are only interested in the detection of coincident events between the four output modes $m \in \{a, b, c, d\}$. In each of these modes there are two detectors, whose 'clicks' indicate a detection of one of the two eigenstates $e_{i_m}^{b_m}$, where $i_m \in \{0, 1\}$ (with 0 for the state with the positive and 1 for the negative eigenvalue) of the chosen measurement basis b_m . In most of the cases $b_m \in \{X, Y, Z\} = \{1, 2, 3\}$. We denote the detected number of clicks by $C_{i_a, i_b, i_c, i_d}^{b_a, b_b, b_c, b_d}$. One advantage of using a polarization analysis where both eigenstates are detected in each mode is that for one measurement setting $\vec{B} = \{b_a, b_b, b_c, b_d\}$ the complete number of 16 four-fold coincidences are detected. This allows to infer the relative frequency of each detection event out of only one measurement setting, e.g. for detection event $C_{i_a, i_b, i_c, i_d}^{\vec{B}}$ the relative frequency $c_{i_a, i_b, i_c, i_d}^{\vec{B}}$ is given by:

$$c_{i_a, i_b, i_c, i_d}^{\vec{B}} = \frac{C_{i_a, i_b, i_c, i_d}^{\vec{B}}}{\sum_{i'_a, i'_b, i'_c, i'_d=0}^1 C_{i'_a, i'_b, i'_c, i'_d}^{\vec{B}}}. \quad (4.14)$$

If a polarization analysis is only based on polarizers, i.e. detects only one eigenstate, then the total four-fold coincidence count rate has to be inferred from 16 different measurement

¹³Perkin/Elmer C309025QC-02

settings under the assumption of constant count rates. Thus, longer measurement times are necessary and at the same stability of the experimental setup is more important.

To further process the data we need to obtain the expectation value of some observable with the experimentally prepared state ρ . For now, let us take the observable $\hat{O}_{\vec{B}}$ corresponding to a single measurement setting \vec{B} :

$$K_{\vec{B}} = \langle \hat{O}_{\vec{B}} \rangle = \text{Tr} \left[\hat{O}_{\vec{B}} \rho_{\text{exp}} \right] = \text{Tr} \left[(\sigma_{b_a} \otimes \sigma_{b_b} \otimes \sigma_{b_c} \otimes \sigma_{b_d}) \rho \right]. \quad (4.15)$$

The value $K_{\vec{B}}$ is the *four qubit correlation* for the chosen measurement setting \vec{B} . One can easily calculate how this is related to the detection probabilities by expanding the Pauli matrices into the projectors of the eigenstates $\sigma_b = |e_0^b\rangle\langle e_0^b| - |e_1^b\rangle\langle e_1^b| = P_0^b - P_1^b$. Hence we get:

$$\begin{aligned} K_{\vec{B}} &= \sum_{i_a, i_b, i_c, i_d=0,1} \left((-1)^{i_a+i_b+i_c+i_d} \cdot \text{Tr} \left[(P_{i_a}^{b_a} \otimes P_{i_b}^{b_b} \otimes P_{i_c}^{b_c} \otimes P_{i_d}^{b_d}) \rho \right] \right) \\ &= \sum_{i_a, i_b, i_c, i_d=0,1} \left((-1)^{i_a+i_b+i_c+i_d} \cdot p_{i_a, i_b, i_c, i_d}^{\vec{B}} \right), \end{aligned} \quad (4.16)$$

where $p_{i_a, i_b, i_c, i_d}^{\vec{B}}$ is the probability for a certain detection event to occur. In experiments, we cannot measure probabilities but just relative frequencies of occurrence. Thus, when we determine the correlation from the measurement, the probabilities $p_{i_a, i_b, i_c, i_d}^{\vec{B}}$ are substituted by the corresponding relative frequencies $c_{i_a, i_b, i_c, i_d}^{\vec{B}}$. The error on the correlation is then calculated via Poissonian counting statistics.

Some correlations also contain the identity $\mathbb{1}$, which corresponds to tracing over the corresponding qubit. To rewrite the correlation in terms of projectors we use $\mathbb{1} = P_0^b + P_1^b$. Note that this expression is independent of the basis b . Thus, if several measurements are available, it may become possible to use more than one measurement for the evaluation of the corresponding correlation. For example, if we have the choice to substitute the identity with projectors from all standard basis, then we can use all of them and take the average:

$$\mathbb{1} = \frac{1}{3} (P_0^X + P_1^X + P_0^Y + P_1^Y + P_0^Z + P_1^Z). \quad (4.17)$$

By using as much as possible of the available measurement data, errors on the correlations are reduced. In the following, different ways of evaluation to characterize a quantum state will be discussed based on the previous considerations.

4.3.2 Quantum state tomography

Methods that are used to obtain a complete density matrix of a quantum state from measured data are called quantum state tomography. A lot of different ways for quantum state tomography have been developed (one of the first works was [163]; a variety of methods are summarized in [164]). From a decomposition of the density matrix into projectors one can easily express the density matrix in terms of probabilities for detecting a certain coincidence. Relative frequencies obtained in a measurement are, however, subject to poissonian counting statistics, giving slight deviations from the real probabilities. Therefore, taking these errors into account, the deduced density matrices might be consistent

with, but not necessarily directly resulting in a physical density matrix, e.g. one might find negative eigenvalues. Therefore, several different approaches for fitting a general physical density matrix to the measured data have been developed. There are, however, still discussions about the best method (see e.g. a recent publication [165]).

To perform quantum state tomography we need a complete, so-called tomographic, set of measurement data. James and coworkers [163] discussed tomographic sets, and showed how to generally deduce the density matrix from measurement data, when a certain tomographic set is available. In their experiment they used simply a polarizer for polarization analysis detecting only one eigenstate for each measurement basis and therefore relying basically on a tomographic set based on the projectors similar to (here exemplarily shown for the two-qubit case): $P_a \otimes P_b$ where $a, b \in \{H, V, +, L\}$. Measurements from three different conjugate bases for each qubit are necessary (namely X, Y, Z) to determine these values.

Here, we rely on the detection of both eigenvalues of a measurement basis at the same time. Still, we need to measure in three conjugate bases to obtain a tomographic set of data. Thus, we directly register projections on six polarizations for each qubit: $\{H, V, +, -, R, L\}$. This set of data is overcomplete. Yet, as count rates are often low we do not want to discard the additional information. We can, however choose another tomographic set to include all measurement data, thereby either reducing measurement times or errors due to counting statistics. The density operator can, for example, be rewritten in a decomposition based on the standard bases (i.e., based on $\{\hat{\sigma}_0 = \mathbb{1}, \hat{\sigma}_x, \hat{\sigma}_y, \hat{\sigma}_z\}$):

$$\rho = \frac{1}{2^N} \sum_{\{b_j\}=0}^3 K_{\{b_j\}} \prod_{j=1}^N \hat{\sigma}_{b_j}. \quad (4.18)$$

The coefficients $K_{\{b_j\}}$ are correlations. This can be treated with the formalism in [163] but relies then on a complicated way to treat the errors, as they become correlated. Here, we derive a simple expression that allows to rewrite the density matrix as a linear combination of operators (that substitute the Pauli operators) with the *probabilities* of the detection events as coefficients. This allows to use the complete set of data in a very simple and natural way, giving a direct relation between the measured relative frequencies and the density operator. The advantage of this approach will also become apparent in section 4.3.3.

A density matrix ρ can be expressed as a linear combination of Pauli matrices. This decomposition is rewritten by extracting the correlations with $\hat{\sigma}_0 = \mathbb{1}$. Here, the derivation is restricted to the two-qubit case for simplicity and the indices $\{0, 1, 2, 3\}$ instead of $\{\mathbb{1}, X, Y, Z\}$ are used:

$$\begin{aligned} \rho &= \frac{1}{4} \sum_{k,l=0}^3 K_{k,l} \hat{\sigma}_k \otimes \hat{\sigma}_l = \\ &= \frac{1}{4} \left(K_{0,0} \mathbb{1} \otimes \mathbb{1} + \sum_{k=1}^3 K_{k,0} \hat{\sigma}_k \otimes \mathbb{1} + \sum_{l=1}^3 K_{0,l} \mathbb{1} \otimes \hat{\sigma}_l + \sum_{k,l=1}^3 K_{k,l} \hat{\sigma}_k \otimes \hat{\sigma}_l \right) \end{aligned} \quad (4.19)$$

The Pauli matrices were rewritten according to equation 4.16 and equation 4.17. Now, we show how a correlation that includes $\mathbb{1}$ is given by an average over other correlations. As

example we use a correlation with $\mathbb{1}$ for the first qubit expressed by an average of three correlations made up of six relative frequencies, where the signs depend on the projector for the second qubit. For $K_{0,2}$ we get:

$$K_{0,2} = \sum_{i,j=0}^{+1} (-1)^j c_{1,2}^{i,j} = \sum_{i,j=0}^{+1} (-1)^j c_{2,2}^{i,j} = \sum_{i,j=0}^{+1} (-1)^j c_{3,3}^{i,j} = \frac{1}{3} \sum_{k=1}^3 \sum_{i,j=0}^{+1} (-1)^j c_{k,2}^{i,j} \quad (4.20)$$

Hence, we see that $K_{0,2}$ is an average over three measurements, namely X,Y and Z on qubit 1. Special is the term $K_{0,0} = 1$ which is unity due to normalization of the probabilities. It can also be averaged over all contributing terms (e.g. 9 terms for 2 qubits):

$$K_{0,0} = 1 = \sum_{i,j=0}^{+1} c_{1,1}^{i,j} = \sum_{i,j=0}^{+1} c_{1,2}^{i,j} = \dots = \sum_{i,j=0}^{+1} c_{3,3}^{i,j} = \frac{1}{3^2} \sum_{k,l=1}^3 \sum_{i,j=0}^{+1} c_{k,l}^{i,j} \quad (4.21)$$

If we include these expressions into equation 4.19 we find:

$$\begin{aligned} \rho &= \frac{1}{4} \sum_{k,l=1}^3 \sum_{i,j=0}^{+1} c_{k,l}^{i,j} \left(\frac{1}{3^2} \mathbb{1} \otimes \mathbb{1} + \frac{1}{3} (-1)^i \hat{\sigma}_k \otimes \mathbb{1} + \frac{1}{3} (-1)^j \mathbb{1} \otimes \hat{\sigma}_l + (-1)^{(i+j)} \hat{\sigma}_k \otimes \hat{\sigma}_l \right) \\ &= \frac{1}{4} \sum_{k,l=1}^3 \sum_{i,j=0}^{+1} c_{k,l}^{i,j} \left(\frac{1}{3} \mathbb{1} + (-1)^i \hat{\sigma}_k \right) \otimes \left(\frac{1}{3} \mathbb{1} + (-1)^j \hat{\sigma}_l \right) \\ &= \frac{1}{4} \sum_{k,l=1}^3 \sum_{i,j=0}^{+1} c_{k,l}^{i,j} \left(\gamma_k^i \otimes \gamma_l^j \right) \end{aligned} \quad (4.22)$$

This corresponds formally to a decomposition as in equation 4.19. The sum consists, however, of 36 terms (instead of 16) and the coefficients are the relative frequencies of the count rates (instead of correlations), where the new basis vectors $\gamma_k^i = (\frac{1}{3} \mathbb{1} + (-1)^i \hat{\sigma}_k)$ are non-orthogonal in the vector space of density matrices (which is overdefined by this number of vectors). The same decomposition is also possible for higher numbers of qubits as is calculated directly in appendix C. Here, we state the result for N qubits:

$$\rho = \frac{1}{2^N} \sum_{\{b_j\}=1}^3 \sum_{\{i_j\}=0}^{+1} c_{\{b_j\}}^{\{i_j\}} \prod_{j=1}^N \left(\frac{1}{3} \mathbb{1} + s_j \hat{\sigma}_{b_j} \right). \quad (4.23)$$

Using this decomposition, the density matrix can be directly deduced from *all* measured count rates.

As mentioned above, in general we use the data directly for evaluation of certain observables of the state. If necessary, however, this decomposition can also be used for fitting a physical density matrix to the data. For example, the maximum likelihood approach as presented in [163] can be used with the expectation values of the operators γ_k^i instead of the tomographic set of projectors. Again the advantage is the usage of the complete measurement data, reducing measurement times.

4.3.3 Evaluation of relevant values

With the density operator obtained from quantum state tomography, any information we seek to know about a quantum state can be determined. Yet, it requires, in particular for multipartite states, a big experimental effort to measure all corresponding correlations. Thus, when we are interested only in certain informations, we might be able to do with only a restricted set of measurements.

Furthermore, even if the complete set of correlations is necessary, it is advantageous to determine values directly from the measurement data because the error calculation is simplified. This is particularly important, as the measured data reproduces a physical state only within the statistical errors.

In the following, the derivation of characteristic values of a quantum state will be presented. We discuss the evaluation of observables, then of entanglement measures.

Observables

The first experiments on entangled quantum states (at least with the explicit goal to study entanglement) were Bell tests. Here, one determines a set of correlations and calculates whether the experimental results were in agreement with the predictions from classical (better: local hidden variable) theories, or whether they exceeded the predicted values in accordance with quantum mechanics. Complete knowledge about the state is not necessary.

In a similar way, the information whether a state is, for example, separable or symmetric does not require complete knowledge of a quantum state. Yet, usually we cannot measure the expectation values of the corresponding observables \hat{O} (witness or swap operators, respectively) directly, as they are in general non-local. In our experiments, we can only measure local observables, i.e. correlations of the type $K_{\vec{B}} = \langle \hat{O}_{\vec{B}} \rangle$. One can, however, express \hat{O} as linear combination of local observables. The expectation value of \hat{O} can then be calculated from the different correlations due to the linearity of the trace. As this decomposition is not unique, we seek to find a minimal local decomposition, i.e. a decomposition into local observables such that as few measurement settings as possible are needed to evaluate \hat{O} .

Most of the entanglement witnesses we discuss are already designed such that they consist out of few measurement settings. Also the linear decomposition of the swap operator is given in equation 2.32. It may be a little unexpected that also the fidelity of an observed state relative to the desired one can be determined with reduced measurement settings. It is given by the expectation value of the projector on the expected pure state $|\psi\rangle$:

$$F_{\rho}^{\psi} = \text{Tr} [|\psi\rangle\langle\psi| \rho] = \langle \psi | \rho | \psi \rangle \quad (4.24)$$

Note, here, the close relation to the generic entanglement witness:

$$\text{Tr} [\mathcal{W}_{\psi} \rho] = \text{Tr} [(\alpha \mathbb{1} - |\psi\rangle\langle\psi|) \rho] = \alpha - F_{\rho}^{\psi} \quad (4.25)$$

Minimal local decompositions of generic entanglement witnesses have been studied in [166].

In particular the fidelity to graph states is, due to their special structure, easy to determine from 2^N correlations for N qubits. This will be demonstrated on the example

of the four-qubit cluster state. The stabilizing group consists of 16 elements (which are summarized in table 6.1). All other standard bases have zero correlations. Using the decomposition of the density operator in terms of the standard bases we get:

$$\begin{aligned}
 F_\rho^{\mathcal{C}_4} = \langle \mathcal{C}_4 | \rho | \mathcal{C}_4 \rangle &= \sum_{i,j,k,l=0}^3 K_{ijkl} \langle \mathcal{C}_4 | \hat{\sigma}_i \otimes \hat{\sigma}_j \otimes \hat{\sigma}_k \otimes \hat{\sigma}_l | \mathcal{C}_4 \rangle \\
 &= \sum_{m=1}^{16} K_m \langle \mathcal{C}_4 | \hat{S}_m | \mathcal{C}_4 \rangle
 \end{aligned} \tag{4.26}$$

where S_m are the stabilizing operators and K_m are the corresponding measured correlations. Then, if the operators' signs are chosen such that $\langle \mathcal{C}_4 | \hat{S}_m | \mathcal{C}_4 \rangle = 1$, the fidelity is simply the average over these 16 correlations. In dependence on their explicit form the number of measurement settings might be even smaller – in our example 9 settings are necessary. Compared to a state tomography with 81 settings this is a drastic reduction of the effort. For graph states the problem is particularly simplified, but also for other quantum states a strong reduction of settings is possible. For example, all states of the first SLOCC-family of four-qubit entanglement (section 3.1), including the state $D_4^{(2)}$, have at maximum 40 non-zero correlations, where at maximum 21 measurement settings are necessary to evaluate the fidelity.

For the estimation of the errors we chose the straightforward approach: As the different correlations partly stem from the same measurement setting, the expectation value of the measured observable is expressed as linear combination of the different relative frequencies instead of correlations. The errors on these are due to Poissonian counting statistics plus errors on the detection efficiencies of the APDs. The total error is then calculated by gaussian error propagation.

Entanglement measures

Entanglement measures like the concurrence, the entanglement of formation, the negativity and the geometric measure of entanglement, which were introduced in the first chapter, are not linearly dependent on the density matrix. Therefore, we need (to our best knowledge) the complete density matrix of the state for their evaluation, in contrast to the evaluation of the entanglement witnesses, symmetry etc. introduced before. For a lower bound on the geometric measure of entanglement we use a smaller set of data, as demonstrated in the first chapter.

The concurrence and negativity of two-qubit states, however, will be calculated explicitly according to equation 2.45 and equation 2.49 (pages 18 and 19). With the density matrix obtained with the method demonstrated in section 4.3.2 these values can easily be obtained. As mentioned before, these matrices are not physical. Yet, we expect the correct physical matrix to be within the error bounds of the data. The estimation of the error on the entanglement measures is, however, not as straightforward as in the last section and will be outlined shortly in the following.

The error on the concurrence can be estimated via perturbation theory of non-hermitian matrices as presented in James et al. [163]. The decomposition of the density matrix they used can easily be substituted with the decomposition in equation 4.23.

The negativity can be calculated by using the measurement data directly via a slight modification of the presented tomography. To do so, the partial transpose with regard to one subsystem (here the second) is directly applied on our decomposition (equation 4.22):

$$\rho_{\text{exp}}^{PT} = \left(\sum_{k,l=1}^3 \sum_{i,j=0}^{+1} c_{k,l}^{i,j} \left(\gamma_k^i \otimes \gamma_l^j \right) \right)^{PT} = \sum_{k,l=1}^3 \sum_{i,j=0}^{+1} c_{k,l}^{i,j} \left(\gamma_k^i \otimes (\gamma_l^j)^T \right). \quad (4.27)$$

Thus, simply transposing the γ -matrices of one qubit allows the calculation of the partially transposed density matrices, where the coefficients given by the measurement data are left unchanged. This can, naturally, be also applied to multiqubit density matrices, where several qubits can be transposed this way in equation 4.23. To obtain the negativity, the eigenvalues of this density matrix are calculated. The reduction of the problem to the calculation of eigenvalues reduces the error calculation to a known problem. In [163] the calculation of the errors on the eigenvalues of a density matrix derived from tomography via perturbation theory is presented.

In this section, the determination of all values that are calculated in the experimental analyses in chapters 5, 6 and 7 were completed. The calculation of all values is reduced directly to measurement data. To do so even for entanglement measures, which are not observables, we rely on a new kind of tomographic decomposition that is suited to our strategy of state analysis (equation 4.23). In the following, the tomography of a quantum process will be demonstrated.

4.3.4 Quantum process tomography

In addition to the description of quantum states, it is of interest to describe also the processes acting on quantum states. This constitutes, for example, an important part of the analysis of the phase gate whose experimental realization is presented in the next chapter. Several quantum operations have already been introduced in the first chapter, section 2.2.3. These operations mapped pure onto pure states. Real processes, however, often cause mixing. Thus, a general quantum process describes a map of density matrices onto density matrices. The experimental determination of a full description of such a process is called quantum process tomography (QPT). There is some literature on this subject (e.g. [44, 46, 167–169]), and the process tomography we use¹⁴ is mostly along the lines of [44, 46, 168], however, without the restriction to trace-preserving processes. To describe a quantum process we need to develop two things: a strategy to determine the necessary parameters experimentally and a convenient way to represent the process.

Firstly, a complete description of a quantum process \hat{Q} should make predictions about the output state ρ_{out} for arbitrary input states ρ_{in} . Assuming linearity of the process one can see, that it is sufficient to describe the process only for a tomographic set of input states \hat{B}_i :

$$\hat{Q}(\rho_{in}) = \hat{Q}\left(\sum_i \lambda_i \hat{B}_i\right) = \sum_i \lambda_i \hat{Q}(\hat{B}_i). \quad (4.28)$$

¹⁴Similar to the case of quantum state tomography, we omit the fitting to general physical matrices. We prefer the approach presented in the following chapter, i.e., fitting a model of the physical process to the data.

In case the process is lossy this results in a reduced trace of $\hat{Q}(\rho_{in})$ which corresponds to the probability p_{out} of not losing the state (in the following called success probability). Accordingly the normalized output state is:

$$\rho_{out} = \frac{\hat{Q}(\rho_{in})}{Tr(\hat{Q}(\rho_{in}))} \Rightarrow \hat{Q}(\rho_{in}) = Tr(\hat{Q}(\rho_{in}))\rho_{out} = p_{out}\rho_{out} \quad (4.29)$$

Thus, the complete information about the process is described by the output state and the probability of success. Using equation 4.28 we get:

$$p_{out}\rho_{out} = \hat{Q}(\rho_{in}) = \sum_i \lambda_i \hat{Q}(\hat{\mathcal{B}}_i) = \sum_i \lambda_i p_i \hat{\mathcal{B}}'_i \quad (4.30)$$

where $\hat{\mathcal{B}}'_i$ is the normalized state after action of the process \hat{Q} , and p_i is the corresponding probability of success. By rewriting $\hat{\mathcal{B}}'_i$ in terms of $\hat{\mathcal{B}}_i$ the quantum process is described by a matrix μ_{ij} :

$$\hat{\mathcal{B}}'_i = \sum_j \mu_{ij} \hat{\mathcal{B}}_j. \quad (4.31)$$

Secondly, in order to obtain a convenient representation of the quantum process we start from the operator-sum representation (Kraus representation [170]):

$$\hat{Q}(\rho) = \sum_k \xi_k U_k \rho U_k^t \quad (4.32)$$

where U_i are unitary operators depending on the process and ξ_k are real coefficients, denoting the probability of occurrence of U_i . This can further be translated to some standard representation by rewriting the unitary operators in terms of the bases E_j : $U_k = \sum_i \tau_{ik} E_j$. In general, E_j are the 3^N tensor products of Pauli matrices (N is the number of qubits). Thus, the operation can finally be expressed in the form

$$\hat{Q}(\rho) = \sum_{i,j} \sum_k \xi_k \tau_{ik} \tau_{jk} E_i \rho E_j^t = \sum_{i,j} \chi_{ij} E_i \rho E_j^t \quad (4.33)$$

where $\chi_{ij} = \sum_k \xi_k \tau_{ik} \tau_{jk}$ is a complete representation of the process, as the basis E_i is a fixed set of unitary operations and the whole equation describes the action on any quantum state.

Finally, the same physical process is described by equation 4.31, which includes expressions that can be determined experimentally, and equation 4.33, which can be used for its convenient representation. Thus, we find χ_{ml} for a chosen tomographic set of states by:

$$p_i \sum_j \mu_{ij} \hat{\mathcal{B}}_j = \hat{Q}(\hat{\mathcal{B}}_i) = \sum_{m,l} \chi_{ml} \hat{E}_m \hat{\mathcal{B}}_i \hat{E}_l^\dagger \quad (4.34)$$

The tomographic set we use consists of separable input states, because separability can be guaranteed (in contrast to entanglement) by simply applying local projective measurements on the photons.

By using polarizers in combination wave plates we choose the following set of 16 input states: ($|HH\rangle$, $|HV\rangle$, $|H+\rangle$, $|H-\rangle$, $|VH\rangle$, $|VV\rangle$, $|V+\rangle$, $|VL\rangle$, $|+H\rangle$, $|+V\rangle$, $|++\rangle$, $|+L\rangle$, $|LH\rangle$, $|LV\rangle$, $|L+\rangle$, $|LL\rangle$). The explicit procedure how to derive χ_{ml} for the standard transformations out of the corresponding $\hat{Q}(\hat{\mathcal{B}}_i)$ can be found in [46].

Before this transformation can be performed we need to know the success probabilities p_i . In the following, a one-qubit example will be used to demonstrate how p_i can be derived from the measurement. For this we use pure separable input states, analyse in the standard bases and assume that the components in the setup are well-aligned with the H/V coordinate system. Imagine the transformation introduced by a beam splitter with perfect transmission for horizontal and 50% transmission for vertical polarization acting on a single photon under the condition of its transmission. The transformation leaves horizontal and vertical polarizations unchanged. Superpositions of the two are, however, transformed:

$$|+\rangle\langle+| = \frac{1}{2} \begin{pmatrix} 1 & 1 \\ 1 & 1 \end{pmatrix} \xrightarrow{BS} \frac{1}{2} \begin{pmatrix} 1 & \frac{1}{\sqrt{2}} \\ \frac{1}{\sqrt{2}} & \frac{1}{2} \end{pmatrix} = |\nu\rangle\langle\nu| \quad (4.35)$$

where $|\nu\rangle = \sqrt{\frac{2}{3}}(|H\rangle + \frac{1}{\sqrt{2}}|V\rangle)$ ¹⁵. As one can see, the diagonal elements are the transmission probabilities for horizontal and vertical polarization. In the same way, we can express all the diagonal elements of output density matrices in terms of the transmission and reflection probabilities in the case of many qubits, e.g. for two qubits by p_{HH} , p_{HV} , p_{VH} and p_{VV} . Reversely, we can also infer these probabilities from the diagonal elements of the output density matrices for the whole tomographic set of input states. With this, all the ingredients necessary to derive the whole process matrix (also called superoperator) χ_{ij} are collected.

The superoperator of the ideal phase gate, which was introduced in section 2.2.3, is shown in figure 4.3. The two axes represent the transformations E_i acting from the left hand side on a state and E_j^t acting from the right hand side in equation 4.33. The structure of the matrices is easily understandable by recalling the representation of C_P in the standard basis (equation 2.30):

$$C_P = \frac{1}{2}(\mathbb{1} \otimes \mathbb{1} + \mathbb{1} \otimes \hat{\sigma}_z + \hat{\sigma}_z \otimes \mathbb{1} - \hat{\sigma}_z \otimes \hat{\sigma}_z) \quad (4.36)$$

The diagonal elements of $\chi_{ij}^{C_P}$ show the probabilities for the four different terms to act on the state. The off-diagonal elements demonstrate the introduced changes in the coherences, making the negative phase for the $\hat{\sigma}_z \otimes \hat{\sigma}_z$ term clearly visible.

In chapter 5 we quantify how well certain processes χ_p reproduce the phase gate operation. To this end we use, in analogy to the fidelity for states, the process fidelity [44]:

$$F_p = \text{Tr} [\bar{\chi}_p \chi_{C_P}], \quad (4.37)$$

where $\bar{\chi}_p = \chi_p / \text{Tr} [\chi_p]$ is the normalized process matrix to be tested, which is not necessary in case it is trace preserving.

¹⁵This is a POVM on a single qubit, see section 4.2.

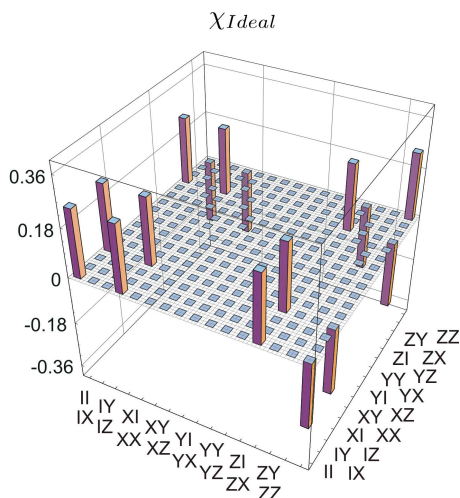


Figure 4.3: Superoperator of an ideal phase gate. The z-axis shows the amplitude of the different contributing unitary transformations action from left (x-axis) and right (y-axis) on the density matrix of the input states. Diagonal elements correspond to the different unitary transformations, the off-diagonal elements to the coherences created between the corresponding parts of the output state. The negative phase introduced by the gate is visible in the off-diagonal elements along the ZZ-row and column.

4.4 Summary

In this chapter, the techniques that are common to the experiments presented in the following chapters are summarized.

As source of photons we rely on type-II spontaneous parametric down conversion. Two different configurations are used in our experiments. In chapters 5 and 6, the non-collinear configuration allows to coincidentally create entangled photon pairs in two distinct spatial modes. In contrast, for the observation of the symmetric Dicke state (chapter 7), the collinear configuration is advantageous, because the photons are collected in one spatial mode and therefore indistinguishable up to polarization, which makes them intrinsically symmetric under permutation. For further processing of the photons we rely on linear optics and conditional detection. Here, different types of beam splitters serve as a flexible tool to implement stochastic local operations and, more important, two-qubit gates. Further, any local unitary operation can be implemented with birefringent crystals.

The analysis of quantum states that are observed with these techniques relies on local polarization analysis in each spatial mode. The data collected in the first place are basically coincidence count rates for every setting of the polarization analysis. From these we evaluate all the quantities we use to describe the entangled state. Also density matrices and values derived thereof are directly inferred from the counting statistics (which is in contrast to the strategy of fitting the data to a physical state). To this end we derived a tomographic representation of the density matrix that is particularly suited to our way of polarization analysis. The description of a whole quantum process is possible when the density matrices for a tomographic set of input states is measured. This type of analysis will be used in the following chapter as basis for the investigation of the experimentally obtained phase gate operation.

5 The Phase Gate

The controlled phase gate forms together with single qubit operations a universal set of quantum gates, that means any quantum computation can be implemented with these operations. Further, this gate operation can be used for the initialization of a one-way quantum computer, where cluster states are created by next-neighbor interaction. Both applications are due to the gates capability to create maximal pairwise entanglement from separable qubits. Even if big quantum networks cannot yet be built for technical reasons, already a single gate can serve for several applications, e.g. for complete Bell state analysis [171, 172] to obtain a four-qubit cluster state by entangling two EPR-pairs (chapter 6).

One of the main advantages of photons, their weak interaction with the environment, becomes the major challenge for the implementation of a phase gate (or its close relative, the C_{NOT} gate) due to low nonlinear interaction efficiencies. A possible solution is to use linear optics components together with ancillary single photons and photon number resolving detectors to introduce the non-linearity [151]. Several proof-of-principle experiments demonstrated the feasibility of this approach once the necessary components become available on a larger scale [173–175]. In case one is interested in only a limited number of quantum operations, however, a solution that was already discussed in the previous chapter is available: linear optics and conditional detection. It enables the implementation of probabilistic quantum gates in the coincidence basis. A first idea for the realization of a phase gate with this technique was recently introduced and implemented experimentally [41–44] with a setup that was based on a combination of first and second order interference resulting in a gate with success probability $1/9$. The stability required due to the first order interference are, however, on the order of a wavelength, making multiphoton applications of the gate difficult.

Here, a linear optics controlled phase gate that is based solely on a single two-photon interference at a polarization dependent beam splitter is introduced. The advantage of the gate is its simplicity: Neither first order interference nor ancillary photons are required. The reduced stability requirements are on the order of the coherence length of the photons and make it a perfect tool for multiphoton experiments, e.g. complete Bell state analysis for quantum communication [171] or the observation of a cluster state (chapter 6). Note that together with our experiment two similar ones were performed [176–178].

This chapter is divided into three parts. First, the basic idea for the implementation of a linear optics phase gate is introduced. A more accurate description of the resulting setup is obtained by a model that takes real experimental parameters into account. It allows a deeper understanding of the real requirements on the implementation and plays a central role in testing the gate. Then, the experimental setup and the parameters characterizing the corresponding components are described. In the third part, the obtained gate operation is characterized in two steps. First, the process is reconstructed from a tomographic set of measurement data (the method was described in section 4.3.4). This allows the quantification of the gate quality. Via a fit of the model presented in the first

part to the resulting process matrix, we obtain all relevant physical parameters of the gate and in addition a physical density matrix for further evaluation. In the last part, a focus is put on the gates capability to entangle. Here, we rely on the one hand, on entanglement observed in the experiment, on the other hand on the predictions from the model which are then compared to the measured data and used to infer the real entangling capability and the reason for its decrease in the real gate.

5.1 Basic idea and model

In section 4.2 it was mentioned that the second order interference (Hong-Ou-Mandel interference [158, 179]) of a photon pair at a beam splitter can, together with conditional detection, serve as a useful tool for the implementation of quantum gates. It was, for example, often applied successfully for Bell state analysis. There, destructive interference between two-photon transmission and reflection of a symmetric two-photon state occurs because beam splitters (BS) introduce a π -phase shift between the amplitudes for the two cases [155]. Here, we benefit from such a phase shift at a special BS introducing the phase necessary to implement the controlled phase gate.

5.1.1 Scheme for ideal phase gate

To implement the C_P -operation (see section 2.2.3), we need to realize the following actions on a general state in the computational basis:

$$\begin{aligned} C_P |\psi_{in}\rangle &= C_P (c_{HH} |HH\rangle + c_{HV} |HV\rangle + c_{VH} |VH\rangle + c_{VV} |VV\rangle) = \\ |\psi_{out}\rangle &= (c_{HH} |HH\rangle + c_{HV} |HV\rangle + c_{VH} |VH\rangle - c_{VV} |VV\rangle), \end{aligned} \quad (5.1)$$

where c_{HH} denotes the amplitude of the $|HH\rangle$ -term and analogous for the other terms.

The basic idea is to implement the π -phase shift via second-order interference at a polarization dependent beam splitter (PDBS) (figure 5.1). Two input modes a and b are overlapped at PDBS_O, with perfect transmission for horizontal and 1/3 transmission for vertical polarization¹. The latter results in a total amplitude of $-1/3$ for the $|VV\rangle$ output terms. This can be seen by adding the amplitudes contributing to a coincident detection, i.e. transmission or reflection of both photons:

$$(T_V^a \cdot T_V^b) + (iR_V^a \cdot iR_V^b) = \sqrt{\frac{1}{3}}\sqrt{\frac{1}{3}} - \sqrt{\frac{2}{3}}\sqrt{\frac{2}{3}} = -1/3, \quad (5.2)$$

where T_i^x (R_i^x) is the amplitude for transmission (reflection) of state $|i\rangle$ in mode x . Perfect transmission of horizontal polarization prevents interference of the contributions $|HH\rangle$, $|HV\rangle$ and $|VH\rangle$, because for these terms a coincidence is only achieved if both qubits are transmitted. For perfect gate operation, the absolute values of all amplitudes have to be equal, independent of the input state. Thus, we still need to attenuate the contributions that include horizontal polarization. This is achieved by adding PDBS_{a/b} in the two output modes, respectively. These beam splitters exhibit the transmission 1/3 for horizontal polarization and perfect transmission for vertical polarization. All together, we find a probability of 1/9 to obtain a coincidence in the outputs and thus a gate operation.

¹The value 1/3 can be derived from the conditions resulting from the calculation in section 5.1.3.

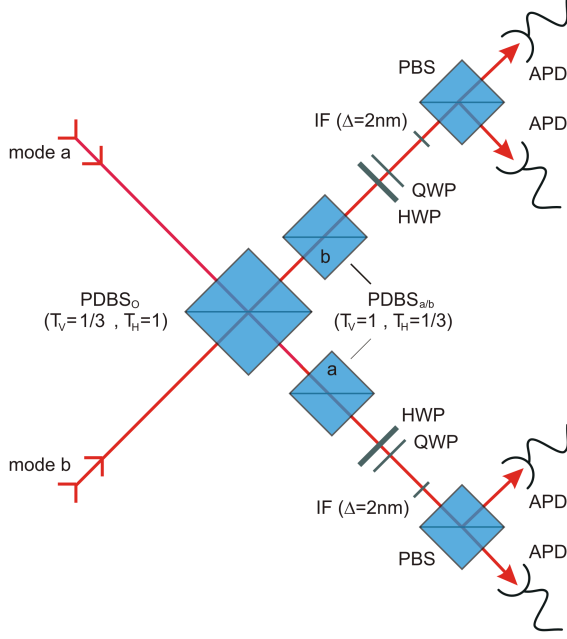


Figure 5.1: Realization of a linear optical controlled phase gate: Two polarized photons from different spatial modes are overlapped at a polarization dependent beam splitter $PDBS_O$ with perfect transmission for horizontal and $1/3$ for vertical polarization. Further, beam splitters $PDBS_{a,b}$ with the inverse splitting ratio in both output modes, respectively, compensate the partially polarizing effect of $PDBS_O$. The C_P operation is achieved by coincident detection of photons in the two output modes. For analysis of the gate operation a polarization analysis unit (figure 4.2 b) is placed in each of these spatial modes.

Let us express the operations introduced by the different BSs in terms of matrices. To do so, it will be instructive to express the processes for transmission and reflection of both photons independently. Assuming perfect interference, the two resulting process matrices simply need to be added up.

In case the two photons are transmitted through the setup, the following matrix acts on the state:

$$\begin{aligned}
 P\hat{D}BS_a \cdot P\hat{D}BS_b \cdot P\hat{D}BS_O^{tt} &= \hat{M}_{tt} \quad (5.3) \\
 \begin{pmatrix} \frac{1}{\sqrt{3}} & 0 & 0 & 0 \\ 0 & \frac{1}{\sqrt{3}} & 0 & 0 \\ 0 & 0 & 1 & 0 \\ 0 & 0 & 0 & 1 \end{pmatrix} \cdot \begin{pmatrix} \frac{1}{\sqrt{3}} & 0 & 0 & 0 \\ 0 & 1 & 0 & 0 \\ 0 & 0 & \frac{1}{\sqrt{3}} & 0 \\ 0 & 0 & 0 & 1 \end{pmatrix} \cdot \begin{pmatrix} 1 & 0 & 0 & 0 \\ 0 & \frac{1}{\sqrt{3}} & 0 & 0 \\ 0 & 0 & \frac{1}{\sqrt{3}} & 0 \\ 0 & 0 & 0 & \frac{1}{3} \end{pmatrix} &= \begin{pmatrix} \frac{1}{3} & 0 & 0 & 0 \\ 0 & \frac{1}{3} & 0 & 0 \\ 0 & 0 & \frac{1}{3} & 0 \\ 0 & 0 & 0 & \frac{1}{3} \end{pmatrix}
 \end{aligned}$$

Further, the case when two photons are reflected is represented by:

$$\begin{aligned}
 P\hat{D}BS_a \cdot P\hat{D}BS_b \cdot P\hat{D}BS_O^{rr} &= \hat{M}_{rr} \quad (5.4) \\
 \begin{pmatrix} \frac{1}{\sqrt{3}} & 0 & 0 & 0 \\ 0 & \frac{1}{\sqrt{3}} & 0 & 0 \\ 0 & 0 & 1 & 0 \\ 0 & 0 & 0 & 1 \end{pmatrix} \cdot \begin{pmatrix} \frac{1}{\sqrt{3}} & 0 & 0 & 0 \\ 0 & 1 & 0 & 0 \\ 0 & 0 & \frac{1}{\sqrt{3}} & 0 \\ 0 & 0 & 0 & 1 \end{pmatrix} \cdot \begin{pmatrix} 0 & 0 & 0 & 0 \\ 0 & 0 & 0 & 0 \\ 0 & 0 & 0 & 0 \\ 0 & 0 & 0 & -\frac{2}{3} \end{pmatrix} &= \begin{pmatrix} 0 & 0 & 0 & 0 \\ 0 & 0 & 0 & 0 \\ 0 & 0 & 0 & 0 \\ 0 & 0 & 0 & -\frac{2}{3} \end{pmatrix}
 \end{aligned}$$

The total operation acting on a state $|\psi\rangle$ is then:

$$\hat{M}_{tt}|\psi\rangle + \hat{M}_{rr}|\psi\rangle = (\hat{M}_{tt} + \hat{M}_{rr})|\psi\rangle = \begin{pmatrix} \frac{1}{3} & 0 & 0 & 0 \\ 0 & \frac{1}{3} & 0 & 0 \\ 0 & 0 & \frac{1}{3} & 0 \\ 0 & 0 & 0 & -\frac{1}{3} \end{pmatrix} |\psi\rangle = \frac{1}{3} C_P |\psi\rangle. \quad (5.5)$$

Thus, the operation C_P is indeed realized with an amplitude of $\frac{1}{3}$, i.e., a success probability of $\frac{1}{9}$. In the following two sections the presented setup is taken as starting point to discuss deviations of the experimentally realized phase gate from the ideal one caused by imperfect interference on the one hand and imperfect components on the other.

5.1.2 Modeling distinguishable photons

The gate operation described before assumes perfectly indistinguishable photons and therefore perfect interference. The related operation is not unitary due to loss, can however be treated like a unitary gate operation with an additional attenuation, because the losses are polarization independent. Thus, the gate maps pure states onto pure states. In multiphoton experiments there are, however, so far no photon sources that allow the creation of completely indistinguishable photons. It was argued in section 4.1.1 that the indistinguishability of photons from pulsed SPDC is achieved by spectral filtering, relying on a trade-off between good visibility and high count rates. Additionally, the imperfect spatial matching of the two input modes in the gate leads to an increased distinguishability². Accordingly, we need to consider the effect of partially distinguishable photons in the phase gate.

The phase gate relies on the interference between the terms of two transmitted and two reflected photons. Distinguishability of photons implies, that it is in principle possible to ascertain the path they have taken, e.g. by their spectrum. Thus the detected events can be split into three categories: indistinguishable photons and distinguishable photons that were transmitted or reflected. Thus, the action of a realistic phase gate \overline{PG}_{mod} on a mixed state ρ is (in contrast to the perfect operation in equation 5.5):

$$\begin{aligned} \overline{PG}_{mod}\rho\overline{PG}_{mod}^\dagger &= \mathcal{Q}'(M_{tt} + M_{rr})\rho(M_{tt} + M_{rr})^\dagger \\ &+ (1 - \mathcal{Q}')(M_{tt}\rho M_{tt}^\dagger + M_{rr}\rho M_{rr}^\dagger), \end{aligned} \quad (5.6)$$

where the quality factor \mathcal{Q}' denotes the probability to observe an indistinguishable pair of photons. If the distinguishable parts are not negligible, this results in two important effects. Firstly, additional mixing: pure states are in general mapped to mixed states. Secondly, as will be argued in the following, the probability to obtain an output (which is the trace of the output state) becomes dependent on the input state and the process can thus not be considered as trace preserving.

For a general input state, the terms $|HH\rangle$, $|HV\rangle$, $|VH\rangle$ are not subject to interference because the photons are always transmitted, therefore there is no difference whether the photons are distinguishable or not. In contrast, we find two completely different behaviors for the term $|VV\rangle$. If the two photons are indistinguishable, then the amplitudes for both being transmitted or reflected have to be summed up: $\sqrt{\frac{1}{3}} - \sqrt{\frac{2}{3}} = -\frac{1}{3}$ resulting in a probability of $p_{VV}^{ind.} = \frac{1}{9}$ of a $|VV\rangle$ detection. In contrast for distinguishable photons, one considers the sum of the probabilities $p_{VV}^{ind.} = \left|\sqrt{\frac{1}{3}}\right|^2 + \left|-\sqrt{\frac{2}{3}}\right|^2 = \frac{5}{9}$ of the two respective

²The spatial distinguishability is not an issue of an imperfect source but rather of the quality of the achieved spatial overlap at the beam splitter. However, it has the same effect and cannot be separated from the spectral distinguishability.

cases. Therefore, the probability to obtain an output from the incoherent part of the photons is, for two vertically polarized photons, higher by a factor of five compared to the case of coherent, indistinguishable photons.

5.1.3 Modeling general components

The previous considerations showed that the gate operation is affected by photon properties. Apart from this, the theoretically expected parameters for the $PDBS$ s cannot be perfectly reproduced by real components. In addition, the values obtained for the components in the experiment strongly depend on their alignment in the experimental setup. In order to enable a description of the influence of real components, the setup is modeled with general beam splitting ratios. Thereby, we find that the requirements on the components necessary for a phase gate operation can be slightly relaxed. Consider a general input state (as in equation 5.1):

$$|\psi_{in}\rangle = (c_{HH} a_H^\dagger b_H^\dagger + c_{HV} a_H^\dagger b_V^\dagger + c_{VH} a_V^\dagger b_H^\dagger + c_{VV} a_V^\dagger b_V^\dagger) |0\rangle \quad (5.7)$$

with e.g. $a_H^\dagger b_V^\dagger |0\rangle = |HV\rangle$. Using the definition of the action of a general beam splitter in equation 4.10 we obtain as operator:

$$\begin{aligned} & (c_{HH} T_H^a T_H^b - c_{HH} R_H^a R_H^b) a_H^\dagger b_H^\dagger \\ & + (c_{HV} T_H^a T_V^b - c_{VH} R_V^a R_H^b) a_H^\dagger b_V^\dagger \\ & + (c_{VH} T_V^a T_H^b - c_{HV} R_H^a R_V^b) a_V^\dagger b_H^\dagger \\ & + (c_{VV} T_V^a T_V^b - c_{VV} R_V^a R_V^b) a_V^\dagger b_V^\dagger. \end{aligned} \quad (5.8)$$

Here, only the contributions where the photons split up are considered, because we rely on conditional detection. The second pair of beam splitters ($PDBS_{a,b}$) is used only in transmission as attenuating plates. The corresponding transmission (reflection) amplitudes of these attenuation plates are labeled as X_Y (X_Y^x) where X denotes the spatial mode and Y the polarization:

$$\begin{aligned} a_H^\dagger & \rightarrow (A_H a_H^\dagger + iA_H^x a_{xH}^\dagger) \\ a_V^\dagger & \rightarrow (A_V a_V^\dagger + iA_V^x a_{xV}^\dagger) \\ b_H^\dagger & \rightarrow (B_H b_H^\dagger + iB_H^x b_{xH}^\dagger) \\ b_V^\dagger & \rightarrow (B_V b_V^\dagger + iB_V^x b_{xV}^\dagger). \end{aligned} \quad (5.9)$$

For simplicity, the amplitudes X_Y and X_Y^x are complex and contain also the relative phase shifts between H and V that can, if necessary, be set via additional birefringent wave plates (as argued in section 4.2). As the reflected modes (superscript x) are ancillary they are not considered in the following. We obtain:

$$\begin{aligned} & (c_{HH} T_H^a T_H^b A_H B_H - c_{HH} R_H^a R_H^b A_H B_H) a_H^\dagger b_H^\dagger \\ & + (c_{HV} T_H^a T_V^b A_H B_V - c_{VH} R_V^a R_H^b A_H B_V) a_H^\dagger b_V^\dagger \\ & + (c_{VH} T_V^a T_H^b A_V B_H - c_{HV} R_H^a R_V^b A_V B_H) a_V^\dagger b_H^\dagger \\ & + (c_{VV} T_V^a T_V^b A_V B_V - c_{VV} R_V^a R_V^b A_V B_V) a_V^\dagger b_V^\dagger \end{aligned} \quad (5.10)$$

The first requirement that we use to simplify this calculation is that the amplitudes for input states $|HV\rangle$ and $|VH\rangle$, i.e., c_{HV} and c_{VH} , should be left unchanged by the gate. An equal reduction of the amplitude by a factor f is, however, allowed, resulting in:

$$\begin{aligned} c_{HV}T_H^aT_V^bA_HB_V - c_{VH}R_V^aR_H^bA_HB_V &= c_{HV} \cdot f \\ c_{VH}T_V^aT_H^bA_VB_H - c_{HV}R_H^aR_V^bA_VB_H &= c_{VH} \cdot f. \end{aligned} \quad (5.11)$$

By removing f we get:

$$T_H^aT_V^bA_HB_V - T_V^aT_H^bA_VB_H = \frac{c_{VH}}{c_{HV}}R_V^aR_H^bA_HB_V a_H^\dagger b_V^\dagger - \frac{c_{HV}}{c_{VH}}R_H^aR_V^bA_VB_H a_V^\dagger b_H^\dagger. \quad (5.12)$$

As the coefficients of the input state are arbitrary, we can finally conclude (after removing trivial cases) two possible conditions:

$$1) R_H^a = 0 = R_H^b, \quad (5.13)$$

$$2) R_V^a = 0 = R_V^b. \quad (5.14)$$

We choose the first (equation 5.13), as it is consistent to the originally introduced idea. From equation 5.12 we get then:

$$\begin{aligned} & c_{HH}T_H^aT_H^bA_HB_H && a_H^\dagger b_H^\dagger \\ + & c_{HV}T_H^aT_V^bA_HB_V && a_H^\dagger b_V^\dagger \\ + & c_{VH}T_V^aT_H^bA_VB_H && a_V^\dagger b_H^\dagger \\ + & (c_{VV}T_V^aT_V^bA_VB_V - c_{VV}R_V^aR_V^bA_VB_V) && a_V^\dagger b_V^\dagger. \end{aligned} \quad (5.15)$$

After this simplification, the action of the parameters by $PDBS_{a,b}$ and $PDBS_O$ cannot be separated anymore. Thus, they are substituted by total transmission ($\tau_X^Y = T_X^Y \cdot Y_X$) and reflection (ρ_X^Y) amplitudes. We get:

$$\begin{aligned} & c_{HH}\tau_H^a\tau_H^b && a_H^\dagger b_H^\dagger \\ + & c_{HV}\tau_H^a\tau_V^b && a_H^\dagger b_V^\dagger \\ + & c_{VH}\tau_V^a\tau_H^b && a_V^\dagger b_H^\dagger \\ + & (c_{VV}\tau_V^a\tau_V^b - c_{VV}\rho_V^a\rho_V^b) && a_V^\dagger b_V^\dagger. \end{aligned} \quad (5.16)$$

As we require all amplitudes to be equal, the operation has to fulfill the condition:

$$\tau_H^a\tau_H^b = \tau_H^a\tau_V^b = \tau_V^a\tau_H^b = -(\tau_V^a\tau_V^b - \rho_V^a\rho_V^b). \quad (5.17)$$

Therefore we can conclude:

$$\tau_H^a = \tau_V^a =: \tau^a, \quad (5.18)$$

$$\tau_H^b = \tau_V^b =: \tau^b, \quad (5.19)$$

$$\rho_V^a\rho_V^b = 2\tau^a\tau^b. \quad (5.20)$$

This finally leads to four conditions (together with equation 5.13) that the experimental setup has to fulfill in order to result in a probabilistic phase gate operation:

1. $R_H^a = 0 = R_H^b$
The reflectivity of the overlap beam splitter $PDBS_O$ for horizontal polarization should be zero.
2. $\frac{R_V^a R_V^b}{T_V^a T_V^b} = 2$
This ratio of transmission and reflection amplitudes of $PDBS_O$ is the substitute for the fixed values of $R_V = \sqrt{2}T_V = \sqrt{2/3}$ in the ideal case.
3. $T_H^a A_H = T_V^a A_V$
This is the only condition on the attenuation plate in mode a. The transmission amplitude for both polarizations needs to be such that the polarization of a single photon transmitted through the whole setup from mode a is conserved, i.e. the effect of $PDBS_O$ is compensated.
4. $T_H^b B_H = T_V^b B_V$
The same condition as 3.) for the attenuation plate in mode b.

The parameters of the originally presented ideal phase gate follow from these conditions under the assumption of a loss free, symmetric overlap beam splitter. The whole calculation was performed for indistinguishable photons to discuss the distinct imperfections separately. The considerations of section 5.1.2 and section 5.1.3 are combined by expressing the matrices \hat{M}_{tt} and \hat{M}_{rr} (section 5.1.2) in terms of the parameters derived here.

These four conditions establish requirements on the three components independently and therefore turn out to be extremely useful for the alignment of the experimental setup, which will be presented in detail in the following section.

5.2 Experimental setup

In this section, the actual experimental implementation of the phase gate will be described. This includes the quantification of the distinguishability of the photons used to test the phase gate via an Hong-Ou-Mandel type (HOM) interference experiment. Further, the components used in the setup are characterized with respect to the parameters discussed in the last section. For a detailed description of how the setup was built, the interested reader may refer to the Diploma thesis by Ulrich Weber [156].

For the experimental investigation of the gate we use photon pairs emitted from a non-collinear SPDC source, as described in section 4.1.1. As perfect entanglement cannot be guaranteed, we prefer to use separable states as input for the phase gate. Therefore, a horizontally and a vertically aligned polarizer are placed in the two emission modes, respectively, before they are coupled into single mode fibers. These fibers guide the photons to the phase gate. Via stress induced birefringence in the fiber, the polarizations of the photons are rotated at will to arbitrary separable input states. Thus, the preparation of the input states is completely independent of the phase gate setup itself. The spectral filtering of the photons (filter bandwidth ≈ 2 nm FWHM) is achieved by interference filters mounted in the phase gate setup together with the polarization analysis. While the actual position of the filters is irrelevant, this choice has the advantage that by filtering in the output ports of $PDBS_O$ possible differences between the filter functions have less

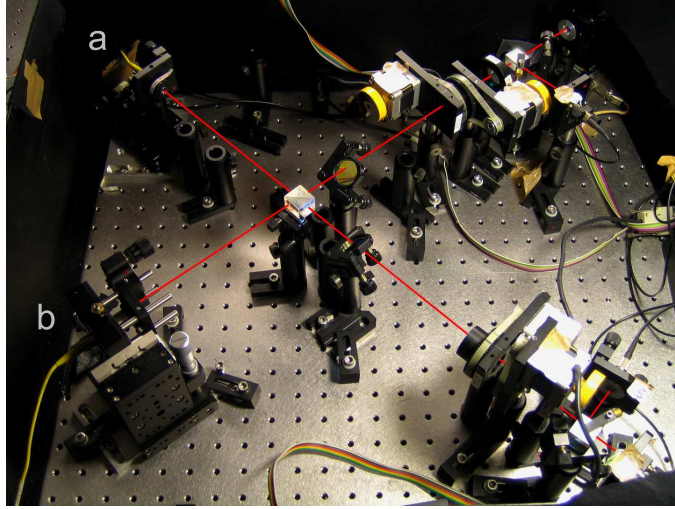


Figure 5.2: Photo of the linear optics controlled phase gate setup. On the left hand side, the two couplers where the photons enter the gate are located. The actual gate operation takes place at the three beam splitters in the center of the picture. The photons are overlapped at the cube and attenuated at the round *PDBS* plates. On the right hand side, the polarization analysis is mounted consisting of two motorized rotation mounts for the wave plates, an interference filter, a PBS and multimode fibers that guide the photons to the APDs (section 4.2).

influence, because the filter function does not "label" the photon by its mode. Thus, better indistinguishability is guaranteed.

A picture of the experimentally realized phase gate is shown in figure 5.2. The photons enter the setup in modes a and b via two different fiber coupling systems. In mode a, the fiber coupler is mounted on a translation stage moving parallel to the photons spatial mode. Thereby, the optical path length of the photon from the SPDC crystal to $PDBS_O$ can be set. This allows to compensate arbitrary time delays of the two photons at the overlap beam splitter. The other coupler allows alignment of the transverse position and direction of the spatial mode b. In addition, the position of the focus of the emitted gaussian beam can be set (the corresponding divergence is equal for both modes due to usage of identical optics components). Thus, the spatial overlap of mode b with mode a can in principle be achieved. For details on the alignment procedure, refer to [156].

The three beam splitters $PDBS_O$, $PDBS_a$ and $PDBS_b$ are custom made and were coated for perfect transmission of p- and 2/3 transmission for s- polarization for photons with a wavelength of 780 nm. The overlap beam splitter $PDBS_O$ is a cube mounted such that $|H\rangle$ is perfectly transmitted. For attenuation, we use beam splitting plates ($PDBS_a$ and $PDBS_b$) with the same coating as $PDBS_O$, however the mount is rotated by 90° such that the roles of horizontal and vertical polarizations are exchanged. Real beam splitters do not exactly reproduce the desired values and are, in addition, dependent on the angle of incidence (AOI) of the photons. Therefore, it is very useful to apply the four conditions derived in the previous section (see equation 5.1.3, page 66) for their alignment. Conditions 1.) and 2.) are requirements on $PDBS_O$ only and cannot be compensated by additional components. Thus, we first seek to align the AOI of $PDBS_O$

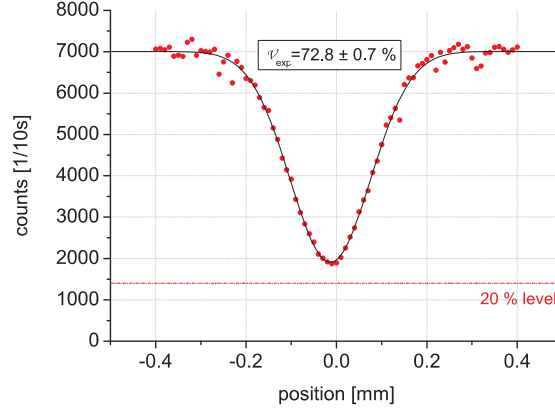


Figure 5.3: Hong-Ou-Mandel interference at the polarization dependent overlap beam splitter $PDBS_O$ in the phase gate for a $|VV\rangle$ input. In case of perfect interference the count rate should drop down to 20% leading to a theoretically achievable dip visibility of 80%.

such that these conditions are fulfilled as good as possible. Because we observed that condition 1.) does not depend on the AOI of $PDBS_O$ we optimize 2.) reaching a value of 2.018 ± 0.003 for the respective ratio³. The corresponding value for condition 1.) is then $|T_H^a|, |T_H^b| \approx 0.993$. Finally, following conditions 3.) and 4.), the attenuation plates $PDBS_a$ and $PDBS_b$ are tilted such that the polarization of a single photon transmitted through the whole setup (mode a or b) is preserved as good as possible.

As argued before, a perfect overlap of the two gaussian modes a and b can be achieved by alignment of the coupler in mode b . Furthermore, we need to ensure equal optical path length for both photons between the crystal and $PDBS_O$. To do so, we use a HOM-type measurement [158, 179] providing information about the position of zero delay and about the quality factor Q' that describes the indistinguishability of the photons for each delay. By scanning the delay between the two photons, using the coupler in mode a , it is possible to sample the $|VV\rangle$ -coincidence count rates for the transition from completely distinguishable to maximally indistinguishable photons. The outcome of a typical measurement is shown in figure 5.3. When the photons become less distinguishable, the count rate drops. This is due to the fact that, as argued in section 5.1.2, the probability of a coincident detection of $|VV\rangle$ at the output of the phase gate is lower when interference occurs (in the ideal case by a factor of five).

The gaussian shape of the resulting curve is mainly determined by the interference filters used for spectral filtering of the photons. Thus, we can use a gaussian function to fit this curve:

$$c(x) = A \left(1 - \mathcal{V} e^{-\frac{(x-x_0)^2}{2\Delta^2}} \right), \quad (5.21)$$

where A is the count rate for big delay, \mathcal{V} is the visibility of the HOM-dip, Δ is its width and x_0 is the position of the minimum, where zero delay between the two path lengths is reached. All measurements for the characterization of the gate made in the following are

³The ratio R_V/T_V is equal for both $PDBS_O$ input modes. For a loss free beam splitter this corresponds to a transmittivity (reflectivity) of the vertical polarization of $T_V^2 = 0.331$ ($R_V^2 = 0.669$).

taken with the translation stage in mode a at x_0 .

The value of interest for determination of the indistinguishability of two photons is \mathcal{V} . It can be expressed as $\mathcal{V} = (c_\infty - c_0)/c_\infty$ where c_∞ is the count rate at positions with big delay, i.e. perfect distinguishability, and c_0 the rate at zero delay. In a typical HOM-experiment at a symmetric beam splitter, the ideal value is 1, which means vanishing count rates for perfect indistinguishability. Here, we have to consider the special splitting ratio of the beam splitter. For large delay, the success probability $p_{VV}^\infty = 5/9$, which reduces in the ideal case to $p_{VV}^0 = 1/9$ for perfect indistinguishability. This results in an ideal visibility of $\mathcal{V}_{ideal} = 80\%$. Experimentally we find $\mathcal{V}_{exp} = 72.8\% \pm 0.7\%$. From this we can calculate the fraction of indistinguishable photons as $\mathcal{Q} = \mathcal{V}_{exp}/\mathcal{V}_{th} = 91.0\% \pm 0.9\%$. This also means that the probability of observing a coincidence from two vertically polarized input photons is increased by an admixture of the state $|VV\rangle\langle VV|$, which is obtained for any input state that includes $|VV\rangle$ -terms. This admixture plays an important role in the further analysis and will henceforth be referred to as VV -noise. It is directly visible in figure 5.3 as the difference between the minimum count rate and the 20%-level.

5.3 Experimental analysis of the gate

The experimental analysis of the phase gate is conducted in two steps:

First, a complete set of data describing the gate operation is measured. With the quantum process tomography described in section 4.3.4 an experimental superoperator χ_{Data} is derived. We proceed with the evaluation as depicted in figure 5.4: The model that was presented in section 5.1 is fitted to χ_{Data} resulting in a physical process matrix χ_{Fit} . Then, we use the fitted model to estimate the process that is obtained by the phase gate when the photons are completely indistinguishable (χ_{IP}). In the discussion, a major focus is put on the ability of the model to reproduce the experimental gate and on the

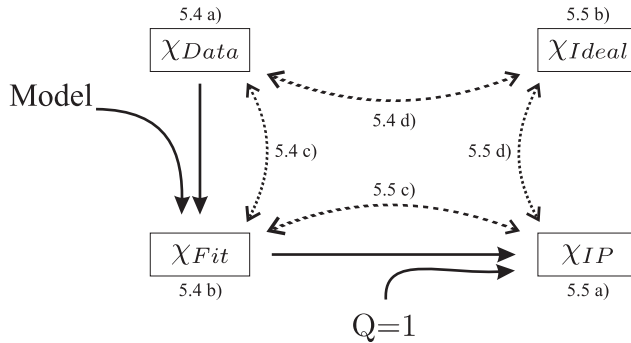


Figure 5.4: Overview of the process tomography evaluation. The superoperator inferred linearly from the measured data (χ_{Data}) is fitted with the model derived in section 5.1, resulting in a physical superoperator (χ_{Fit}). To learn more about the influence of the gates' components we study the process resulting from χ_{Fit} when we assume indistinguishable photons (χ_{IP}), i.e. $Q = 1$. To simplify the comparison of these operators with each other and an ideal probabilistic phase gate (χ_{Ideal}), the differences between the superoperators that are connected with dashed arrows are shown in the figure indicated by the corresponding labels.

$ \psi_{in}\rangle$	$ \psi_{out}\rangle = C_P \psi_{in}\rangle$	$\langle \psi_{out} \rho_{out} \psi_{out} \rangle$
$ HH\rangle$	$ HH\rangle$	0.993
$ HV\rangle$	$ HV\rangle$	0.962
$ VH\rangle$	$ VH\rangle$	0.934
$ H+\rangle$	$ H+\rangle$	0.954
$ +H\rangle$	$ +H\rangle$	0.933
$ HL\rangle$	$ HL\rangle$	0.956
$ LH\rangle$	$ LH\rangle$	0.954
$ VV\rangle$	$ VV\rangle$	0.981
$ V+\rangle$	$ V-\rangle$	0.814
$ +V\rangle$	$ -V\rangle$	0.818
$ VL\rangle$	$ VR\rangle$	0.815
$ LV\rangle$	$ RV\rangle$	0.856
$ ++\rangle$	$\frac{1}{\sqrt{2}}(H+\rangle + V-\rangle)$	0.799
$ +L\rangle$	$\frac{1}{\sqrt{2}}(HL\rangle - i VR\rangle)$	0.785
$ L+\rangle$	$\frac{1}{\sqrt{2}}(LH\rangle - i RV\rangle)$	0.867
$ LL\rangle$	$\frac{1}{\sqrt{2}}(HL\rangle + i VR\rangle)$	0.835

Table 5.1: Fidelity of the observed output states ρ_{out} of the phase gate for a complete tomographic set of input states $|\psi_{in}\rangle$. Errors on all values are ≈ 0.01 .

quality of the observed gate operation compared to an ideal one (χ_{Ideal}). Further, the influence of the major error, i.e. indistinguishable photons, is studied by comparison of χ_{IP} to χ_{Fit} and χ_{Ideal} .

Then, we focus on the most important property of the phase gate, i.e., its power to entangle two photons. The entanglement that is obtained experimentally from completely separable input states is studied. The results are compared to the ones obtained with the fitted model process matrix χ_{Fit} . From the model, we can then predict measurement outcomes for all other input states. This way, we establish a value of the maximally achievable entanglement (entanglement capability) and identify influences of the different imperfections of the gate on the experimental data. Further, the entanglement that could be achieved with perfectly indistinguishable photons but real gate components is discussed.

5.3.1 Description of the experimental process

It was argued in section 4.3.4 that a superoperator of a quantum process can be determined from the output density matrices of a complete tomographic set of input states. Here, we choose a tomographic set of separable input states, as they can be prepared with almost perfect fidelity. An overview of these states together with the corresponding expected output states and the experimentally achieved fidelity is shown in table 5.1⁴. This data was obtained with a count rate of about 420-820 counts/min (dependent on the input state) and a measurement time of 180 min per output state.

⁴Note that these values are, like in [156], derived with the tomography method in [163].

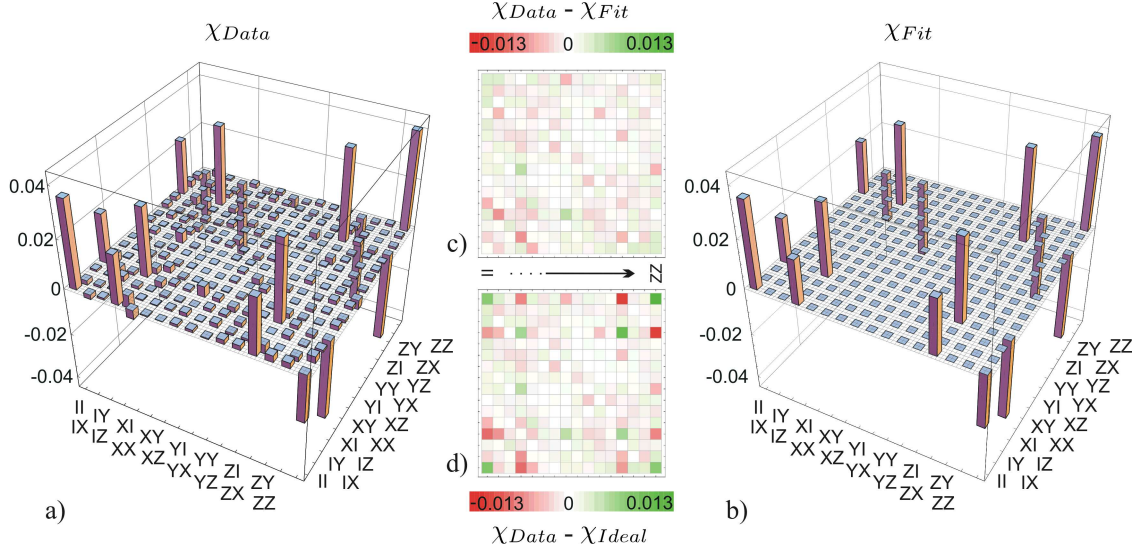


Figure 5.5: Process matrices deduced from the measurement data. Matrix a) is the representation of the process directly deduced from the measured data (χ_{Data}). For comparison, the physical process matrix χ_{Fit} achieved by fitting the model to χ_{Data} is depicted in b). The differences between the matrices are visualized as density plot in c). Matrix d) shows the differences between the χ_{Data} and an ideal density matrix with success probability $1/9$ (χ_{Ideal} , figure 5.6 b). For all matrices only the real part is shown, imaginary parts are comparable to the noise in the respective real part.

Using the quantum process tomography formalism introduced in section 4.3.4 we can now derive the superoperator for the process. In the first step, we need to find the probability to obtain an outcome from the input states $|HH\rangle$, $|HV\rangle$, $|VH\rangle$ and $|VV\rangle$ (success probabilities). They could be inferred directly from the observed count rate, but as we cannot be sure that the rate of created photon pairs was constant over the measurement time, we obtain these probabilities from the diagonal elements of the output density matrices as described on page 59 (example in equation 4.35): We express the four diagonal elements of 16 general output density matrices in terms of the 4 success probabilities. Then, these expressions are fitted to the diagonal elements of the experimentally obtained output density matrices via a least square fit. From this we obtain the following success probabilities:

$$p_{HH} = 0.111 \quad p_{HV} = 0.136 \quad p_{VH} = 0.110 \quad p_{VV} = 0.228 \quad (5.22)$$

The difference between the values of the 64 fitted diagonal elements predicted with these probabilities and the experimentally obtained ones is on average 0.00 ± 0.04 . It is clearly visible that the success probability of $|VV\rangle$ is enhanced, as expected for partially distinguishable photons (see discussion of VV -noise in section 5.2, page 70). An additional observation is that the value for $|HV\rangle$ is also higher. This cannot be attributed to the imperfect interference but rather to phase gate parameters – a point that will be discussed in more detail later.

Knowing the success probabilities in the computational basis, we can now determine (equation 4.34) the unphysical process matrix (χ_{Data}) obtained directly from the measure-

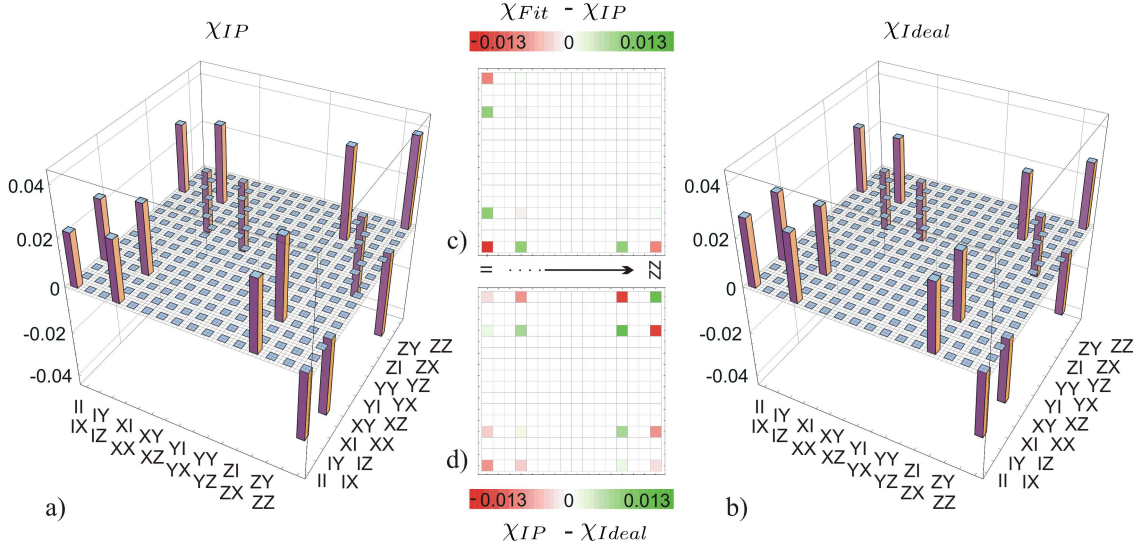


Figure 5.6: Matrix a) is the representation of the process (χ_{IP}) predicted by the model with the phase gate parameters and perfectly indistinguishable photons. An ideal phase gate matrix with success probability $1/9$ is visualized in b). The differences between these matrices are shown as density plot in d) for better comparison. Matrix c) shows the differences between the process achieved from the fitted model with the experimental and with perfect indistinguishability of the input photons.

ment data (figure 5.5 a). Further, by fitting the model (section 5.1) to this operator, we obtain a physical process matrix (χ_{Fit} , figure 5.5 b). Here, the basic set of transformations for representation are the Pauli matrices, $E_i \in \{\mathbb{1}, \hat{\sigma}_z, \hat{\sigma}_x, \hat{\sigma}_y\}$, which are represented by $\{\mathbb{1}, Z, X, Y\}$ in the figures. The discussion of this result is conducted in three steps: First, we can compare the parameters obtained from the fit with the independently determined ones. Then, the validity of the fitted model will be discussed. Finally, a comparison between the operation induced by the experimental and an ideal phase gate will be discussed.

The free parameters in the model consist of the variables in the four conditions equation 5.1.3 and the quality factor quantifying the indistinguishability of the photons in equation 5.6. For simplicity we assume for $PDBS_O$ additionally the reflection of the horizontal polarization to be negligible (i.e. condition 1. as fulfilled) and the parameters in both modes to be equal. Then we obtain, by fitting the model to the experimental superoperator, the quality factor $Q_{Fit} = 0.904$, which is comparable with the value found in the HOM-experiment (figure 5.3) of 0.91 ± 0.009 . Further, we find for condition 2.) $T_V^2/R_V^2 = 2.035$ from the fit, which is comparable with the value of 2.019 ± 0.003 determined in the characterization of $PDBS_O$. Conditions 3.) and 4.) concern the alignment of $PDBS_a$ and $PDBS_b$ (see explanations of conditions page 66). In mode a we find $a_V T_V = 1.0 \cdot a_H T_H$, which means that the alignment of $PDBS_a$ is completely correct, as perfect polarization conservation is also predicted by the fit. In mode b a significant deviation from the expected ratio is observed: $b_V T_V = 1.16 \cdot b_H T_H$. The reason for this deviation could not yet be clarified, but is qualitatively consistent with the observation of the increased success probability of p_{HV} (see 5.22).

A comparison between the measured and the fitted superoperators (figure 5.5) shows that a good agreement is achieved, despite of the few degrees of freedom used in the model. The major difference is the missing noise on the unexpected events, which is partly caused by errors due to counting statistics, whereas the model does not include any effects that might cause these contributions. In order to allow for a better comparison, the difference between χ_{Data} and χ_{Fit} is visualized in figure 5.6 c) as density plot. There is no obvious structure in the plot, values are between -0.005 and +0.005. The noise is thus homogeneous and the differences on the high peaks deviate as much between the fitted and the unfitted version as all other contributions. This demonstrates that the fitted physical superoperator reproduces the physical process quite well. To further compare the predictions of the fit with the experimental data, we calculate the measurement outcomes for the input states in table 5.1 and compare those with the measured data: The fidelities between the measured and the calculated matrix is on average $F_{mod}^{exp} = 96.6 \pm 1.7\%$, demonstrating a good agreement. The most relevant examples, i.e. the ones where entanglement is introduced, are discussed in more detail in the next section. Thus, we can reproduce the experiment with our model and the parameters obtained from the fit or independent measurements quite well. To study one possible explanation for the remaining deviations, white noise was included in an alternative model. This did, however, not change this results significantly. Other possible sources of noise are higher order emissions of the SPDC photon source and counting statistics.

Let us now turn to the question, how well the experimental gate reproduces an ideal probabilistic phase gate (χ_{Ideal} , figure 5.6 b). The characteristic peaks are clearly visible in both, χ_{Data} (figure 5.5 a) and χ_{Fit} (figure 5.5 b). The height of the diagonal elements is not equal, in contrast to the ideal gate. The biggest change, however, are the reduced off-diagonal elements compared to χ_{Ideal} . This is made more visible in figure 5.5 d) where the difference between χ_{Data} and χ_{Ideal} is shown. The reduction of these off-diagonal elements shows a loss of coherence in the output states, which can be attributed to distinguishability of photons. However, as we have seen, also the gate components introduce some errors.

One big advantage of fitting the model we used is, in comparison to the usual procedure of fitting a general physical process matrix (e.g. [169, 180]), that we can vary gate parameters. To investigate the errors that result only from the gate components, the operation obtained when the photons are completely indistinguishable is calculated (χ_{IP} , figure 5.6 a). Here, the off-diagonal elements are higher showing that the coherence is increased in comparison to χ_{Fit} . In addition, the diagonal peak corresponding to the operation $\mathbb{1} \otimes \mathbb{1}$ decreased. These changes are better visible in figure 5.6 c) where the difference between the two model process matrices is depicted. The resulting operator is very similar to χ_{Ideal} . The remaining differences are caused by gate components and are made more visible in figure 5.6 d) where the differences between χ_{Ideal} and χ_{IP} are shown.

The tool of choice to quantify the quality with which the process matrices reproduces an ideal phase gate is the process fidelity (see section 4.3.4, [44]). The measured process matrix has a fidelity of:

$$F_{Data} = 81.6\%,$$

the fitted process matrix has a slightly higher fidelity:

$$F_{Fit} = 84.6\%.$$

The increase can mostly be attributed to the non-existence of the noise in the unexpected contributions. This can be seen by cutting these contributions in χ_{Data} (everything smaller than 0.1) which results in a fidelity of 84.1%. Finally, when we assume perfectly indistinguishable photons, the fidelity is almost perfect:

$$F_{IP} = 98.8\%.$$

The two similar values for F_{Data} and F_{Fit} show once more the agreement between the model and the real process. As we can see, the fidelity is drastically increased when the photons are indistinguishable, identifying this imperfection as the most important source of errors. In contrast, the quality of the components has a minor influence, which is in agreement with a similar analysis conducted for the previous version of a phase gate [41].

5.3.2 Entangling capability of the gate

A point of major importance concerning the analysis of quantum gates is the capability of the gate to entangle separable states. Even more so, as we use the gate to entangle two Bell states in order to obtain a Cluster state (chapter 6). But also in other publications where a quantum gate is demonstrated, this part of the analysis usually constitutes an important step [43, 44, 135, 175, 176, 178, 180]. Thus, it allows the comparison of different implementations of two-qubit gates.

In this context we can ask, on the one hand, how strongly different separable states become entangled, on the other hand, what is the best entanglement we can achieve. The latter is called entanglement capability [167]. In either case, different entanglement measures can be used for quantification. In the bipartite case, the most common and at the same time most easily calculable ones are the concurrence and the logarithmic negativity, which were introduced in the previous section. Both measures will be applied in the following. In analogy to the analysis of the process itself presented in section 5.3.1, three aspects are analyzed: The entanglement of the directly measured states and the entanglement of the output states predicted by the model with all fit parameters and with the quality factor set to $\mathcal{Q} = 1$, i.e., assuming indistinguishable photons. Only our complete knowledge of the process allows to determine the entanglement capability, as it is the maximally achievable entanglement for *all* input states, not only for a tomographic set.

A phase gate operation creates entanglement whenever two separable input qubits are superpositions of $|H\rangle$ and $|V\rangle$. For example, with a state that is a tensor product of $|+\rangle$ and an unequal superposition of horizontal and vertical polarization given by $|\psi(\theta)\rangle = (\cos(\theta)|H\rangle + \sin(\theta)|V\rangle)$, we obtain with the operation C_P the state:

$$\begin{aligned} |+\rangle \otimes |\psi(\theta)\rangle &= 1/\sqrt{2}(\cos(\theta)|HH\rangle + \sin(\theta)|HV\rangle + \cos(\theta)|VH\rangle + \sin(\theta)|VV\rangle) \\ &\xrightarrow{C_P} 1/\sqrt{2}(\cos(\theta)|HH\rangle + \sin(\theta)|HV\rangle + \cos(\theta)|VH\rangle - \sin(\theta)|VV\rangle) \\ &= (\mathcal{H} \otimes \mathbf{1})(\cos(\theta)|HH\rangle + \sin(\theta)|VV\rangle). \end{aligned} \quad (5.23)$$

Thus, the result is an entangled state for $\theta \neq 0$. The strength of entanglement is dependent on θ . Its dependence for the logarithmic negativity (solid line) and the concurrence (dashed line) can be seen as the blue curve in figure 5.7 b), with a maximum at $\theta = \pi/2$.

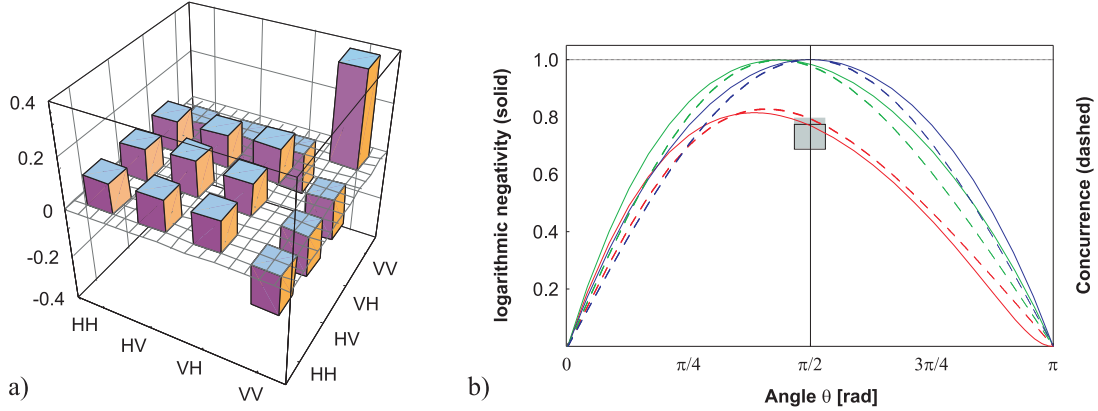


Figure 5.7: Entanglement capability of the controlled phase gate. In a), the entangled state obtained after action of the experimental phase gate on the input state $|++\rangle$ is shown. In b), a plot of the logarithmic negativity and concurrence of the output states for input states $|\psi(\theta)\rangle$ for three different situations is depicted: The gate obtained by the fitted model (red), the model with the fitted parameters but indistinguishable photons (green), and the operation of an ideal phase gate (blue). The experimental results for logarithmic negativity (concurrence) are within the filled (open) box.

Note that for the ideal gate and for the model this result does not depend on the phase between $|H\rangle$ and $|V\rangle$ (i.e. it is also valid for e.g. $|L\rangle$ instead of $|+\rangle$ in the first qubit).

Experimentally, we analyze the output density matrices obtained for all combinations of input states $|L\rangle$ and $|+\rangle$. They would all lead to maximally entangled states in an ideal phase gate. Separable input states can be prepared very well from the SPDC emission using polarizers and waveplates. In particular separability is then guaranteed, which is an important precondition for testing the increase of entanglement due to the gate. Exemplarily, the real part of the output density matrix for the input state $|+\rangle \otimes |+\rangle$ is shown in figure 5.7 a). The phase introduced by the gate is responsible for the off-diagonal terms that are negative due to the π -phase shift. The enhanced $|VV\rangle\langle VV|$ -term is caused by the incoherent VV -noise that was discussed in section 5.2. The fidelity to the expected state is $F = 80.4 \pm 0.5\%$. The entanglement of the observed state in terms of the logarithmic negativity and concurrence is $E_{lN} = 0.745 \pm 0.007$ and $C = 0.731 \pm 0.007$. The range where the entanglement lies for all experimentally observed states is depicted as boxes in figure 5.7 b) at $\pi/2$, where the filled box represents logarithmic negativity and the open one concurrence.

With process matrix χ_{Fit} obtained from our phase gate model in the last section, we can now estimate the entanglement that is achieved for every state $|\psi(\theta)\rangle$. The corresponding functions are shown in figure 5.7 b) as red lines, where $E_{lN}(\theta)$ is the solid and $C(\theta)$ the dashed curve. The predicted curves reach values at $\pi/2$ that are in the upper region of what is observed in the measurement: $E_{lN}(\pi/2) = 0.770$ and $C(\pi/2) = 0.794$.

The dependences show that there are two effects leading to reduced entanglement in the observed states. The curves' maximum is reduced and shifted to a different angle θ in comparison with an ideal phase gate. Thus, the measured values are not corresponding to the entanglement capability of the gate. The maximally achievable entanglement predicted by the model is in terms of the two measures: $E_{lN}(0.385\pi) = 0.815$ and $C(0.409\pi) = 0.827$.

This can be explained by looking at the curve obtained from indistinguishable photons:

The red curves show the prediction of the model calculation when perfect indistinguishability of the interfering photons is assumed. The maximum of the curves is still not at $\theta = \pi/2$, but reaches almost the value of one: $E_{IN}(0.436\pi) = 0.999$ and $C(0.436\pi) = 0.998$. Thus, we can conclude that the shift of the maximum can be attributed to imperfections in the optical components in the gate. The reduced entanglement capability can almost totally be attributed to partial distinguishability of the photons.

5.4 Summary

In this chapter, the scheme, experimental implementation and analysis of a new type of linear optics controlled phase gate was presented. The design is simple and has, in comparison to previous experiments, the advantage of a high degree of stability. Thus, it opens the possibility to be used as a tool in multiphoton experiments.

The experimental phase gate reproduces the characteristic transformations expected for an ideal controlled phase gate very well. The fidelity of the process is 81.6%. An elaborate model of the gate revealed the major source of error, which is an admixture of incoherent separable noise of vertically polarized photon pairs. This is caused by the distinguishability of the photons used in the analysis of the gate. Without this effect we expect a process fidelity of 98.8%, showing that imperfections in the gates components play a minor role (in agreement with the analysis of a similar gate, [41]).

Further, the gate exhibits a high capability to entangle separable states. We could demonstrate this experimentally detecting entangled states with a logarithmic negativity of $E_{LN} = 0.745$ and a concurrence of $C = 0.731$. Using our model calculation it was possible to show that the gates capability to entangle is basically solely reduced by the incoherent noise stemming from partially distinguishable photons.

Thus, the present gate reaches, despite of the simplification of the experimental setup, a similar quality as previous versions of quantum gates that were harder to implement. Our experimental analysis showed that further improvements should mainly focus on better indistinguishability of the photons, in particular concerning the gates entangling capability. Yet, the gate operation is achieved in such good quality and long term stability with the present photon source that it can be utilized in a multiphoton experiment, as presented in the next chapter.

6 The Cluster State

This chapter describes the experimental observation and analysis of the four-photon entangled cluster state. We obtain the state by entangling two Bell states created in type-II SPDC using the controlled phase gate presented in the previous chapter. A combination of these techniques becomes possible only due to the high stability of the phase gate.

We give a detailed analysis of the entanglement properties of the observed quantum state, particularly in comparison with the ideally expected cluster state $|\mathcal{C}_4\rangle$. Hereby, we rely completely on the efficient non-tomographic methods, which were presented in chapter 4. First, general properties of the state, i.e., its four-qubit entanglement, symmetry and local entropy are studied. Then, the entanglement in three- and two-qubit subsets after projective measurements on, or loss of photons is investigated. At this point, differences and similarities with the GHZ_4 state, which is the only other four-qubit graph state, become particularly obvious. The significance of the experimentally obtained results for an application of the state in multiparty quantum communication.

6.1 Experimental setup

According to the construction rules of graph states [79], we can obtain a four qubit cluster state by entangling two photons from two different two-qubit cluster states, respectively. Bipartite cluster states are, up to local unitary operations, Bell states, which can be created directly via SPDC. Entanglement between these pairs is obtained with the controlled phase gate presented in chapter 5, according to the following scheme:

The diagram illustrates the construction of a four-qubit cluster state. It shows two separate bipartite cluster states (Bell states) on the left, each consisting of two qubits (1,2 and 3,4) connected by a line. A green arrow labeled 'phase gate' points to the right, where the two pairs are now connected into a single chain of four qubits (1,2,3,4). To the right of the diagram, the mathematical representation of the states is given:

$$\frac{1}{2}(|\phi^+\rangle \otimes |\phi^+\rangle) = \frac{1}{2}(|HHHH\rangle + |HHVV\rangle + |VVHH\rangle + |VVVV\rangle)$$

$$|\mathcal{C}\rangle = \frac{1}{2}(|HHHH\rangle + |HHVV\rangle + |VVHH\rangle - |VVVV\rangle)$$

The experimental setup is shown in figure 6.1 and will be described in the following. We use a non-collinear SPDC source (section 4.1.1) in double pass configuration, in order to create, with a certain probability, two independent photon pairs from the same pulse. A first pair of photons can be created when the UV pump pulse passes the BBO crystal the first time (forward direction). A mirror reflects the beam back and a second pair of photons can be created (backward direction). The pump beam needs to be collimated into the crystal in order to obtain a good collection efficiency of the created photons into single mode fibers that serve as spatial mode filters. Its Rayleigh length is about 40 cm. Thus, by using a flat UV mirror for the back reflection in a distance of about 3 cm from the crystal, we achieve a quasi collimated beam for both SPDC processes. The resulting count rate and entanglement quality of the two SPDC emissions is comparable. The emission

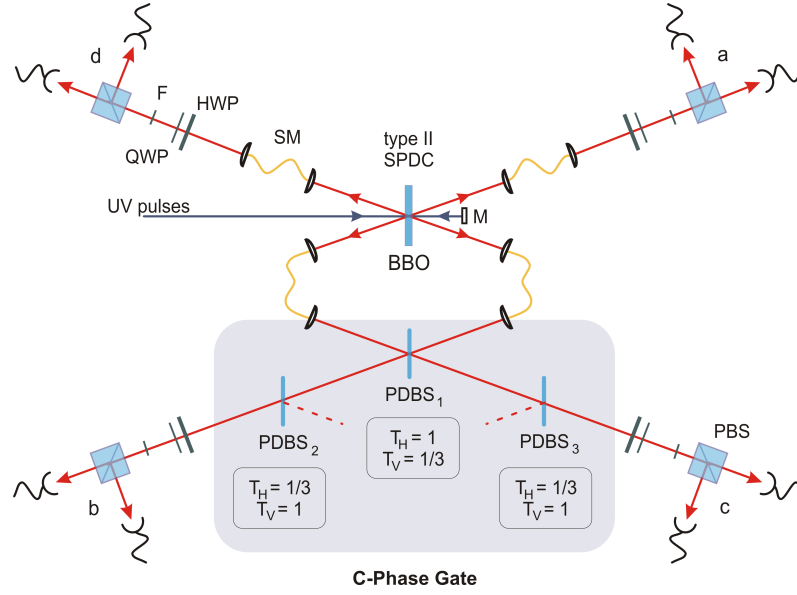


Figure 6.1: Experimental setup for the demonstration of the four-photon polarization-entangled cluster state. Two entangled photon pairs originate from type II SPDC by pumping a β -Barium Borate (BBO) crystal in a double pass configuration and are collected by single mode fibers (SM). The cluster state is observed after entangling the two EPR-pairs via a linear optics controlled phase gate (chapter 5). Spectral filters (F) in modes b and c have 2 nm bandwidth and 3 nm in modes a and d . Half- and quarter wave plates (HWP, QWP) together with polarizing beam splitters (PBS) are used for the polarization analysis.

angle between signal and idler photons are approximately 6° . Therefore they do not hit the 0.3 cm broad UV-mirror in forward direction.

The two SPDC emissions occur with a small delay due to the time difference between the pump beams first and the second passage through of the crystal. This delay has to be compensated, because the photons need to arrive at the same time at the overlap beam splitter in the controlled phase gate. Most of the delay is compensated by a difference in the length of the fibers that guide the photons to the linear optics setup. The remaining fine adjustment is done via the translation stage at one fiber coupler of the phase gate.

Further, we use stress induced birefringence in the fibers to transform the SPDC emissions to the states $|\phi^+\rangle$, as this state cannot be directly created in our type-II SPDC configuration. For spectral filtering we use 3 nm bandwidth interference filters in the spatial modes of photons that are not processed any further (a and d). In the phase gate setup (modes b and c) we use 2 nm interference filters to increase the quality of the second order interference.

The fine adjustment of the time of arrival of both photons at the overlap beam splitter in the phase gate is, like in section 5.2, achieved by an HOM-type experiment. Here, the difference is that the interfering photons are created in two different down conversion processes, i.e., in the first and second pass of one pump pulse through the BBO-crystal (figure 6.1). Interference occurs when two vertically polarized photons are overlapped in the phase gate, i.e., when we detect a vertically polarized photon pair in modes $\{a, b\}$ and $\{c, d\}$ in coincidence. Figure 6.2 shows the dependence of this four-fold VVVV-coincidence

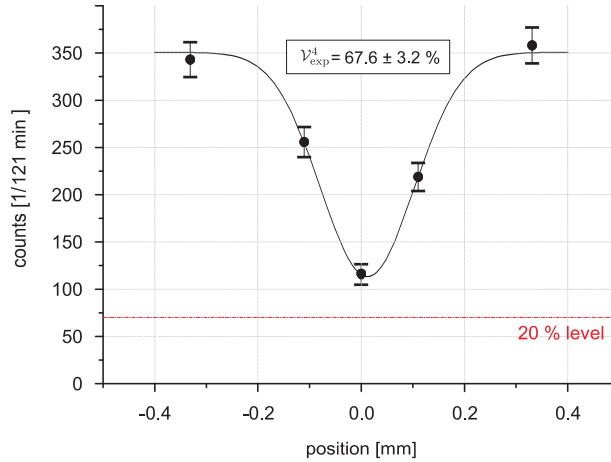


Figure 6.2: Four-photon Hong-Ou-Mandel interference at $PDBS_O$ with triggered vertically polarized single photons from the two SPDC sources shown in figure 6.1.

count rate on the position of the translation stage, which is mounted in the phase gate (see section 5.2¹). The position of the minimum of the gaussian curve is the position of zero delay between the time of arrival of both photons. At this position, we observe the cluster state with a count rate of about 2.5 four-fold coincidence counts per minute in a typical measurement.

The visibility of the HOM-interference is $\mathcal{V}_{\text{exp}}^4 = 67.6 \pm 3.2\%$ is slightly below the visibility of $\mathcal{V}_{\text{exp}}^2 = 72.8 \pm 0.7\%$, which was achieved with a photon pair from the same SPDC-process shown in figure 5.3. The four-fold visibility corresponds to a photon indistinguishability of $\mathcal{Q}^4 = 84.5 \pm 4.0\%$. In chapter 5 we saw that the partial distinguishability of photons in the phase gate causes an incoherent admixture of $|VV\rangle\langle VV|$, which was called VV-noise (section 5.2, page 70). In complete analogy, this effect translates here to an incoherent admixture of $|VVVV\rangle\langle VVVV|$ to the cluster state, which is henceforth referred to as VVVV-noise. This noise reduces, as we will see, the quality of the state. It is visible in figure 6.2 as the difference between the VVVV-count rate in the minimum and the 20%-level.

6.2 Experimental analysis

Several characteristic properties of the cluster state were presented in chapter 3. Experimentally, different imperfections cause deviations of the observed from the ideal state, thereby reducing its quality. The question is, whether the state changes its properties due to these imperfections or not, i.e., whether it can still be used as the same kind of quantum resource. Thus, it is necessary to analyze, in addition to a quantification of the states fidelity, its properties, in particular when they can be associated with a certain task.

To perform the analysis of the experimentally observed state we rely on the tools introduced in the first three chapters. We use solely direct, non-tomographic methods instead

¹The translation stage is here in the spatial mode b .

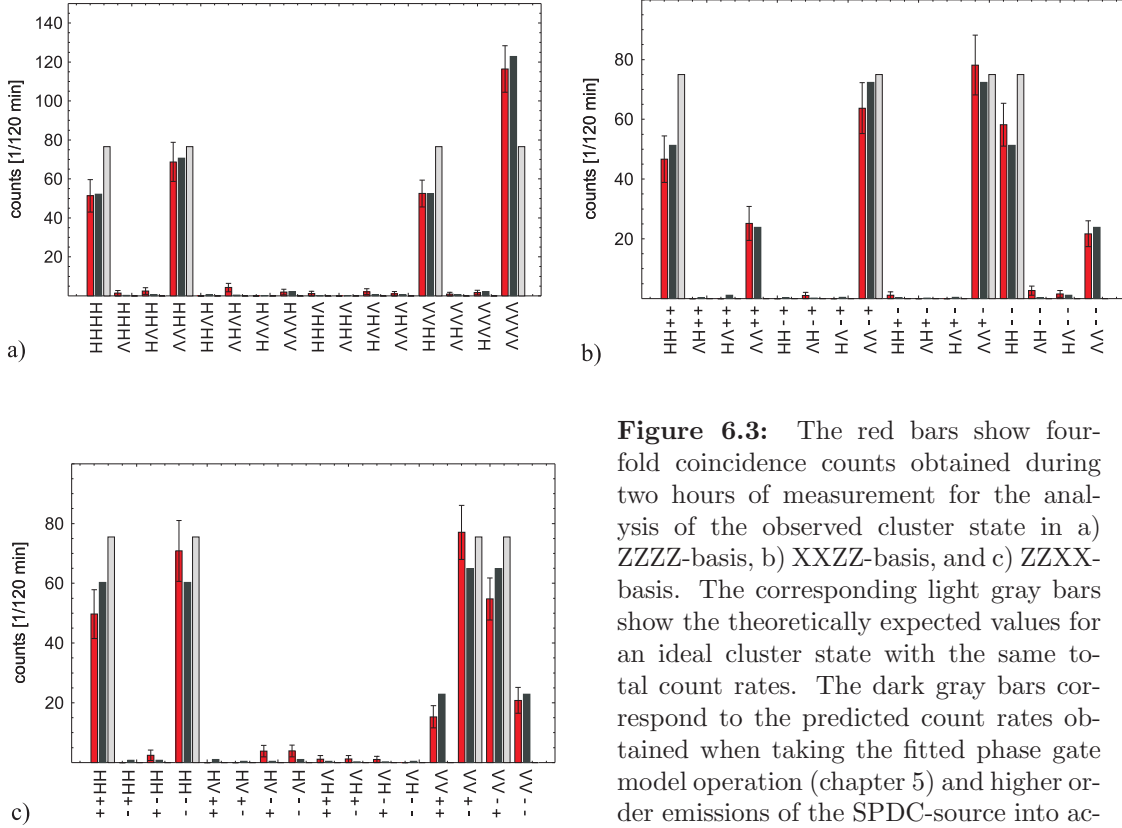


Figure 6.3: The red bars show four-fold coincidence counts obtained during two hours of measurement for the analysis of the observed cluster state in a) ZZZZ-basis, b) XXZZ-basis, and c) ZZXX-basis. The corresponding light gray bars show the theoretically expected values for an ideal cluster state with the same total count rates. The dark gray bars correspond to the predicted count rates obtained when taking the fitted phase gate model operation (chapter 5) and higher order emissions of the SPDC-source into account.

of estimating the complete density matrix. We apply the methods introduced in chapter 4 and take particular advantage of the fact that the state $|\mathcal{C}_4\rangle$ is completely described by the stabilizer formalism. The following analysis is structured in three parts: Characteristic global properties of the state are tested including its local entropy and four-fold entanglement, which are important features of the corresponding entanglement class. Further, the fidelity to the ideal state, estimation of entanglement measures and an analysis of permutation symmetry are used to quantify its quality. In the second part, we focus on connectedness in the cluster state, which is an important property for a representative of graph states: it describes the best entanglement observed after projective measurements. Here, the applicability of the observed state for quantum communication and one-way quantum computation will be discussed, as well. Finally, the cluster state distinguishes itself from the only other four-qubit graph state by its higher persistency of entanglement against photon loss, which will be studied in the third part.

6.2.1 Global properties

Population and Coherence

As a first step, the experimentally observed state is analyzed in the computational basis to study how well the characteristic four-term structure of $|\mathcal{C}_4\rangle$ is reproduced. Further, coherence between the observed terms is made visible by an analysis of the state in other

measurement bases. In figure 6.3, the experimentally observed data for three measurement bases are shown (red bars). For comparison, the expected outcome for an ideal state $|\mathcal{C}_4\rangle$ obtained with the same total count rate is shown (light grey). Furthermore, the data is compared to the results expected when we take the phase gate model with the quality factor $\hat{Q} = 84.5\%$ and higher order emissions of the SPDC sources into account.

In the experiment, we clearly observe (figure 6.3 a) the four characteristic terms of the state $|\mathcal{C}_4\rangle$ in the computational basis: $HHHH$, $HHVV$, $VVHH$ and $VVVV$. While these contributions are ideally equally weighted, this is not the case for the observed cluster state, which is consistent with the predictions of the model. The enhanced $VVVV$ -contribution is caused by the non-perfect indistinguishability of the photons at the overlap beam splitter, which was also discussed in the context of the HOM-dip measurement (section 6.1). In addition, we observe a slightly enhanced $HHVV$ contribution, as a result of the higher transmission of vertical compared to horizontal polarization in the phase gate in mode c (section 5.3.1, page 73). Note that this effect is also responsible for an additional increase of the term $VVVV$.

Coherence between these contributions is made visible by a study of the counting statistics of the four-fold coincidences in other measurement bases. Exemplarily, two correlated bases are shown in figure 6.3: In b), photons in mode a and b are analyzed in Z -basis and in mode c and d in X -basis; vice versa in c). The four highest terms in each measurement correspond to the only contributions expected for the ideal state $|\mathcal{C}_4\rangle$ with equal weighting. Experimentally and in agreement with the model calculation, these terms are most strongly emphasized, but accompanied by two additional smaller terms. The four high terms demonstrate the coherence between the contributions obtained in the computational basis. The imperfect interference in the phase gate causes the additional detection of the terms $VVxx$ (b), or $xxVV$ (c), respectively (where $x = +/-$).

All together a very good agreement between the measured data and the outcomes expected with the model is found for the computational basis. For the two bases in figure 6.3 b) and c) we find quantitatively still a good agreement with small deviations, that are not explained by the model. In the analysis of the state fidelity this will be further quantified.

Entanglement Detection

The state $|\mathcal{C}_4\rangle$ is genuinely four-partite entangled. This is one of its most fundamental properties and needs to be fulfilled by the experimentally prepared state, as well. Efficient detection of genuine four-partite entanglement is possible, as presented in section 3.2.1, via an entanglement witness for cluster states that is based on the stabilizer formalism. The stabilizing operators that determine a cluster state (as discussed in section 3.2.1) suffice, according to [106], to obtain an entanglement witness²:

$$\begin{aligned} \mathcal{W}_{\mathcal{C}_4} := 3 \cdot \mathbb{1}^{\otimes 4} & - \frac{1}{2} (\hat{\sigma}_z \otimes \hat{\sigma}_z \otimes \mathbb{1} \otimes \mathbb{1} + \mathbb{1}^{\otimes 4}) (\mathbb{1} \otimes \hat{\sigma}_z \otimes \hat{\sigma}_x \otimes \hat{\sigma}_x + \mathbb{1}^{\otimes 4}) \\ & - \frac{1}{2} (\hat{\sigma}_x \otimes \hat{\sigma}_x \otimes \hat{\sigma}_z \otimes \mathbb{1} + \mathbb{1}^{\otimes 4}) (\mathbb{1} \otimes \mathbb{1} \otimes \hat{\sigma}_z \otimes \hat{\sigma}_z + \mathbb{1}^{\otimes 4}), \end{aligned} \quad (6.1)$$

²Note that the example in section 3.2.1 (equations 3.13) is constructed for $|\mathcal{C}_l\rangle = (\mathcal{H} \otimes \mathbb{1} \otimes \mathbb{1} \otimes \mathcal{H}) |\mathcal{C}_4\rangle$. Therefore, those stabilizing operators differ from the ones used in the present witness by a Hadamard transformation on the first and fourth qubit.

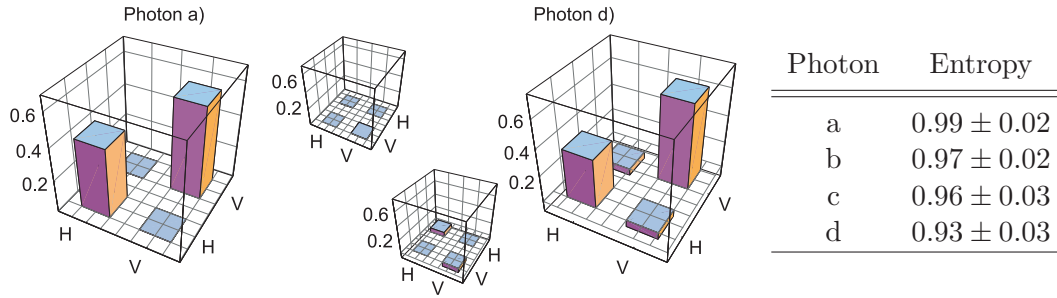


Figure 6.4: Analysis of the local entropy in the cluster state. In the table on the right, the local von Neumann entropy of all four photons are summarized. For the ideal state $|\mathcal{C}_4\rangle$, they have the maximum value of 1. Exemplarily, the corresponding single qubit density matrices of the photons in modes a and d are depicted. The small matrices show the imaginary parts.

with the optimal value of $\text{Tr}(\mathcal{W}_{\mathcal{C}_4} |\mathcal{C}_4\rangle\langle\mathcal{C}_4|) = -1$. Two measurement settings are sufficient to evaluate this witness, i.e., in the XXZZ - and ZZXX - basis. These are exactly the measurements depicted in figure 6.3 b) and c). Out of these data we find experimentally $\text{Tr}(\mathcal{W}_{\mathcal{C}_4} \rho^{\mathcal{C}_4}) = -0.299 \pm 0.050$. Thus, the observed cluster state is indeed genuinely four-photon entangled.

Local entropy

In section 3.1, it was discussed that several different families of genuine four-partite entanglement exist. The cluster state belongs to the first family, G_{abcd} , which is characterized by maximal local entropy [24]. In the following, it will be studied how well this property is reproduced by our state. To this end, single qubit density matrices after tracing out three qubits are determined. This can be done for all qubits with only three measurement settings (ZZZZ , XXXX and YYYY ; see section 3.3.1). Here, however, the complete set of data measured for the determination of the fidelity (see next section) is used instead. The resulting density matrix for the photons in modes a and d are exemplarily depicted in figure 6.4. As one can see, there is hardly any coherence left between the horizontal and vertical part. The latter is slightly more emphasized, which can be explained by the observed VVVV -noise (section 6.1). As measure of the local entropy we calculate the von Neumann entropy (see section 2.3.2) of the single qubits, which becomes zero for pure states and 1 for white noise. The resulting values for all four photons are summarized in table 6.4. We indeed observe a local von Neumann entropy close to the maximal value of 1 for all qubits³.

It is important to note that mixed states in general cannot be easily connected with the SLOCC-classification for pure states. Thus, the observation of maximal local entropy alone is not a proof for a detection of a state in the SLOCC-family G_{abcd} . We have, however, already shown that the state is genuinely four-partite entangled and several other properties will follow. In this context, the maximal local entropy of the observed state is a property which we require for a cluster state and which was indeed shown to be fulfilled very well in the experiment.

³For pure states the von Neumann entropy is zero.

	operators	correlation
(1)	$\hat{\sigma}_z \otimes \hat{\sigma}_z \otimes \mathbb{1} \otimes \mathbb{1}$	0.935 ± 0.037
(2)	$\hat{\sigma}_x \otimes \hat{\sigma}_x \otimes \hat{\sigma}_z \otimes \mathbb{1}$	0.713 ± 0.044
(3)	$\mathbb{1} \otimes \hat{\sigma}_z \otimes \hat{\sigma}_x \otimes \hat{\sigma}_x$	0.638 ± 0.045
(4)	$\mathbb{1} \otimes \mathbb{1} \otimes \hat{\sigma}_z \otimes \hat{\sigma}_z$	0.931 ± 0.036
(5)	$-\hat{\sigma}_y \otimes \hat{\sigma}_y \otimes \hat{\sigma}_z \otimes \mathbb{1}$	0.679 ± 0.043
(6)	$\hat{\sigma}_z \otimes \mathbb{1} \otimes \hat{\sigma}_x \otimes \hat{\sigma}_x$	0.707 ± 0.045
(7)	$\hat{\sigma}_z \otimes \hat{\sigma}_z \otimes \hat{\sigma}_z \otimes \hat{\sigma}_z$	0.931 ± 0.064
(8)	$\hat{\sigma}_x \otimes \hat{\sigma}_y \otimes \hat{\sigma}_y \otimes \hat{\sigma}_x$	0.729 ± 0.062
(9)	$\hat{\sigma}_x \otimes \hat{\sigma}_x \otimes \mathbb{1} \otimes \hat{\sigma}_z$	0.673 ± 0.044
(10)	$-\mathbb{1} \otimes \hat{\sigma}_z \otimes \hat{\sigma}_y \otimes \hat{\sigma}_y$	0.626 ± 0.067
(11)	$\hat{\sigma}_y \otimes \hat{\sigma}_x \otimes \hat{\sigma}_y \otimes \hat{\sigma}_x$	0.628 ± 0.066
(12)	$-\hat{\sigma}_y \otimes \hat{\sigma}_y \otimes \mathbb{1} \otimes \hat{\sigma}_z$	0.690 ± 0.060
(13)	$-\hat{\sigma}_z \otimes \mathbb{1} \otimes \hat{\sigma}_y \otimes \hat{\sigma}_y$	0.616 ± 0.067
(14)	$\hat{\sigma}_x \otimes \hat{\sigma}_y \otimes \hat{\sigma}_x \otimes \hat{\sigma}_y$	0.681 ± 0.066
(15)	$\hat{\sigma}_y \otimes \hat{\sigma}_x \otimes \hat{\sigma}_x \otimes \hat{\sigma}_y$	0.681 ± 0.064
(16)	$\mathbb{1} \otimes \mathbb{1} \otimes \mathbb{1} \otimes \mathbb{1}$	1.000 ± 0.017
		$F^{\mathcal{C}_4} = 0.741 \pm 0.013$

Table 6.1: The expectation values of this stabilizer group are the characteristic correlations of the state $|\mathcal{C}_4\rangle$. In this table, the experimentally obtained values, which can be deduced from nine measurement settings, are summarized. Their average value is the fidelity of the observed to the ideal state $F^{\mathcal{C}_4}$.

Fidelity

In order to explicitly quantify how close the observed state is to $|\mathcal{C}_4\rangle$, we need to employ a distance measure. The most commonly used one is the fidelity (equation 2.18). It was demonstrated before (equation 3.15) that it is sufficient to study expectation values of the 16 stabilizers of $|\mathcal{C}_4\rangle$ to evaluate the fidelity. For the ideal state, these correlations are perfect and at the same time the only standard bases where the state is correlated at all – in that sense they are characteristic. The results of the corresponding correlation measurements are summarized in table 6.1. Nine different measurement settings are sufficient to evaluate these sixteen correlations and with them the fidelity, instead of 81 settings that are needed for a complete state tomography.

The fidelity is simply the average value of these correlations and evaluates in our experiment to $F^{\mathcal{C}_4} = 74.1 \pm 1.3\%$. The connection between the fidelity and the generic entanglement witness allows an additional confirmation of genuine four-partite entanglement of the state [106]:

$$\mathcal{W}_{\mathcal{C}_4}^g = \frac{1}{2} \mathbb{1}^4 - |\mathcal{C}_4\rangle\langle\mathcal{C}_4| \quad (6.2)$$

$$\text{Tr} [\mathcal{W}_{\mathcal{C}_4}^g \rho^{\mathcal{C}_4}] = \frac{1}{2} - F^{\mathcal{C}_4} = -0.24 \pm 0.013. \quad (6.3)$$

Thus, genuine four-partite entanglement is also detected with the fidelity, as it exceeds the value of $\frac{1}{2}$ by approximately 17 standard deviations.

There are several different influences that are responsible for a reduction of the experimentally observed fidelity. As we have seen in chapter 5 the quality of the phase gate operation is reduced by imperfect components on the one hand and partially distinguishable photons on the other. In addition to this, noise is caused by higher order emissions from the SPDC sources. The model described in section 5.1.3 allows to calculate the expected fidelity when exclusively imperfect linear optics components are taken into account: We find a fidelity $F = 99.3\%$ showing that this is only a minor contribution. If we consider additionally the distinguishability of the overlapped photons, with the quality factor determined in the HOM-measurement (figure 6.2) $\hat{Q} = 84.5\%$, we find the major reduction of the state quality down to $F = 77.9\%$. A detailed calculation that takes second order emission and imperfect detection efficiencies into account⁴ (based on the SPDC parameters presented in table 4.1) reveals approximately 8% of additional noise that causes the fidelity to drop further to a value of $F = 74.7\%$. This is consistent with the fidelity observed in the experiment. Altogether, it is thus the distinguishability of the overlapped photons that causes the main reduction of state quality.

Apart from the interpretation of the fidelity as a distance measure, it is hard to draw additional conclusions from this value. An obvious threshold that the observed state should exceed is the maximal fidelity reached by the closest biseparable states of 0.5 (which we have fulfilled). Concerning applications of the state, it is advantageous to calculate directly the relevant values, e.g. the maximal singlet fraction of the residual bipartite state for quantum telecloning (section 3.3.2). The fidelity is, however, useful for a comparison with other experiments. A four-qubit cluster state was observed in experiments performed approximately simultaneously with ours as presented in [35] and for its further application in [36, 38]. There, a fidelity of about 63% is reported. It is important to note, however, that the linear optics setup used there achieves higher count rates⁵. Thus, the present scheme has, in comparison, a lower efficiency, but achieves a higher fidelity. Note that in [20] the observation of a six-photon cluster state is reported with a fidelity $F > 59\%$ ⁶. A value for the fidelity of the four-photon cluster state after projection of two qubits is, however, not given there.

The knowledge of the fidelity can also be used to put a lower bound on the geometric measure of entanglement (see section 2.3.4, equation 2.55, based on [72]), given that the geometric measure of the ideal state is known. With the value for the geometric measure of the cluster state ($E_G(\mathcal{C}_4) = 0.750$) (table 3.2.3 and appendix A) we find:

$$E_G(\rho^{\mathcal{C}_4}) \geq 0.243 \pm 0.013. \quad (6.4)$$

As the value does not exceed any of the measures for the states given in table 3.2.3, we cannot draw further conclusions for state discrimination. The possibility of determining bounds on *multipartite* entanglement measures experimentally was developed only recently. It can be expected that in the future, more experiments will use this tool and that

⁴For simplicity we assume equal detection efficiencies in all modes.

⁵Due to the different detection scheme we could not directly calculate the ratio between the count rates; one can, however, estimate a ratio of approximately 12.

⁶The distance to the next biseparable state in the six-qubit case is, like for four qubits, 0.5.

it provides a means for further comparison of experimentally observed quantum states, even if they are of different kind or number of qubits. Note that lower bounds for other measures of entanglement were found for the observed state [71], as well.

Symmetry

The state $|\mathcal{C}_4\rangle$ is invariant under several permutations of qubits. In contrast to the symmetric Dicke states or the GHZ_4 state it is not symmetric under all permutations. With respect to the three generators of the whole permutation group (S_{bacd} , S_{abdc} , S_{acbd}) it is an eigenstate of the first two (section 3.3.1).

For the efficient examination of these symmetries in the experimentally observed state, we follow the analysis method introduced in section 3.3.1. This results in the following expectation values for the symmetry operators (where the theoretical values are shown in parenthesis):

$$\begin{aligned}\langle S_{bacd} \rangle &= 0.98 \pm 0.07 \text{ (1.0)} \\ \langle S_{acbd} \rangle &= 0.62 \pm 0.09 \text{ (0.5)} \\ \langle S_{abdc} \rangle &= 0.98 \pm 0.08 \text{ (1.0)}\end{aligned}$$

We find that the permutation symmetry between the pairs a, b and c, d is indeed fulfilled very well. However, the value S_{acbd} is higher than the theoretical one. This can be attributed to the $VVVV$ -noise (section 6.1, page 81): the noise is an admixture of the state $|VVVV\rangle\langle VVVV|$ which is symmetric under all permutations of qubits and thus makes the resulting mixed state more symmetric with respect to S_{acbd} .

The symmetry properties of the cluster state, also turn out to be useful for its further experimental analysis. They allow the generalization of results on persistency and connectedness observed for one subset of qubits to other subsets. The following two subsections concern this part of the experimental analysis.

6.2.2 Connectedness

As pointed out by Briegel et al. [81] and discussed in chapter 3, cluster states possess the property of maximal connectedness: Projective measurements can be chosen such that only the measured qubit is removed from the cluster state. The remaining qubits still form a graph state independent of the measurement result. The following experiments demonstrate that the experimentally prepared state indeed reproduces this property. Maximal connectedness leads to an application of the state for open destination teleportation. The performance of the experimental state for this quantum information protocol is estimated.

Three-qubit subsets

First, we calculate explicitly the states after projective measurements on $|\mathcal{C}_4\rangle$. The measurement basis suited to obtain maximal entanglement in the residual state is the X-basis independent of the qubit to be measured (here we take exemplarily d):

$$|\mathcal{C}_3^\pm\rangle_{abc} =_d \langle +|\mathcal{C}_4\rangle_{abcd} = \frac{1}{\sqrt{2}}(|HH\pm\rangle_{abc} + |VV\mp\rangle_{abc}) \quad (6.5)$$

Qubit i	Projection	
	P_i^+	P_i^-
a	-0.288 ± 0.093	-0.256 ± 0.084
b	-0.543 ± 0.091	-0.277 ± 0.087
c	-0.276 ± 0.091	-0.304 ± 0.083
d	-0.362 ± 0.090	-0.392 ± 0.082

Table 6.2: Expectation values of the entanglement witnesses (equation 6.8) with the states obtained after projection of the photons in all spatial modes i onto the states $|+\rangle$ and $|-\rangle$, respectively. Negative values prove the detection of genuine tripartite entanglement.

By permutation of qubits according to the symmetry of $|\mathcal{C}_4\rangle$, we obtain the corresponding states for projective measurements of the qubits in the modes a, b, c . The resulting states are GHZ states independent of the measurement result, as can be seen by the following LU transformations:

$$|\mathcal{C}_3^+\rangle_{abc} = -(\mathbb{1}_a \otimes \mathbb{1}_b \otimes \mathcal{H}_c) |GHZ_3\rangle_{abc}, \quad (6.6)$$

$$|\mathcal{C}_3^-\rangle_{abc} = -(\mathbb{1}_a \otimes \mathbb{1}_b \otimes (\hat{\sigma}_z \cdot \mathcal{H})_c) |GHZ_3\rangle_{abc}. \quad (6.7)$$

The analysis of the three-photon states obtained with this operation is conducted in two steps: We use a witness operator to test the entanglement after a projective measurement on each of the photons. This is followed by a more detailed analysis of the GHZ state obtained by the projective measurement on the photon in mode d .

As the expected state is also a Graph state, an efficient witness for the detection of tripartite entanglement can be constructed using the stabilizer formalism [106]:

$$\begin{aligned} \mathcal{W}_{\mathcal{C}_{abc}^\pm} &= \frac{3}{2} \cdot \mathbb{1}^{\otimes 3} - \hat{\sigma}_x \otimes \hat{\sigma}_x \otimes \hat{\sigma}_z \\ &\quad - \frac{1}{2} (\hat{\sigma}_z \otimes \hat{\sigma}_z \otimes \mathbb{1} \pm \hat{\sigma}_z \otimes \mathbb{1} \otimes \hat{\sigma}_x \pm \mathbb{1} \otimes \hat{\sigma}_z \otimes \hat{\sigma}_x). \end{aligned} \quad (6.8)$$

Again, the witness operators for projection of other qubits can be obtained according to the symmetry of $|\mathcal{C}_4\rangle$. The expectation values can be determined with two measurement settings only, which allows to easily test the entanglement for projections on every single qubit. The results are summarized in table 6.2. Their negative values clearly prove genuine tripartite entanglement for all of the obtained states.

These states are not only tripartite entangled, but are indeed GHZ states. How well this is fulfilled for the observed state is, in the following, exemplarily investigated for the case of a projection of the photon in mode d . To this end, we determine the stabilizer correlations. This allows, in analogy to section 6.2.1, to derive the fidelity to the corresponding GHZ state and a bound on the geometric measure of entanglement. The expectation values observed for the GHZ states' stabilizers are summarized in table 6.3. The fidelities are determined as the average of their absolute values: $F^{\mathcal{C}_3^+} = 0.756 \pm 0.028$ and $F^{\mathcal{C}_3^-} = 0.753 \pm 0.026$.

In order to strictly proof GHZ-type entanglement, the generic entanglement witness is an appropriate tool [89, 92]:

$$\mathcal{W}_{\mathcal{C}_3^\pm}^{GHZ} = \frac{3}{4} \mathbb{1}^{\otimes 3} - |\mathcal{C}_3^\pm\rangle\langle\mathcal{C}_3^\pm|. \quad (6.9)$$

operators	correlation after P_d^+	correlation after P_d^+
(1) $\hat{\sigma}_x \otimes \hat{\sigma}_y \otimes \hat{\sigma}_y$	0.741 ± 0.088	-0.716 ± 0.088
(2) $\hat{\sigma}_y \otimes \hat{\sigma}_x \otimes \hat{\sigma}_y$	-0.639 ± 0.098	0.617 ± 0.088
(3) $\hat{\sigma}_y \otimes \hat{\sigma}_y \otimes \hat{\sigma}_z$	0.692 ± 0.088	0.598 ± 0.086
(4) $\hat{\sigma}_z \otimes \hat{\sigma}_z \otimes \mathbb{1}$	0.985 ± 0.094	0.948 ± 0.081
(5) $\hat{\sigma}_z \otimes \mathbb{1} \otimes \hat{\sigma}_x$	0.661 ± 0.070	-0.744 ± 0.059
(6) $\mathbb{1} \otimes \hat{\sigma}_z \otimes \hat{\sigma}_x$	0.576 ± 0.065	-0.707 ± 0.061
(7) $\hat{\sigma}_x \otimes \hat{\sigma}_x \otimes \hat{\sigma}_z$	0.751 ± 0.090	0.693 ± 0.084
(8) $\mathbb{1} \otimes \mathbb{1} \otimes \mathbb{1}$	1.000 ± 0.035	1.000 ± 0.033
$F^{\mathcal{C}_3^+} = 0.756 \pm 0.028$		$F^{\mathcal{C}_3^-} = 0.753 \pm 0.026$

Table 6.3: The expectation values of the present stabilizer group are the characteristic correlations of the states $|\mathcal{C}_3^\pm\rangle_{abc}$. In this table, the experimentally obtained values are summarized. They were deduced from six measurement settings. The average absolute values give the fidelities of the observed states to the ideal one: $F^{\mathcal{C}_3^\pm}$.

The prefactor of $\frac{3}{4}$ is necessary to exclude detection of W-type states (biseparability is excluded with $\frac{1}{2}$). We find $\text{Tr} \left[\mathcal{W}_{\mathcal{C}_3^+}^{\text{GHZ}} \rho_{abc}^{\mathcal{C}_4} \right] = -0.006 \pm 0.028$ and $\text{Tr} \left[\mathcal{W}_{\mathcal{C}_3^-}^{\text{GHZ}} \rho_{abc}^{\mathcal{C}_4} \right] = -0.003 \pm 0.026$. Thus, the outcomes are only insignificantly negative and we cannot conclusively prove detection of GHZ-type entanglement. Note that the witness criterion is only sufficient and therefore even values greater than zero do not exclude the presence of GHZ-type entanglement. It is likely that an entanglement witness that accounts for the specific $VVVV$ -noise (section 6.1) that is the main influence for the distortion of our state may still detect GHZ-type entanglement in the state.

Further we use the fidelity to estimate a lower bound for the geometric measure of entanglement:

$$E_G(\rho_{abc}^{\mathcal{C}_3^+}) \geq 0.071 \pm 0.017 \quad (6.10)$$

$$E_G(\rho_{abc}^{\mathcal{C}_3^-}) \geq 0.069 \pm 0.015 \quad (6.11)$$

The geometric measure of the ideal GHZ states is $E_G(\mathcal{C}_3^\pm) = 0.5$. Thus, the projective measurement on one photon strongly reduces the geometric measure of entanglement (remember $E_G(\mathcal{C}_4) = 0.75$) for the ideal states causing the lower bound to drop almost to zero. Note that the situation is very different for $|D_4^{(2)}\rangle$ in chapter 7.

Two-qubit subsets

For Cluster states, projective measurements on all except for two qubits can be performed such that an entangled residual state is obtained with certainty. Note that from the permutation symmetry of the state $|\mathcal{C}_4\rangle$ one can conclude that these measurements can be performed on two different types of qubit pairs: Either a pair that leaves the state unchanged under permutation (pairs $\{a, b\}$ or $\{c, d\}$) or a pair that does not (pairs $\{a, c\}$, $\{a, d\}$, $\{b, c\}$, and $\{b, d\}$). A maximally entangled bipartite residual state is obtained by

Projection	Residual State	Fidelity	Log. Negativity	Concurrence
$ HH\rangle_{cd}$	$ \phi^+\rangle_{ab}$	$96.3 \pm 5.4\%$	0.959 ± 0.070	0.757 ± 0.057
$ VV\rangle_{cd}$	$ \phi^-\rangle_{ab}$	$77.2 \pm 3.7\%$	0.629 ± 0.064	0.495 ± 0.037
$ ++\rangle_{bc}$	$(\mathbb{1} \otimes \mathcal{H}) \phi^+\rangle_{ad} = (C_P ++\rangle)_{ad}$	$77.7 \pm 3.1\%$	0.660 ± 0.051	0.503 ± 0.034
$ +-\rangle_{bc}$	$(\mathbb{1} \otimes \mathcal{H}) \psi^+\rangle_{ad} = (C_P +-\rangle)_{ad}$	$77.6 \pm 2.9\%$	0.666 ± 0.048	0.562 ± 0.031
$ -+\rangle_{bc}$	$(\mathbb{1} \otimes \mathcal{H}) \phi^-\rangle_{ad} = (C_P -+\rangle)_{ad}$	$73.6 \pm 3.1\%$	0.582 ± 0.055	0.425 ± 0.034
$ --\rangle_{bc}$	$(\mathbb{1} \otimes \mathcal{H}) \psi^-\rangle_{ad} = (C_P --\rangle)_{ad}$	$80.3 \pm 2.7\%$	0.720 ± 0.042	0.642 ± 0.030

Table 6.4: The states obtained after projection of two photons in $|\mathcal{C}_4\rangle$ are shown. To obtain entangled states, ZZ-basis measurements in modes c and d and XX-basis measurements in modes b and c are performed. For their analysis, we used quantum state tomography (see also figure 6.5) and summarize deduced values like the fidelity to the ideal states and measures of the residing entanglement.

measurements in the Z-basis for the first case and by X-basis measurements for the second one. We restrict ourselves exemplarily to the pairs $\{c, d\}$ and $\{b, c\}$, respectively. The states obtained after the respective projective measurements are summarized in table 6.4. Note that only two measurement results (parallel polarizations) can occur in the first case, while in the latter, all four measurement results occur with equal probability.

We analyze the density matrices of the qubit pairs $\{a, b\}$ and $\{a, d\}$ after the described projective measurements. To this end, a quantum state tomography of the resulting bipartite states is performed. The fidelity is determined, which can also be viewed as a lower bound on the maximal singlet fraction (F_{MSF}). Further, the density matrix allows to retrieve the entanglement measures that were presented in section 2.3, i.e., the concurrence and the negativity for the resulting states (table 6.4).

We observe strong entanglement between any of the resulting qubit pairs. There is a significant difference between the two entangled states observed in the subset $\{a, b\}$. The reason is clearly visible in figure 6.5. The VVVV-noise (section 6.1, page 81) is responsible for a strongly exaggerated $|VV\rangle\langle VV|$ peak in the matrix after projection on $|VV\rangle$ resulting in a strongly reduced quality of the entanglement (figure 6.5 b). The state after projection on $|HH\rangle$ is not at all affected by this (figure 6.5 a). In figure 6.5 c), one example for the subset $\{a, d\}$ is shown (projection $P_{b,c}^{++}$). Here, the influence of the VVVV-noise is not dependent on the measurement result. This kind of projective measurement is the implementation of a measurement based phase gate operation, where (see table 6.4) the state of qubits $\{a, d\}$ after the projection corresponds to the gate output states (for more details see [172]). This should not be confused with the phase gate operation that was implemented directly in 5, where the gate acts directly on the qubits. Here, in contrast, the gate operation is intrinsic to the entanglement of the cluster state and the entangled output photons were created in different processes and have never interacted (see further [171]). This also explains why the entanglement observed in section 5.3.2 is slightly better.

It was explained in section 3.3.3 that maximally connected states can be used for deterministic open destination teleportation. As we can deterministically obtain entangled bipartite states between any pair of parties in the cluster state, this state is as well suited for this task as the GHZ state. Due to the different permutation symmetry, however,

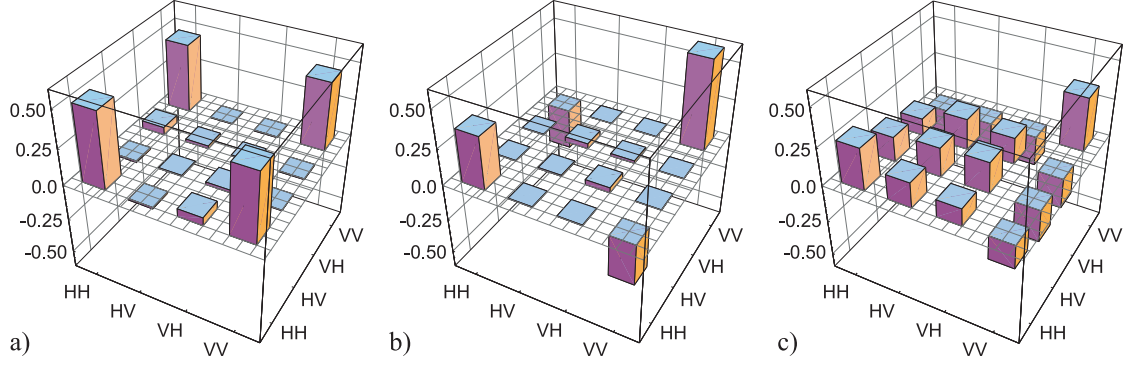


Figure 6.5: Real part of entangled states obtained after projective measurements on two photons of the observed cluster state. Projection of qubits c and d onto $|HH\rangle$ and $|VV\rangle$ are shown in a) and b), respectively. In b) the admixture of $|VV\rangle$ due to incoherent noise is clearly visible. In c) the state after a projection of qubits b and c onto $|++\rangle$ is depicted as one example with the four possible outcomes for this measurement setting. Noise on real and imaginary parts are comparable for all matrices.

the projective measurements have to be adapted to the pair of parties chosen for the teleportation. Using equation 2.38 (page 16) one can conclude that the observed state allows open destination teleportation fidelities (averaged over all input states) between $86.8 \pm 1.5\%$ and $98.2 \pm 2.7\%$ (using equation 2.38), in all cases strongly exceeding the classical limit of $F_{class} = 2/3$ (see section 2.2.4). These values are achieved assuming a perfect Bell state analysis and a single photon as input state.

In summary, it was demonstrated in this section that projective measurements of the experimentally observed cluster state indeed allow for the preparation of highly entangled states in a lower number of qubits. That is, explicitly, GHZ states of three qubits and Bell pairs of two qubits. The latter observation shows that open destination teleportation far beyond the classical limit is possible with the observed state. In the following, the results will be discussed in the light of one-way quantum computation.

6.2.3 Persistency against photon loss

It is a major difference between the cluster and the GHZ states that, in comparison, the entanglement of the latter is much more fragile against photon loss [81] (see section 3.2.1). This persistency of entanglement in the four-photon cluster state is, however, restricted to the loss of a single photon, in contrast to the persistency of the symmetric Dicke states. This will be explored experimentally in the following by first studying residual three- and then two-qubit subsets of the state after photon loss.

Three-qubit subsets

The state after loss of a single photon (exemplarily in mode d) is:

$$\rho_d^{\mathcal{C}_4} = Tr_d[|\mathcal{C}_4\rangle\langle\mathcal{C}_4|] = \frac{1}{2}(|\phi^+H\rangle\langle\phi^+H| + |\phi^-V\rangle\langle\phi^-V|), \quad (6.12)$$

where $|\phi^+H\rangle = |\phi^+\rangle \otimes |H\rangle$ and $|\phi^-V\rangle = |\phi^-\rangle \otimes |V\rangle$. This state is the mixture of two states of the form $|AB\rangle|C\rangle$. Thus, no genuine tripartite entanglement is present

Mode i	$\langle \mathcal{W}_{\rho_i^{c_4}} \rangle$
a	-0.570 ± 0.057
b	-0.639 ± 0.058
c	-0.609 ± 0.058
d	-0.648 ± 0.057

Table 6.5: Expectation values of three-qubit entanglement witness. The negative values prove entanglement in the residual state after loss of one qubit from $|\mathcal{C}_4\rangle$.

any more. The pair AB of photons, however, contains the entanglement that survived the measurement on photon d . It can be verified by a type of witness that was constructed to detect entanglement in subsets of up to four qubits that are part of a cluster state [105, 130]:

$$\mathcal{W}_{\rho_d^{c_4}} = \mathbb{1}^{\otimes 3} - \hat{\sigma}_z \otimes \hat{\sigma}_z \otimes \mathbb{1} - \hat{\sigma}_x \otimes \hat{\sigma}_x \otimes \hat{\sigma}_z, \quad (6.13)$$

where the witnesses for loss of the other qubits can simply be derived by permutation of the qubits according to the symmetry of $|\mathcal{C}_4\rangle$. The fact that only two settings are necessary allowed to easily study all four three-qubit subsets. The experimentally obtained expectation values are summarized in table 6.5. The negative values clearly prove that entanglement in the state after loss of one qubit is present and therefore verify the entanglement persistency in the observed cluster state.

Two-qubit subsets

For the study of the entanglement after loss of a second qubit we take again advantage of the symmetry properties of the observed and the ideal cluster state. As before, we distinguish two different cases: Loss of a pair of qubits that can ($\{a, b\}$, $\{c, d\}$) or cannot ($\{a, c\}$, $\{a, d\}$, $\{b, c\}$, $\{b, d\}$) be permuted without changing the state.

Consider the loss of a second qubit from the state in equation 6.12, for example from modes a or c :

$$\begin{aligned} Tr_{cd} [|\mathcal{C}_4\rangle\langle\mathcal{C}_4|] &= Tr_c \left[\frac{1}{2} (|\phi^+H\rangle\langle\phi^+H| + |\phi^-V\rangle\langle\phi^-V|) \right] \\ &= \frac{1}{2} (|\phi^+\rangle\langle\phi^+| + |\phi^-\rangle\langle\phi^-|) = \frac{1}{2} (|HH\rangle\langle HH| + |VV\rangle\langle VV|), \\ Tr_{bd} [|\mathcal{C}_4\rangle\langle\mathcal{C}_4|] &= Tr_b \left[\frac{1}{2} (|\phi^+H\rangle\langle\phi^+H| + |\phi^-V\rangle\langle\phi^-V|) \right] \\ &= \frac{1}{2} \left(\frac{\mathbb{1}}{2} \otimes |H\rangle\langle H| + \frac{\mathbb{1}}{2} \otimes |V\rangle\langle V| \right) = \frac{\mathbb{1}^{\otimes 2}}{4} \end{aligned} \quad (6.14)$$

The latter case is not very surprising: The loss of one photon from the entangled pair in the residual state of equation 6.15 results in complete disentanglement. The first case is, however, more instructive. The loss of the qubit that is not entangled with the others leads also to complete disentanglement. This is one of the puzzling features of mixed state entanglement. Here, the loss of classical correlation between the third qubit and the Bell

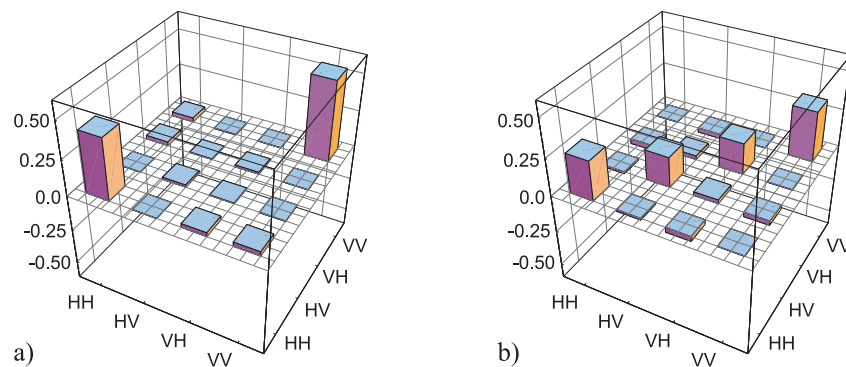


Figure 6.6: Real part of entangled states after loss of the photons in modes b, c and c, d are depicted in a) and b), respectively. Two different kinds of noise are obtained: strongly classically correlated noise in a) and approximately white noise in b).

state present in the entangled pair leads to mixing of the respective Bell states and thus to complete cancellation of coherence.

In order to study the loss of entanglement for the bipartite states experimentally, we cannot rely on tools like entanglement witnesses. The reason is that a positive expectation value of an entanglement witness is only a necessary, but not sufficient criterion for a state to be separable (see section 2.3.4). Instead, the tool of choice here is the Peres-Horodecki criterion, as it is necessary and sufficient in the two-qubit case. For the two different types of qubit pairs existing due to the symmetry of the cluster state (equation 6.14 and equation 6.15) we study exemplarily remaining states in the pairs $\{a, b\}$ and $\{a, c\}$. Note that we can expect similar results for pairs that are obtained by permuting the indices with S_{bacd} and S_{abdc} , as these symmetries were shown to be fulfilled very well in the experiment.

Two independent measurements give the density matrices of the respective photon pairs: $\rho_{ab}^{C_4}$ and $\rho_{bc}^{C_4}$. Their real parts are shown in figure 6.2.3, (the imaginary parts are negligible). In a) the correlated noise (equation 6.14) is clearly visible and hardly any coherence is left. The smallest eigenvalue of the partially transposed matrix (PTM) is $\lambda_{min} = -0.024 \pm 0.028$ and therefore consistent with the theoretical value of 0, demonstrating that the residual state contains virtually no entanglement. In b) completely white noise was expected (equation 6.14). Experimentally we still see a slightly enhanced VV contribution which is explainable by the $VVVV$ -noise (section 6.1). Further, there is a not clarified HH enhancement. Important, that hardly any coherence is left between any of the populations (the imaginary part is negligible, except for one entry of 0.067). For this state, we can conclusively prove that the state is indeed disentangled: The smallest eigenvalue of the PTM is $\lambda_{min} = 0.159 \pm 0.011$ (theoretically 0.25).

6.3 Summary

In conclusion, a setup for the experimental observation of a four-photon cluster state was presented, followed by a detailed analysis of the obtained quantum state conducted solely with efficient, non-tomographic tools. Thereby, it was possible to show that the observed

state exhibits qualitatively the same properties as the state $|\mathcal{C}_4\rangle$. A quantitative model that accounts for the known imperfections of the controlled phase gate and for higher order emissions of the SPDC sources showed good agreement with the experimental data and allows a detailed explanation of the deviations from the ideal state. The major source of noise is thereby caused by imperfect interference in the controlled phase gate, resulting in an admixture of the state $|VVVV\rangle\langle VVVV|$.

In the experiment, a fidelity of the observed state to $|\mathcal{C}_4\rangle$ of $74.1\pm 1.3\%$ is obtained. The close relation to the SLOCC-family G_{abcd} was demonstrated by the detection of high local von Neumann entropies and genuine four-partite entanglement in the state. The cluster state exhibits, in contrast to the other four-qubit graph state $|GHZ_4\rangle$, persistency against the loss of one qubit (but not two) [33], which could also be verified experimentally. In the first case, bipartite entanglement can be detected, while it has disappeared in the latter. As a graph state, the cluster state is further characterized by a high connectedness, i.e. entanglement of all qubits after certain projective measurements. This property is also present in the experiment: Firstly, genuine tripartite entanglement after projection of one photon was detected via entanglement witnesses for the remaining groups of three photons; a more detailed analysis in one case results in a fidelity of about 75% to the GHZ state, which is just at the border to prove that the entanglement is indeed GHZ_3 -type. An entanglement witness that is better tailored to our specific noise ($VVVV$ -noise) might be able to give a conclusive proof. Also two projective measurements leave the remaining two pairs of photons in highly entangled states, where the detected Bell state depends on the measurement result (which is in contrast to what we observe for $|D_4^{(2)}\rangle$ in the next chapter). As the observed state was shown to exhibit almost the same permutation symmetry as $|\mathcal{C}_4\rangle$, similar results can be expected for other residual photon pairs. With these results we could conclude the feasibility of non-classical open destination teleportation with the experimental cluster state as resource.

7 The symmetric Dicke state with two excitations

In the following chapter, the first experimental observation and analysis of the symmetric Dicke state with two excitations $|D_4^{(2)}\rangle$ is presented. The experimental setup is inspired by the symmetry of the state under all permutations of qubits: It relies on the symmetric distribution of four photons, which are created via collinear SPDC, onto four spatial modes. The setup allows to observe the state $|D_4^{(2)}\rangle$ without any additional interference effects, which is an advantage for its stability and thus for the quality of the observed state.

With the count rates achieved, it is possible to obtain a complete tomographic set of measurement data and to derive the experimentally observed state's density matrix. This allows to directly compare the observed with the ideal state and ensures that any quantity characterizing the state is in principle calculable. For the further characterization, we rely, in analogy to the last chapter, completely on efficient, non-tomographic tools¹. Thus, the obtained results can, in general, be deduced from smaller sets of measurement data, and in addition, comparability between the results deduced for the two observed quantum states is ensured.

We investigate general properties of the observed state, i.e. genuine four-qubit entanglement, local entropy and permutation symmetry. Further, we focus on the analysis of tri- and bipartite states after projection or loss of photons. Especially here, differences to other quantum states can be found: It will be shown that $|D_4^{(2)}\rangle$ has a higher persistency against loss of photons than the cluster state in the sense that even after loss of two qubits entanglement is observed. The quantitative analysis of the latter also serves to delimit the observed state from W_4 -states. It will further be demonstrated that, depending on the orientation of the measurement on one photon, the remaining photons are projected to the two SLOCC-inequivalent classes of genuine tripartite entanglement, i.e. the GHZ_3 - and W_3 classes. Finally, the applicability of the experimental state as resource in quantum communication protocols is discussed.

7.1 Experimental setup

The symmetric Dicke state with two excitations $|D_4^{(2)}\rangle$ is a superposition of the six possibilities to distribute two horizontally and two vertically polarized photons onto four modes:

$$|D_4^{(2)}\rangle = \sqrt{\frac{1}{6}}(|HHVV\rangle + |HVHV\rangle + |HVVH\rangle + |VHHV\rangle + |VHVH\rangle + |VVHH\rangle). \quad (7.1)$$

¹In contrast to evaluating the data from a fitted physical density matrix; see the discussion in section 4.3.4.

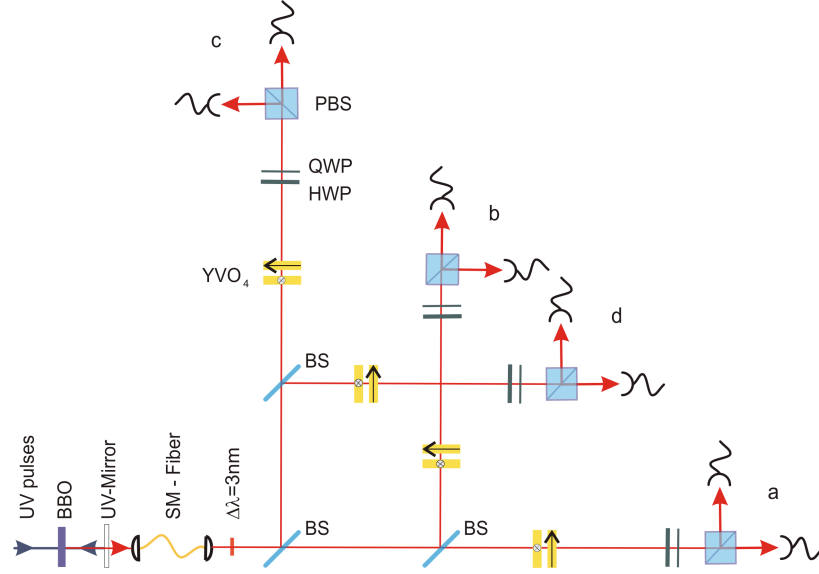


Figure 7.1: Experimental setup for the observation of the four-photon polarization-entangled state $|D_4^{(2)}\rangle$. It is detected after the symmetric distribution of four photons onto spatial modes a , b , c , and d via non-polarizing beam splitters (BS). The photons are obtained from type-II collinear spontaneous parametric down conversion (SPDC) in a 2 mm β -Barium Borate (BBO) crystal pumped by 600 mW UV-pulses. The phases between the four output modes are set via pairs of birefringent Yttrium-Vanadate-crystals (YVO₄). Half- and quarter-wave plates (HWP, QWP) together with polarizing beam splitters (PBS) are used for the polarization analysis.

Thus, we create for its observation four indistinguishable photons in one spatial mode, two are horizontally and two vertically polarized, and distribute them with polarization independent beam splitters (BS) onto four modes (figure 7.1) [181]. If one photon is detected in each of the four output modes, we observe the state $|D_4^{(2)}\rangle$.

As photon source, we use the collinear type-II SPDC as described in section 4.1.1. It creates probabilistically, in second order emission, the desired four photons with appropriate polarizations. In order to separate the emission at 780 nm from the 390 nm pump beam, we use two dichroic UV-mirrors at an angle of incidence of 180° and a transmittivity at IR of about 99%. A half-wave plate together with a 1 mm thick BBO crystal compensate for walk-off effects. We exactly define the spatial mode by coupling the four photons into a single mode fiber. Spectral filtering is achieved with one interference filter ($\Delta\lambda = 3$ nm) at the fiber output. In order to split the four photons we use the type of polarization independent BSs that were introduced in section 4.2. With their polarization independent but unequal ratio between transmission T and reflection R of $T/R \approx 1.5$ we achieve a probability to distribute four photons onto four spatial modes of:

$$\binom{4}{2} T^2 R^2 \cdot (2TR)^2 = 24T^4 R^4 \approx 7.96\%. \quad (7.2)$$

For the ideal splitting ratio of $T/R = 1$ one would expect a probability of 9.38%. These beam splitters also introduce undesired additional phases between horizontal and vertical

polarization. To compensate the phases, we use strongly birefringent Yttrium-Vanadate crystals (YVO_4) as phase shifters (see section 4.2.1). They are mounted with exchanged fast and slow axes with respect to each other such that one crystal compensates dispersion effects of the other.

With the presented setup we achieve a count rate of approximately 60 counts/min, which is about a factor of 30 times higher than for the cluster state. The setup is stable over several days. It is mainly limited by disalignment effects in the pump laser system, which affects rather the count rate than the quality of the observed state.

7.2 Experimental analysis

The high count rate and stability allows to add one ingredient to the state analysis: It allowed to obtain a complete tomographic set of measurement data in one run of 35 h (for 81 measurement settings) and therefore to derive the density matrix of the observed state (section 4.3.2). This ensures that any functional (e.g. entanglement measure) that is developed for state characterization in the future can be calculated for our data. It was discussed in section 4.3.2 that linear tomography often leads to unphysical density matrices due to Poissonian counting statistics. This can be circumvented by fitting the data to a general physical state, where there are still differing opinions on the right approach for such optimizations. All values that we evaluate here can be calculated from the data directly, where we take account for the statistical errors (which make the state unphysical) with a proper error calculation, instead of deriving the values from a fitted physical density matrix. In analogy to the evaluation of the cluster state in the last chapter we thereby rely on non-tomographic tools where usually only a smaller part of the data is required. This approach has the additional advantage of allowing a good comparability between the observed cluster and Dicke state.

The analysis of the observed state is structured in three parts: Global properties of the state are studied in the beginning. We use an efficient entanglement witness that is based on the complete permutation symmetry of $|D_4^{(2)}\rangle$ to detect four-partite entanglement. Whether the symmetry properties are fulfilled in the observed state is further studied explicitly with the methods presented in section 3.3.1. An analysis of the local entropy makes the connection to the SLOCC-family of the state. The density matrix of the state is derived and deviations from the expected matrix are discussed. These are further quantified by the fidelity, which also allows conclusions on the geometric measure of entanglement. In the second part, the connectedness of the observed Dicke state is analyzed. Here, an interesting property of $|D_4^{(2)}\rangle$ arises: A single projective measurement can be used to obtain a residual GHZ_3 -type or W_3 state deterministically. Further, the experimental state's applicability for open destination teleportation from the point of view of two-qubit connectedness is discussed. Finally, in the third part, the persistency against photon loss is analyzed. As argued in section 3.2.2, Dicke states are in general highly persistent against photon loss. We study this property for the experimentally observed state, where a focus is put on the comparison with the four-qubit W_4 state. Further, the related issue of experimental applicability of the state for quantum telecloning is discussed.

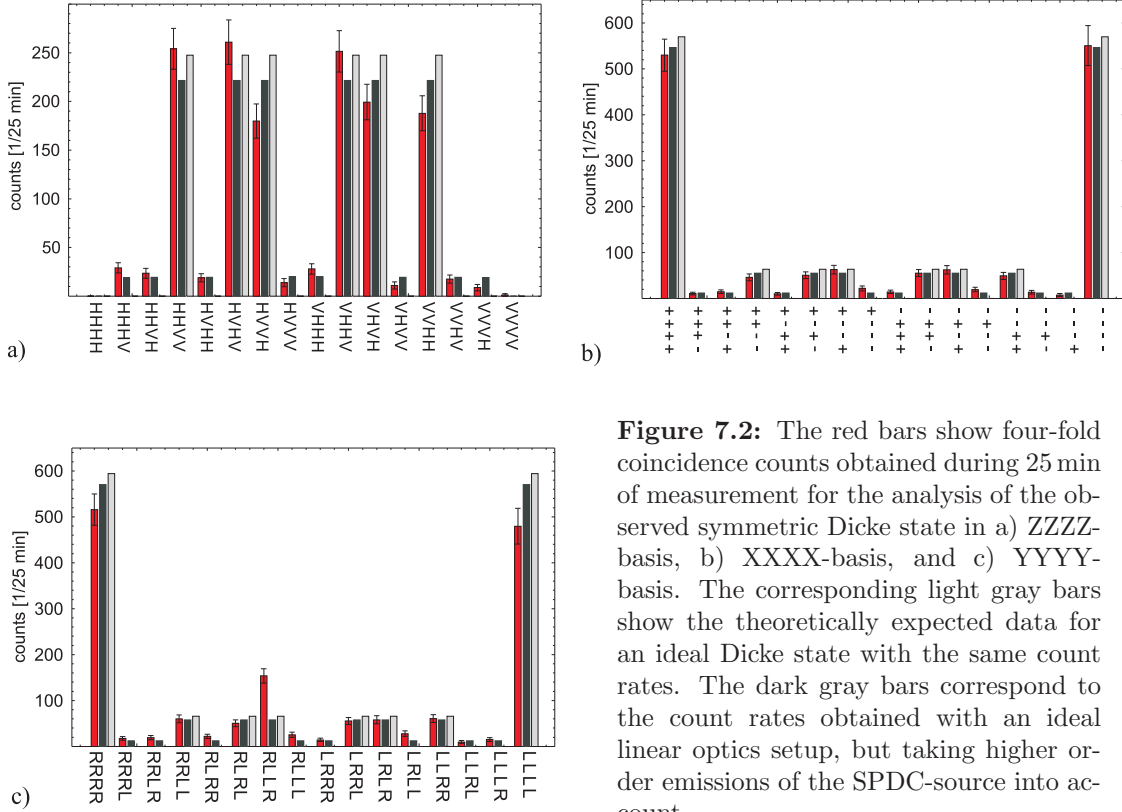


Figure 7.2: The red bars show four-fold coincidence counts obtained during 25 min of measurement for the analysis of the observed symmetric Dicke state in a) ZZZZ-basis, b) XXXX-basis, and c) YYYY-basis. The corresponding light gray bars show the theoretically expected data for an ideal Dicke state with the same count rates. The dark gray bars correspond to the count rates obtained with an ideal linear optics setup, but taking higher order emissions of the SPDC-source into account.

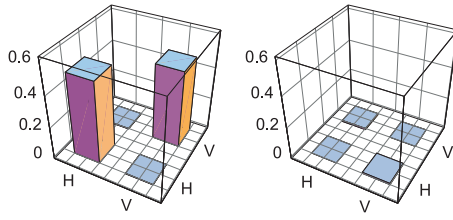
7.2.1 Global properties

Population and Coherence

The state $|D_4^{(2)}\rangle$ exhibits a characteristic six-term structure in the computational basis. We first analyze the counting statistics we observe in this case experimentally. Then, coherence between the different terms can be demonstrated by an analysis of the state in the XXXX- and YYYY-basis, where the structure of $|D_4^{(2)}\rangle$ is dominated by GHZ-like contributions (equation 3.24). In figure 7.2, the experimentally observed counting statistics for these measurement bases are shown (red bars). For comparison, the outcome of an ideal Dicke state with the same total count rate is depicted (light gray). Furthermore, the simulated results for an ideal setup, when higher order emissions of the down conversion are taken into account, is shown (dark gray).

Experimentally, the expected six term structure is clearly visible (figure 7.2 a). The small, undesired contributions can be mainly attributed to noise from higher order emissions of the SPDC-source, as a comparison with the simulated results reveals. The structure in the six peaks, where three terms are slightly stronger than the others could not be conclusively explained, might, however, be caused by a not perfectly polarization independent beam splitter.

Coherence between the contributions are made visible by the counting statistics in the XXXX- and YYYY-basis (figure 7.2 b) and c). The expected statistics is reproduced



Qubit	Entropy
a	0.999 ± 0.004
b	0.999 ± 0.004
c	0.999 ± 0.004
d	0.999 ± 0.004

Figure 7.3: Analysis of the local entropy in the observed symmetric Dicke state. On the left, the single qubit density matrix of photon a is depicted, looking, apart from slight coherence, like white noise. The table on the right shows the von Neumann entropy of the four qubits, confirming that the single qubits are practically unpolarized – a signature of entanglement if the whole state is not completely mixed.

very well for both bases (apart from the unexplained enhanced $|RLLR\rangle$ contribution in c). The small additional contributions can, as a comparison with the simulation shows, be explained by higher order emission events of the source. Note that the measurement in only one of these bases mimics a noisy GHZ_4 state (as expected from equation 3.24). This demonstrates that the mere similarity of two states in the counting statistics of one measurement basis does not indicate similarity of the complete states, as the Dicke state and the GHZ_4 state exhibit, as we will see, extremely different properties.

Entanglement Detection

The state $|D_4^{(2)}\rangle$ is genuinely four-partite entangled. To test this property also for the observed state, we use the symmetry based entanglement witness that was discussed in section 3.2.2 (equation 3.17). It relies only on two collective, non-local operators, which can be deduced from two measurement settings (section 3.2.2). In the four-qubit case, the witness is [127, 128]:

$$\langle \mathcal{W}_4^s \rangle = \langle J_x^2 \rangle + \langle J_y^2 \rangle \leq 7/2 + \sqrt{3} \approx 5.23, \quad (7.3)$$

where $|D_4^{(2)}\rangle$ reaches the maximal value of 6. With the correlations of the measurements presented in figure 7.2 we find:

$$\text{Tr}[\mathcal{W}_4^s \rho^{D_4^{(2)}}] = 5.58 \pm 0.02, \quad (7.4)$$

which is exceeding the required bound by 17.5 standard deviations. Thus, also the observed Dicke state was indeed detected as genuinely four-partite entangled.

Local Entropy

In section 3.1, we have seen that the state $|D_4^{(2)}\rangle$ belongs (like $|\mathcal{C}_4\rangle$) to the SLOCC-family G_{abcd} (equation 3.10), which is characterized by maximal local entropy [24]. To study the local entropy in the experimentally observed state, the density matrix of a single photon after tracing over the other three is calculated. Basically, the three measurements shown in figure 7.2 are sufficient for this evaluation. We use, however, the complete set of data that was obtained for the quantum state tomography. In figure 7.3, the real and imaginary

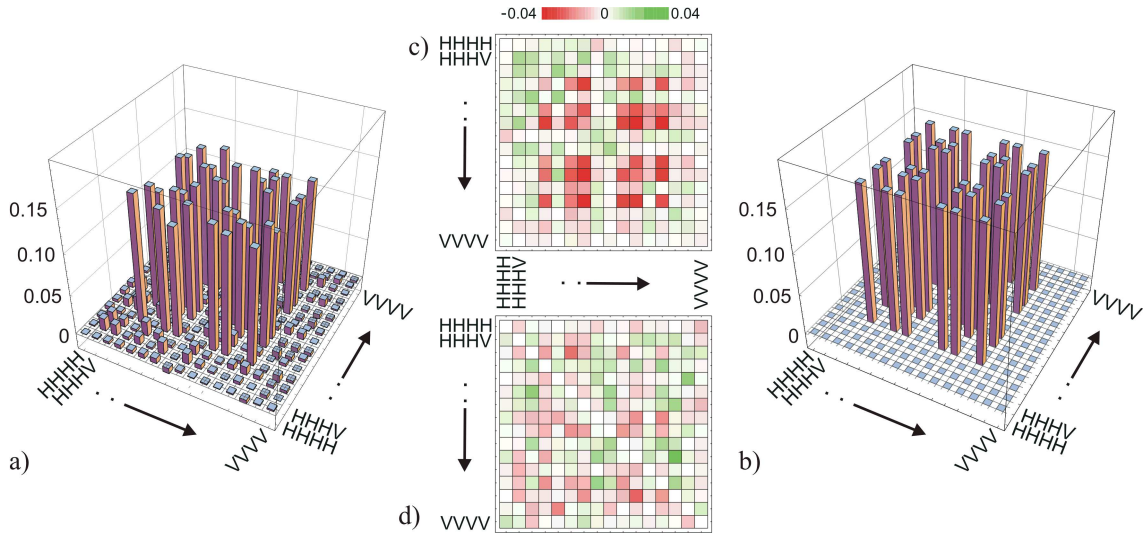


Figure 7.4: Real part of the density matrix of the experimentally observed Dicke state (a). Six characteristic terms are visible in the diagonal; the off-diagonal terms show coherence between all populations. The ideally expected state $|D_4^{(2)}\rangle$ is shown in b). For better comparison, a density plot of the difference between the density matrices is depicted in c) (real part) and d) (imaginary part). The imaginary part of the ideal matrix is zero everywhere.

part of the density matrix of the photon in mode a is depicted on the left side, showing completely white noise. This observation is confirmed for all four qubits in the table on the right, where the local von Neumann entropies of all four photons are shown. All von Neumann entropies are consistent with the maximum value of one, demonstrating that the property of maximal local entropy is practically perfectly fulfilled in the experimentally observed state. Note that the other entangled symmetric Dicke state $|W_4\rangle$ does not exhibit this property (single qubit von Neumann entropy: 0.81).

Quantum state tomography and fidelity

We are interested in a comparison between the observed state and the ideal state $|D_4^{(2)}\rangle$. Their density matrices are depicted in figure 7.4 a) and b). The structure of these matrices is basically the same: six terms in the diagonal and positive coherence between all of them. In order to facilitate the comparison, density plots of the real (c) and imaginary part (d) of the difference between the two matrices are shown. The noise that is visible on the elements expected to be zero is mainly caused by higher order emissions, partly also by imperfect compensation of the birefringence of fiber and beam splitters. Further, a reduction of the off-diagonal elements is visible, which can be attributed to a loss of coherence, probably caused by finite spectral bandwidth. The latter can be improved with narrower filters but at the expense of lower count rates.

To quantify the distance between the observed and the ideal state, the fidelity is calculated. In the evaluation enters (similar to the case of the cluster state) only a restricted set of data, not the complete density matrix. While the state $|D_4^{(2)}\rangle$ is not described by

local stabilizing operators, there are still only 40 non-zero standard correlations. Even when the fidelity is calculated from the matrix in figure 7.4 a) only these 40 correlations enter the evaluation. We find a fidelity of $F^{D_4^{(2)}} = 84.4 \pm 0.8\%$. Thus, the state $|D_4^{(2)}\rangle$ was prepared with an even higher quality than the cluster state. This can be attributed to the simplicity of the experimental setup that does not rely on additional interference. As one of the possible reasons for deviation from the ideal state (mentioned above), we can calculate the influence of higher order emissions from the SPDC-source. With the parameters for the source presented in table 4.1² and assuming an otherwise perfect linear optics setup we find a fidelity of $F \approx 91\%$. Thus, the higher order emissions are indeed identified as a significant source of noise.

The information about the states' fidelity can be used to gain further insights. The corresponding result for the generic witness $\mathcal{W}_{D_4^{(2)}}^g$ [128] for the state $|D_4^{(2)}\rangle$ is:

$$\text{Tr}(\mathcal{W}_{D_4^{(2)}}^g \rho^{D_4^{(2)}}) = \frac{2}{3} - F^{D_4^{(2)}} = -0.177 \pm 0.008. \quad (7.5)$$

Thus, genuine four-partite entanglement could also be deduced from the fidelity, with $\approx 22\sigma$. Note that 21 measurement settings enter this value. Thus, the measurement time using this witness was about 7 times higher than for the detection of four-partite entanglement with $\approx 18\sigma$ using equation 7.4. This shows that the efficiency of the symmetry based witness in equation 7.4 is (for the state observed here) indeed better than the one of the generic witness.

Further, conclusions on the geometric measure of entanglement of the observed state can be drawn. Using equation 2.55 (section 2.3.4, based on [72]) we find:

$$E_G(\rho^{D_4^{(2)}}) \geq 0.235 \pm 0.009, \quad (7.6)$$

where the ideal state reaches a value of $E_G(D_4^{(2)}) = 0.625$. The experimental value does not indicate a higher geometric measure of entanglement than any of the states presented in table 3.2.3, thus cannot be used to delimit the observed state from them. It is, however, potentially useful for comparison with the entanglement observed in future experiments (independent of the type of state created) where this entanglement measure is analyzed.

Symmetry

By definition, the symmetric Dicke state with two excitations is invariant under all permutations of qubits. This is in contrast to the state $|C_4\rangle$ which cannot be transformed into a completely symmetric state.

For an investigation of this property, we follow the analysis method introduced in section 3.3.1 by determining the expectation values of permutation operators. As in the last chapter, this is done for the generators of the complete permutation group:

$$\begin{aligned} \langle S_{bacd} \rangle &= 0.92 \pm 0.02 \quad (1.0), \\ \langle S_{acbd} \rangle &= 0.97 \pm 0.02 \quad (1.0), \\ \langle S_{abdc} \rangle &= 0.94 \pm 0.02 \quad (1.0). \end{aligned}$$

²That means we take the efficiency of the photon creation and imperfect coupling and detector efficiencies into account.

In other words, the probability to project the corresponding qubit pairs into the symmetric subspace is (equation 3.29) at least $96 \pm 1\%$. With the complete set of measurement data at hand, it is also possible to calculate the expectation values for all other permutations, resulting in values close to the maximum of 1 between 0.92 - 0.98 and statistical errors of, at maximum, 0.09. The slight deviations can be interpreted as follows: They can partly be caused by the mentioned imperfections of the SPDC source. As the photons are, however, symmetrically distributed, the fact that the values are not equal can only be explained by minor imperfections in the linear optics setup, e.g. slight polarization dependence of beam splitters or not totally compensated phases.

As a complete set of correlations is known, we can basically calculate any relevant value. Still, it is important to emphasize that 21 measurements would have been sufficient to demonstrate the states symmetry under all permutations. As we have discussed in chapter 6, the analysis of entanglement in subsets of qubits is drastically simplified, when permutation symmetry of the state is demonstrated. This approach is even more efficient for states with a higher number of qubits and especially suited for states that are completely symmetric under permutation of qubits. However, as a complete set of data is available here, the following investigation includes evaluations on all subsets of photons, where only few representative examples are depicted.

7.2.2 Connectedness

It was discussed in chapter 3 that symmetric Dicke states show a very different behavior in comparison with graph states, when qubits are projected. An important insight was that here the resulting entanglement depends on the measurement result and not only on the measurement basis. As will be shown, there are also differences between the states within the family of symmetric Dicke states. In the following, particular properties of the state $|D_4^{(2)}\rangle$ in this respect will be presented. We experimentally analyze the corresponding properties thereby distinguishing the observed state from other quantum states than $|D_4^{(2)}\rangle$.

Three-qubit subsets

Particularly interesting are the states after projection of one photon in horizontal or vertical direction, or in any equally weighted superposition thereof, e.g. the state $|-\rangle$:

$$\begin{aligned} \langle V | D_4^{(2)} \rangle &= \frac{1}{\sqrt{6}}(|HHV\rangle + |H VH\rangle + |VHH\rangle) \\ &= \frac{1}{\sqrt{2}}|W_3\rangle, \end{aligned} \quad (7.7)$$

$$\begin{aligned} \langle - | D_4^{(2)} \rangle &= \frac{1}{\sqrt{12}}(|HVV\rangle + |VHV\rangle + |VVH\rangle - |HHV\rangle - |H VH\rangle - |VHH\rangle) \\ &= \frac{1}{2}(|\bar{W}_3\rangle - |W_3\rangle) = \frac{1}{\sqrt{2}}|G_3^-\rangle. \end{aligned} \quad (7.8)$$

Indices enumerating the qubits were dropped here, because $|D_4^{(2)}\rangle$ is symmetric under permutation of qubits and thus results for projections of any qubit are equal. Other projections in the standard basis lead to similar results (equal up to LU). The first observation

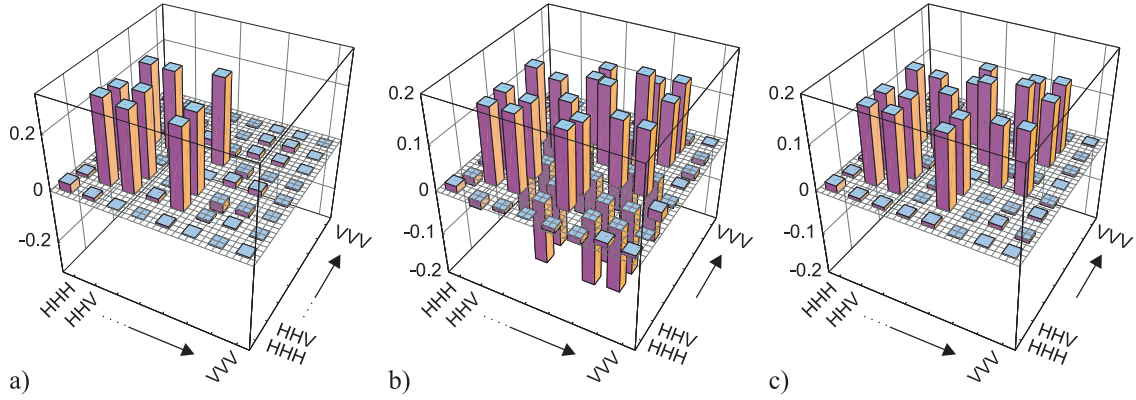


Figure 7.5: Real parts of density matrices for the W state after projection of photon d onto $|V\rangle$ (a), G_3 state after projection of photon d onto $|-\rangle$ (b), and the residual state after loss of photon d (c). The imaginary parts consist of noise only, comparable to the noise in the real part.

is that in both cases genuinely tripartite entangled states are observed (section 3.1.1). This property is quite special and distinguishes the state $|D_4^{(2)}\rangle$ from the states discussed before. In addition, and even more important, note that it was shown in section 3.1.1 that the G_3 state belongs to the GHZ_3 class, because its tangle is $\tau^{G_3} = 1/3$. This means that we can decide by choice of the measurement basis on a single qubit, whether the state $|D_4^{(2)}\rangle$ shall be reduced to a GHZ_3 class or a W_3 state. Neither the GHZ_4 and cluster state, nor the W_4 state have this property.

One can draw more conclusions from this concerning the type of entanglement in the state $|D_4^{(2)}\rangle$. Both, GHZ - and cluster states can be extended to a graph state of a higher particle number by entangling *one* qubit of the state with one additional qubit. For photons this can be realized by the gate presented in chapter 5 or methods presented in [153, 182]. Also W states can be created from W states of a lower number of qubits by symmetrizing an additional qubit with *a single* qubit of the smaller W state (similar to the scheme in [91]). None of these operations can, however, be used to obtain $|D_4^{(2)}\rangle$ from a W_3 - or GHZ_3 state: If any GHZ_3 - or W_3 state could, by an interaction of one additional qubit with one qubit of these states, be extended to $|D_4^{(2)}\rangle$, then a local projective measurement could be used to obtain the respective other kind of state. The ancillary qubit could be transformed back to its original polarization, which would, all together, mean a catalytic transformation of one class to the other, which is impossible as shown in [84]. Therefore, it is also from this point of view very reasonable to consider the entanglement in $|D_4^{(2)}\rangle$ as a different type of entanglement compared to the GHZ_4 -, cluster or W_4 state.

These properties will be studied in the following for the experimentally observed states. Exemplarily, the real parts of the density matrices after projections of the photon in mode d) are shown in figure 7.5 a) and b), for the W_3 and the G_3 -state, respectively. The structure of the two states is nicely seen: Three populations for the W_3 state with equally weighted coherences between them. The G_3 state's matrix shows the same terms but also the corresponding spin flipped ones. The negative off-diagonal terms show the coherence

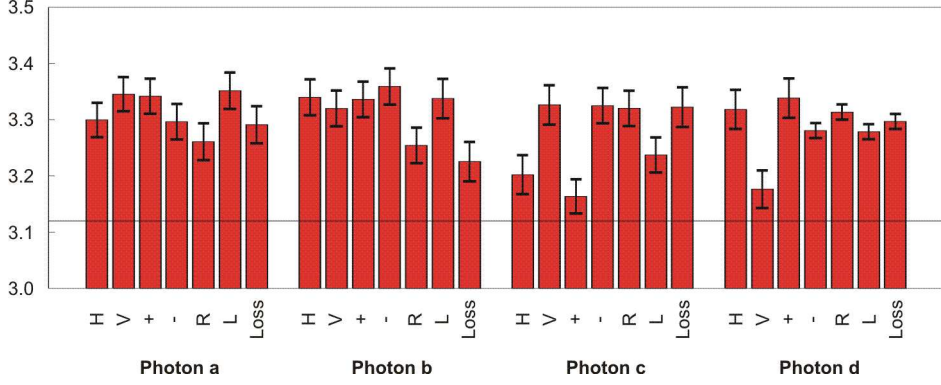


Figure 7.6: The outcomes of the entanglement witness measurements for detection of tripartite entanglement after different operations on each qubit: Projective measurements in the standard bases or qubit loss. Values over 3.12 indicate the detection of genuine tripartite entanglement.

between the W_3 and \overline{W}_3 contribution.

The experimental investigation of the discussed properties will be conducted in three steps: First we demonstrate that the projective measurements indeed result in genuinely tripartite entangled states. Then, it will be shown that the obtained G_3 state indeed exhibits GHZ_3 -type entanglement, which requires a more sophisticated application of an entanglement witness. Finally, we study the W_3 - and the G_3 state in more detail.

In order to demonstrate the tripartite entanglement observed in the state after projective measurements in the X- and Z-basis, we use again the type of entanglement witness in equation 3.17, but with the bound for genuine tripartite entanglement:

$$\langle \mathcal{W}_3^s \rangle = \langle J_x^2 \rangle + \langle J_y^2 \rangle \leq 2 + \sqrt{5}/2 \approx 3.12. \quad (7.9)$$

Note the specific characteristic of this entanglement witness: It can be used with the same bound for any superposition and mixing of the states $|W_3\rangle$ and $|\overline{W}_3\rangle$. All of these states give the optimal expectation value of 3.5. This is in contrast to the generic and the stabilizer witnesses that were used before, which were optimal exclusively for one state. In figure 7.6 the results are summarized for all standard bases (X , Y , and Z), measurement results ($\{H, V\}$, $\{+, -\}$, $\{R, L\}$), and modes (a, b, c, d) where the projection is performed. All resulting states exceed the bound and are thus proved to exhibit genuine tripartite entanglement. The average overall expectation values is 3.30 ± 0.03 .

While being very practical for the detection of genuine tripartite entanglement in general, the witness presented before is not suited to detect GHZ_3 -type entanglement. Thus, we rely on the generic witness for GHZ_3 states to test whether the projection onto $|+\rangle$ and $|-\rangle$ indeed results in GHZ -type entanglement. The witness was used before in equation 3.8 and allows to exclude W_3 class states:

$$\mathcal{W}_{GHZ_3} = \frac{3}{4}\mathbb{1} - |GHZ_3\rangle\langle GHZ_3|. \quad (7.10)$$

This witness is not suited to detect the entanglement in a G_3 state or in the experimentally observed state directly (the corresponding expectation values are positive). It is, however,

possible to optimize it for the observed state by application of local filtering operations (LFO) $\widehat{F} = A \otimes B \otimes C$ [21, 183]. The resulting new witness operator is then $\mathcal{W}' = \widehat{F}^\dagger \mathcal{W}_{GHZ_3} \widehat{F}$. Here A, B and C are 2×2 complex matrices determined through numerical optimization to find the optimal witness for the detected state [184]. Note, that \mathcal{W}' still detects GHZ-type entanglement as \widehat{F} is an SLOCC operation which does not change the entanglement class. In the measurement, GHZ-type entanglement is indeed detected with an expectation value of $Tr(\rho_G \mathcal{W}') = -0.029 \pm 0.023$ showing that the observed state is *not* W_3 class³.

It would be desirable to prove that the state after projections in the Z-basis is W_3 -type. There is, however, no entanglement witness or other means known to us that allows to prove this conclusively. We can, however, study the entanglement in the state obtained after the projective measurement in more detail. Exemplarily, the W_3 state after projection of the photon in mode d onto $|V\rangle$ is analyzed. The density matrix of the corresponding state is shown in figure 7.5 a). Its fidelity to the state $|W_3\rangle$ is 0.882 ± 0.015 . The evaluation of the generic entanglement witness from [89] gives:

$$\mathcal{W}_{W_3}^g = \frac{2}{3} \mathbb{1}^3 - |W_3\rangle\langle W_3|. \quad (7.11)$$

We find $Tr(\mathcal{W}_{W_3} \rho_{W_3}) = -0.222 \pm 0.015$ and the corresponding lower bound on the geometric measure of entanglement $E_G(\rho^{W_3^+}) \geq 0.283 \pm 0.021$. This value already shows that the experimentally observed state is stronger entangled than G_3 states are, with respect to the geometric measure. The fidelity achieved here is slightly above the value (fidelity 0.863 ± 0.018) that can be calculated for the experiment reported in [91, 92], where we observed the W_3 state for the first time. The efficiency of the present setup is, however, much higher with about 30 counts/min compared to about 2 counts/min. It can, for the observation of the state $|W_3\rangle$ even be improved in efficiency by a different choice of beam splitters [181].

Two-qubit subsets

Projective measurements of two qubits in the same measurement basis lead probabilistically to maximal bipartite entanglement between the other two qubits. For the standard bases this is shown in the following calculation:

$$\begin{aligned} \langle HV | D_4^{(2)} \rangle &= \langle VH | D_4^{(2)} \rangle = \sqrt{\frac{1}{6}}(|HV\rangle + |VH\rangle) = \sqrt{\frac{1}{3}}|\psi^+\rangle, \\ \langle +- | D_4^{(2)} \rangle &= \langle -+ | D_4^{(2)} \rangle = \sqrt{\frac{1}{12}}(|HH\rangle - |VV\rangle) = \sqrt{\frac{1}{6}}|\phi^-\rangle, \\ \langle RL | D_4^{(2)} \rangle &= \langle LR | D_4^{(2)} \rangle = \sqrt{\frac{1}{12}}(|HH\rangle + |VV\rangle) = \sqrt{\frac{1}{6}}|\phi^+\rangle. \end{aligned}$$

Thus, all symmetric Bell states can be prepared when orthogonal measurement results are found for XX-, YY- and ZZ-measurements. In the latter case, the probability is $2/3$, for the other two $1/3$ ⁴. Thus, we can *choose the Bell state* that we want to obtain, but

³For the evaluation of this witness we need the complete set of data of the observed G_3 state.

⁴Because detection of $|HV\rangle$ and $|VH\rangle$ lead to the same results. The same is valid for $|+-\rangle/|-\rangle$ and $|RL\rangle/|LR\rangle$.

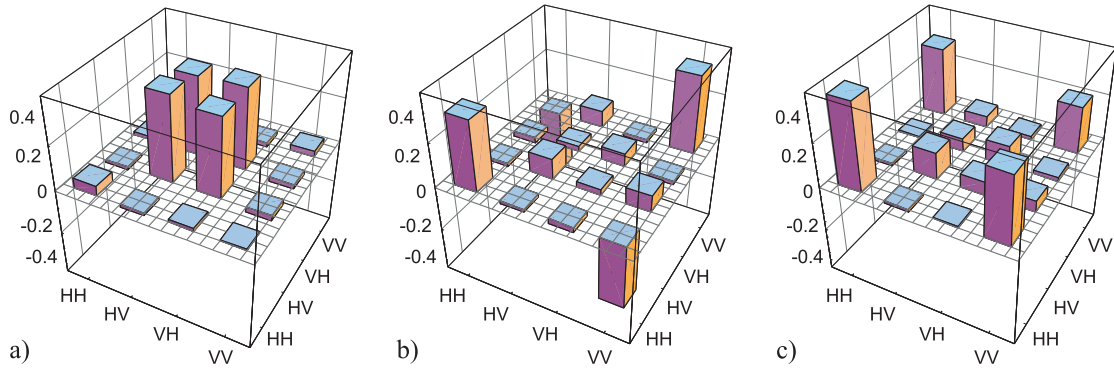


Figure 7.7: The density matrices of the state of photons in modes b and c after detection of orthogonal polarizations in modes a and d . In a), $|\psi^+\rangle$ is observed after projection onto $|HV\rangle$, in b) $|\phi^-\rangle$ is observed after projection onto $|+-\rangle$, and in c) $|\phi^+\rangle$ is observed after projection onto $|RL\rangle$.

its preparation is probabilistic. Remember the property of the cluster state: There, we can choose to prepare some Bell state deterministically, but which Bell state exactly is obtained is probabilistic.

In figure 7.7, the density matrices for the three cases (with projections on photons in modes a and d) are depicted, illustrating qualitatively the expected behavior. One can clearly identify the density matrices of states close to $|\psi^+\rangle$ for a projection onto $|HV\rangle$ (a), to $|\phi^-\rangle$ for a projection onto $|+-\rangle$ (b), and to $|\phi^+\rangle$ for a projection onto $|RL\rangle$ (c). In order to quantify these observations, the following table shows the achieved fidelity to the respectively expected states, their logarithmic negativity, and the concurrence for the three bases and averaged over all qubit pairs and measurement results:

	Fidelity	E_{LN}	C
HV	0.89 ± 0.03	0.85 ± 0.04	0.77 ± 0.03
$+-$	0.74 ± 0.04	0.62 ± 0.07	0.50 ± 0.04
RL	0.73 ± 0.04	0.60 ± 0.07	0.48 ± 0.04

The given errors are the averaged values of the single errors, which are approximately equal for the whole set of data. In addition, figure 7.8 shows a histogram of all achieved values. We see that there are two groups of data. The entangled state after projections in the XX - and YY -bases all give approximately the same value for the observed entanglement. They exhibit fidelities that allow teleportation fidelities exceeding the classical bound⁵. The entanglement is even higher for projections in ZZ -basis. The reason is that the photons are emitted with the "right" polarizations in the computational basis, independent of the coherence between the photons. Thus, the quality of the entangled state after a ZZ -basis measurement is determined only by the coherence between the residual photon pair. For measurements that are not in the standard bases, also the entanglement between the projected and the residual photons influences the quality of the obtained states leading to a stronger reduction of the quality. Altogether, the presented data shows that the

⁵The fidelity to a certain Bell state is a lower bound to F_{MSF} , which is the fidelity to the closest Bell state. The relation between F_{MSF} and the average teleportation fidelity is given in equation 2.38.

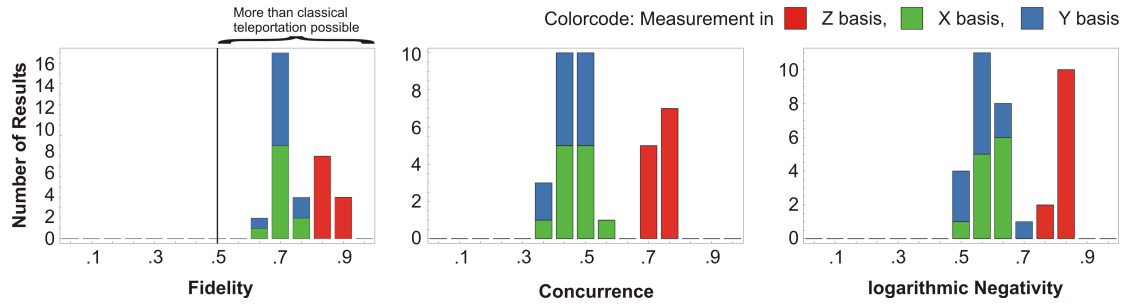


Figure 7.8: The fidelity, logarithmic negativity, and concurrence of the entangled states after detection of orthogonal polarizations on two qubits are summarized. The highest entanglement and the best fidelity is observed for the ZZ-measurements (red). Also in the other standard bases we observe entanglement and a fidelity higher than 0.5, necessary to reach an average teleportation fidelity beyond the classical limit.

observed Dicke state indeed allows to tailor the entangled states of one photon pair via projective measurements on the other.

The fact that it is probabilistically possible to make two projective measurements such that the two residual qubits are maximally entangled can, as mentioned in section 3.3, be used to establish an open destination protocol (ODT, see figure 3.5 b). Note that here, in contrast to the ODT-protocols for the cluster and the GHZ_4 states section 6.2.3, the protocol works only probabilistically. With the experimentally prepared state, there are two reasons to purely rely on projection onto the ZZ-basis: higher probability of success and a better quality of the resulting state. The corresponding fidelities for an open destination teleportation from any sender to any receiver are between $0.938 \pm .014$ and $0.954 \pm .014$ for a perfect Bell state analysis (calculated with equation 2.38 and starting from the fidelity to the observed state). Thus, while the protocol is, in contrast to the cluster state ODT, only probabilistic, the quality that can experimentally be achieved is higher.

Here, the fact that two parties can probabilistically prepare a particular Bell state for the other parties is not used for the ODT protocol. It may hold, however, a high potential for application in multiparty quantum cryptography because the parties sharing the Bell state can only use it as soon as the other parties broadcast the measurement basis they used.

7.2.3 Persistency against photon loss

As a symmetric entangled Dicke state, $|D_4^{(2)}\rangle$ exhibits a strong entanglement persistency against qubit loss. Accordingly, the corresponding experimentally observed residual states will be studied, leading to interesting possibilities to discriminate the state from GHZ_4 , cluster and W_4 states.

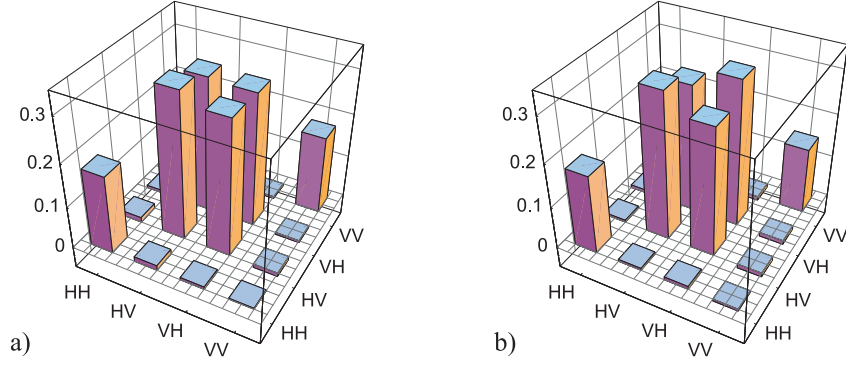


Figure 7.9: Real parts of the density matrices after loss of two photons. In a), photons b and c are lost, in b) photons c and d . In both cases, the same (non-maximally) entangled state is observed.

Three-qubit subsets

Remarkably, even the loss of a photon leaves the residual state genuinely tripartite entangled:

$$\text{Tr}_d \left[|D_4^{(2)}\rangle \langle D_4^{(2)}| \right] = \frac{1}{2} (|W_3\rangle + |\bar{W}_3\rangle). \quad (7.12)$$

This state is an equally weighted mixture between $|W_3\rangle$ and $|\bar{W}_3\rangle$ looking like a three-qubit entangled state in this particular decomposition. Yet, a separable decomposition might exist. That it is indeed tripartite entangled can be shown with the same entanglement witness as used for the analysis after projective measurements (equation 7.9). The ideal state reaches an expectation value of 3.5. In figure 7.6 the values achieved for the entanglement witnesses after tracing out each of the four single photons in the experiment are summarized together with the corresponding values after projective measurements. All values clearly exceed the bound of 3.12, showing that the residual three-photon states are indeed genuinely tripartite entangled. Exemplarily, the corresponding output state after loss of one qubit is shown in figure 7.5. We observe the contributions of W_3 and \bar{W}_3 without any further coherences, in contrast to the G_3 state (figure 7.5 b).

Note that it was discovered only very recently that the state we obtain after tracing out one qubit from $|D_4^{(2)}\rangle$ (equation 7.12) exhibits a very special type of correlations: It is multipartite entangled but has no multipartite classical correlations [185].

Tripartite entanglement after qubit loss is a property that neither the GHZ_4 nor the cluster state possess. It was argued in chapter 3 that entangled symmetric Dicke states exhibit this property: The W_3 state also exhibits tripartite entanglement after qubit loss, even though it is of a different kind. Note, that also the state $|\Psi^{(4)}\rangle$ (section 3.2.3) still exhibits some tripartite entanglement after qubit loss [83], which can be detected with the same entanglement witness as used before ($\text{Tr} [W_3^s | \Psi^{(4)}\rangle \langle \Psi^{(4)}|] = 3.17 > 3.12$, equation 7.9).

Two-qubit subsets

As we have seen in chapter 6, the entanglement in the two graph states is not persistent against two-qubit loss. Therefore, we focus in the study of bipartite entanglement after

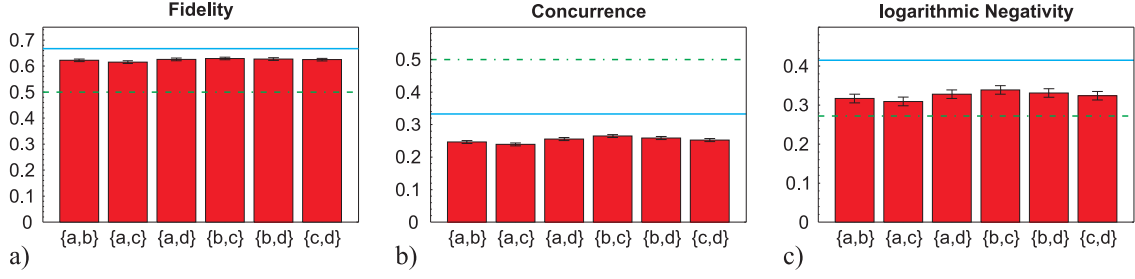


Figure 7.10: Analysis of the persistency against photon loss using different quantities: For loss of the six different pairs of photons, the experimentally obtained values for the fidelity, the concurrence, and the logarithmic negativity are shown. In each figure, the dashed line indicates the value achieved by an ideal state $|W_4\rangle$ and the solid line by the ideal state $|D_4^{(2)}\rangle$. Note that the persistency of the experimentally observed state is, concerning the logarithmic negativity and the maximal singlet fraction, higher than the entanglement persistency of $|W_4\rangle$.

tracing out two qubits mainly on a comparison of our Dicke state with $|W_4\rangle$. A quantitative comparison reveals hereby interesting differences between $|D_4^{(2)}\rangle$ and $|W_4\rangle$ that allow to distinguish between them.

In the state $|D_4^{(2)}\rangle$, the loss of a second qubit also leaves the residual two qubits entangled:

$$\rho_{ij}^{D_4^{(2)}} = \text{Tr}_{ij} [|D_4^{(2)}\rangle\langle D_4^{(2)}|] = \frac{2}{3} |\psi^+\rangle\langle\psi^+| + \frac{1}{6} (|HH\rangle\langle HH| + |VV\rangle\langle VV|). \quad (7.13)$$

Due to the permutation symmetry of $|D_4^{(2)}\rangle$, the resulting state is independent of which qubits i, j have been lost.

The state $|W_4\rangle$ has also a high entanglement persistency against the loss of two qubits:

$$\rho_{ij}^{W_4} = \text{Tr}_{ij} [|W_4\rangle\langle W_4|] = \frac{1}{2} (|\psi^+\rangle\langle\psi^+| + |HH\rangle\langle HH|). \quad (7.14)$$

W states are often taken as *the* example for a state exhibiting high persistency against photon loss [23, 92, 186]. Indeed, the concurrence of the W_4 state ($C(\rho_{ij}^{W_4}) = 1/2$) is higher than for the residual state of $|D_4^{(2)}\rangle$ ($C(\rho_{ij}^{D_4^{(2)}}) = 1/3$). In contrast, however, the maximal singlet fraction F_{MSF} of the residual qubit pairs is higher for the state $|D_4^{(2)}\rangle$: $F_{MSF}(\rho_{ij}^{W_4}) = 1/2$ and $F_{MSF}(\rho_{ij}^{D_4^{(2)}}) = 2/3$ [127]. The value $2/3$ is actually the maximally achievable after loss of two qubits from a pure four-photon state when all qubit pairs are taken into account [143]. Yet, this quantity is not an entanglement monotone (section 2.3) despite of the fact that it quantifies the teleportation fidelity of a state. It is interesting to make the comparison also with the logarithmic negativity: $E_{LN}(\rho_{ij}^{W_4}) \approx 0.272$ and $E_{LN}(\rho_{ij}^{D_4^{(2)}}) \approx 0.415$. Thus, also with respect to the negativity, the persistency of $|D_4^{(2)}\rangle$ is higher than the persistency of $|W_4\rangle$. Therefore, a statement about the state exhibiting maximal entanglement persistency depends strongly on the chosen measure of entanglement!

The residual two-photon state we obtained experimentally in modes a and d after loss of the other two photons is depicted in figure 7.9 a); correspondingly for modes a and b in figure 7.9 b). Coherence between the populations with orthogonal photons represents the $|\psi^+\rangle$ -part. The populations with equal polarizations are incoherent. In order to test, whether the observed state has indeed a higher persistency than the state $|W_4\rangle$ concerning negativity and F_{MSF} , we analyzed the density matrices for all two-qubit subsets. The results are summarized in figure 7.10 a) and c), where the the fidelity to $|\psi^+\rangle$ (which is a lower bound on the F_{MSF} , as argued before) and the logarithmic negativity are shown. The green, dashed line represents the value achieved by the ideal W_4 state; the blue, solid line the value for $|D_4^{(2)}\rangle$. For all cases we clearly exceed the value of the W_4 state and therefore demonstrate that even the experimentally observed state exhibits a higher persistency against photon loss with respect to these measures. In figure 7.10 b) the values for the concurrence are depicted in the same way, showing the inverse ordering of the theoretical values, where the experimentally obtained residual states are, as expected, below the value for $|W_4\rangle$. These results also clearly distinguish the observed state from $|W_4\rangle$.

With the knowledge from section 3.3.2, we can conclude that maximal persistency of the state $|D_4^{(2)}\rangle$ concerning F_{MSF} indicates that it is optimal for $1 \rightarrow 3$ quantum teleporting (QTC, see figure 3.5 a). Optimal means that the highest possible fidelity of $7/9$ averaged over all input states is reached [187]. Note that for the state $|D_4^{(2)}\rangle$ the achieved teleporting fidelity is input state dependent. The experimentally achievable value in the quantum teleporting protocol, assuming perfect Bell state analysis and a single photon input state is, averaged over all input states, found to be $F_{tel} = 74.9 \pm 0.4\%$, exceeding the classically achievable value of $F_{class} = 2/3$.

Note further the flexibility of the state $|D_4^{(2)}\rangle$ as quantum resource for the two quantum communication protocols: The photons are distributed to four parties. Only then, it is decided who should act as the sender, when he performs the Bell state measurement with the input qubit. Then, they decide whether each party wants to use its clone (which is then QTC) or whether they collaborate to transfer the initial qubit probabilistically to one receiving party (ODT).

7.3 Summary

In conclusion, a setup for the experimental observation of a four-photon Dicke state was presented, followed by a detailed analysis of the obtained quantum state. To this end we performed a complete tomographic set of measurements on the state, reconstructed the density matrix and applied several non-tomographic tools for the analysis of particular properties. It was shown that the state exhibits qualitatively the properties of an ideal symmetric Dicke state with two excitations, delimiting the observed state from the other Dicke state of four qubits, i.e. $|W_4\rangle$, from the GHZ_4 state and the state analyzed in chapter 6, i.e. the cluster state $|\mathcal{C}_4\rangle$.

The observed state was found to exhibit a fidelity of $84.4 \pm 0.8\%$ to $|D_4^{(2)}\rangle$. The close relation to the SLOCC-family G_{abcd} was demonstrated by the confirmation of very high local von Neumann entropies of the single qubits and the detection of genuine four-partite entanglement in the state. The latter was conducted with an entanglement witness that

exploits the high permutation symmetry of $|D_4^{(2)}\rangle$. The observed state's symmetry could also be shown directly.

We further found an unusual property exhibited by the state $|D_4^{(2)}\rangle$ under the projective measurement of a single qubit: Tripartite entanglement is obtained, independent of the measurement basis; the entanglement class, however, is selected by the choice of measurement basis. Density matrices of the remaining states showed the experimental observation of the states $|W_3\rangle$ and $|G_3\rangle$, respectively. Genuine tripartite entanglement, as well as the GHZ_3 -type entanglement in the observed G_3 state were proven with entanglement witnesses. Thus, we could indeed demonstrate this extraordinary property also for the observed state.

The connectedness of the state concerning two projective measurements was successfully demonstrated by showing the high entanglement in the residual photon pairs. Hereby, the specific symmetric Bell state, which is obtained probabilistically, depends on the chosen measurement basis, i.e. can be selected at will.

As an entangled symmetric Dicke state, $|D_4^{(2)}\rangle$ is highly persistent against photon loss. Detection of non-biseparability in any two- and tripartite subsets of photons in the observed quantum state confirms this property in the experiment. In particular the quantitative evaluation of the persistency against loss of two photons reveals an interesting insight: A comparison between the states $|W_4\rangle$ and $|D_4^{(2)}\rangle$ shows that the notion of maximal persistency (which is usually attributed to W states) depends strongly on the chosen entanglement measure: The state $|W_4\rangle$ exhibits the highest entanglement persistency concerning the concurrence. The state $|D_4^{(2)}\rangle$, however, is more persistent with respect to the logarithmic negativity. In addition to this statement about maximal persistency, we gain from these considerations also a method to discriminate the two states. Experimentally we find that the entanglement persistency of the observed quantum state with respect to negativity is indeed much higher than the persistency of $|W_4\rangle$.

Both, two-qubit connectedness and persistency are conditions for applicability of a state for quantum telecloning and open destination teleportation. By a calculation of lower bounds on the fidelities that are expected to be achieved for these protocols, we showed that, under the condition of a perfect Bell state analysis and input state, both protocols can be implemented with the experimentally observed state with far more than classical fidelities.

8 Conclusions and Outlook

In conclusion, we have experimentally implemented and analyzed two highly four-photon polarization entangled states: the cluster state $|\mathcal{C}_4\rangle$ and the symmetric Dicke state with two excitations $|D_4^{(2)}\rangle$. The observation of the desired entanglement was verified by showing that the experimentally observed states reproduce characteristic properties of the ideal states with a high quality. The set of analyzed properties could be evaluated based on efficient non-tomographic methods. Besides known characteristics of the states we found several new insights on their entanglement structure and their applicability in quantum communication.

To experimentally observe the entangled states we relied on spontaneous parametric down conversion (SPDC), linear optics and conditional detection. We achieved long-term stability of the setups on the order of a few days for the observation of both states: The setup for the Dicke state is based on a non-interferometric solution which ensures its stability. At the core of the cluster state setup is a new tool, which we designed for linear optics quantum processing: A controlled phase gate, where the non-linear phase shift is implemented via a HOM-type interference at an asymmetric beam splitter. We demonstrated that this technique requires an easily achievable stability on the order of the coherence length of the input photons, i.e. greater than $100\ \mu\text{m}$. With this, the gate is stable over several days and allowed the first application of a universal entangling gate in a multiphoton experiment. The characterization of the gate via quantum process tomography yielded a process fidelity of 81.6%. In addition we showed that separable states can be entangled such that they have a fidelity to a Bell state of $\geq 80.4\%$. The latter is basically only limited by a residual distinguishability of the input photons and not by the gate parameters, as a detailed analysis of the gate showed.

Based on efficient non-tomographic tools, different aspects of the states were analyzed systematically: Firstly, a global analysis, focusing on properties that apply to the complete state. Secondly, an analysis of the entanglement that can be achieved via projective measurements performed on the state. Thirdly, the states' persistency of entanglement under loss of photons.

The states $|\mathcal{C}_4\rangle$ and $|D_4^{(2)}\rangle$ both belong to the same family of SLOCC classes G_{abcd} (equation 3.10, [24]). Characteristic for states of this SLOCC-family are four-partite entanglement and maximal local entropy. Efficient entanglement witnesses that were tailored to the states' properties allowed to prove genuine four-partite entanglement in both cases. Further, a high local von Neumann entropy was found for the single qubit density matrices of the two states. Permutation symmetry was argued to be useful for the non-tomographic analysis of quantum states. To exploit the symmetries exhibited by $|\mathcal{C}_4\rangle$ and $|D_4^{(2)}\rangle$, it must be verified to be present in the observed states. To this end we introduced a method to test this permutations symmetry efficiently in the experiment and confirmed a high degree of the expected symmetry for both observed quantum states.

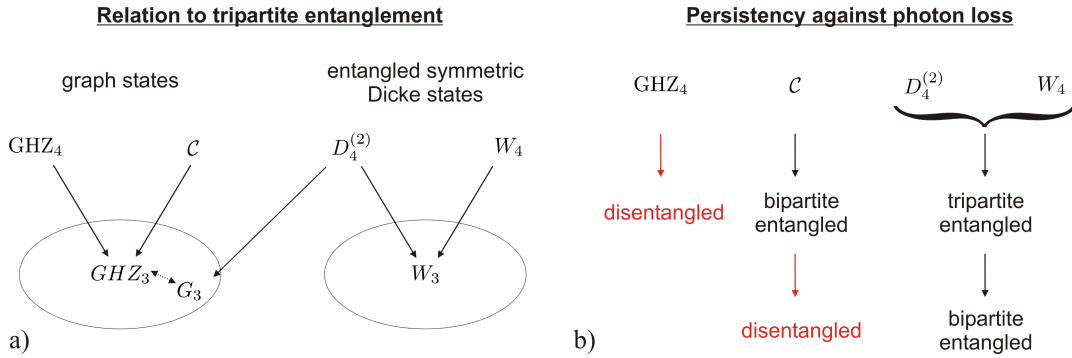


Figure 8.1: Displayed is in a) an overview of the entanglement that can be obtained probabilistically and/or in the right measurement basis after projective measurements on one qubit. The only state that connects the two inequivalent classes of tripartite entanglement is $|D_4^{(2)}\rangle$. In b) an overview of the residual entanglement after loss of photons is demonstrated, showing that symmetric Dicke states are more persistent than graph states and that the GHZ_4 state is maximally fragile.

An important property of graph states was demonstrated for the experimentally observed cluster state by showing that it can be deterministically reduced to cluster states of three and two qubits (i.e. GHZ and Bell states, respectively). As shown in figure 8.1 a), the GHZ_4 - and W_4 states are also connected to their own entanglement family via projective measurements. Surprisingly, the state $|D_4^{(2)}\rangle$ connects both inequivalent SLOCC-classes, i.e. the W_3 - and the G_3 state. An optimized entanglement witness allowed to verify this experimentally. Note, further, that these results constitute alternative experimental implementations of the two states $|GHZ_3\rangle$ and $|W_3\rangle$ and further the first observation of the G_3 state. From the connectedness of $|\mathcal{C}_4\rangle$ and $|D_4^{(2)}\rangle$ we further inferred their applicability as resource for open destination teleportation. In the experiment we could show that the observed states indeed allow to implement this protocol with a teleportation fidelity exceeding the classical bound.

Another property that is relevant for quantum communication is a state's persistency against photon loss. It differs strongly in its quality between the four-photon graph and symmetric Dicke states (see figure 8.1 b): The GHZ state is known to be maximally fragile, losing all entanglement with the loss of one photon. The cluster state is more persistent and exhibits bipartite entanglement after loss of one photon. The highest persistency is observed in the symmetric Dicke states because they cannot be disentangled by loss of one or two qubits. Experimentally, this was confirmed perfectly for the investigated states. Further, we showed that the common notion that W states exhibit the highest entanglement persistency depends on the bipartite entanglement measure chosen for comparison: For the logarithmic negativity, the state $|D_4^{(2)}\rangle$ exceeds the value reached by $|W_4\rangle$, which was also confirmed in the experiment. The fact that $D_4^{(2)}$ has further the maximal possible singlet fraction in the photon pairs implies its applicability for optimal $1 \rightarrow 3$ telecloning. It was shown that also the experimentally observed states can be used as resource for this application achieving fidelities beyond the classical limit.

The applications previously discussed are directly related to our analysis, there are, however, more: On the one hand the cluster state can be used for proof-of-principle exper-

iments on measurement based quantum computation. On the other hand, the controlled phase gate is a powerful tool with several applications, e.g. teleportation and entanglement swapping. Experiments in both directions will be presented in the PhD thesis of Christian Schmid [172].

The presented analysis of quantum states is more than just an approach to position them inside the space of mixed four-photon entangled states. By the choice of meaningful properties it was possible to gain a deeper understanding for the type of entanglement that is exhibited by the states. A natural question is now, whether there are other properties that are worth studying. Particularly interesting are further criteria that allow, similar to the arguments based on the maximal singlet fraction that were used here, to judge the applicability of a state for other tasks, e.g. quantum secret sharing. In reverse, such criteria should allow to identify further relevant quantum states.

It is common practice to invent for each quantum state that is identified as relevant a corresponding linear optics setup. Another possibility in the development of new linear optics solutions is to design more flexible setups, where different types of entanglement can be obtained by a simple variation of an experimental parameter. This would allow, for example, to observe the transition between different types of entanglement. One possible approach to this task is the implementation of a quantum state of a high photon number that can be used to obtain the desired states via adequate projective measurements. That this is possible was shown in our experiment where reducing the state $|D_4^{(2)}\rangle$ allowed to obtain a GHZ_3 class and a W_3 state. Another approach is the design of the linear optics such that local manipulations at an early stage of the setup lead to non-local effects in its output. At the moment one can only speculate that these new types of sources hold a high potential for applications in quantum communication and new types of communication protocols that rely on switching between different types of quantum states.

Concerning the further development towards the entanglement of more photons, it is worth noting that the presented schemes are generic for the observation of similar types of entanglement in states with a higher photon number: Symmetric Dicke states of the form $|D_N^{(N/2)}\rangle$ can be observed by symmetric distribution of higher order emissions of a collinear SPDC source. Graph states can be obtained by using the controlled phase gate to enlarge the graph states with additional photon pairs successively. However, despite of the observation of up to six photon graph states in some experiments [20], the further development of states of higher photon numbers with SPDC, linear optics and conditional detection faces several challenges: On the one hand, the probabilistic character of linear optics schemes cause the experimental setups to grow inefficient, on the other hand the necessity to increase the photon creation probability increases at the same time the noise observed due to higher order emissions. Thus, it is for the moment preferable to achieve a higher efficiency of coincidence detection either by further engineering of the photon source, or by improving the single photon detectors. In the long run, however, other techniques are required to get rid of higher order emissions, e.g. the use of nonlinear elements, photon number resolving detectors or the combination of SPDC and single photon sources.

The long-term goal of understanding and experimentally controlling multipartite entanglement is the application in quantum computation and quantum communication. It is still an open question, which physical implementation will be best suited for these tasks.

Photonic quantum systems like the presented ones seem to be particularly interesting for applications in quantum communication as fast carriers of information with a low interaction with the environment. Yet, also universal, deterministic linear optics quantum computation was theoretically shown to be possible [151] and with the development of new measurement based schemes, several new ideas for photonic quantum computation have been invented [33, 34, 153, 188, 189]. Based on these ideas, experimental proof of principle demonstrations of quantum algorithms have very recently been successfully demonstrated with photons [35–38, 172] and there is certainly much more to come...

A Geometric measures of entanglement

This part of the appendix documents the sources for the values of the geometric measure of entanglement given in table 3.2.3. Most of this is based on the publication by Wei et al.[75], where a generalization of the geometric measure of entanglement [74] for mixed states is presented. There, the geometric measure of entanglement for several quantum states is given and the connection to entanglement witnesses explained. For several states of interest here, the geometric measure of entanglement can be directly taken from [75]:

$$E_G(GHZ_n) = 1/2 = 0.5, \quad (\text{A.1})$$

$$E_G(D_4^{(2)}) = 5/8 = 0.625, \quad (\text{A.2})$$

$$E_G(W_3) = 5/9 \approx 0.556, \quad (\text{A.3})$$

where the state $|D_4^{(2)}\rangle$ corresponds to $|\Psi\rangle$ in the notation of [75]. Using equation (15)¹ it is also easy to derive:

$$E_G(W_4) = 37/64 \approx 0.578, \quad (\text{A.4})$$

which exceeds the value for the W_3 state only slightly. Furthermore, the G_3 state is part of the family of states in equation (20)¹ with its geometric measure of entanglement given by:

$$E_G(G_3) = 1/4 = 0.25. \quad (\text{A.5})$$

This value is not only achieved for the superposition, but also for the equally weighted mixture of the states W_3 and \overline{W}_3 ; a state we also observe in the experiment (see equation 7.12).

The geometric measure of entanglement for a variety of Graph states has been derived by Markham et al. [190]. For the four-qubit cluster state the value is:

$$E_G(\mathcal{C}_4) = 3/4 = 0.75. \quad (\text{A.6})$$

Finally, the geometric measure of the state $|\Psi^{(4)}\rangle$ has, together with a whole group of similar quantum states, numerically been calculated by Eisert et al. [191]:

$$E_G(\Psi^{(4)}) = 2/3 \approx 0.667. \quad (\text{A.7})$$

¹Refers to equation number in [75]

B Relation between different states

B.1 Local transformations between G_3 and GHZ_3

In section 3.1.1, the fact that G_3 (equation 3.7) belongs to the GHZ_3 class was inferred from its non-vanishing tangle. Here, this observation will be supplemented by giving the direct SLOCC transformation between the states $|G_3\rangle$ and $|GHZ_3\rangle$ (equation 3.1).

The relation is best seen, when both states are first transformed by a \mathcal{H} gate on each qubit:

$$(\mathcal{H} \otimes \mathcal{H} \otimes \mathcal{H})|GHZ_3\rangle = \frac{1}{2}(|HHH\rangle + |HVV\rangle + |VHV\rangle + |VVH\rangle), \quad (\text{B.1})$$

$$(\mathcal{H} \otimes \mathcal{H} \otimes \mathcal{H})|G_3\rangle = \frac{1}{2}(\sqrt{3}|HHH\rangle - \frac{1}{\sqrt{3}}|HVV\rangle - \frac{1}{\sqrt{3}}|VHV\rangle - \frac{1}{\sqrt{3}}|VVH\rangle). \quad (\text{B.2})$$

The amplitudes can be accordingly manipulated with the following non-unitary transformations acting on each qubit:

$$\mathcal{T} = \begin{pmatrix} \frac{1}{\sqrt{3}} & 0 \\ 0 & i \end{pmatrix}; \quad \bar{\mathcal{T}} = \begin{pmatrix} 1 & 0 \\ 0 & -\frac{i}{\sqrt{3}} \end{pmatrix}. \quad (\text{B.3})$$

Altogether we find:

$$(\mathcal{H} \otimes \mathcal{H} \otimes \mathcal{H})(\mathcal{T} \otimes \mathcal{T} \otimes \mathcal{T})(\mathcal{H} \otimes \mathcal{H} \otimes \mathcal{H})|G_3\rangle = \frac{1}{3}|GHZ_3\rangle, \quad (\text{B.4})$$

$$(\mathcal{H} \otimes \mathcal{H} \otimes \mathcal{H})(\bar{\mathcal{T}} \otimes \bar{\mathcal{T}} \otimes \bar{\mathcal{T}})(\mathcal{H} \otimes \mathcal{H} \otimes \mathcal{H})|GHZ_3\rangle = \frac{1}{\sqrt{3}}|G_3\rangle. \quad (\text{B.5})$$

This provides an additional proof for the SLOCC equivalence of the two states. Furthermore, these stochastic local operations (no classical communication necessary) can straightforwardly be implemented via wave plates and the type of polarization dependent beam splitter (section 4.2) that was also used in the controlled phase gate experiment (see chapter 5). The conversion happens with a probability of $1/9$.

B.2 Direct proof of state classification

Here, it will be shown explicitly how the states presented in section 3.2 fit in the classification presented in [24]. Most states belong to the family of SLOCC classes parametrized as presented in equation 3.10:

$$\begin{aligned} G_{abcd} &= \frac{a+d}{2}(|HHHH\rangle + |VVVV\rangle) + \frac{a-d}{2}(|HHVV\rangle + |VVHH\rangle) \\ &+ \frac{b+c}{2}(|HVHV\rangle + |VHVV\rangle) + \frac{b-c}{2}(|HVVH\rangle + |VHHV\rangle), \quad (\text{B.6}) \end{aligned}$$

where a , b , c , and d are complex parameters with positive real part.

- The GHZ_4 state is:

$$|GHZ_4\rangle = \frac{1}{\sqrt{2}}(|HHHH\rangle + |VVVV\rangle).$$

Thus, the coefficients are $a = d = \sqrt{\frac{1}{2}}$, $b = c = 0$. As we have seen that the state is locally equivalent to the G_4 state (equation 3.20). Thus, the latter naturally also belongs to this SLOCC-family.

- The state $|\mathcal{C}_4\rangle$ is under LU ($\sqrt[4]{\hat{\sigma}_z}$ on every qubit) equivalent to a state that follows the above parametrization:

$$\begin{aligned} & (\sqrt[4]{\hat{\sigma}_z})^{\otimes 4} |\mathcal{C}_4\rangle \\ &= (\sqrt[4]{\hat{\sigma}_z})^{\otimes 4} \left[\frac{1}{2} (|HHHH\rangle + |HHVV\rangle + |VVHH\rangle - |VVVV\rangle) \right] \\ &= \frac{1}{2} (|HHHH\rangle + i|HHVV\rangle + i|VVHH\rangle + |VVVV\rangle) \end{aligned}$$

The coefficients for this state are $a = (1 + i)/2$, $d = (1 - i)/2$, $b = c = 0$.

- The state $D_4^{(2)}$ equation 3.23 needs to be transformed with spin-flips on the last two qubits:

$$\begin{aligned} (\mathbb{1} \otimes \mathbb{1} \otimes \hat{\sigma}_x \otimes \hat{\sigma}_x) |D_4^{(2)}\rangle &= \sqrt{\frac{1}{6}} \left(|HHHH\rangle + |HVHV\rangle + |HVVH\rangle \right. \\ &\quad \left. + |VHHV\rangle + |VHVH\rangle + |VVVV\rangle \right) \quad (\text{B.7}) \end{aligned}$$

It can thus be directly identified with the parametrization of G_{abcd} for $a = d = \frac{1}{\sqrt{6}}$, $b = \frac{2}{\sqrt{6}}$, $c = 0$.

- The state $|\Psi^{(4)}\rangle$ after the same transformation gives:

$$\begin{aligned} (\mathbb{1} \otimes \mathbb{1} \otimes \hat{\sigma}_x \otimes \hat{\sigma}_x) \Psi^{(4)} &= \frac{1}{\sqrt{3}} (|HHHH\rangle + |VVVV\rangle) \quad (\text{B.8}) \\ &\quad - \frac{1}{\sqrt{12}} (|HVHV\rangle + |HVVH\rangle + |VHHV\rangle + |VHVH\rangle). \end{aligned}$$

Thus, the coefficients in G_{abcd} are $a = b = d = \frac{1}{\sqrt{3}}$, $c = 0$.

- For completeness, the relation of W_4 to its SLOCC-family (see equation 3.11) is given:

$$\begin{aligned}
 L_{ab_3} = & a(|HHHH\rangle) & (B.9) \\
 & + \frac{a-b}{2}(|HVVH\rangle + |VHHV\rangle) + \frac{a+b}{2}(|HVHV\rangle + |VHVH\rangle) \\
 & + |VVVV\rangle) + \frac{i}{\sqrt{2}}(|HHHV\rangle + |HHVH\rangle + |HVVV\rangle + |VHVV\rangle)
 \end{aligned}$$

Up to normalization and an irrelevant global phase, we obtain this state with $a = b = 0$. In this case, only the last term is not vanishing, which can be obtained via a spin-flip on the third and fourth qubit:

$$\begin{aligned}
 & (\mathbb{1} \otimes \mathbb{1} \otimes \hat{\sigma}_x \otimes \hat{\sigma}_x) |W_4\rangle \\
 = & (\mathbb{1} \otimes \mathbb{1} \otimes \hat{\sigma}_x \otimes \hat{\sigma}_x) \left[\frac{1}{2}(|HHHV\rangle + |HHVH\rangle + |HVHH\rangle + |VHHH\rangle) \right] \\
 = & \frac{1}{2}(|HHVH\rangle + |HHHV\rangle + |HVVV\rangle + |VHVV\rangle)
 \end{aligned}$$

C Linear multiqubit tomography

We conduct the calculation for a linear N -qubit tomography along the lines presented in section 4.3.2 for two qubits resulting in equation 4.23. The calculation is started from the decomposition of the density matrix of N qubits (equation 4.18):

$$\rho = \frac{1}{2^N} \sum_{\{b_j\}=0}^3 K_{\{b_j\}} \prod_{j=1}^N \hat{\sigma}_{b_j}, \quad (\text{C.1})$$

where $\{b_j\} = \{b_1, b_2, \dots, b_N\}$, i.e. the summation is taken over all N indices b_j with $j \in \{0, 1, \dots, N\}$. We split this sum in $N + 1$ sums that are taken over correlations with an equal number of indices 0. In other words, each term has only tensor products of Pauli matrices that contain the same number of $\hat{\sigma}_0 = \mathbb{1}$, in decreasing order:

$$\rho = \frac{1}{2^N} \left(K_{0\dots 0} \mathbb{1}^{\otimes N} + \sum_{\mu=1}^N \sum_{b_\mu=1}^3 K_{\dots 0, b_\mu, 0, \dots} \mathbb{1}^{\otimes \mu-1} \otimes \hat{\sigma}_{i_\mu} \otimes \mathbb{1}^{\otimes N-\mu} + \dots + \sum_{\{b_j\}=1}^3 K_{\{i_j\}} \prod_j \hat{\sigma}_{b_j} \right). \quad (\text{C.2})$$

For the N -party case the correlations can, as in equation 4.20, be expressed in terms of count rates. Exemplarily, this is shown here for an arbitrary correlation:

$$K_{0\dots 0, b_\mu, 0, \dots, 0, b_\nu, 0, \dots} = \frac{1}{3^{(N-2)}} \sum_{\{b_l\} \in \Gamma} \sum_{\{s_l\} \in \Xi} s_\mu s_\nu c_{\{b_j\}}^{\{s_j\}}, \quad (\text{C.3})$$

where Γ are all N -tuples of the form $\{\{1, 1, \dots, 1\}, \{1, 1, \dots, 2\}, \dots, \{3, 3, \dots, 3\}\}$ and Ξ are all N -tuples of the form $\{\{-1, -1, \dots, -1\}, \{-1, -1, \dots, 1\}, \dots, \{1, 1, \dots, 1\}\}$. Then $\{s_j\}$ denote the eigenvalues for all operators $\{\hat{\sigma}_{b_j}\}$; further, $\{b_l\} = \{b_1 \dots b_{\mu-1} b_{\mu+1} \dots b_{\nu-1} b_{\nu+1} \dots b_N\}$, i.e. is the list of operator indices where the μ -th and ν -th element are missing. The factor $\frac{1}{3^{(N-2)}}$ appears when the $\hat{\sigma}_0$ matrices are expressed in terms of an average of relative frequencies c_b^s for all bases, i.e. for all $b \in \{1, 2, 3\}$.

By substituting all correlations derived this way in equation C.2, the summations are again taken over all N operators. Note that for only one correlation (as in equation C.3) the summation was taken over a smaller set of operators. Thus, the sums over the bases and the signs $\{s_j\}$ can be taken out:

$$\rho = \sum_{\{b_j\}=1}^3 \sum_{\{s_j\}=\pm 1} c_{\{b_j\}}^{\{s_j\}} \left(\frac{1}{3^N} \mathbb{1}^{\otimes N} + \sum_{j=1}^N \frac{1}{3^{N-1}} \mathbb{1}^{\otimes j-1} \otimes \hat{\sigma}_{b_j} \otimes \mathbb{1}^{\otimes N-j} + \dots + \prod_j \hat{\sigma}_{b_j} \right) \quad (\text{C.4})$$

It is easily seen that the operator for the different count rates can be written as a product:

$$\rho = \sum_{\{b_j\}=1}^3 \sum_{\{s_j\}=-1}^{+1} c_{\{b_j\}}^{\{s_j\}} \prod_j \left(\frac{1}{3} \mathbb{1} + s_j \hat{\sigma}_{b_j} \right). \quad (\text{C.5})$$

With this, the result used in equation 4.23) is derived.

D Publication list

C. Schmid, **N. Kiesel**, W. Wieczorek and H. Weinfurter.
The entanglement of the four-photon cluster state,
New J. Phys. **9**, 236 (2007).

C. Schmid, **N. Kiesel**, W. Laskowski, E. Solano, G. Tóth,
M. Żukowski and H. Weinfurter.
The Entanglement of the Symmetric Four-photon Dicke State.
In *Quantum Communication and Security*,
edited by M. Żukowski, S. Kilin, J. Kowalik, NATO workshop (2007).

N. Kiesel, C. Schmid, G. Tóth, E. Solano and H. Weinfurter.
Experimental Observation of Four-Photon Entangled Dicke State with High Fidelity,
Phys. Rev. Lett. **98**, 063604 (2007).

C. Schmid, **N. Kiesel**, U. Weber, R. Ursin and H. Weinfurter:
Experimental Analysis of a simple linear optics phase gate
Int. J. Quant. Inf. **5**, 235 (2007)

W. Wieczorek, **N. Kiesel**, C. Schmid and H. Weinfurter.
Efficient non-tomographic tools for the characterization of multipartite entanglement.
Proceedings of the QCMC06, Tsukuba, Japan (2006)

M. Bourennane, M. Eibl, S. Gaertner, **N. Kiesel**,
C. Kurtsiefer and H. Weinfurter.
Entanglement Persistency of Multiphoton Entangled States,
Phys. Rev. Lett. **96**, 100502 (2006).

N. Kiesel, C. Schmid, U. Weber, R. Ursin and H. Weinfurter.
Linear Optics Controlled-Phase Gate Made Simple,
Phys. Rev. Lett. **95**, 210505 (2005).

N. Kiesel, C. Schmid, U. Weber,
G. Tóth, O. Gühne, R. Ursin and H. Weinfurter.
Experimental Analysis of a Four-Qubit Photon Cluster State,
Phys. Rev. Lett. **95**, 210502 (2005).

M. Eibl, **N. Kiesel**, M. Bourennane, C. Kurtsiefer and H. Weinfurter.
Experimental Realization of a Three-Qubit Entangled W State,
Phys. Rev. Lett. **92**, 077901 (2004).

N. Kiesel, M. Bourennane, C. Kurtsiefer, H. Weinfurter,
D. Kaszlikowski, W. Laskowski and M. Żukowski.
Three-photon W-state,
J. Mod. Optic. **50**, 1131 (2003).

M. Bourennane, M. Eibl, S. Gaertner, **N. Kiesel**, C. Kurtsiefer,
M. Żukowski and H. Weinfurter.
Multiphoton entanglement and interferometry,
Fortschr. Physik **51**, 273 (2003).

M. Bourennane, M. Eibl, S. Gaertner, **N. Kiesel**, C. Kurtsiefer,
M. Żukowski and H. Weinfurter.
Multiphoton entanglement,
In *Quantum Optics in Computing and Communications*,
edited by S. Liu, G. Guo, H.-K. Lo and N. Imoto, volume 4917, SPIE (2002).

C. Schmid, **N. Kiesel**, W. Wieczorek, R. Pohlner and H. Weinfurter.
Multiphoton entanglement engineering via projective measurements,
to be published in
Proceedings of the SPIE Optics East 2007, Boston, USA (2007).

C. Schmid, **N. Kiesel**, W. Laskowski, and H. Weinfurter.
State Discrimination with characteristic Bell Inequalities.
to be submitted

C. Schmid, **N. Kiesel**, U. Weber, R. Ursin, A. Zeilinger and H. Weinfurter.
Teleportation and entanglement swapping completed.
to be submitted

Bibliography

- [1] N. Bohr: *Albert Einstein als Philosoph und Naturforscher*, Paul Arthur Schlipp, 1949.
- [2] A. Einstein, B. Podolsky and N. Rosen. Can Quantum-Mechanical Description of Physical Reality Be Considered Complete?, *Phys. Rev.* **47**, 777 (1935).
- [3] E. Schrödinger. Die gegenwärtige Situation in der Quantenmechanik, *Naturwissenschaften* **V23**, 807 (1935).
- [4] J.S. Bell. On the Einstein-Podolsky-Rosen paradox, *Physics* **1**, 195 (1964).
- [5] S.J. Freedman and J.F. Clauser. Experimental Test of Local Hidden-Variable Theories, *Phys. Rev. Lett.* **28**, 938 (1972).
- [6] J.F. Clauser and A. Shimony. Bell's theorem. Experimental tests and implications, *Rep. Prog. Phys.* **41**, 1881 (1978).
- [7] A. Aspect, P. Grangier and G. Roger. Experimental Tests of Realistic Local Theories via Bell's Theorem, *Phys. Rev. Lett.* **47**, 460 (1981).
- [8] G. Weihs, T. Jennewein, C. Simon, H. Weinfurter and A. Zeilinger. Violation of Bell's Inequality under Strict Einstein Locality Conditions, *Phys. Rev. Lett.* **81**, 5039 (1998).
- [9] M.A. Rowe, D. Kielpinski, V. Meyer, C.A. Sackett, W.M. Itano, C. Monroe and D.J. Wineland. Experimental violation of a Bell's inequality with efficient detection, *Nature* **409**, 791 (2001).
- [10] R.F. Werner. Quantum states with Einstein-Podolsky-Rosen correlations admitting a hidden-variable model, *Phys. Rev. A* **40**, 4277 (1989).
- [11] A.K. Ekert. Quantum cryptography based on Bell's theorem, *Phys. Rev. Lett.* **67**, 661 (1991).
- [12] C.H. Bennett, G. Brassard, C. Crépeau, R. Jozsa, A. Peres and W.K. Wootters. Teleporting an unknown quantum state via dual classical and Einstein-Podolsky-Rosen channels, *Phys. Rev. Lett.* **70**, 1895 (1993).
- [13] R. Feynman. Simulating Physics with Computers, *Int. J. Theor. Phys.* **21**, 467 (1982).
- [14] D. Deutsch. Quantum theory, the church-turing principle and the universal quantum computer, *Proceedings of the Royal Society of London A* **400**, 97 (1985).

- [15] P.W. Shor. Polynomial-Time Algorithms for Prime Factorization and Discrete Logarithms on a Quantum Computer, *SIAM J.Sci.Statist.Comput.*, *arXiv:quant-ph/9508027v2* **26**, 1484 (1997).
- [16] L.K. Grover. Quantum Mechanics Helps in Searching for a Needle in a Haystack, *Phys. Rev. Lett.* **79**, 325 (1997).
- [17] D. Bouwmeester, J.W. Pan, M. Daniell, H. Weinfurter and A. Zeilinger. Observation of Three-Photon Greenberger-Horne-Zeilinger Entanglement, *Phys. Rev. Lett.* **82**, 1345 (1999).
- [18] J.W. Pan, D. Bouwmeester, M. Daniell, H. Weinfurter and A. Zeilinger. Experimental test of quantum nonlocality in three-photon Greenberger-Horne-Zeilinger entanglement, *Nature* **403**, 515 (2000).
- [19] D. Bouwmeester, J.W. Pan, K. Mattle, M. Eibl, H. Weinfurter and A. Zeilinger. Experimental Quantum Teleportation, *Nature* **390**, 575 (1997).
- [20] C.Y. Lu, X.Q. Zhou, O. Gühne, W.B. Gao, J. Zhang, Z.S. Yuan, A. Goebel, T. Yang and J.W. Pan. Experimental entanglement of six photons in graph states, *Nat. Phys.* **3**, 91 (2007).
- [21] H. Haffner, W. Hansel, C.F. Roos, J. Benhelm, D. Chek-al kar, M. Chwalla, T. Körber, U.D. Rapol, M. Riebe, P.O. Schmidt, C. Becher, O. Gühne, W. Dur and R. Blatt. Scalable multiparticle entanglement of trapped ions, *Nature* **438**, 643 (2005).
- [22] D. Leibfried, E. Knill, S. Seidelin, J. Britton, R.B. Blakestad, J. Chiaverini, D.B. Hume, W.M. Itano, J.D. Jost, C. Langer, R. Ozeri, R. Reichle and D.J. Wineland. Creation of a six-atom "Schrodinger cat" state, *Nature* **438**, 639 (2005).
- [23] W. Dür, G. Vidal and J.I. Cirac. Three qubits can be entangled in two inequivalent ways, *Phys. Rev. A* **62**, 062314 (2000).
- [24] F. Verstraete, J. Dehaene, B.D. Moor and H. Verschelde. Four qubits can be entangled in nine different ways, *Phys. Rev. A* **65**, 052112 (2002).
- [25] L. Lamata, J. Leon, D. Salgado and E. Solano. Inductive classification of multipartite entanglement under SLOCC, *quant-ph/0603243* (2006).
- [26] L. Lamata, J. Leon, D. Salgado and E. Solano. Inductive Entanglement Classification of Four Qubits under SLOCC, *quant-ph/0610233* (2006).
- [27] O. Mandel, M. Greiner, A. Widera, T. Rom, T.W. Hänsch and I. Bloch. Controlled collisions for multi-particle entanglement of optically trapped atoms, *Nature* **425**, 937 (2003).
- [28] D. Schlingemann and R.F. Werner. Quantum error-correcting codes associated with graphs, *Phys. Rev. A* **65**, 012308 (2001).

-
- [29] R. Cleve and H. Buhrman. Substituting quantum entanglement for communication, *Phys. Rev. A* **56**, 1201 (1997).
- [30] M. Żukowski, A. Zeilinger, M. Horne and H. Weinfurter. Quest for GHZ states, *Acta Phys. Pol.* **93**, 187 (1998).
- [31] M. Hillery, V. Bužek and A. Berthiaume. Quantum secret sharing, *Phys. Rev. A* **59**, 1829 (1999).
- [32] R. Cleve, D. Gottesman and H.K. Lo. How to Share a Quantum Secret, *Phys. Rev. Lett.* **83**, 648 (1999).
- [33] R. Raussendorf and H.J. Briegel. A One-Way Quantum Computer, *Phys. Rev. Lett.* **86**, 5188 (2001).
- [34] M.A. Nielsen. Optical Quantum Computation Using Cluster States, *Phys. Rev. Lett.* **93**, 040503 (2004).
- [35] P. Walther, K.J. Resch, T. Rudolph, E. Schenck, H. Weinfurter, V. Vedral, M. Aspelmeyer and A. Zeilinger. Experimental one-way quantum computing, *Nature* **434**, 169 (2005).
- [36] R. Prevedel, P. Walther, F. Tiefenbacher, P. Böhi, R. Kaltenbaek, T. Jennewein and A. Zeilinger. High-speed linear optics quantum computing using active feed-forward, *Nature* **445**, 65 (2007).
- [37] C.Y. Lu, D.E. Browne, T. Yang and J.W. Pan. Demonstration of Shor's quantum factoring algorithm using photonic qubits, *arXiv:0705.1684v1* (2007).
- [38] M.S. Tame, R. Prevedel, M. Paternostro, P. Böhi, M.S. Kim and A. Zeilinger. Experimental Realization of Deutsch's Algorithm in a One-Way Quantum Computer, *Phys. Rev. Lett.* **98**, 140501 (2007).
- [39] R.H. Dicke. Coherence in Spontaneous Radiation Processes, *Phys. Rev.* **93**, 99 (1954).
- [40] J.K. Stockton, J.M. Geremia, A.C. Doherty and H. Mabuchi. Characterizing the entanglement of symmetric many-particle spin-(1/2) systems, *Phys. Rev. A* **67**, 022112 (2003).
- [41] T.C. Ralph, N.K. Langford, T.B. Bell and A.G. White. Linear optical controlled-NOT gate in the coincidence basis, *Phys. Rev. A* **65**, 062324 (2002).
- [42] H.F. Hofmann and S. Takeuchi. Quantum phase gate for photonic qubits using only beam splitters and postselection, *Phys. Rev. A* **66**, 024308 (2002).
- [43] J.L. O'Brien, G.J. Pryde, A.G. White, T.C. Ralph and D. Branning. Demonstration of an all-optical quantum controlled-NOT gate, *Nature* **426**, 264 (2003).
- [44] J.L. O'Brien, G.J. Pryde, A. Gilchrist, D.F.V. James, N.K. Langford, T.C. Ralph and A.G. White. Quantum Process Tomography of a Controlled-NOT Gate, *Phys. Rev. Lett.* **93**, 080502 (2004).

- [45] C. Cohen-Tannoudji, B. Diu and F. Laloe: *Quantum Mechanics I*, Wiley Interscience, 1977.
- [46] M.A. Nielsen and I.L. Chuang: *Quantum Computation and Quantum Information*, Cambridge University Press, 2000.
- [47] B. Schumacher. Quantum coding, *Phys. Rev. A* **51**, 2738 (1995).
- [48] A. Uhlmann. The "transition probability" in the state space of a *-algebra, *Rep. Mat. Phys.* **9**, 273 (1976).
- [49] R. Horodecki, P. Horodecki, M. Horodecki and K. Horodecki. Quantum entanglement, *quant-ph/0702225v2* (2007).
- [50] T. Sleator and H. Weinfurter. Realizable Universal Quantum Logic Gates, *Phys. Rev. Lett.* **74**, 4087 (1995).
- [51] B. Kraus: *Entanglement Properties of Quantum States and Quantum Operations*, Leopold-Franzens-Universität Innsbruck, Dissertation, January 2003.
- [52] C. Bennett and G. Brassard. Quantum Cryptography: Public Key Distribution and Coin Tossing, *Proceedings of IEEE International Conference on Computers Systems and Signal Processing, Bangalore India* page 175 (1984).
- [53] R. Ursin, F. Tiefenbacher, T. Schmitt-Manderbach, H. Weier, T. Scheidl, M. Lindenthal, B. Blauensteiner, T. Jennewein, J. Perdigues, P. Trojek, B. Oemer, M. Fürst, M. Meyenburg, J. Rarity, Z. Sodnik, C. Barbieri, H. Weinfurter and A. Zeilinger. Free-Space distribution of entanglement and single photons over 144 km, *quant-ph/0607182v2* (2006).
- [54] T. Schmitt-Manderbach, H. Weier, M. Furst, R. Ursin, F. Tiefenbacher, T. Scheidl, J. Perdigues, Z. Sodnik, C. Kurtsiefer, J.G. Rarity, A. Zeilinger and H. Weinfurter. Experimental Demonstration of Free-Space Decoy-State Quantum Key Distribution over 144 km, *Phys. Rev. Lett.* **98**, 010504 (2007).
- [55] N. Gisin and R. Thew. Quantum communication, *Nat. Photon.* **1**, 165 (2007).
- [56] M. Horodecki, P. Horodecki and R. Horodecki. General teleportation channel, singlet fraction, and quasidistillation, *Phys. Rev. A* **60**, 1888 (1999).
- [57] J. Eisert and M.B. Plenio. A comparison of entanglement measures, *J. Mod. Optic.* **46**, 145 (1999).
- [58] M. Horodecki. Entanglement measures, *Quantum Inform. Compu.* **1**, 3 (2001).
- [59] D. Bruss. Characterizing Entanglement, *Jour. Math. Phys.* **43**, 4237 (2002).
- [60] J. Eisert and D. Gross. Multi-particle entanglement, *quant-ph/0505149* (2005).
- [61] V. Vedral and M.B. Plenio. Entanglement measures and purification procedures, *Phys. Rev. A* **57**, 1619 (1998).

-
- [62] M. Horodecki, P. Horodecki and R. Horodecki. Limits for Entanglement Measures, *Phys. Rev. Lett.* **84**, 2014 (2000).
- [63] G. Vidal. Entanglement monotones, *J. Mod. Optic.* **47**, 355 (2000).
- [64] M.J. Donald, M. Horodecki and O. Rudolph. The uniqueness theorem for entanglement measures, *Jour. Math. Phys.* **43**, 4252 (2002).
- [65] C.H. Bennett, H.J. Bernstein, S. Popescu and B. Schumacher. Concentrating partial entanglement by local operations, *Phys. Rev. A* **53**, 2046 (1996).
- [66] W.K. Wootters. Entanglement of Formation of an Arbitrary State of Two Qubits, *Phys. Rev. Lett.* **80**, 2245 (1998).
- [67] V. Coffman, J. Kundu and W.K. Wootters. Distributed entanglement, *Phys. Rev. A* **61**, 052306 (2000).
- [68] A. Peres. Separability Criterion for Density Matrices, *Phys. Rev. Lett.* **77**, 1413 (1996).
- [69] M. Horodecki and P. Horodecki. Reduction criterion of separability and limits for a class of distillation protocols, *Phys. Rev. A* **59**, 4206 (1999).
- [70] G. Vidal and R.F. Werner. Computable measure of entanglement, *Phys. Rev. A* **65**, 032314 (2002).
- [71] J. Eisert, F. Brandao and K. Audenaert. Quantitative entanglement witnesses, *quant-ph/0607167* (2006).
- [72] O. Gühne, M. Reimpell and R. Werne. Estimating entanglement measures in experiments, *quant-ph/0607163* (2006).
- [73] A. Shimony. Degree of entanglement, *Ann. N. Y. Acad. Sci.* **755**, 675 (1995).
- [74] H. Barnum and N. Linden. Monotones and invariants for multi-particle quantum states, *J. Phys. A* **34**, 6787 (2001).
- [75] T.C. Wei and P.M. Goldbart. Geometric measure of entanglement and applications to bipartite and multipartite quantum states, *Phys. Rev. A* **68**, 042307 (2003).
- [76] C.H. Bennett, S. Popescu, D. Rohrlich, J.A. Smolin and A.V. Thapliyal. Exact and asymptotic measures of multipartite pure-state entanglement, *Phys. Rev. A* **63**, 012307 (2000).
- [77] M. Grassl, A. Klappenecker and M. Rötteler: *Graphs, Quadratic Forms, and Quantum Codes* *Graphs, Quadratic Forms, and Quantum Codes*, , In *Proc. 2002 IEEE International Symposium on Information Theory, Lausanne, Switzerland.* (2002) page 45.
- [78] M. Hein, J. Eisert and H.J. Briegel. Multiparty entanglement in graph states, *Phys. Rev. A* **69**, 062311 (2004).

- [79] M. Hein, W. Dür, J. Eisert, R. Raussendorf, M.V. den Nest and H.J. Briegel. Entanglement in Graph States and its Applications, *quant-ph/0602096* (2006).
- [80] J.K. Stockton, R. van Handel and H. Mabuchi. Deterministic Dicke-state preparation with continuous measurement and control, *Phys. Rev. A* **70**, 022106 (2004).
- [81] H.J. Briegel and R. Raussendorf. Persistent Entanglement in Arrays of Interacting Particles, *Phys. Rev. Lett.* **86**, 910 (2001).
- [82] W. Dür. Multipartite entanglement that is robust against disposal of particles, *Phys. Rev. A* **63**, 020303 (2001).
- [83] M. Bourennane, M. Eibl, S. Gaertner, N. Kiesel, C. Kurtsiefer and H. Weinfurter. Entanglement Persistency of Multiphoton Entangled States, *Phys. Rev. Lett.* **96**, 100502 (2006).
- [84] I. Ghiu, M. Bourennane and A. Karlsson. Entanglement-assisted local transformations between inequivalent classes of three-particle entangled states, *Phys. Lett. A* **287**, 12 (2001).
- [85] A. Acín, A. Andrianov, L. Costa, E. Jané, J.I. Latorre and R. Tarrach. Generalized Schmidt Decomposition and Classification of Three-Quantum-Bit States, *Phys. Rev. Lett.* **85**, 1560 (2000).
- [86] B. Chong: *Characterization of Multipartite Entanglement*, Universität Dortmund, Dissertation, June 2006.
- [87] A. Sen(De), U. Sen and M. Żukowski. Unified criterion for security of secret sharing in terms of violation of Bell inequalities, *Phys. Rev. A* **68**, 032309 (2003).
- [88] N. Kiesel: *Experimental Analysis of a Three-Photon Entangled State*, LMU München, Diplomarbeit, October 2002.
- [89] A. Acín, D. Bruss, M. Lewenstein and A. Sanpera. Classification of Mixed Three-Qubit States, *Phys. Rev. Lett.* **87**, 040401 (2001).
- [90] N. Kiesel, M. Bourennane, C. Kurtsiefer, H. Weinfurter, D. Kaszlikowski, W. Laskowski and M. Żukowski. Three-photon W-state, *J. Mod. Optic.* **50**, 1131 (2003).
- [91] M. Eibl, N. Kiesel, M. Bourennane, C. Kurtsiefer and H. Weinfurter. Experimental Realization of a Three-Qubit Entangled W State, *Phys. Rev. Lett.* **92**, 077901 (2004).
- [92] M. Bourennane, M. Eibl, C. Kurtsiefer, S. Gaertner, H. Weinfurter, O. Gühne, P. Hyllus, D. Bruss, M. Lewenstein and A. Sanpera. Experimental Detection of Multipartite Entanglement using Witness Operators, *Phys. Rev. Lett.* **92**, 087902 (2004).
- [93] F. Verstraete, J. Dehaene and B. De Moor. Normal forms and entanglement measures for multipartite quantum states, *Phys. Rev. A* **68**, 012103 (2003).

-
- [94] D. Gottesman: *Stabilizer Codes and Quantum Error Correction*, California Institute of Technology, Dissertation, May 1997.
- [95] J.W. Pan, M. Daniell, S. Gasparoni, G. Weihs and A. Zeilinger. Experimental Demonstration of Four-Photon Entanglement and High-Fidelity Teleportation, *Phys. Rev. Lett.* **86**, 4435 (2001).
- [96] Z. Zhao, Y.A. Chen, A.N. Zhang, T. Yang, H.J. Briegel and J.W. Pan. Experimental demonstration of five-photon entanglement and open-destination teleportation, *Nature* **430**, 54 (2004).
- [97] R.J. Nelson, D.G. Cory and S. Lloyd. Experimental demonstration of Greenberger-Horne-Zeilinger correlations using nuclear magnetic resonance, *Phys. Rev. A* **61**, 022106 (2000).
- [98] T. Aoki, N. Takei, H. Yonezawa, K. Wakui, T. Hiraoka, A. Furusawa and P. van Loock. Experimental Creation of a Fully Inseparable Tripartite Continuous-Variable State, *Phys. Rev. Lett.* **91**, 080404 (2003).
- [99] O. Glöckl, S. Lorenz, C. Marquardt, J. Heersink, M. Brownnutt, C. Silberhorn, Q. Pan, P. van Loock, N. Korolkova and G. Leuchs. Experiment towards continuous-variable entanglement swapping: Highly correlated four-partite quantum state, *Phys. Rev. A* **68**, 012319 (2003).
- [100] A. Karlsson and M. Bourennane. Quantum teleportation using three-particle entanglement, *Phys. Rev. A* **58**, 4394 (1998).
- [101] J. Kempe. Multiparticle entanglement and its applications to cryptography, *Phys. Rev. A* **60**, 910 (1999).
- [102] G.A. Durkin, C. Simon and D. Bouwmeester. Multiphoton Entanglement Concentration and Quantum Cryptography, *Phys. Rev. Lett.* **88**, 187902 (2002).
- [103] C.W. Zhang, C.F. Li, Z.Y. Wang and G.C. Guo. Probabilistic quantum cloning via Greenberger-Horne-Zeilinger states, *Phys. Rev. A* **62**, 042302 (2000).
- [104] J.C. Hao, C.F. Li and G.C. Guo. Controlled dense coding using the Greenberger-Horne-Zeilinger state, *Phys. Rev. A* **63**, 054301 (2001).
- [105] G. Tóth and O. Gühne. Entanglement detection in the stabilizer formalism, *Phys. Rev. A* **72**, 022340 (2005).
- [106] G. Tóth and O. Gühne. Detecting Genuine Multipartite Entanglement with Two Local Measurements, *Phys. Rev. Lett.* **94**, 060501 (2005).
- [107] V. Scarani, A. Acin, E. Schenck and M. Aspelmeyer. Nonlocality of cluster states of qubits, *Phys. Rev. A* **71**, 042325 (2005).
- [108] O. Gühne, G. Tóth, P. Hyllus and H.J. Briegel. Bell Inequalities for Graph States, *Phys. Rev. Lett.* **95**, 120405 (2005).

- [109] G. Tóth, O. Gühne and H.J. Briegel. Two-setting Bell inequalities for graph states, *Phys. Rev. A* **73**, 022303 (2006).
- [110] X. Zou, K. Pahlke and W. Mathis. Generation of arbitrary superpositions of the Dicke states of excitons in optically driven quantum dots, *Phys. Rev. A* **68**, 034306 (2003).
- [111] Y.F. Xiao, Z.F. Han, J. Gao and G.C. Guo. Generation of Multi-atom Dicke States with Quasi-unit Probability through the Detection of Cavity Decay, *quant-ph/0412202* (2004).
- [112] C. Thiel, J. von Zanthier, T. Bastin, E. Solano and G.S. Agarwal. Generation of Symmetric Dicke States of Remote Qubits with Linear Optics, *quant/ph0703137v1* (2007).
- [113] C.E. Lopez, J.C. Retamal and E. Solano. Selective Control of the Symmetric Dicke Subspace in Trapped Ions, *arXiv:0705:0375* (2007).
- [114] R.G. Unanyan and M. Fleischhauer. Decoherence-Free Generation of Many-Particle Entanglement by Adiabatic Ground-State Transitions, *Phys. Rev. Lett.* **90**, 133601 (2003).
- [115] M. Eibl, S. Gaertner, M. Bourennane, C. Kurtsiefer, M. Żukowski and H. Weinfurter. Experimental Observation of Four-Photon Entanglement from Parametric Down-Conversion, *Phys. Rev. Lett.* **90**, 200403 (2003).
- [116] H. Mikami, Y. Li, K. Fukuoka and T. Kobayashi. New High-Efficiency Source of a Three-Photon W State and its Full Characterization Using Quantum State Tomography, *Phys. Rev. Lett.* **95**, 150404 (2005).
- [118] M. Mura0, D. Jonathan, M.B. Plenio and V. Vedral. Quantum telecloning and multiparticle entanglement, *Phys. Rev. A* **59**, 156 (1999).
- [117] D. Bruß, D.P. DiVincenzo, A. Ekert, C.A. Fuchs, C. Macchiavello and J.A. Smolin. Optimal universal and state-dependent quantum cloning, *Phys. Rev. A* **57**, 2368 (1998).
- [119] A.K. Pati. Quantum cobwebs: Universal entangling of quantum states, *quant-ph/0101049* (2001).
- [120] B.S. Shi and A. Tomita. Teleportation of an unknown state by W state, *Phys. Lett. A* **296**, 161 (2002).
- [121] J. Joo and Y.J. Park. Comment on "Teleportation of an unknown state by W states": [Phys. Lett. A 296 (2002) 161], *Phys. Lett. A* **300**, 324 (2002).
- [122] B.S. Shi and A. Tomita. Reply to "Comment on: Teleportation of an unknown state by W state": [Phys. Lett. A 300 (2002) 324], *Phys. Lett. A* **300**, 538 (2002).
- [123] J. Joo, Y.J. Park, S. Oh and J. Kim. Quantum teleportation via a W state, *New J. Phys.* **5**, 136 (2003).

-
- [124] V. Gorbachev, A. Trubilko and A. Rodichkina. Can the states of the W-class be suitable for teleportation, *Phys. Lett. A* **314**, 267 (2003).
- [125] Y. Yeo. Quantum teleportation using three-particle entanglement, *quant-ph/0302030* (2003).
- [126] J. Joo, J. Lee, J. Jang and Y.J. Park. Quantum Secure Communication with W States, *quant-ph/0204003* (2002).
- [127] N. Kiesel, C. Schmid, G. Tóth, E. Solano and H. Weinfurter. Experimental Observation of Four-Photon Entangled Dicke State with High Fidelity, *Phys. Rev. Lett.* **98**, 063604 (2007).
- [128] G. Tóth. Detection of multipartite entanglement in the vicinity of Dicke states with many excitations, *quant-ph/0511237v1* page 6 (2005).
- [130] G. Tóth. Entanglement detection in optical lattices of bosonic atoms with collective measurements, *Phys. Rev. A* **69**, 052327 (2004).
- [129] A. Sorensen, L.M. Duan, J.I. Cirac and P. Zoller. Many-particle entanglement with Bose-Einstein condensates, *Nature* **409**, 63 (2001).
- [131] J.K. Korbicz, J.I. Cirac and M. Lewenstein. Spin Squeezing Inequalities and Entanglement of N Qubit States, *Phys. Rev. Lett.* **95**, 120502 (2005).
- [132] M. Ardehali. Bell inequalities with a magnitude of violation that grows exponentially with the number of particles, *Phys. Rev. A* **46**, 5375 (1992).
- [133] A.V. Belinskii and D.N. Klyshko. Interference of light and Bell's theorem, *Phys.-Usp.+* **36**, 653 (1993).
- [134] D. Collins, N. Gisin, S. Popescu, D. Roberts and V. Scarani. Bell-Type Inequalities to Detect True n -Body Nonseparability, *Phys. Rev. Lett.* **88**, 170405 (2002).
- [135] N. Kiesel, C. Schmid, U. Weber, G. Tóth, O. Gühne, R. Ursin and H. Weinfurter. Experimental Analysis of a Four-Qubit Photon Cluster State, *Phys. Rev. Lett.* **95**, 210502 (2005).
- [136] T. Eggeling: *On multipartite symmetric states in Quantum Information Theory*, TU Braunschweig, Dissertation, April 2003.
- [137] M. Bourennane, M. Eibl, S. Gaertner, C. Kurtsiefer, A. Cabello and H. Weinfurter. Decoherence-Free Quantum Information Processing with Four-Photon Entangled States, *Phys. Rev. Lett.* **92**, 107901 (2004).
- [138] S. Gaertner, M. Bourennane, M. Eibl, C. Kurtsiefer and H. Weinfurter. High-fidelity source of four-photon entanglement, *Appl. Phys. B* **V77**, 803 (2003).
- [139] J. Lau, S. Gaertner, N. Kiesel, M. Bourennane and H. Weinfurter. Experimental Quantum Telecloning, *unpublished* (2007).

- [140] S. Gaertner, C. Kurtsiefer, M. Bourennane and H. Weinfurter. Experimental Demonstration of Four-Party Quantum Secret Sharing, *Phys. Rev. Lett.* **98**, 020503 (2007).
- [141] C. Schmid, P. Trojek, S. Gaertner, M. Bourennane, C. Kurtsiefer, M. Żukowski and H. Weinfurter. Experimental quantum secret sharing, *Fortschr. Physik* **54**, 831 (2006).
- [142] W.K. Wootters and W.H. Zurek. A single quantum cannot be cloned, *Nature* **299**, 802 (1982).
- [143] G. Tóth and E. Solano *private communication*.
- [144] G.M. D'Ariano and P. Lo Presti. Optimal nonuniversally covariant cloning, *Phys. Rev. A* **64**, 042308 (2001).
- [145] B.E.A. Saleh and M.C. Teich: *Fundamentals of Photonics*, John Wiley & Sons, Inc., 1991.
- [146] L. Mandel and E. Wolf: *Optical Coherence and Quantum Optics*, Cambridge University Press, 1995.
- [147] P.G. Kwiat, K. Mattle, H. Weinfurter, A. Zeilinger, A.V. Sergienko and Y. Shih. New high-intensity source of polarization-entangled photon pairs, *Phys. Rev. Lett.* **75**, 4337 (1995).
- [148] H. Weinfurter and M. Żukowski. Four-photon entanglement from down-conversion, *Phys. Rev. A* **64**, 010102 (2001).
- [149] A. Lamas-Linares, J.C. Howell and D. Bouwmeester. Stimulated emission of polarization-entangled photons, *Nature* **412**, 887 (2001).
- [150] C. Kurtsiefer, M. Oberparleiter and H. Weinfurter. High-efficiency entangled photon pair collection in type-II parametric fluorescence, *Phys. Rev. A* **64**, 023802 (2001).
- [151] E. Knill, R. Laflamme and G.J. Milburn. A scheme for efficient quantum computation with linear optics, *Nature* **409**, 46 (2001).
- [152] N. Yoran and B. Reznik. Deterministic Linear Optics Quantum Computation with Single Photon Qubits, *Phys. Rev. Lett.* **91**, 037903 (2003).
- [153] D.E. Browne and T. Rudolph. Resource-Efficient Linear Optical Quantum Computation, *Phys. Rev. Lett.* **95**, 010501 (2005).
- [154] C. Schmid: *Kompakte Quelle verschränkter Photonen und Anwendungen in der Quantenkommunikation*, LMU, Diplomarbeit, January 2004.
- [155] A. Zeilinger. General properties of lossless beam splitters in interferometry, *Am. J. Phys.* **49**, 882 (1981).
- [156] U. Weber: *Das optische Phasengatter und Beobachtung eines vier-Photonen Cluster-Zustands*, LMU München, Diplomarbeit, March 2005.

-
- [157] N. Gisin. Hidden quantum nonlocality revealed by local filters, *Phys. Lett. A* **210**, 151 (1996).
- [158] C.K. Hong, Z.Y. Ou and L. Mandel. Measurement of subpicosecond time intervals between two photons by interference, *Phys. Rev. Lett.* **59**, 2044 (1987).
- [159] H. Weinfurter. Experimental Bell-state analysis, *Europhys. Lett.* **25**, 559 (1994).
- [160] S.L. Braunstein and A. Mann. Measurement of the Bell operator and quantum teleportation, *Phys. Rev. A* **51**, R1727 (1995).
- [161] M. Michler, K. Mattle, H. Weinfurter and A. Zeilinger. Interferometric Bell-state analysis, *Phys. Rev. A* **53**, R1209 (1996).
- [162] S. Gaertner, H. Weinfurter and C. Kurtsiefer. Fast and compact multichannel photon coincidence unit for quantum information processing, *Rev. Sci. Instrum.* **76**, 123108 (2005).
- [163] D.F.V. James, P.G. Kwiat, W.J. Munro and A.G. White. Measurement of qubits, *Phys. Rev. A* **64**, 052312 (2001).
- [164] J. Rehacek and M.G.A. Paris: *Lecture Notes in Physics: Quantum State Estimation*, Springer, 2004.
- [165] R. Blume-Kohout and P. Hayden. Accurate quantum state estimation via "Keeping the experimentalist honest", *quant-ph/0603116* (2006).
- [166] O. Gühne, P. Hyllus, D. Bruß, A. Ekert, M. Lewenstein, C. Macchiavello and A. Sanpera. Detection of entanglement with few local measurements, *Phys. Rev. A* **66**, 062305 (2002).
- [167] J.F. Poyatos, J.I. Cirac and P. Zoller. Complete Characterization of a Quantum Process: The Two-Bit Quantum Gate, *Phys. Rev. Lett.* **78**, 390 (1997).
- [168] I.L. Chuang and M.A. Nielsen. Prescription for experimental determination of the dynamics of a quantum black box, *J. Mod. Optic.* **44**, 2455 (1997).
- [169] M.W. Mitchell, C.W. Ellenor, S. Schneider and A.M. Steinberg. Diagnosis, Prescription, and Prognosis of a Bell-State Filter by Quantum Process Tomography, *Phys. Rev. Lett.* **91**, 120402 (2003).
- [170] K. Kraus, A. Böhm, J.D. Dollard, W.H. Wootters, K. Kraus, A. Böhm, J.D. Dollard and W.H. Wootters, editors *States, Effects, and Operations Fundamental Notions of Quantum Theory*, , volume 190 of *Lecture Notes in Physics*, Berlin Springer Verlag, (1983).
- [171] C. Schmid, N. Kiesel, U. Weber, R. Ursin, A. Zeilinger and H. Weinfurter. Complete Bell State Analysis for Quantum Teleportation, *unpublished* (2007).
- [172] C. Schmid: *in preparation*, LMU München, Dissertation.

- [173] T.B. Pittman, M.J. Fitch, B.C. Jacobs and J.D. Franson. Experimental controlled-NOT logic gate for single photons in the coincidence basis, *Phys. Rev. A* **68**, 032316 (2003).
- [174] K. Sanaka, T. Jennewein, J.W. Pan, K. Resch and A. Zeilinger. Experimental Non-linear Sign Shift for Linear Optics Quantum Computation, *Phys. Rev. Lett.* **92**, 017902 (2004).
- [175] S. Gasparoni, J.W. Pan, P. Walther, T. Rudolph and A. Zeilinger. Realization of a Photonic Controlled-NOT Gate Sufficient for Quantum Computation, *Phys. Rev. Lett.* **93**, 020504 (2004).
- [176] N.K. Langford, T.J. Weinhold, R. Prevedel, K.J. Resch, A. Gilchrist, J.L. O'Brien, G.J. Pryde and A.G. White. Demonstration of a Simple Entangling Optical Gate and Its Use in Bell-State Analysis, *Phys. Rev. Lett.* **95**, 210504 (2005).
- [177] N. Kiesel, C. Schmid, U. Weber, R. Ursin and H. Weinfurter. Linear Optics Controlled-Phase Gate Made Simple, *Phys. Rev. Lett.* **95**, 210505 (2005).
- [178] R. Okamoto, H.F. Hofmann, S. Takeuchi and K. Sasaki. Demonstration of an Optical Quantum Controlled-NOT Gate without Path Interference, *Phys. Rev. Lett.* **95**, 210506 (2005).
- [179] R.A. Campos, B.E.A. Saleh and M.C. Teich. Fourth-order interference of joint single-photon wave packets in lossless optical systems, *Phys. Rev. A* **42**, 4127 (1990).
- [180] A.G. White, A. Gilchrist, G.J. Pryde, J.L. O'Brien, M.J. Bremner and N.K. Langford. Measuring Controlled-NOT and two-qubit gate operation, *quant-ph/0308115* (2003).
- [181] T. Yamamoto, K. Tamaki, M. Koashi and N. Imoto. Polarization-entangled W state using parametric down-conversion, *Phys. Rev. A* **66**, 064301 (2002).
- [182] Y. Sagi. Scheme for generating Greenberger-Horne-Zeilinger-type states of n photons, *Phys. Rev. A* **68**, 042320 (2003).
- [183] W. Dür and J.I. Cirac. Multiparticle entanglement and its experimental detection, *J. Phys. A* **34**, 6837 (2001).
- [184] G. Tóth *Numerical Optimization performed by Géza Tóth*, 2005.
- [185] D. Kaszlikowski, A.S. (De), U. Sen, V. Vedral and A. Winter. Quantum Correlation Without Classical Correlations?, *arXiv:0705.1969* (2007).
- [186] V.N. Gorbachev and A.I. Trubilko. On multiparticle *W* states, their implementations and application in the quantum informational problems, *Laser Phys. Lett.* **3**, 59 (2006).
- [187] N. Gisin and S. Massar. Optimal Quantum Cloning Machines, *Phys. Rev. Lett.* **79**, 2153 (1997).

- [188] R. Raussendorf, D.E. Browne and H.J. Briegel. Measurement-based quantum computation on cluster states, *Phys. Rev. A* **68**, 022312 (2003).
- [189] D. Gross and J. Eisert. Novel Schemes for Measurement-Based Quantum Computation, *Physical Review Letters* **98**, 220503 (2007).
- [190] D. Markham, A. Miyake and S. Virmani. Entanglement and local information access for graph states, *quant-ph/0609102v2* (2007).
- [191] H.S. Eisenberg, G. Khoury, G.A. Durkin, C. Simon and D. Bouwmeester. Quantum Entanglement of a Large Number of Photons, *Phys. Rev. Lett.* **93**, 193901 (2004).

Danksagung

Zum Abschluss will ich nicht versäumen den Personen zu danken, die mich auf diesem Weg begleitet und damit zum Gelingen dieser Arbeit beigetragen haben.

Hier möchte ich zuerst meinen Doktorvater Harald Weinfurter nennen, der mir die Möglichkeit gegeben hat in diesem aufregenden Gebiet der Wissenschaft zu arbeiten. Ich bin sehr dankbar für seine stets offene Tür und die vielen anregenden Diskussionen. Die Freiheit eigene Ideen umzusetzen und die häufige Gelegenheit unsere Ergebnisse auf Tagungen zu präsentieren habe ich immer sehr zu schätzen gewusst.

Besonderer Dank gilt auch Christian Schmid für die harmonische, produktive und abwechslungsreiche Zusammenarbeit. Die vielen gemeinsamen Stunden im Labor, beim Diskutieren und auf Reisen werden mir immer eine schöne Erinnerung an diese Zeit bleiben. Ebenso möchte ich Witlief Wieczorek, dessen erfrischende und aufmunternde Art ich immer sehr zu schätzen wusste, herzlich für die vielen konstruktiven, sprühenden Diskussionen zu jeder Zeit, ob im Labor, Büro oder im Nachtzug, danken. Auch den regen Austausch mit Pavel Trojek habe ich immer sehr genossen, wie auch die vielen gemeinsamen fröhlichen Stunden im MPQ. Dank geht auch an Ulrich Weber für seine Mitwirkung bei unseren Experimenten und seine unerschütterlich gute Laune. Ihr alle habt die letzten Jahre zu etwas Besonderem für mich gemacht. Dafür möchte ich auch Mohamed Bourenane, Manfred Eibl, Reinhold Pohlner, Daniel Richart und Yousef Nazirizadeh meinen herzlichen Dank aussprechen.

Äußerst wertvoll waren auch die vielen angeregten Diskussionen mit unseren Kollaborationspartnern, denen ich für die konstruktive Zusammenarbeit und die vielen neuen Impulse danken möchte, namentlich Otfried Gühne, Enrique Solano, Géza Tóth, Rupert Ursin, Wieslaw Laskowski und Marek Żukowski.

Der Weg von Garching in die Stadt mag weit sein, trotzdem bin ich immer wieder auch gerne in die Schellingstrasse gekommen. Für die angenehme Atmosphäre in unserer Arbeitsgruppe möchte ich allen danken die dazu beitragen, bzw. beigetragen haben: Juliane Bahe, Stefan Berner, Andreas Deeg, Martin Fürst, Florian Henkel, Fredrik Hocke, Gerhard Huber, Christian Jakob, Michael Krug, Christian Kurtsiefer, Jan Lich, Davide Marangon, Nadja Regner, Wenjamin Rosenfeld, Karen Saucke, Daniel Schlenk, Tobias Schmitt-Manderbach, Sebastian Schreiner, Carsten Schuck, Asli Ugur, Jürgen Volz, Johannes Vrana, Chunlang Wang, Markus Weber, Henning Weier.

Ein besonders herzliches Dankeschön möchte ich meinen Eltern, Rosemarie und Werner Kiesel, aussprechen, die mir unendlich viel Verständnis und Unterstützung entgegenbringen. Das Wissen darum ist mir ein unerschöpflicher Vorrat an Kraft und Zuversicht. Was meine Freundin Angelika Krug in dieser Zeit über ihre Geduld und ihren Zuspruch hinaus für mich getan hat, kann ich in Worten nicht ausdrücken. Danke dafür!

Curriculum Vitae

Name: Nikolai Kiesel

Born: February 08, 1977 in Nürnberg, Germany

- 09/83 - 07/87 Grundschole Winkelhaid/Penzenhofen
- 09/88 - 07/96 Simon-Marius-Gymnasium Gunzenhausen
- 07/96 Abitur at the Simon-Marius-Gymnasium Gunzenhausen
- 10/96 - 10/02 Student of physics at the Ludwig-Maximilians-Universität München
- 02/00 - 07/00 ERASMUS student at the University of Coimbra, Portugal
- 10/01 - 10/02 Diploma thesis in the group of Prof. Dr. Harald Weinfurter, LMU München
Thesis: "Experimental Analysis of a Three-Photon Entangled State"
- 10/02 Diploma degree in physics at the Ludwig-Maximilians-Universität München
- since 04/03 PhD student in the group of Prof. Dr. Harald Weinfurter, LMU München
Thesis: "Experiments on Multiphoton Entanglement"